Joint assessment of seismic hazard in the pilot sites of the Greece-Türkiye CBA

Deliverable No: D2.2

WP2. A framework for seismic hazard assessment in the Greece-Türkiye CBA

Task T2.2 Joint assessment of seismic hazard in the pilot sites of the Greece-Türkiye CBA

DELIVERABLE COORDINATED BY:

INSTITUTE OF ENGINEERING SEISMOLOGY & EARTHQUAKE ENGIN.- EARTHQUAKE PLANNING AND PROTECTION ORGANIZATION (ITSAK/EPPO)

INVOLVED PARTNERS:

DIETHNES PANEPISTIMIO ELLADOS (IHU)

ICISLERI BAKANLIGI AFET VE ACIL DURUM YONETIMI BASKANLIGI (AFAD)

GEBZE TEKNIK UNIVERSITESI (GTU)

PROJECT DETAILS

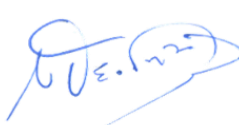|	EUROPEAN COMMISSION Directorate-General for European Civil Protection and Humanitarian Aid Operations (ECHO) ECHO.B – Disaster Preparedness and Prevention B.2 – Prevention and Disaster Risk Management
Project No	101101206
Project Name	Earthquake Resilient Schools
Project Acronym	EReS
Call	UCPM-2022-PP
Topic	UCPM-2022-PP
Type of action	UCPM Project Grants
Granting authority	European Commission-EU
Lead Partner	DIETHNES PANEPISTIMIO ELLADOS (IHU)
Total Budget	923.784,50 Euro (€)
Grant Amount	785.215,92 Euro (€)
Time Frame: Start Date – End Date	01/03/2023 – 28/02/2025
Project Coordinator	Papatheodorou K. (IHU)

DELIVERABLE CONTRIBUTORS

ITSAK/EPPO: Theodoulidis N., Margaris B., Sotiriadis D., Grendas I.

IHU: Papatheodorou K., Evangelidis K., Konstantinidis A., Scordilis E.

AFAD: Yılmaz N., Türkoğlu M., Tekin B., Ateş E.

GTU: Zülfikar C., Fahjan Y., Fercan Ö., Gündoğdu Gök M., Simsek D., Ghassemi P.

DOCUMENT RELEASE SHEET

Deliverable Responsible Partner: PARTNER ACRONYM (e.g. IHU)		
Approval	Konstantinos Papatheodorou (IHU)	Signature 25.04.2024
Approval	Can Zulfikar (GTU)	Signature 25.04.2024
Approval	Murat Nurlu (AFAD)	Signature 25.04.2024
Approval	Nikolaos Theodoulidis (ITSAK/OASP)	Signature 25.04.2024
Distribution:	ALL PARTNERS	

RECORD OF REVISIONS

Release	Date	Description of Change
v.01	**15.04.2024**	First version of document
v.02	20.04.2024	First Revision
v.02	25.04.2024	Final document

TABLE OF CONTENTS

BACKGROUND OF THE DOCUMENT

1.1 RELATED WORKPACKAGE AND TASKS

This document describes the activities that took place in the framework of the WP2: A framework for seismic hazard assessment in the Greece-Türkiye CBA and is related to the Task Task T2.2: Joint assessment of seismic hazard in the pilot sites of the Greece-Türkiye CBA.

This project Activity relates to the joint Seismic Hazard Assessment (PSHA-Part 1) and Deterministic Seismic Hazard Assessment (DSHA-Part 2) on rock conditions, for the Greece-Türkiye CBA.

1.2 SCOPE AND OBJECTIVES

The scope of this document is to outline the activities carried out within the framework of Task 2.2 aimed at accomplishing the project objectives. These efforts are ultimately geared towards attaining the Specific Objective of "Seismic Hazard Assessments" as stipulated by the funding Programme under the Call "Prevention and Preparedness Projects on Civil Protection and Marine Pollution (UCPM-2022-PP)." In pursuit of this goal, the present deliverable places emphasis on the following project objectives:

- In Seismicity of the CBA is studied and presented as an introduction of the following results.
- In Seismic Hazard Assessment (both Probabilistic and Deterministic) as a fundamental component of Seismic Risk estimation of any element at risk. In this project harmonized seismic hazard assessment is attempted in the Greece -Turkiye Cross Border Area (CBA) based on jointly selected input parameters regarding seismic source, propagation path and site factors, aiming at providing rationale seismic actions for school buildings in the Greece-Turkey CBA.

Seismic hazard is assessed for various Ground Motion Intensity Measures (GMIMs), more specifically for Peak Ground Acceleration (PGA), Peak Ground Velocity (PGV), Spectral Acceleration (Sa, (T)=0.3, 0.6, 1.0sec) for mean return periods Tm=100, 475, 950years. In addition, causative seismic faults in the vicinity of the project's pilot sites, are used in seismic scenarios to estimate deterministic seismic hazard intesntity measures as well. These GMIMs are going to be used in the next deliverables with respect to harmonize seismic risk assessment of school buildings in the Greece-Turkiye CBA.

2 TIME INDEPENDENT SEISMICITY TO BE USED IN SEISMIC HAZARD ASSESSMENT UNDER THE ERES PROJECT

The test-sites of the project are four cities in the common border area (CBA) between Greece and Turkiye, namely Alexandroupoli, Canakkale, Izmir and Samos (Vathy) (see table 1). By considering circles of radius R=200km centered on each of these cities, a wide region is defined (yellow circles in figure 1). To avoid any possible phenomena of edge effects, we extended this region by creating a frame bounded by the coordinates 22.5-30.5°E and 35.0-43.0°N. Then we collected information regarding the focal parameters of all available earthquakes that occurred within this frame over a wide period (red dashed line in figure 1). Thus, a new earthquake catalog was created, to be used to assess the seismic hazard of this wide area.

Table 1: Geographical coordinates of the four cities/test-sites of the project in the Greece-Turkiye common border area (CBA).

Site/City	Latitude	Longitude
Alexandroupoli	40.8491	25.8793
Canakkale	40.1467	26.4086
Izmir	38.4237	27.1428
Samos (Vathy)	37.7572	26.9769

The steps that were followed for this purpose are presented in details in the next chapter.
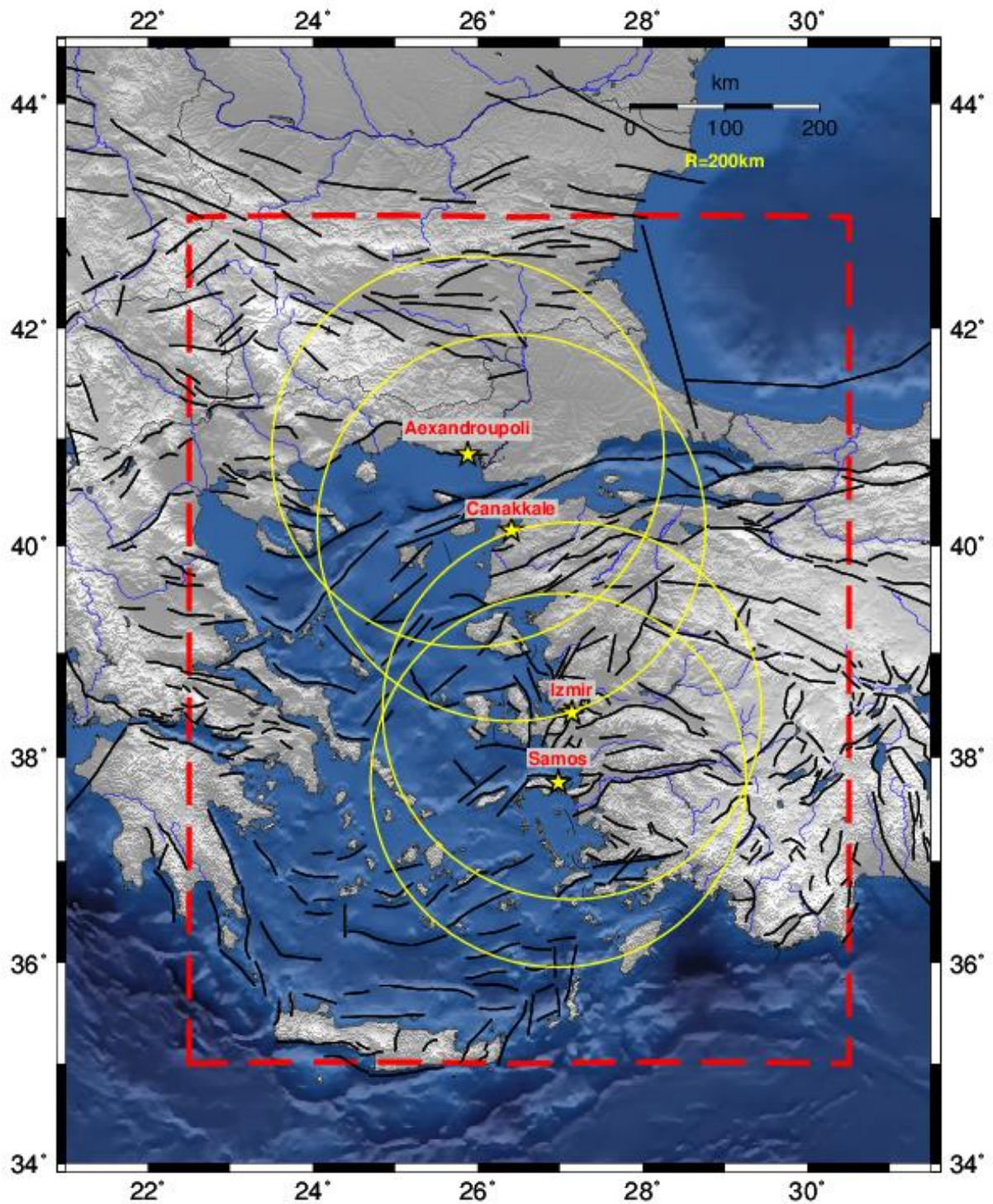
Figure 1: The red dashed line defines the wide region the seismicity of which will be studied. Yellow circles delimit circular areas of R=200km centered on each pilot-site (marked with yellow star).

2.1 CREATION OF THE CATALOG

The catalog to be created must satisfy the following requirements:

1) To span a long period of time in order to be as representative as possible of the background seismicity of the area
2) To include uniformly estimated focal parameters of the earthquakes to assure homogeneity.
3) All the magnitudes must be expressed in one, unique, reliable and widely used magnitude scale.

Several data sources (e.g. bulletins or catalogs of regional centers and networks) were used to prepare the catalog. More specifically, these sources are:

- ISC bulletins (http://www.isc.ac.uk/iscbulletin/)
- Papazachos and Papazachou, (1997)
- Papazachos and Papazachou, (2003)
- Karnik, (1996)
- Engdahl and Villaseñor (2002)
- Comninakis and Papazachos, (1986)
- Pacheco and Sykes, (1992)
- Ambraseys, (2009)
- Gutenberg and Richter (1954, 1956)
- Bulletins of AUTh
- On-line catalog of NOA

To overcome the issue of different focal parameters reported for the same earthquakes by different agencies it is a good practice to adopt solutions published by the International Seismological Center, ISC (figure 2). The main reason is that for the estimation of focal parameters the ISC follows a specific, unified procedure and for this purpose it uses a large amount of data collected from all cooperating regional networks. Therefore, all focal parameters published by the ISC are homogeneously defined and, consequently, consistent with each other. The reviewed data by ISC, at the moment of writing this report, cover the period 1964-2021/09 (figure 2).

For earthquakes that occurred before 1964, their data will be adopted from already published earthquake catalogs (mentioned above).
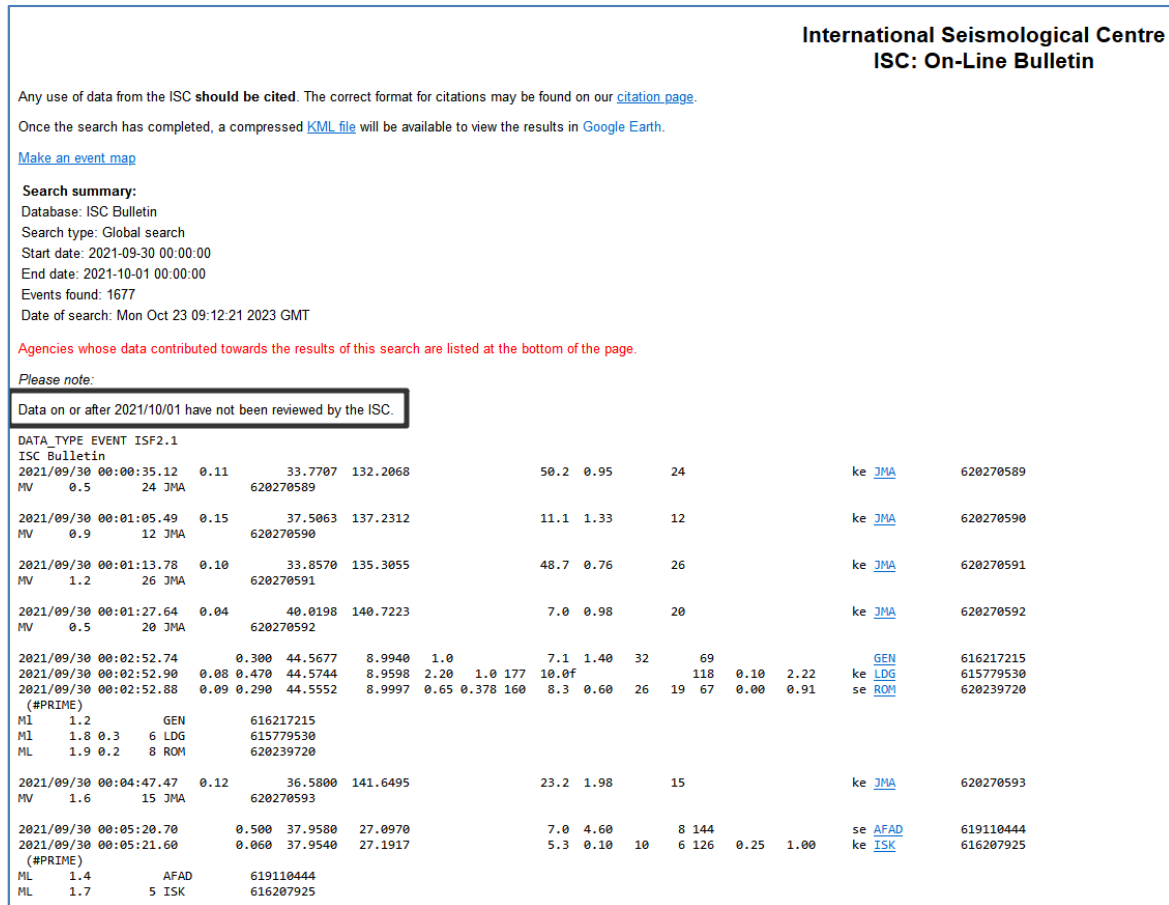
Figure 2: Screen-shot of the output after an ISC bulletin search. It is noticed that *"Data on or after 2021/10/01 have not been reviewed by the ISC"*.

To ensure the magnitude homogeneity of the catalog, the moment magnitude scale has been selected as the reference one because:

- o It scales linearly with seismic moment and energy for a wide magnitude range
- o It does not saturate

All other magnitude types (available from the original sources) were transformed into the moment magnitude scale, M_w, by appropriate formulas already published (e.g. Papazachos et al., 1997; Baba et al., 2000; Scordilis, 2005, 2006; Duni et al., 2010, Tsampas et al., 2016). Indicatively, relations between other magnitude scales and moment magnitude, valid for shallow earthquakes, that are used here, are given in Table 2. Respective relations, valid for intermediate depth earthquakes, were also used (Table 3).

Table 2: Relations used in the present study to convert magnitudes of shallow earthquakes into equivalent moment magnitudes.

Calibrated Magnitudes	Converting Relation	Reference
M JMA	$M_w^* = 0.58 M_{JMA} + 2.25, \quad 3.0 \le M_{JMA} \le 5.5, \quad \sigma = 0.28$	Scordilis (2005)
	$M_w^* = 0.97 M_{JMA} + 0.04, \quad 5.6 \le M_{JMA} \le 8.2, \quad \sigma = 0.22$	
m_b ISC/NEIC	$M_w^* = 0.85 m_b + 1.03, \quad 3.5 \le m_b \le 6.2, \quad \sigma = 0.29$	Scordilis (2006)
Ms ISC/NEIC	$M_w^* = 0.67 M_s + 2.07, \quad 3.0 \le M_s \le 6.1, \quad \sigma = 0.17$	
	$M_w^* = 0.99 M_s + 0.08, \quad 6.2 \le M_s \le 8.2, \quad \sigma = 0.20$	
M Karnik	$M_w^* = 0.80 M_k + 1.31, \quad 4.0 \le M_k \le 5.3, \quad \sigma = 0.41$	
	$M_w^* = 0.70 M_k + 1.80, \quad 5.4 \le M_k \le 6.2, \quad \sigma = 0.29$	
	$M_w^* = 1.04 M_k - 0.33, \quad 6.3 \le M_k \le 8.1, \quad \sigma = 0.31$	
M_L ISK	$M_w^* = 1.39 M_{L-ISK} - 1.08, \quad 2.8 \le M_{L-ISK} \le 5.5, \quad \sigma = 0.30$	Baba et al. (2000)
M_L TIR	$M_w^* = 1.11 M_{L-TIR} + 0.21, \quad 2.3 \le M_{L-TIR} \le 5.2, \quad \sigma = 0.30$	
M_L PDG	$M_w^* = 1.08 M_{L-PDG} + 0.22, \quad 2.6 \le M_{L-PDG} \le 5.9, \quad \sigma = 0.30$	
M_L SKO	$M_w^* = 0.76 M_{L-SKO} + 1.45, \quad 2.1 \le M_{L-SKO} \le 5.7, \quad \sigma = 0.30$	
M_L TIR	$M_w^* = 0.743 M_{L-TIR} + 1.624, \quad 3.2 \le M_{L-TIR} \le 7.2, \quad \sigma = 0.301$	Duni (2010)
M_L PDG	$M_w^* = 0.985 M_{L-PDG} + 0.218, \quad 3.8 \le M_{L-PDG} \le 6.9, \quad \sigma = 0.163$	
M_L ZAG	$M_w^* = 0.979 M_{L-ZAG} + 0.165, \quad 3.9 \le M_{L-ZAG} \le 7.0, \quad \sigma = 0.167$	
M_L BGY	$M_w^* = 0.963 M_{L-BGY} + 0.324, \quad 3.8 \le M_{L-BGY} \le 6.9, \quad \sigma = 0.200$	
M_L SKO	$M_w^* = 0.880 M_{L-SKO} + 0.912, \quad 3.5 \le M_{L-SKO} \le 6.9, \quad \sigma = 0.210$	

Table 3: Relations used in the present study to convert magnitudes of intermediate depth earthquakes into equivalent moment magnitudes.

Calibrated Magnitudes	Converting Relation	Reference
m_b ISC/NEIC	$M_w^* = 0.165 m_{b-IN}^2 - 0.372\, m_{b-IN} + 2.816$ $\sigma = 0.214, \qquad 3.6 \leq m_{b-IN} \leq 6.3$	Tsampas et al. (2016)
m_b MOS	$M_w^* = 0.143 m_{b-MOS}^2 - 0.288\, m_{b-MOS} + 2.716$ $\sigma = 0.257, \qquad 4.3 \leq m_{b-MOS} \leq 6.5$	
m_b BJI	$M_w^* = -0.204\, m_{b-BJI}^2 + 3.515\, m_{b-BJI} - 7.418$ $\sigma = 0.239, \qquad 4.5 \leq m_{b-BJI} \leq 6.4$	
m_B BJI	$M_w^* = -0.207\, m_{B-BJI}^2 + 3.617 m_{B-BJI} - 7.984$ $\sigma = 0,215, \qquad 4.6 \leq m_{B-BJI} \leq 7.9$	
m_b IDC	$M_w^* = 0.045\, m_{b-IDC}^2 + 0.837\, m_{b-IDC} + 0.382$ $\sigma = 0.226, \qquad 3.3 \leq m_{b-IDC} \leq 6.1$	
M_s ISC/NEIC	$M_w^* = 0.790\, M_{s-IN} + 1.551$ $\sigma = 0.199, \qquad 3.1 \leq M_{s-IN} \leq 7.9$	
M_s IDC	$M_w^* = -0.140\, M_{s-IDC}^2 + 2.105\, M_{s-IDC} - 1.120$ $\sigma = 0.229, \qquad 2.9 \leq M_{s-IDC} \leq 6.5$	
M_s BJI	$M_w^* = 0.004 M_{s-BJI}^2 + 0.792\, M_{s-BJI} + 1.300$ $\sigma = 0.224, \qquad 4.2 \leq M_{s-BJI} \leq 7.3$	
M_s MOS	$M_w^* = -0.006\, M_{s-MOS}^2 + 0.850\, M_{s-MOS} + 1.540$ $\sigma = 0.219, \qquad 4.4 \leq M_{s-MOS} \leq 7.7$	
M JMA	$M_w^* = 0.923\, M_{JMA} + 0.370$ $\sigma = 0.233, \qquad 3.5 \leq M_{JMA} \leq 7.4$	

The finally adopted magnitude for each earthquake of the formed catalog is either the **original** moment magnitude (published by Pacheco and Sykes, 1992; GCMT and/or USGS), if available, or the **equivalent** moment magnitude, estimated as the **weighted mean** of the converted magnitudes, by weighting each participating magnitude with the inverse standard deviation of the respective calibrating relation applied.

The final catalog, which created through the above procedure, covers the region bounded by the coordinates 35.0°-43.0°N and 22.5°-30.5°E and expands over the period 550BC-2021 (end of September). It lists 23107 earthquakes with magnitudes (original moment magnitudes or equivalent ones) ranging between 2.7 and 8.3.
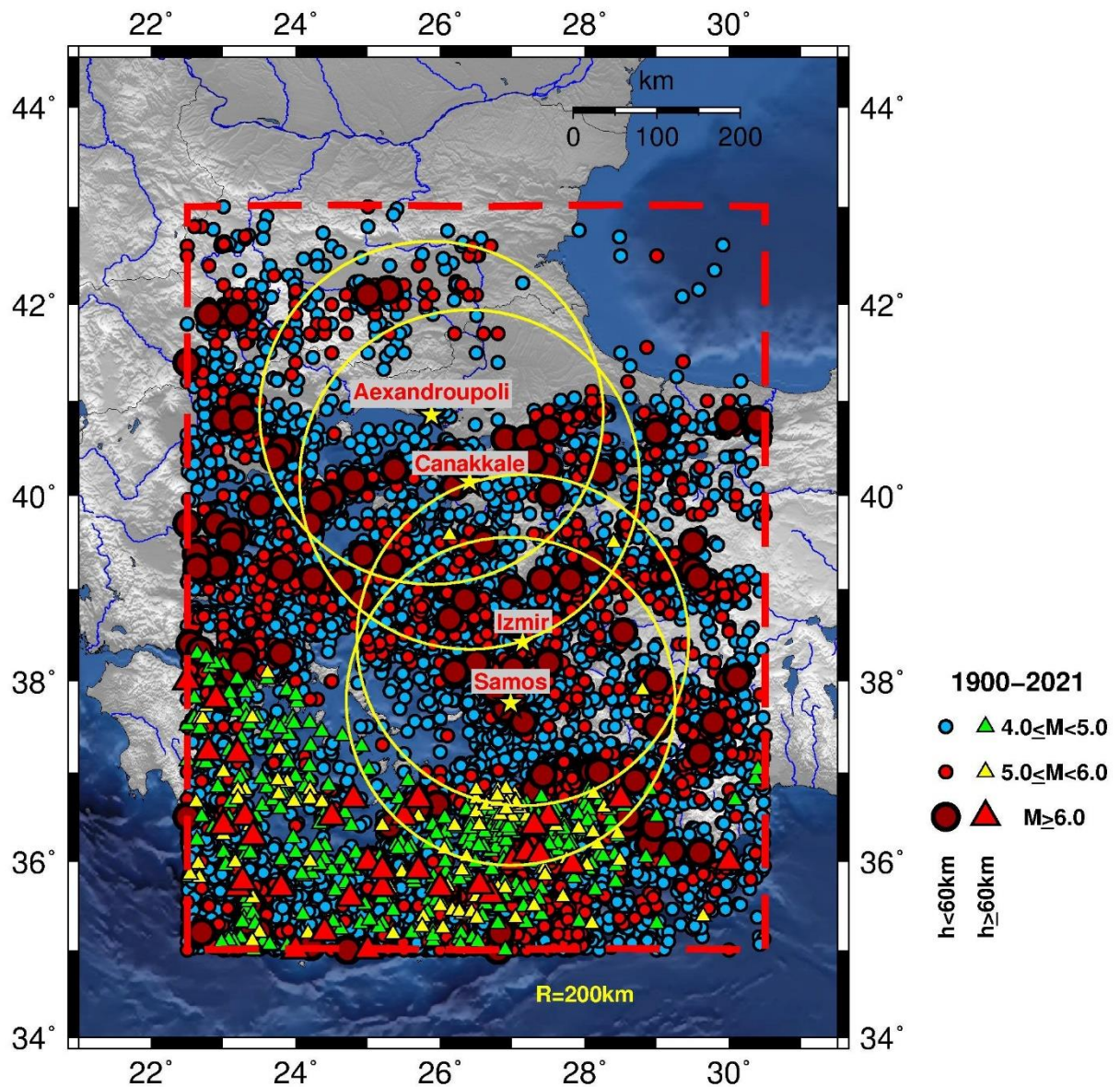
Figure 3: Epicenters of the earthquakes of the catalog that occurred within the defined frame (red dashed lines) during the period 1900-2021 (end of September). Small circles and triangles correspond to epicenters of shallow (0-60km) and intermediate depth (60-200km) earthquakes respectively, with their dimension scaled according to earthquake magnitude. Yellow circles delimit circular areas of R=200km centered on each pilot-site.

The map of figure 3 presents the spatial distribution of the seismicity in this region during the covered period, based on the data of the new catalog. It is clear that shallow earthquakes dominate the catalog despite the presence of some intermediate depth ones in south Aegean along the Hellenic arc (represented by triangles). The absence of seismicity is also distinct in the region of NE Greece (near the city of Alexandroupoli) as well as in NW Turkey and the SW Aegean (Cyclades islands).

The formatted catalog was examined qualitatively and quantitatively by studying the completeness magnitude, as well as its variation both with time and in space. This study was performed for three independent data sets, namely for shallow earthquakes (focal depths 0-59km), for intermediate depth events (focal depths 60-200km) and for the whole data set (focal depths 0-200km).

2.2 THE COMPLETENESS MAGNITUDE, M_C, OF THE CATALOG

In this section, we examine the completeness magnitude of the earthquakes of the formed catalog, as well as its variation with time and in space.

2.2.1 Variation of Mc with time

The variation of Mc with time is a very delicate issue as it is strongly depended on the detectability of the operating regional seismological networks. Therefore, we expect a systematic decay of the Mc values with time.

To check the time-dependency of the catalog's completeness, sample windows of several sizes were considered and repeating estimations after bootstrapping were attempted. Four methods have been applied, namely the maximum curvature method (MAXC), the goodness of fit method (GoF) with confidence limits 90% and 95% and the entire magnitude range method (EMR) with the help of the ZMAP software package (Wiemer, 2001).

2.2.1.1 Shallow events

The graphs of Figures 4, 5, 6, 7, 8 and 9 present the time variation of the completeness magnitude, Mc, of shallow events (focal depths up to 60km) as obtained by combination of the 4 different methods, MAXC, GoF 90%, GoF 95% and EMR. Examination of the corresponding plots reveals rather constant values of Mc for specific periods.
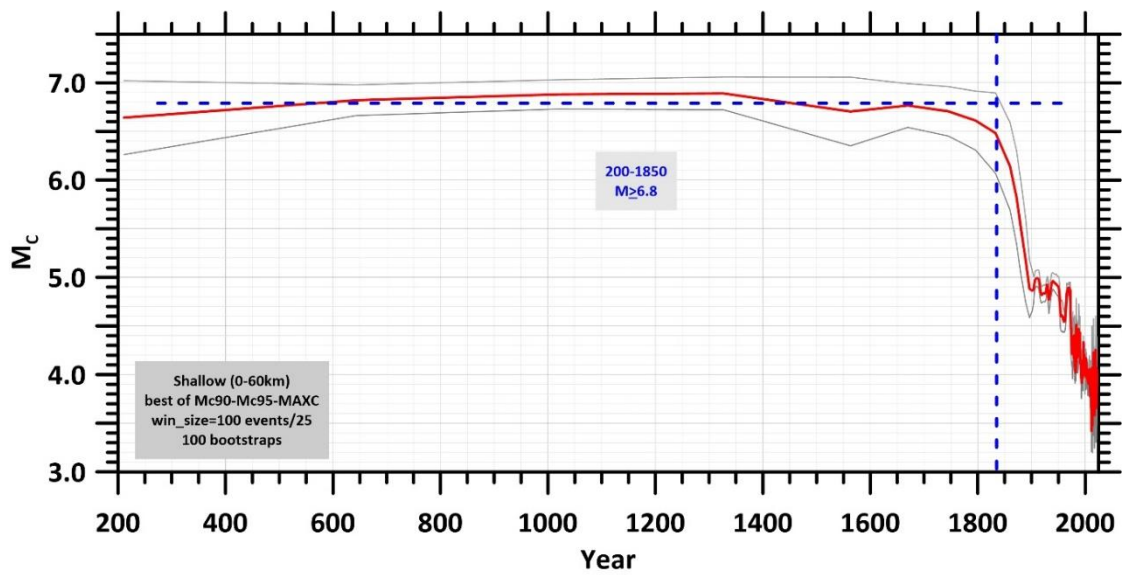
Figure 4: Time variation of the completeness magnitude, Mc, for the compiled catalog (period 550BC-2021, shallow events) resulted after combined application MAXC, GoF 90%, GoF 95% and EMR methods. Gray lines represent the uncertainties revealed after resampling (sample size 100, moving step 25, 100 bootstraps).

Figure 5: Time variation of the completeness magnitude, Mc, for the compiled catalog (period 1900-2021, shallow events) resulted after combined application MAXC, GoF 90%, GoF 95% and EMR methods. Gray lines represent the uncertainties revealed after resampling (sample size 100, moving step 25, 100 bootstraps).
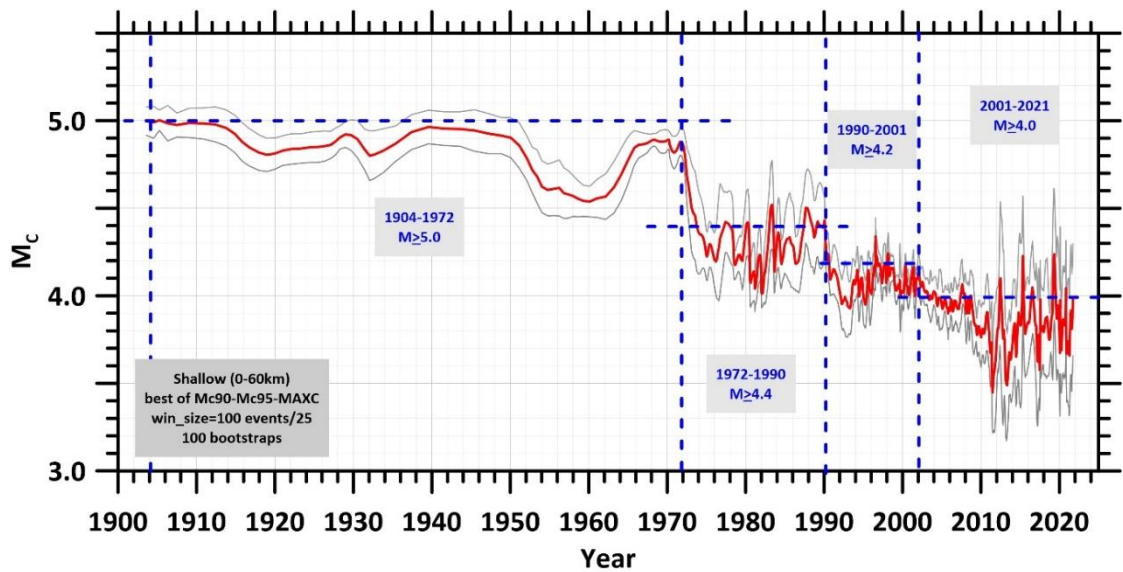
Figure 6: Time variation of the completeness magnitude, Mc, for the compiled catalog (period 1800-1960, shallow events) resulted after combined application MAXC, GoF 90%, GoF 95% and EMR methods. Gray lines represent the uncertainties revealed after resampling (sample size 100, moving step 25, 100 bootstraps).
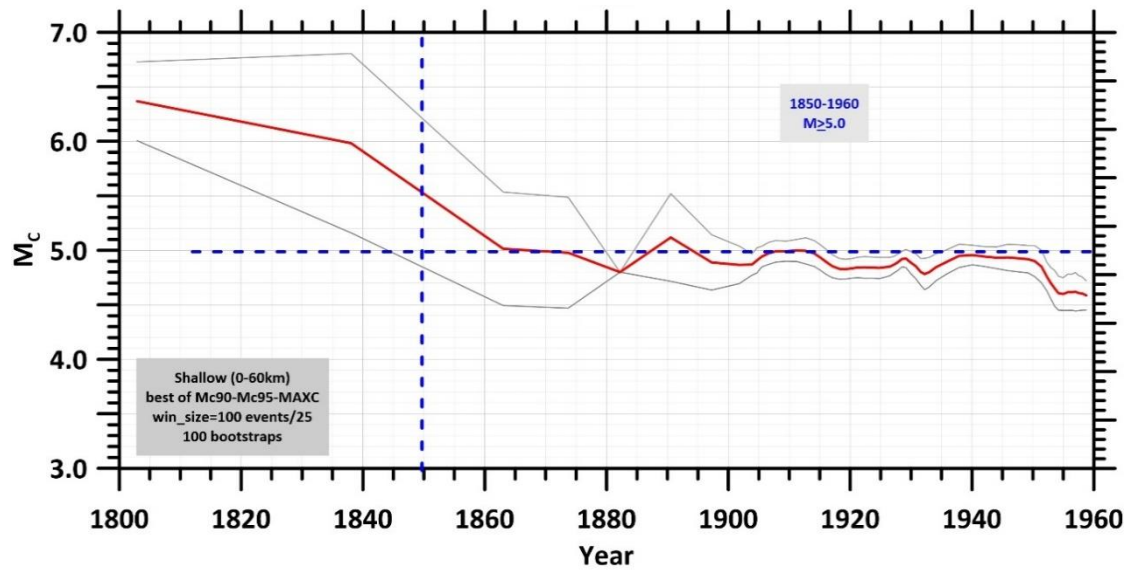

Figure 7: Time variation of the completeness magnitude, Mc, for the compiled catalog (period 1900-1960, shallow events) resulted after combined application MAXC, GoF 90%, GoF 95% and EMR methods. Gray lines represent the uncertainties revealed after resampling (sample size 100, moving step 25, 100 bootstraps).
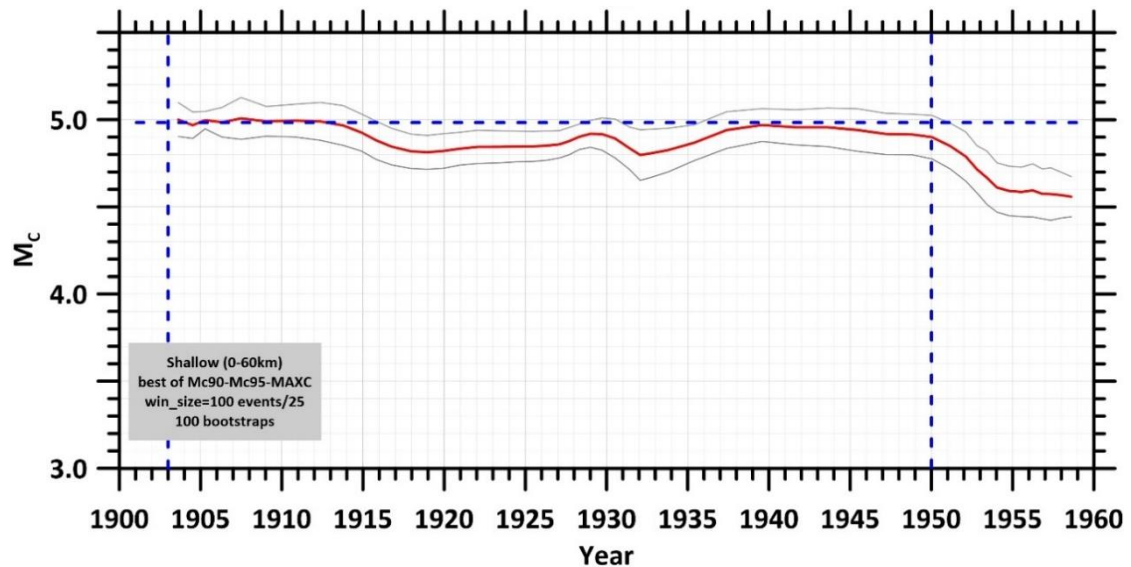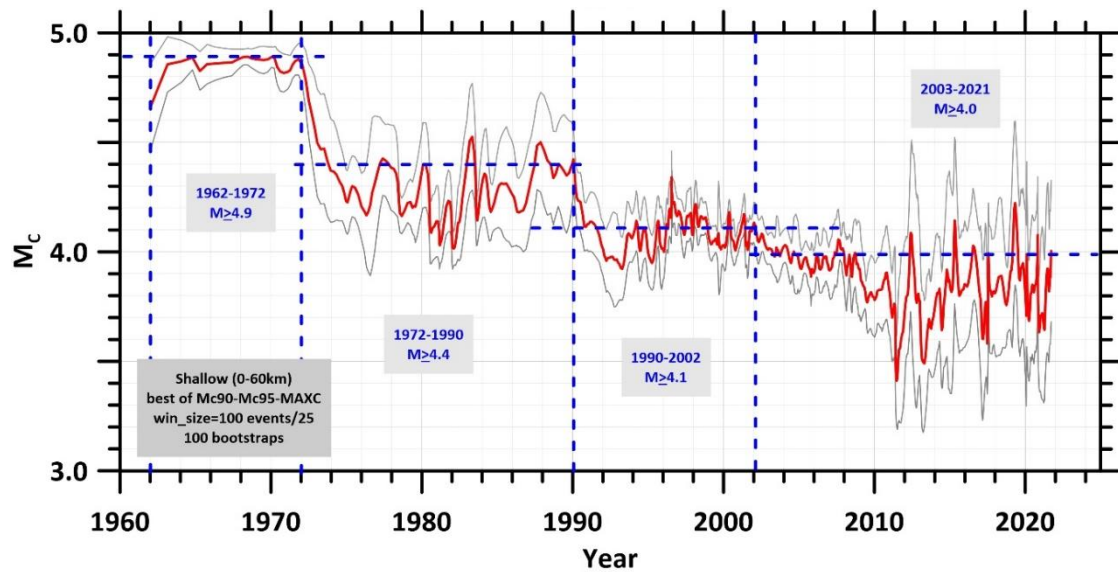
Figure 8: Time variation of the completeness magnitude, Mc, for the compiled catalog (period 1960-2021, shallow events) resulted after combined application MAXC, GoF 90%, GoF 95% and EMR methods. Gray lines represent the uncertainties revealed after resampling (sample size 100, moving step 25, 100 bootstraps).

Figure 9: Time variation of the completeness magnitude, Mc, for the compiled catalog (period 1980-2021, shallow events) resulted after combined application MAXC, GoF 90%, GoF 95% and EMR methods. Gray lines represent the uncertainties revealed after resampling (sample size 100, moving step 25, 100 bootstraps).
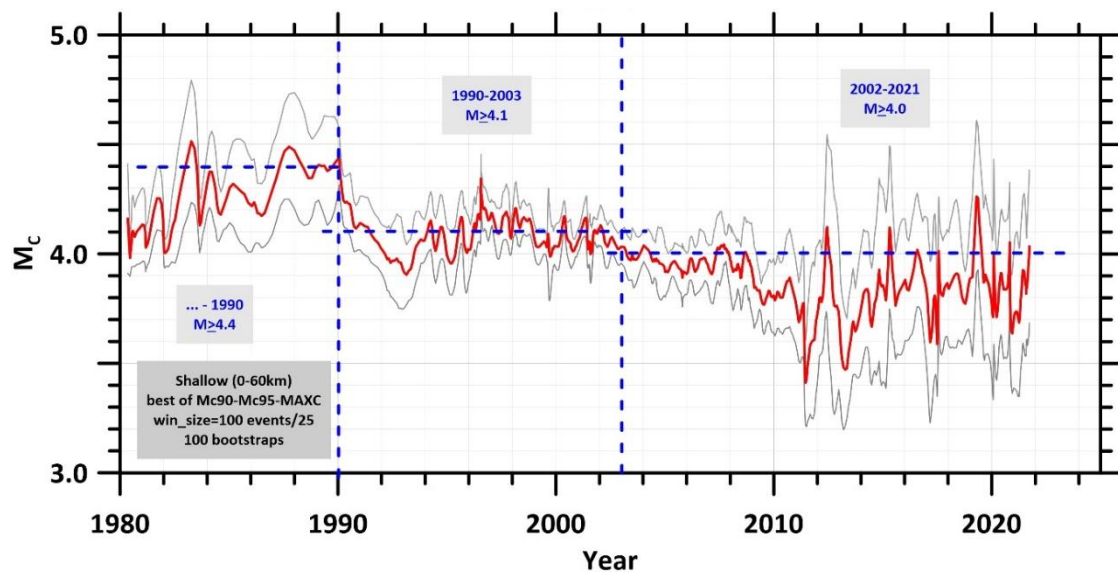
To double check and confirm the results regarding the time variation of Mc, we also studied the rates of seismicity, that is, the time variation of the cumulative number of earthquakes with magnitudes over a certain value (figures 10-13).
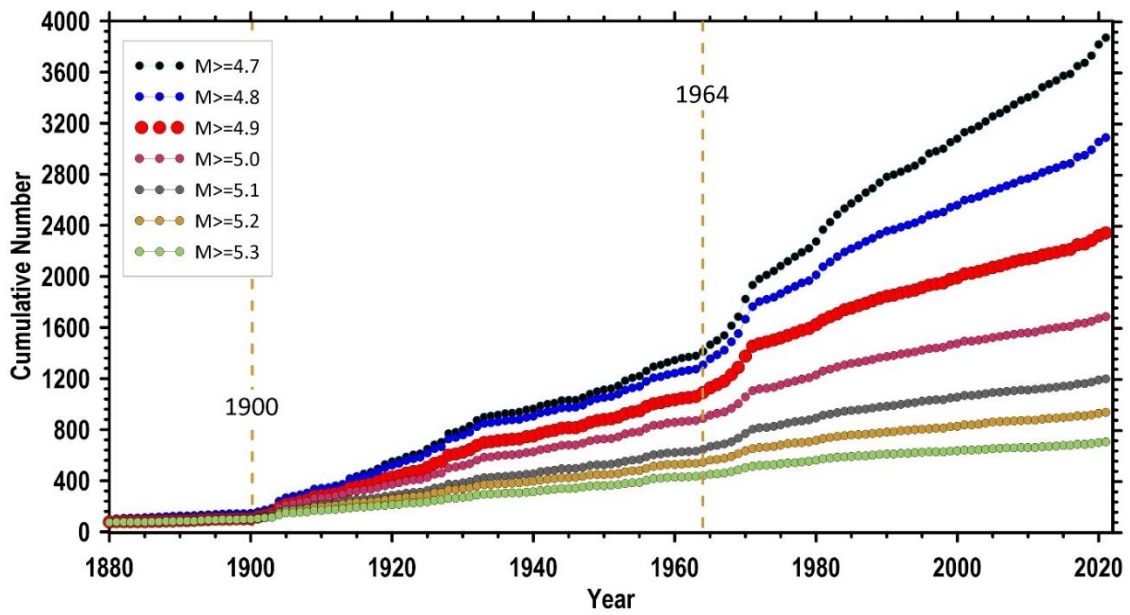
Figure 10: Time variation of the cumulative number of shallow earthquakes (rates) with magnitudes above certain values (period 1880-2021).
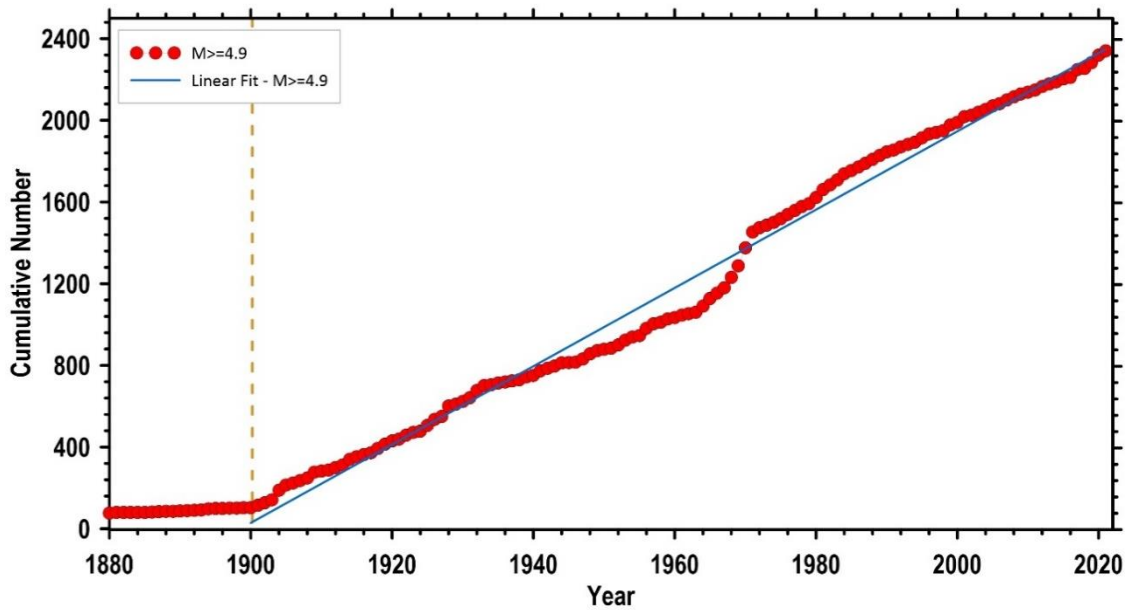

Figure 11: Time variation of the cumulative number of shallow earthquakes (rates) with M≥4.9 (period 1880-2021).
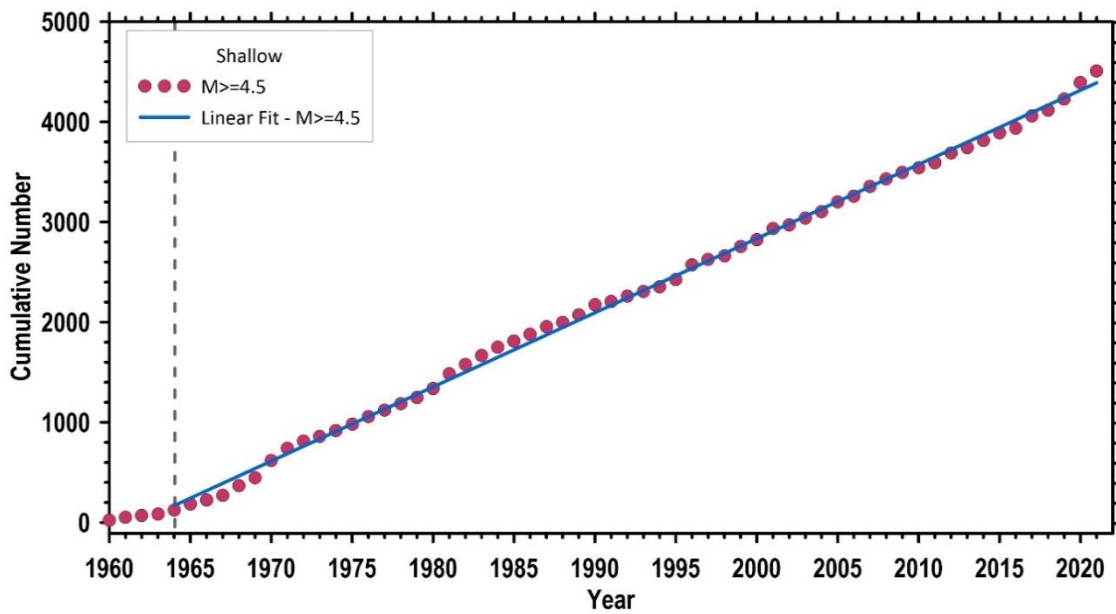
Figure 12: Time variation of the cumulative number of shallow earthquakes (rates) with M≥4.5 (period 1960-2021).
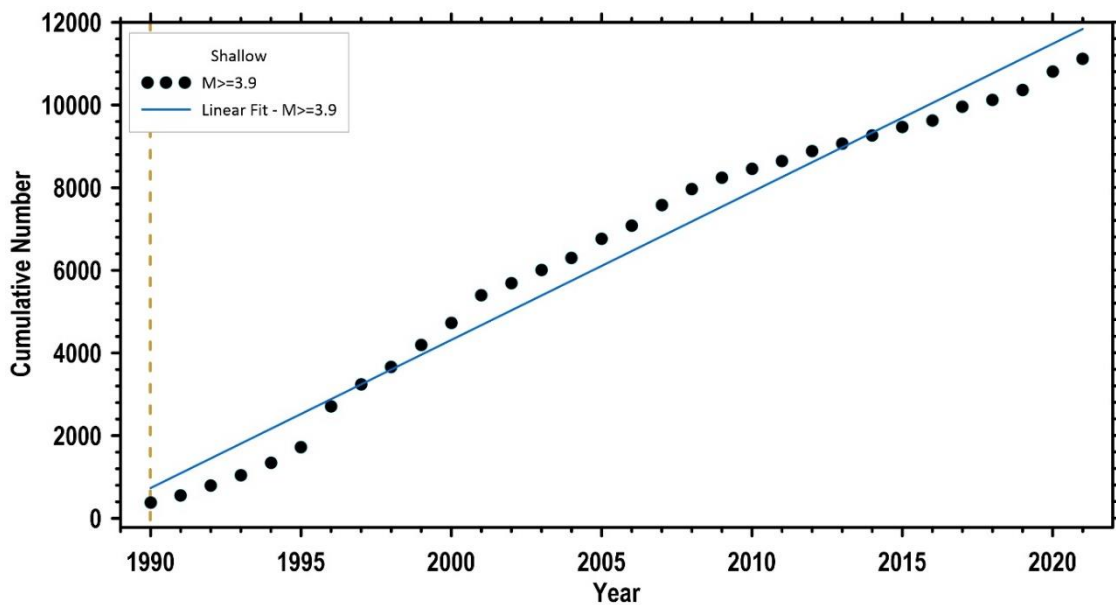
Figure 13: Time variation of the cumulative number of shallow earthquakes (rates) with M≥3.9 (period 1990-2021).

The study of the rates is also pointing to completeness periods and magnitudes almost identical with the ones revealed during the previous stage.

Combining the information provided by all the previously commented figures (figures 4-13), the following finally accepted completeness periods and respective magnitudes are proposed for the shallow (focal depths up to 60km) earthquakes of the catalog:

<1900 M_c=???

$$1900\text{-}2021 \quad M_c=4.9 \tag{1}$$
$$1964\text{-}2021 \quad M_c=4.5$$
$$1990\text{-}2021 \quad M_c=3.9$$

Therefore, and with a rather conservative approach, we will accept that the earthquake catalog is complete for shallow earthquakes of magnitude $M \geq 4.9$ since 1900 and up to 2021.

2.2.1.2 Intermediate depth events

The graphs of Figures 14, 15 and 16 present the time variation of the completeness magnitude, Mc, of intermediate depth (focal depths 60-200km) events as obtained by combination of the 4 different methods, MAXC, GoF 90%, GoF 95% and EMR. Examination of the corresponding plots reveals rather constant values of Mc for specific periods.

Figure 14: Time variation of the completeness magnitude, Mc, for the compiled catalog (period 1840-2021, intermediate depth events) resulted after combined application of the MAXC, GoF 90%, GoF 95% and EMR methods. Gray lines represent the uncertainties revealed after resampling (sample size 50, moving step 20, 100 bootstraps).
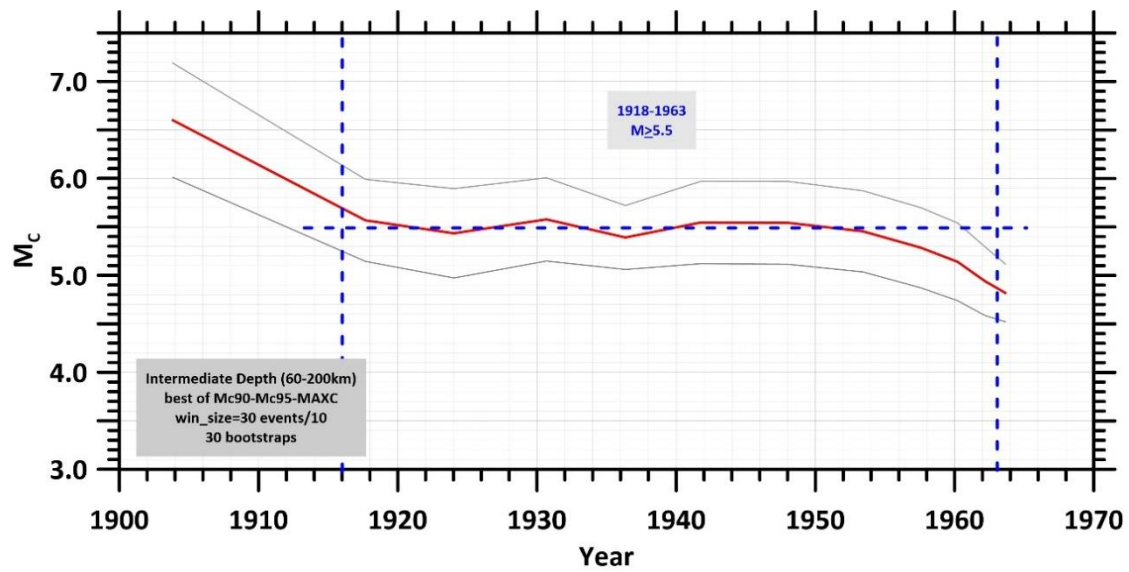
Figure 15: Time variation of the completeness magnitude, Mc, for the compiled catalog (period 1900-1970, intermediate depth events) resulted after combined application of the MAXC, GoF 90%, GoF 95% and EMR methods. Gray lines represent the uncertainties revealed after resampling (sample size 30, moving step 10, 30 bootstraps).
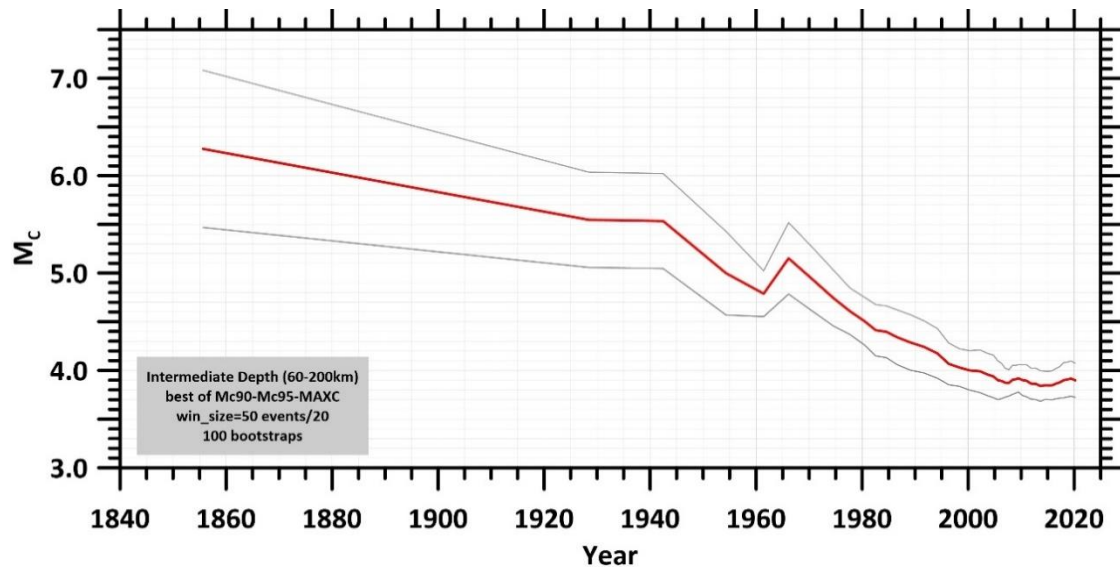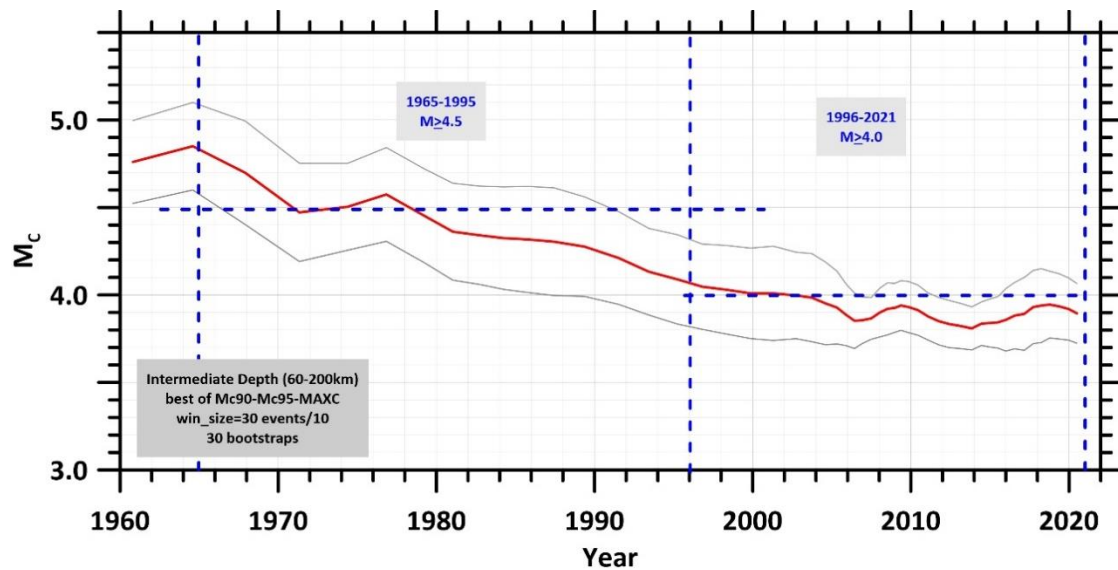
Figure 16: Time variation of the completeness magnitude, Mc, for the compiled catalog (period 1960-2021, intermediate depth events) resulted after combined application of the MAXC, GoF 90%, GoF 95% and EMR methods. Gray lines represent the uncertainties revealed after resampling (sample size 30, moving step 10, 30 bootstraps).

To double check and confirm the results regarding the time variation of Mc of the intermediate depth earthquakes of the catalog, we also studied the rates, that is, the time variation of the cumulative number of earthquakes with magnitudes over a certain value.
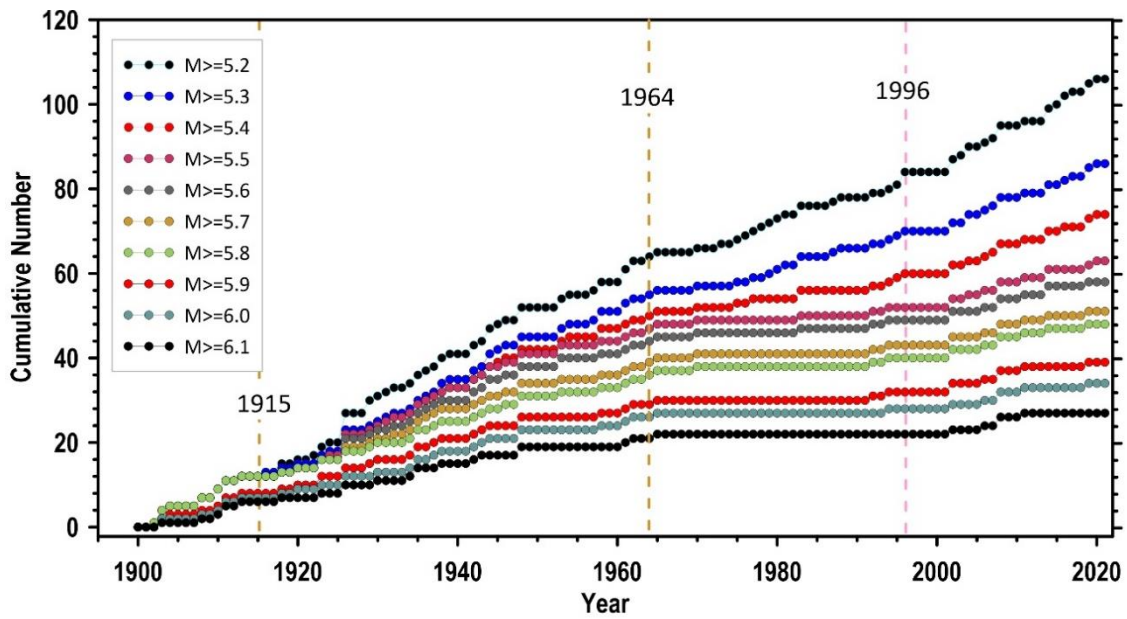
Figure 17: Time variation of the cumulative number of earthquakes (rates) with magnitudes above certain values (period 1900-2021).
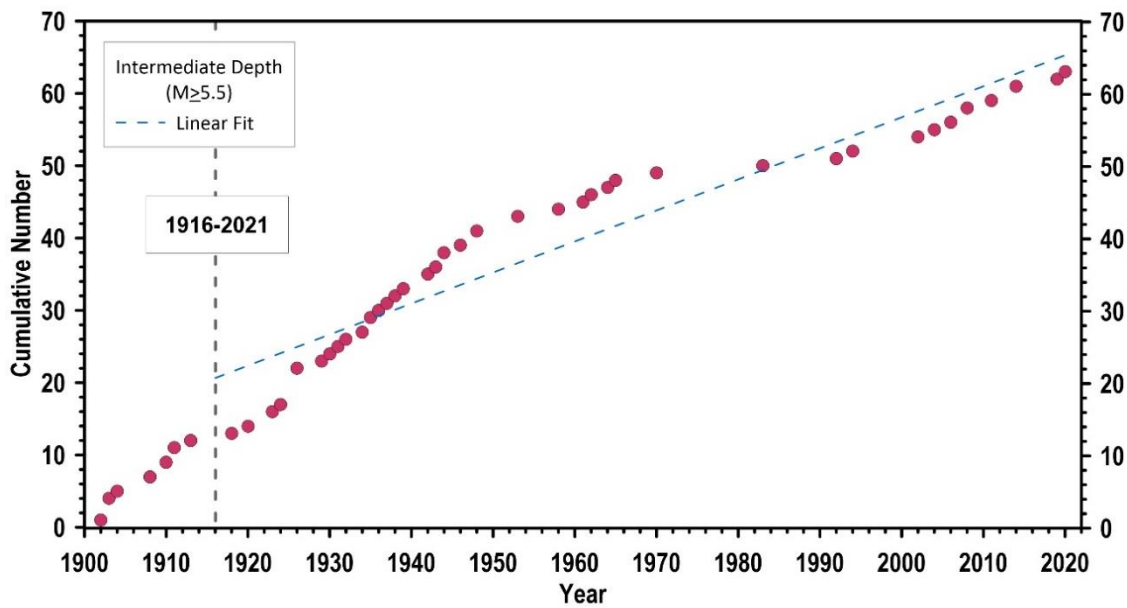
Figure 18: Time variation of the cumulative number of earthquakes (rates) with M≥5.5 (period 1900-2021).
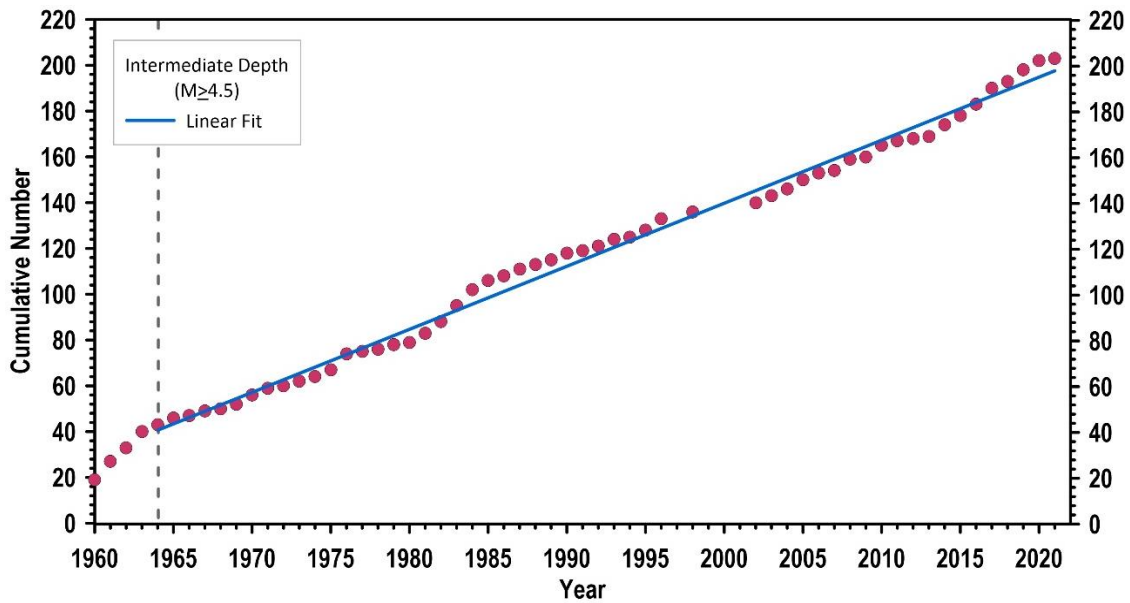
Figure 19: Time variation of the cumulative number of earthquakes (rates) with M≥4.5 (period 1960-2021).
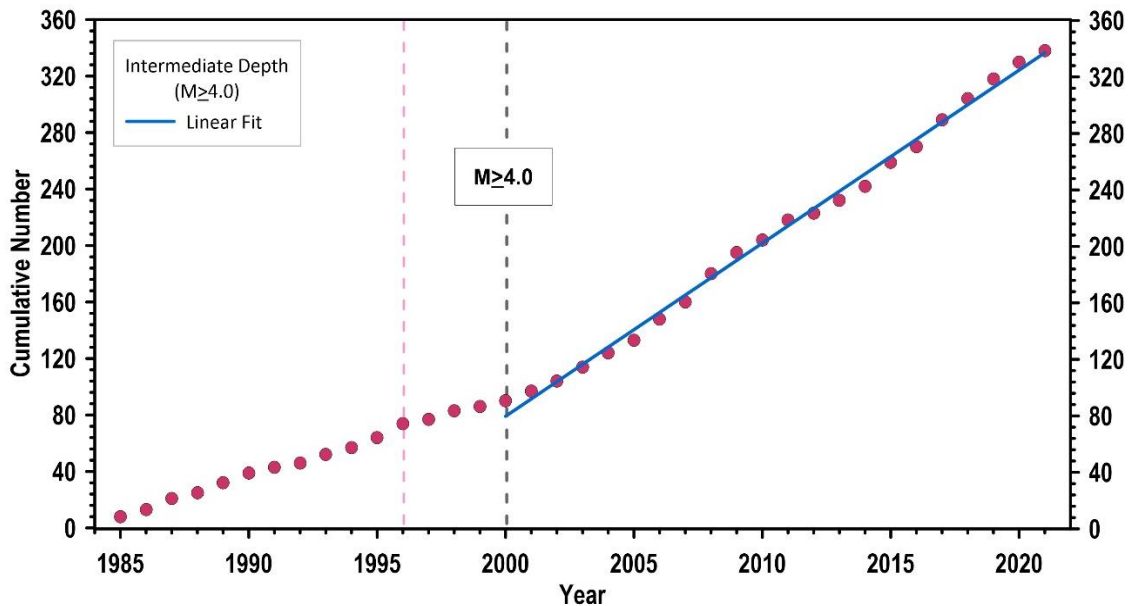
Figure 20: Time variation of the cumulative number of earthquakes (rates) with M≥4.0 (period 1985-2021).

The study of the rates (figures 17-20) is also pointing to completeness periods and magnitudes, relative with the ones revealed during the previous stage.

Especially for the intermediate depth earthquakes of the catalog and due to their limited number, we attempted a third approach, the well-known frequency magnitude distribution, in an effort to further confirm the result of the previous stages regarding the completeness magnitudes of these events and their distribution with time (graphs of figures 21, 22 and 23).
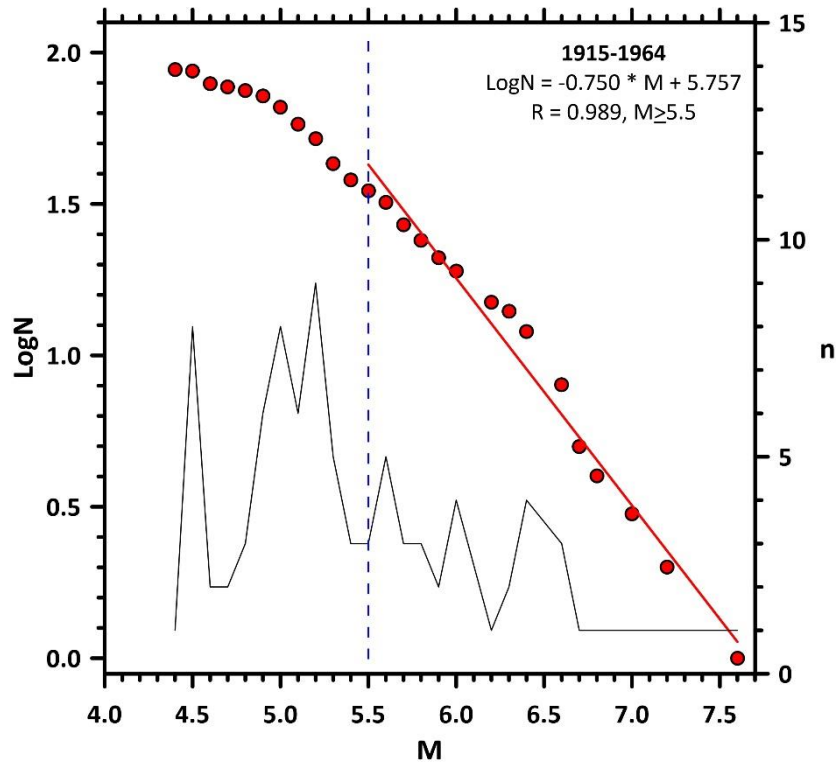
Figure 21: Frequency magnitude distribution of intermediate depth earthquakes during the period 1915-1964. The estimated completeness magnitude is Mc=5.5.
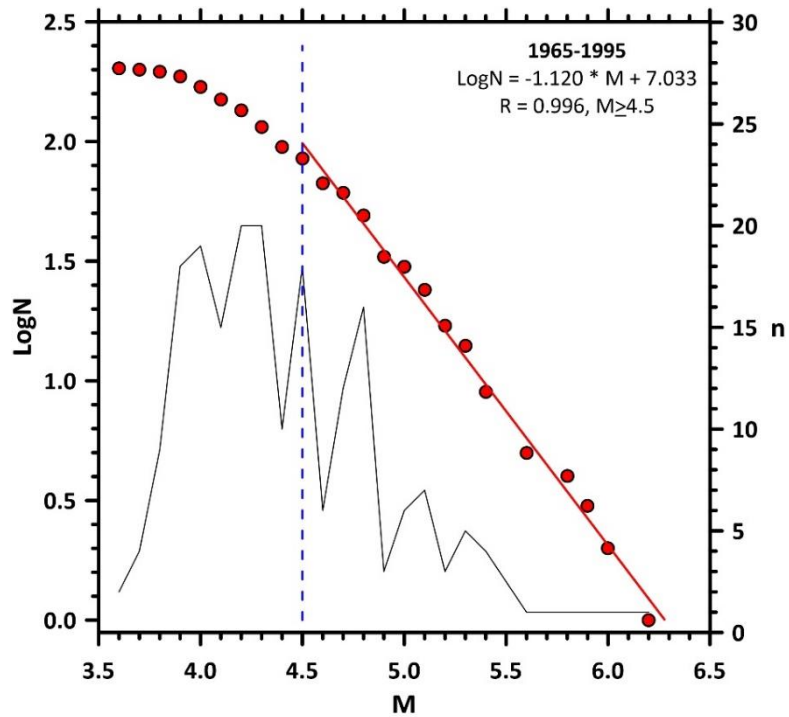
Figure 22: Frequency magnitude distribution of intermediate depth earthquakes during the period 1965-1995. The estimated completeness magnitude is Mc=4.5.
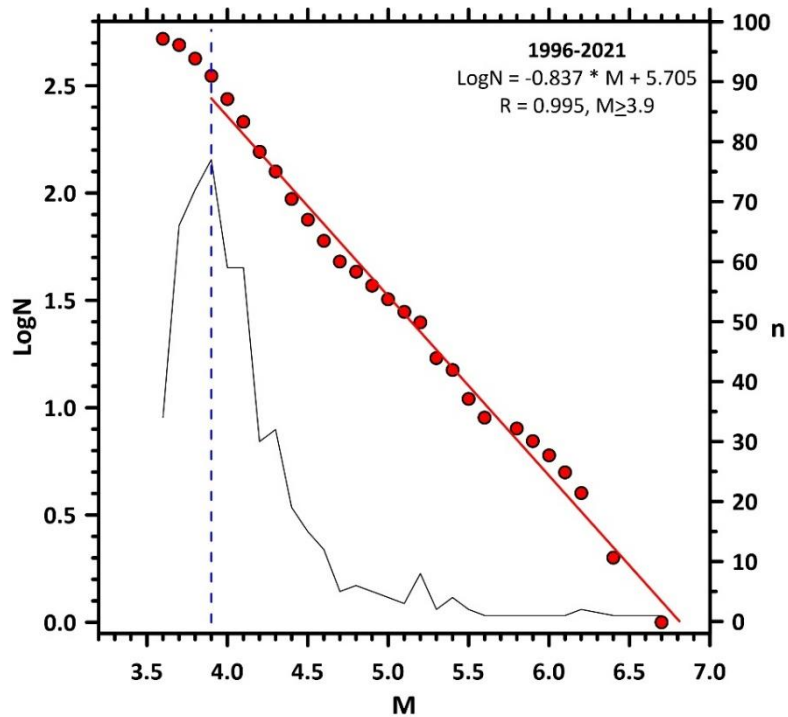
Figure 23: Frequency magnitude distribution of intermediate depth earthquakes during the period 1996-2021. The estimated completeness magnitude is Mc=3.9.

Combining the information provided by the time variation of M_c, the rates and the frequency-magnitude distribution (figures 14-23), the following finally accepted completeness periods and respective magnitudes are proposed for the intermediate depth (focal depths 60-200km) earthquakes of the catalog:

$$
\begin{array}{ll}
<1916 & M_c=??? \\
\mathbf{1916\text{-}2021} & \mathbf{M_c=5.5} \\
1965\text{-}2021 & M_c=4.5 \\
1996\text{-}2021 & M_c=3.9
\end{array}
\qquad (2)
$$

Therefore, and with a rather conservative approach, we will accept that the earthquake catalog is complete for intermediate depth earthquakes of magnitude M≥5.5 since 1916 and up to 2021.

2.2.1.3 All (shallow and intermediate depth) events

The graphs of Figures 24, 25, 26 and 27 present the time variation of the completeness magnitude, Mc, of all (shallow + intermediate depth) events as obtained by combination of four different methods, MAXC, GoF 90%, GoF 95% and EMR. Examination of the corresponding plots reveals rather constant values of Mc for specific periods.
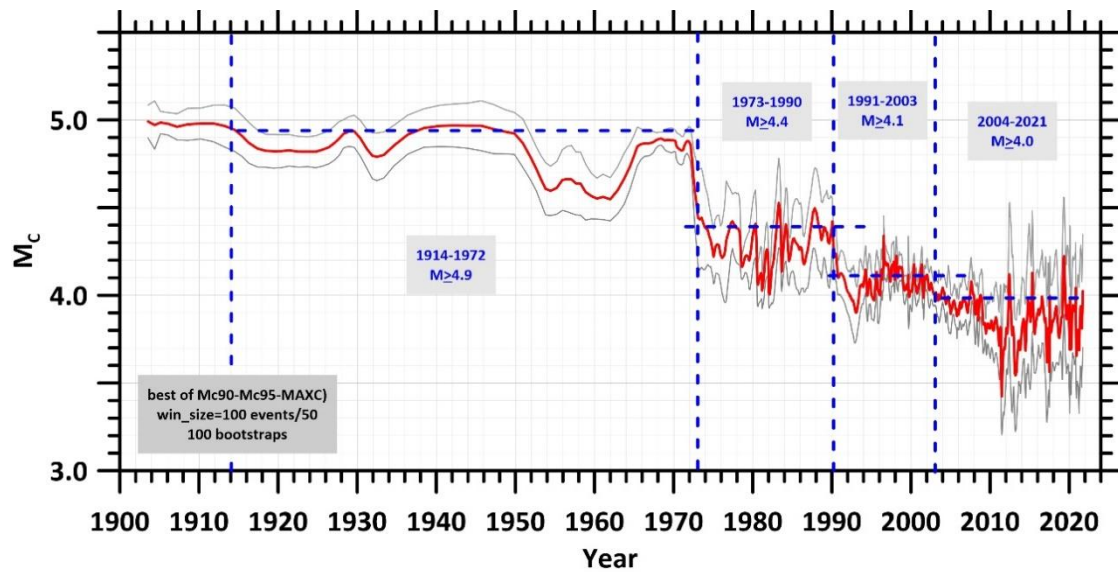
Figure 24: Time variation of the completeness magnitude, Mc, for the compiled catalog (period 1900-2021, all depth events) resulted after combined application of the MAXC, GoF 90%, GoF 95% and EMR methods. Gray lines represent the uncertainties revealed after resampling (sample size 100, moving step 50, 100 bootstraps).
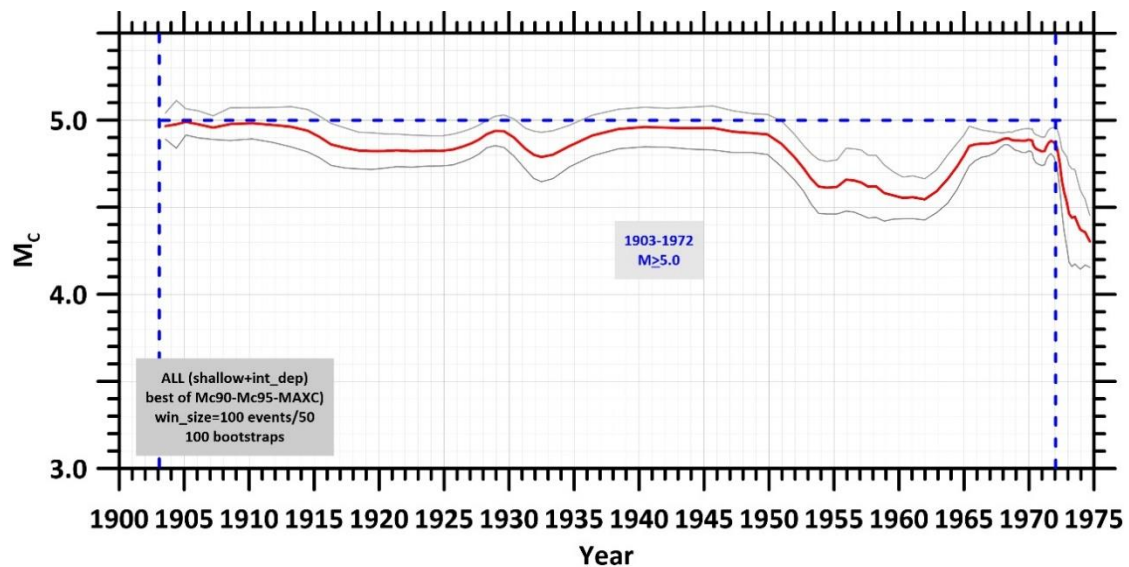
Figure 25: Time variation of the completeness magnitude, Mc, for the compiled catalog (period 1900-1975, all depth events) resulted after combined application of the MAXC, GoF 90%, GoF 95% and EMR methods. Gray lines represent the uncertainties revealed after resampling (sample size 100, moving step 50, 100 bootstraps).
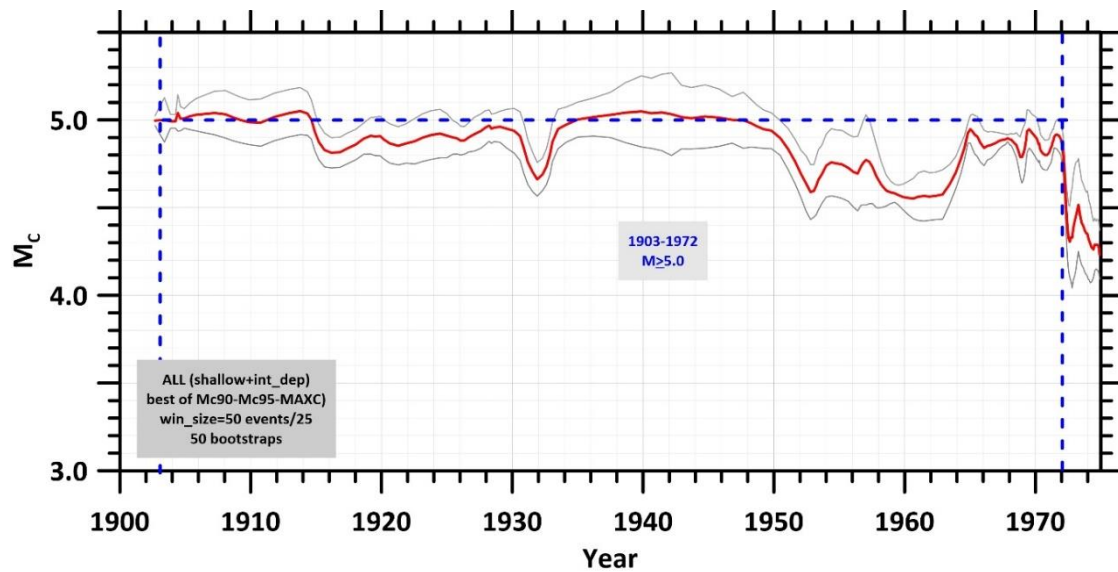
Figure 26: Time variation of the completeness magnitude, Mc, for the compiled catalog (period 1900-1975, all depth events) resulted after combined application of the MAXC, GoF 90%, GoF 95% and EMR methods. Gray lines represent the uncertainties revealed after resampling (sample size 50, moving step 25, 50 bootstraps).
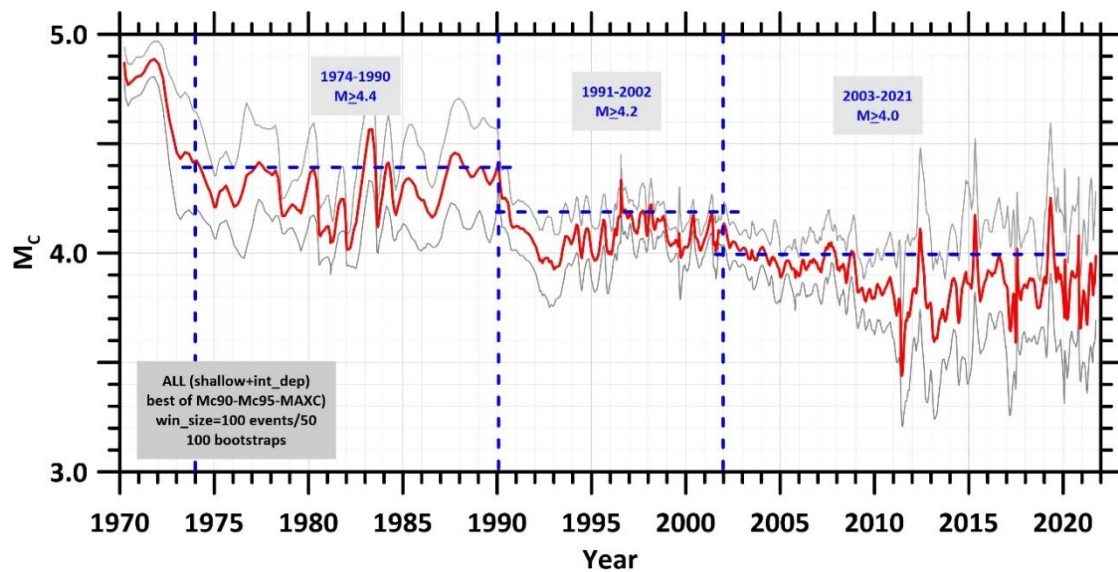
Figure 27: Time variation of the completeness magnitude, Mc, for the compiled catalog (period 1970-2021, all depth events) resulted after combined application of the MAXC, GoF 90%, GoF 95% and EMR methods. Gray lines represent the uncertainties revealed after resampling (sample size 100, moving step 50, 100 bootstraps).

To double check and confirm the results regarding the time variation of Mc, we also studied the rates of seismicity, that is, the time variation of the cumulative number of earthquakes with magnitudes over a certain value (figures 28-32).
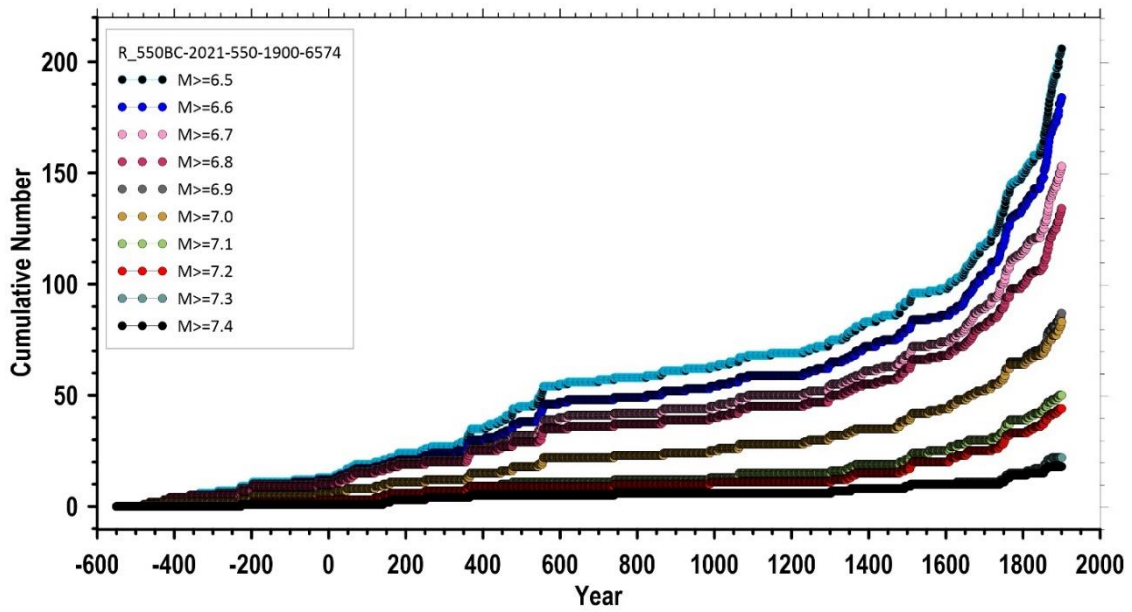
Figure 28: Time variation of the cumulative number of all depth earthquakes (rates) with magnitudes above certain values (period 550BC-2021).
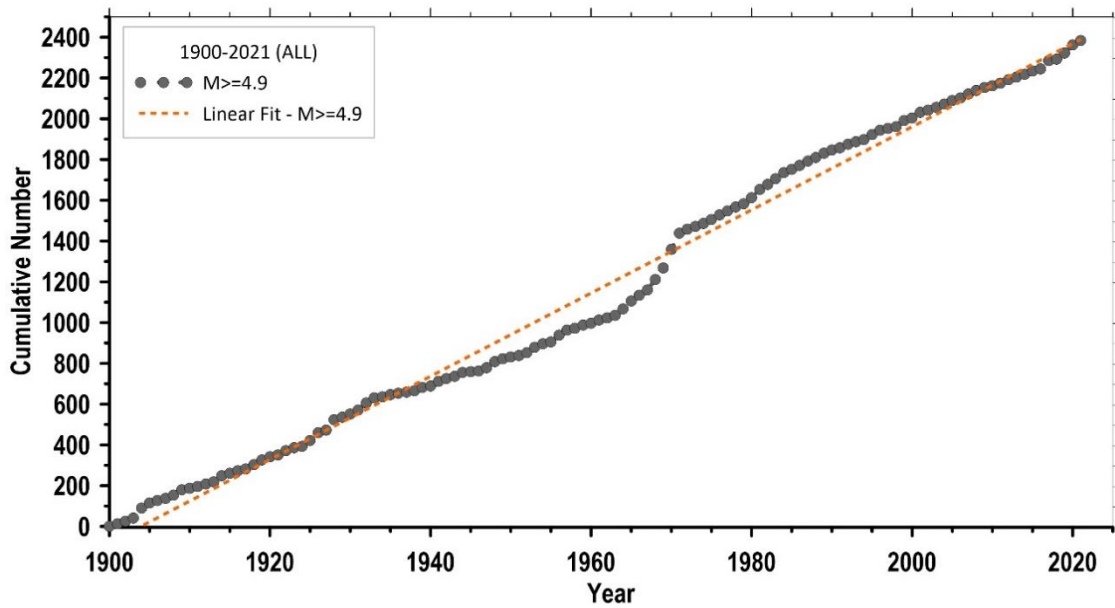
Figure 29: Time variation of the cumulative number of all depth earthquakes (rates) with M≥4.9 (period 1900-2021).
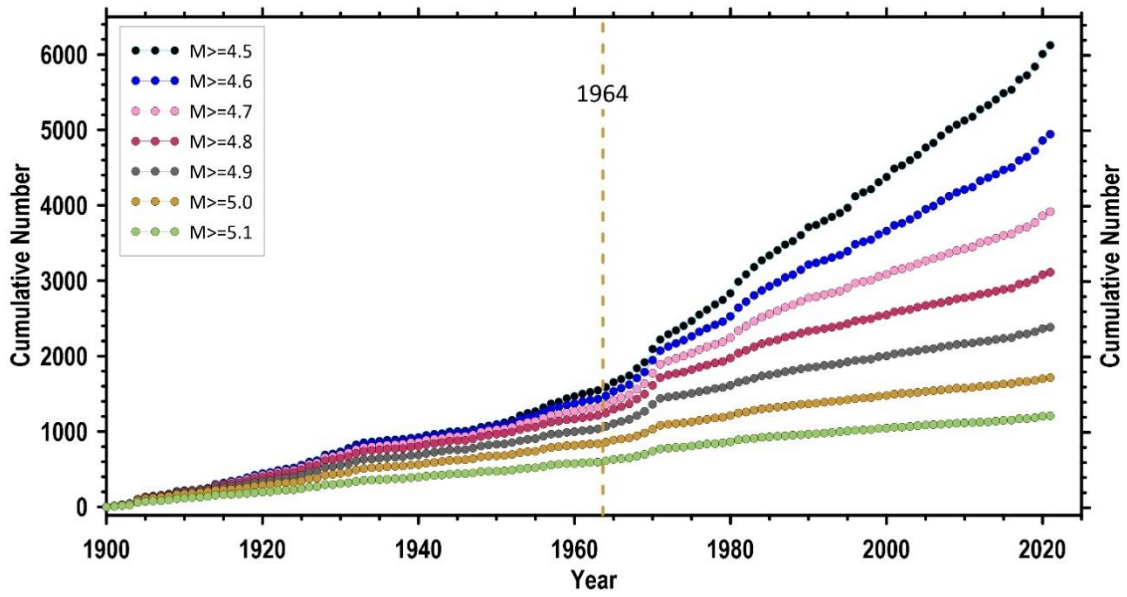
Figure 30: Time variation of the cumulative number of all depth earthquakes (rates) with magnitudes above certain values (period 1900-2021).
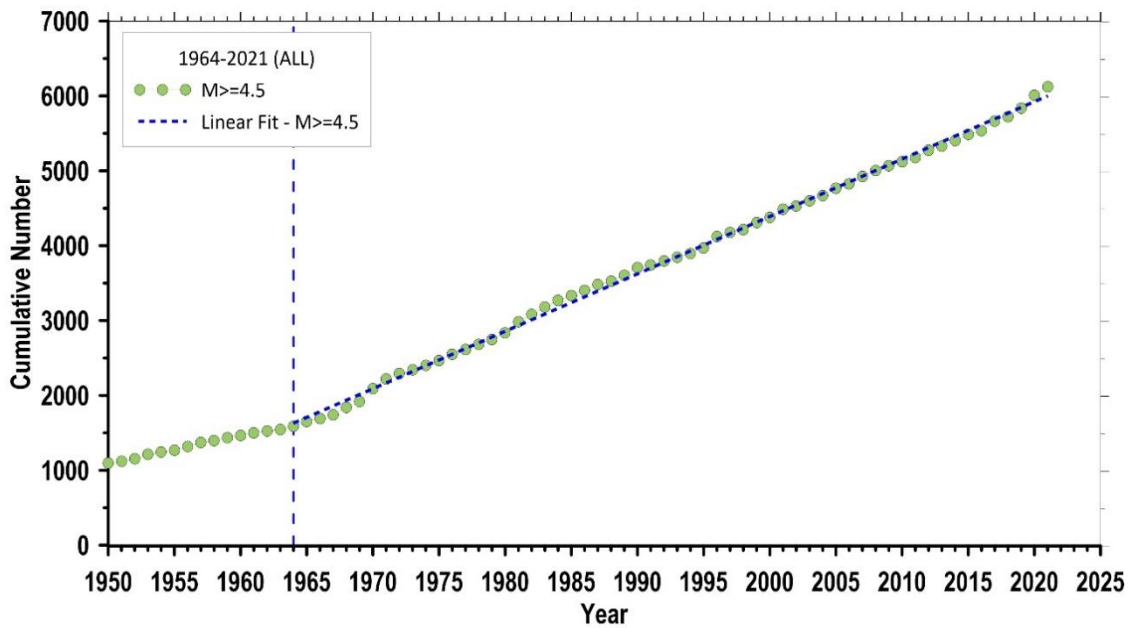
Figure 31: Time variation of the cumulative number of all depth earthquakes (rates) with M≥4.5 (period 1950-2021).
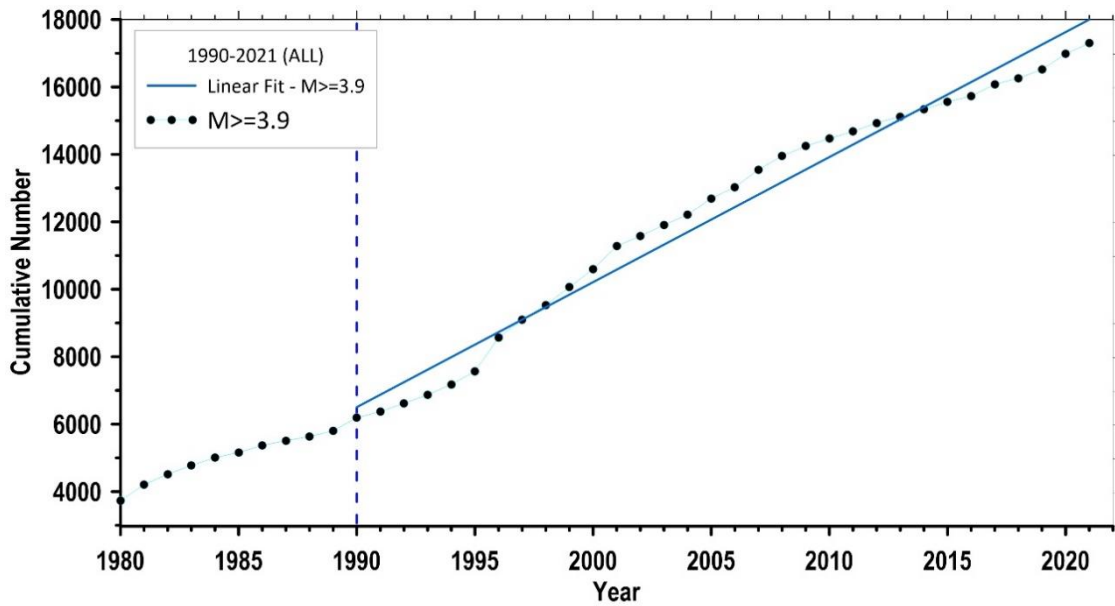
Figure 32: Time variation of the cumulative number of all depth earthquakes (rates) with M≥3.9 (period 1980-2021).

The study of the rates (figures 28-32) is also pointing to completeness periods and magnitudes, relative with the ones revealed during the previous stage.

Combining the information provided by all the previously commented figures (figures 24-32), the following finally accepted completeness periods and respective magnitudes are proposed for the whole catalog (focal depths 0-200km):

$$
\begin{array}{lll}
<1900 & M_c=??? & \\
\mathbf{1900\text{-}2021} & \mathbf{M_c=4.9} & (3) \\
1964\text{-}2021 & M_c=4.5 & \\
1990\text{-}2021 & M_c=3.9 &
\end{array}
$$

Therefore, and with a rather conservative approach, we will accept that the entire earthquake catalog is complete for M≥4.9 earthquakes from 1900 to 2021. The completeness check results for the entire catalog are similar to those for shallow events. This is an expected result as most of the catalog consists of shallow events.

Summarizing the results obtained from the temporal variation of the completeness of the catalog we come to the conclusion-proposition that the earthquakes with a M≥4.9 that occurred in the wide area covered by the catalog during the period 1900-2021 should be the ones that will be used to assess the seismic hazard of the area under study.

2.2.2 Variation of seismicity parameters in space

In this step, we are going to examine the variation in space of several parameters expressing the seismicity of the region under study. Following the previous results regarding the time variation of Mc, the space variation of the seismicity parameters

will be studied for each one of the formatted groups of earthquakes (shallow, intermediate depth and all-depths).

The parameters, the space variation of which will be examined, are:

1) The completeness magnitude, Mc
2) The b-value
3) The a-value of the G-R relation, reduced to one year, a1
4) The most probable annual maximum magnitude, a1/b
5) The mean return period, T6.0, for earthquakes of M≥6.0
6) The mean return period, T6.5, for earthquakes of M≥6.5, according to relation:

$$T_{6.5} = 10^{(b*6.5)-a} \tag{4}$$

7) The probable maximum magnitude for a period of 475 years, M-475, or the magnitude with 10% probability of exceedance within 50 years, according to relations:

$$M_{475} = \frac{a + log475}{b} \tag{5}$$

$$P_{50}^{10} = 1 - \exp\left[-10^{(a-b*M)} * 50\right], with\ P_{50}^{10} = 0.1 \tag{6}$$

2.2.2.1 Shallow events

To study the spatial distribution of seismicity parameters corresponding to shallow events, the entire region (22.5-30.5ºE and 35.0-43.0ºN) was covered by a 0.1°x0.1° grid of points. Then, circular regions centered at each node of the grid were considered and the earthquakes that occurred during the period 1900-2021 with magnitudes M≥4.7 (the completeness magnitude for this period is Mc=4.9, see relations 1) within each circular region were used to estimate all the above seismicity parameters. Several attempts were performed with several radius values and minimum number of earthquakes. The results presented in the following figures (figures 33-39) produced by using radius, R=80km and minimum number of earthquakes with M≥Mc equal to 30.
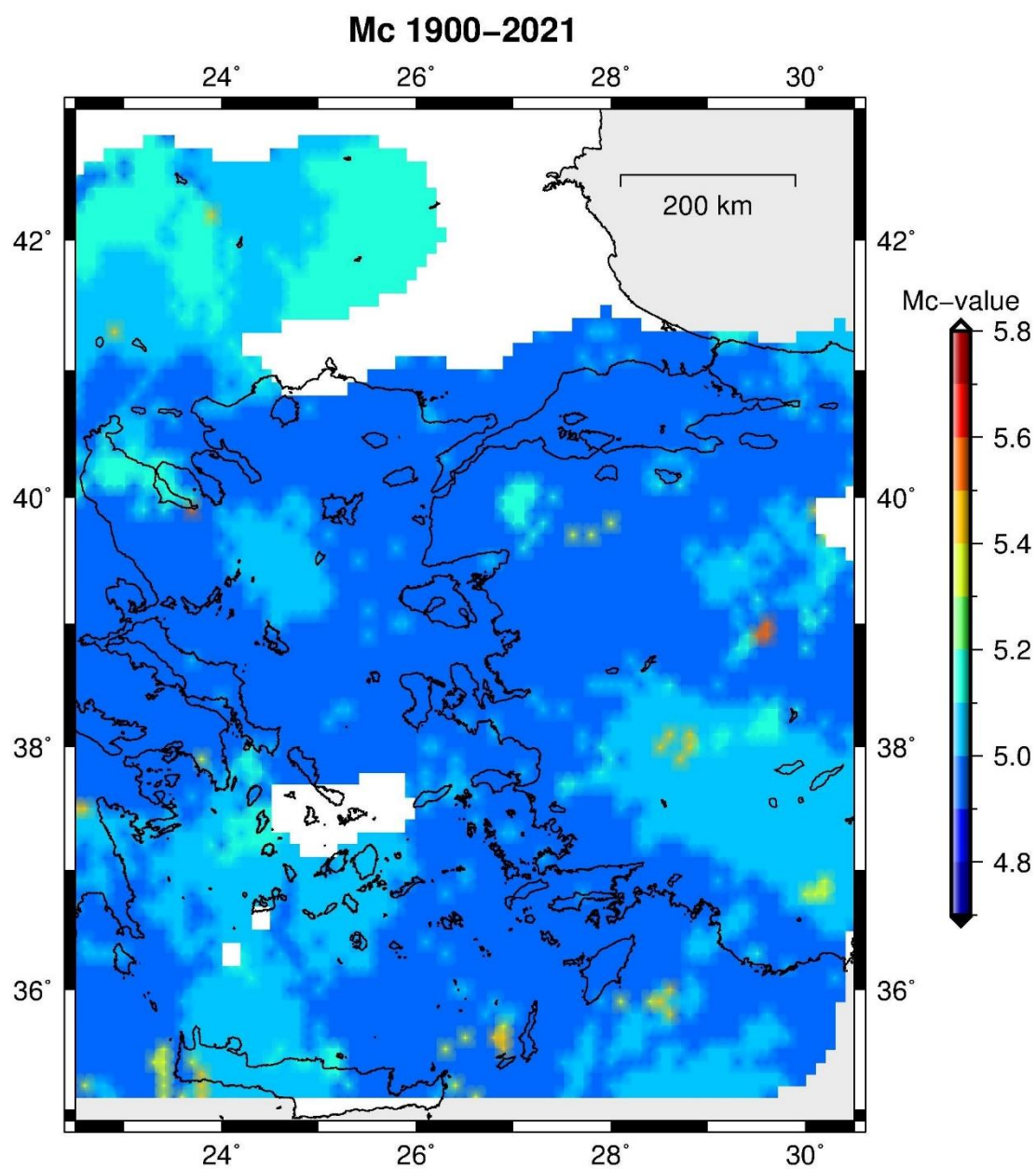
Figure 33: Spatial distribution of Mc for the shallow (focal depth 0-60km) earthquakes that occurred during the period 1900-2021. Circular regions with radius R=80km are considered, centered at the nodes of a 0.1°x0.1° grid.

Figure 34: Spatial distribution of b-value for the shallow earthquakes (focal depth 0-60km). The estimations are based on the complete events (M≥4.9) that occurred during the period 1900-2021. Circular regions are considered, centered at the nodes of a 0.1°x0.1° grid with radius R=80km and minimum required number of complete (M≥4.9) events within each circle, Nmin=30.
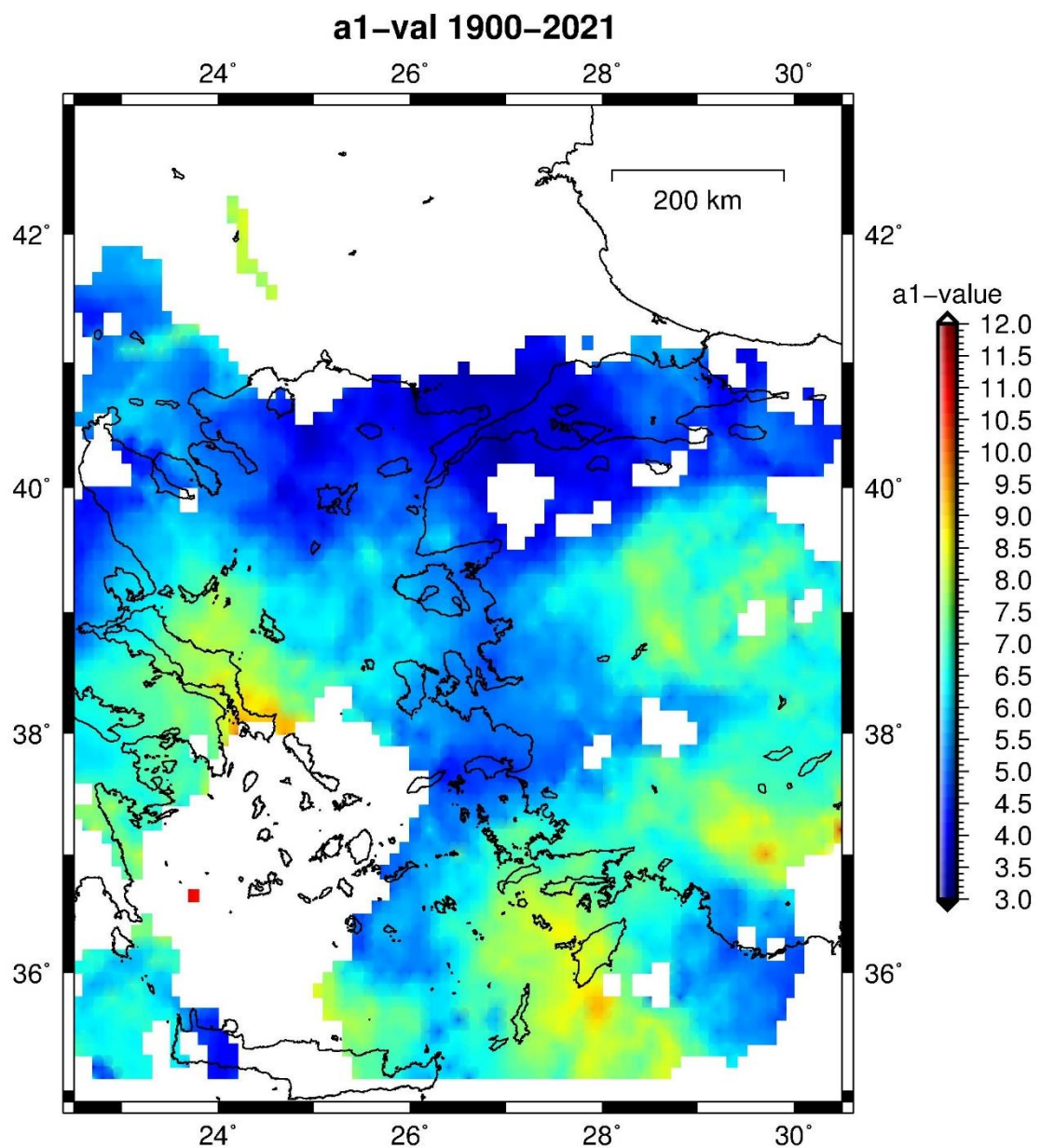
Figure 35: Spatial distribution of a_1-value for shallow (focal depth 0-60km) earthquakes. The estimations are based on the complete events (M≥4.9) that occurred during the period 1900-2021. Circular regions are considered, centered at the nodes of a 0.1°x0.1° grid with radius R=80km and minimum required number of complete events within each circle, Nmin=30.
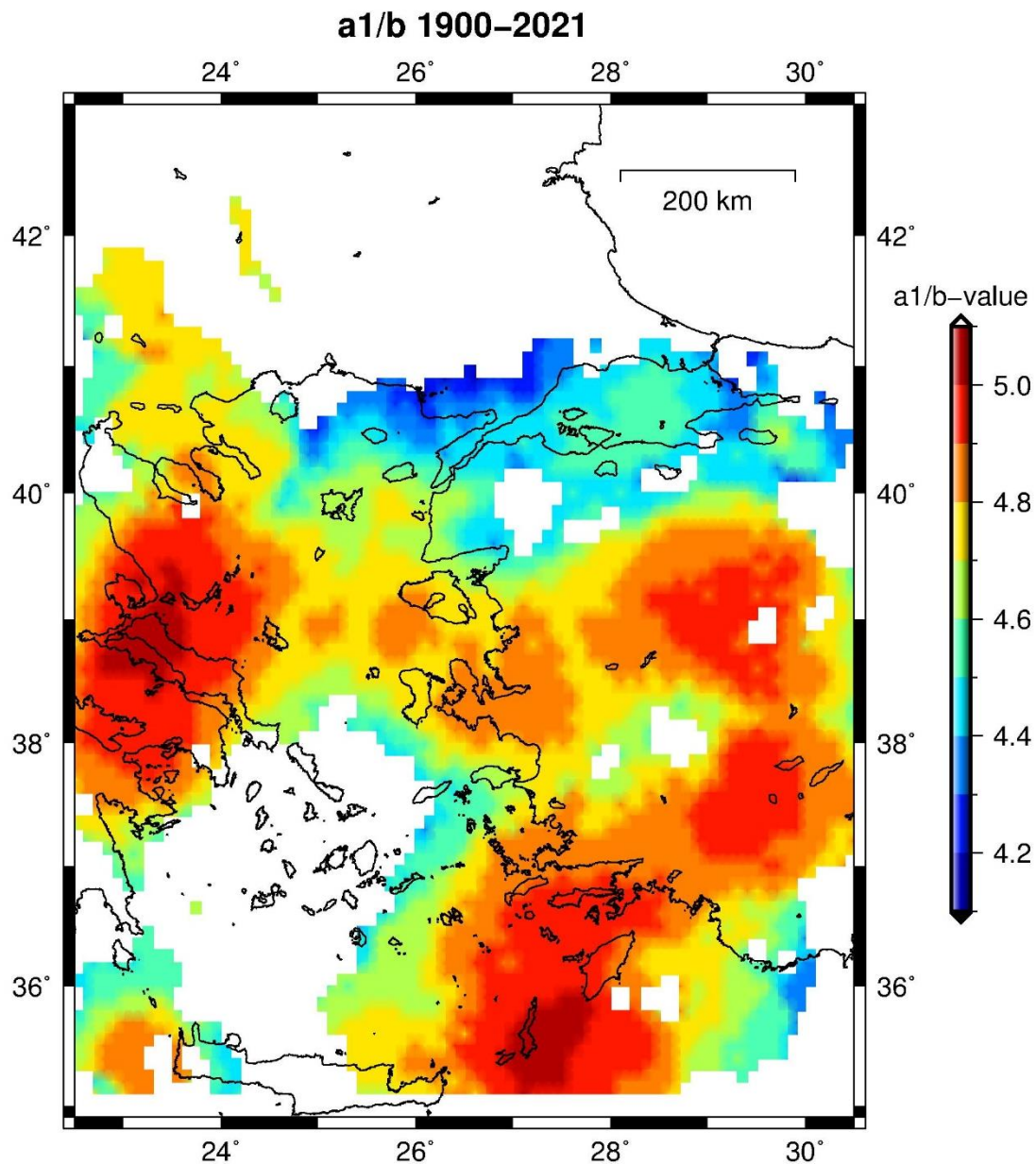
Figure 36: Spatial distribution of a₁/b-value (most probable annual maximum magnitude) for shallow (focal depth 0-60km) earthquakes. The estimations are based on the complete events (M≥4.9) that occurred during the period 1900-2021. Circular regions are considered, centered at the nodes of a 0.1°x0.1° grid with radius R=80km and minimum required number of complete events within each circle, Nmin=30.
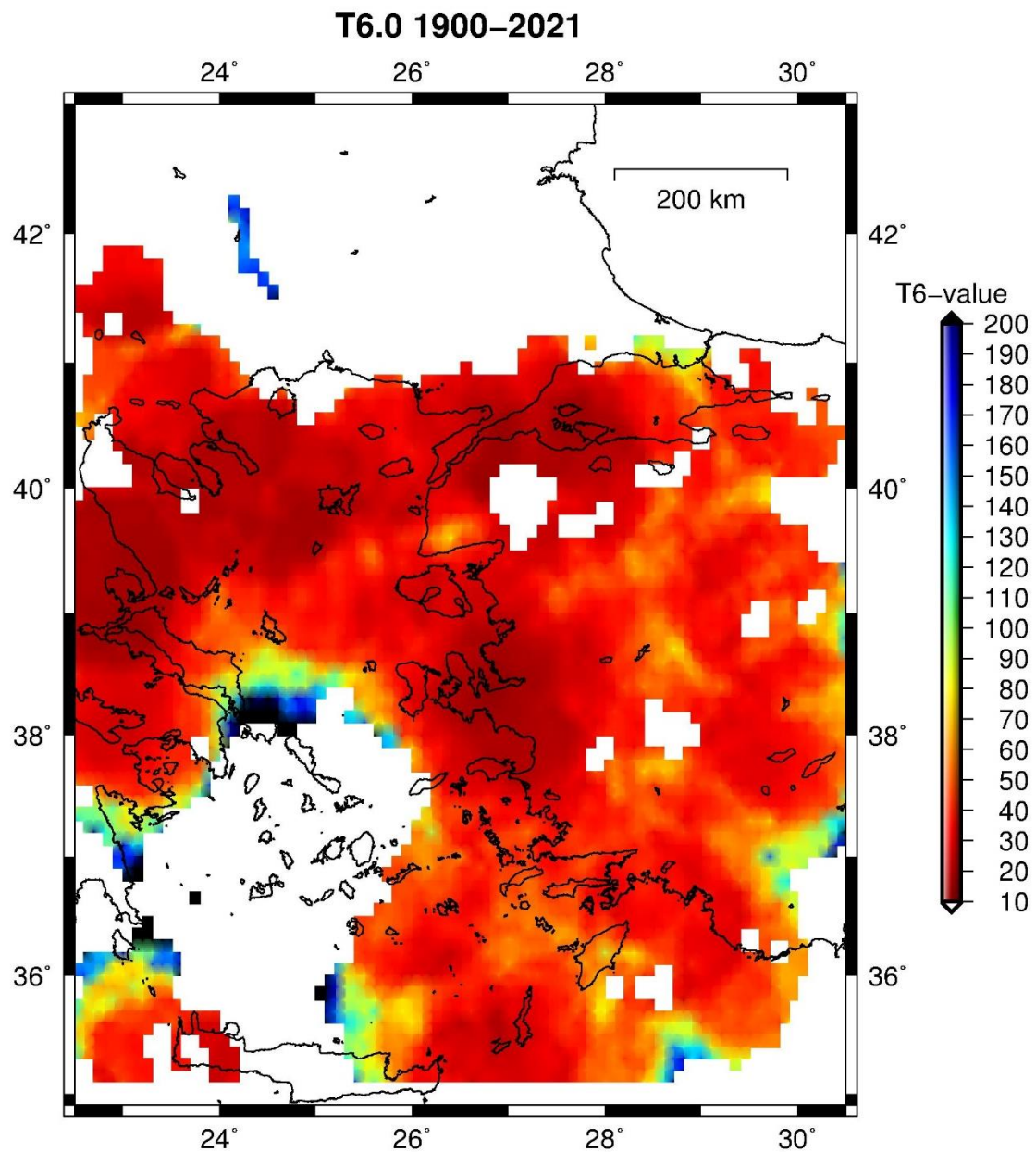
Figure 37: Spatial distribution of the mean return period for shallow (focal depth 0-60km) earthquakes of M≥6.0. The estimations are based on the complete events (M≥4.9) that occurred during the period 1900-2021. Circular regions are considered, centered at the nodes of a 0.1°x0.1° grid with radius R=80km and minimum required number of complete events within each circle, Nmin=30.
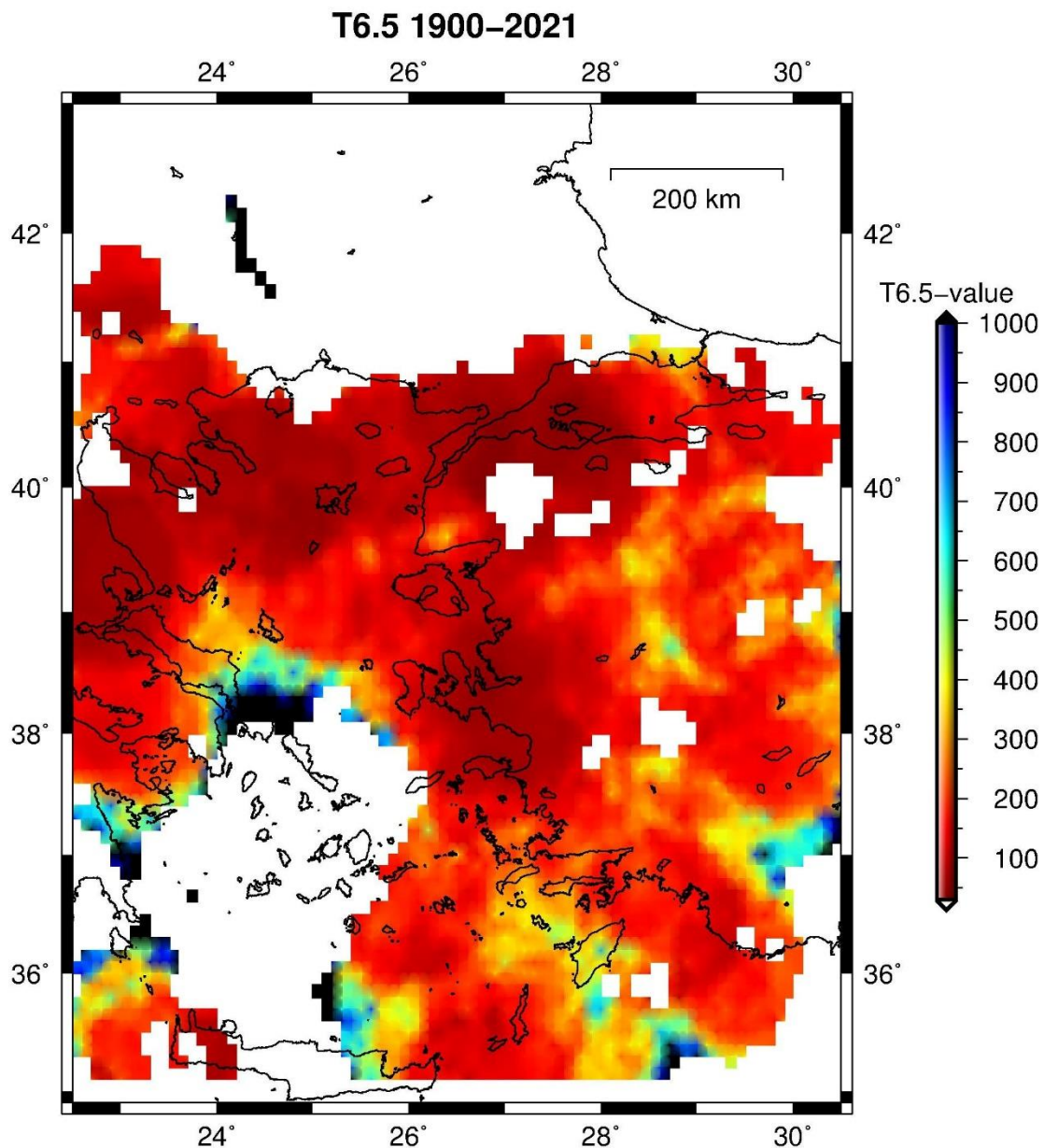
Figure 38: Spatial distribution of the mean return period for shallow (focal depth 0-60km) earthquakes of M≥6.5. The estimations are based on the complete events (M≥4.9) that occurred during the period 1900-2021. Circular regions are considered, centered at the nodes of a 0.1°x0.1° grid with radius R=80km and minimum required number of complete events within each circle, Nmin=30.
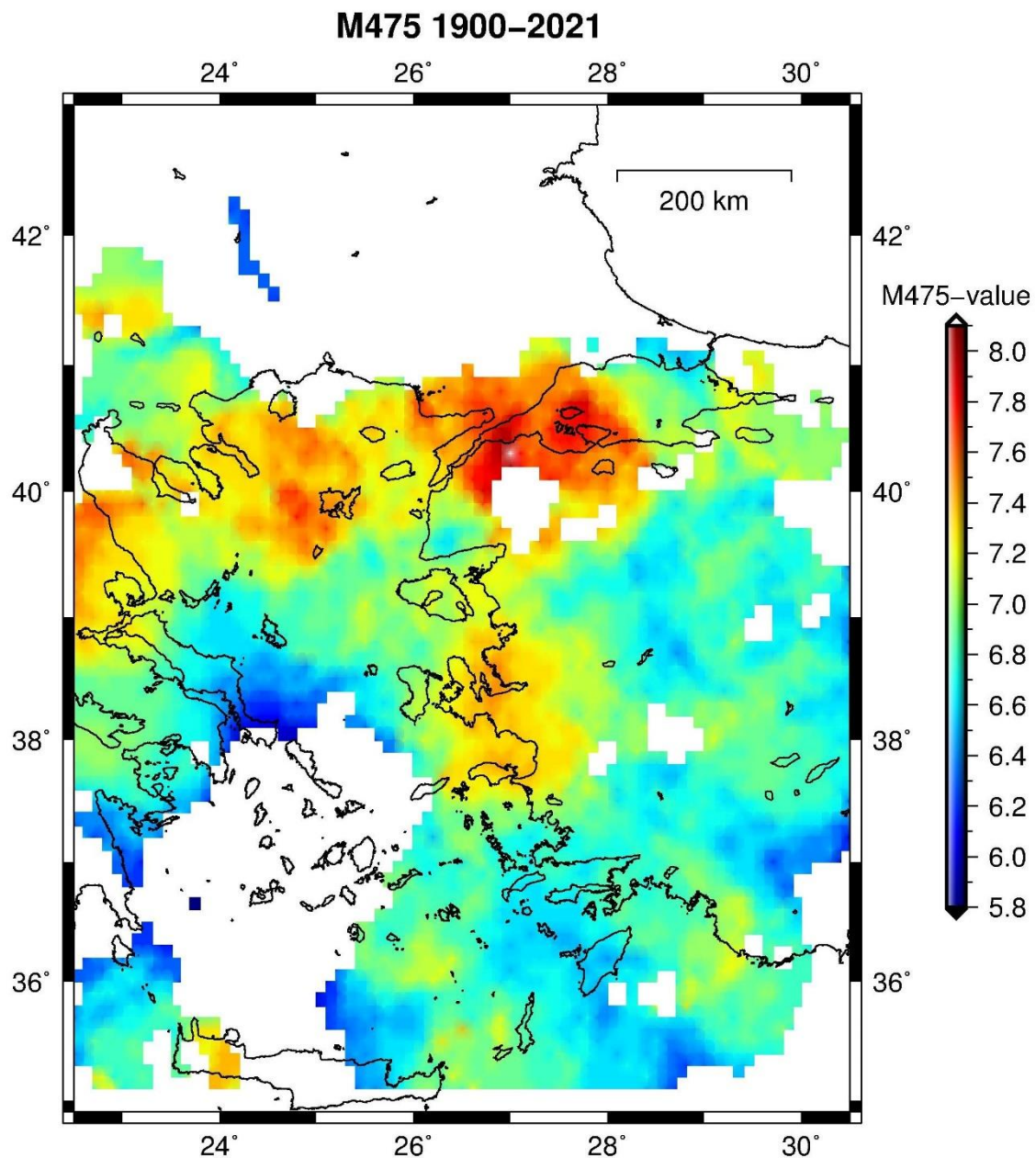
Figure 39: Spatial distribution of the probable maximum magnitude for a 475 years period (or the magnitude with 10% probability of exceedance within 50 years). The estimations are based on the complete shallow (focal depth 0-60km) events (M≥4.9) that occurred during the period 1900-2021. Circular regions are considered, centered at the nodes of a 0.1°x0.1° grid with radius R=80km and minimum required number of complete events within each circle, Nmin=30.

The values of the seismicity parameters used to produce the maps of figures 33-39 and based on shallow earthquakes (focal depths (0-60km) of the catalog, are listed in the files of the accompanying this Deliverable WP2.2, e-Supplement **(1) "Catalog_Shallow&Intermediate_Depth_eqs.zip".**

2.2.2.2 Intermediate depth events

As mentioned earlier, intermediate depth (h=60-200km) events in our data-set were very few. Considering the time variation of the completeness magnitude for these events (see relations 2), we notice that the remaining set of data for the 1st period of completeness (1916-2021) includes just 51 events. **This extremely low number of earthquakes prohibits any attempt for a reliable study of the spatial variation of the completeness magnitude and the corresponding seismicity parameters obtained by exclusively examining the intermediate-depth earthquakes of this region.**

2.2.2.3 All events

To study the spatial distribution of seismicity parameters corresponding to the total set of events (focal depths 0-200km), the same point grid (0.1°x0.1°) as for the shallow events was chosen to cover the entire region (22.5-30.5ºE and 35.0-43.0ºN). Again, circular regions centered at each node of the grid were considered and the earthquakes that occurred during the period 1900-2021 with magnitudes M≥4.7 (the completeness magnitude derived for this period and for the whole data set is Mc=4.9, see relations 3) in each circular region were used to estimate all seven seismicity parameters mentioned earlier. After testing many values for the radius, R and the minimum number, Nmin, of earthquakes with M≥Mc, the R=80km and Nmin=30 were chosen. The results of this study are presented in the figures 40-46.
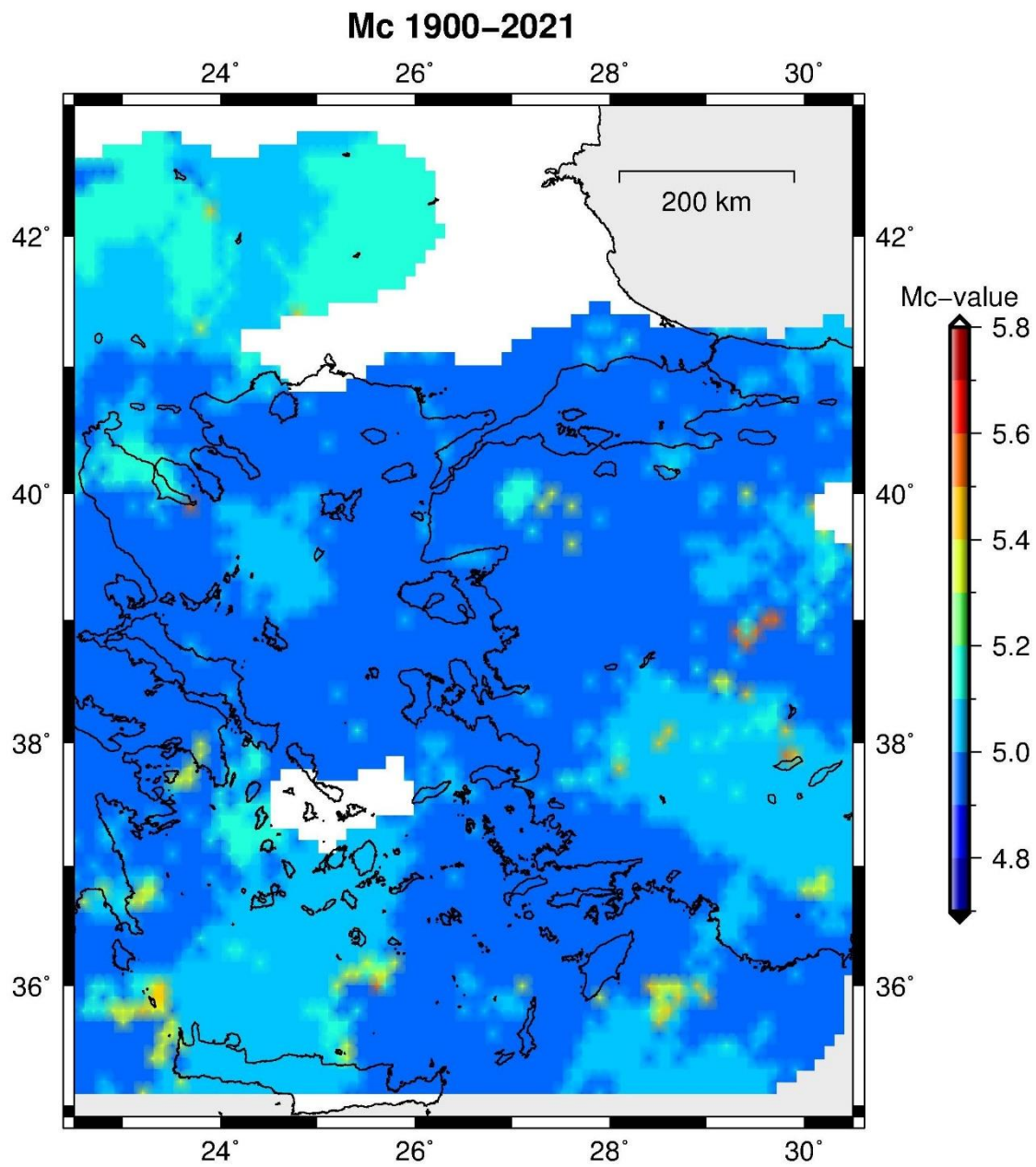
Figure 40: Spatial distribution of Mc for all (focal depths 0-200km) earthquakes that occurred during the period 1900-2021. Circular regions with radius R=80km are considered, centered at the nodes of a 0.1°x0.1° grid.

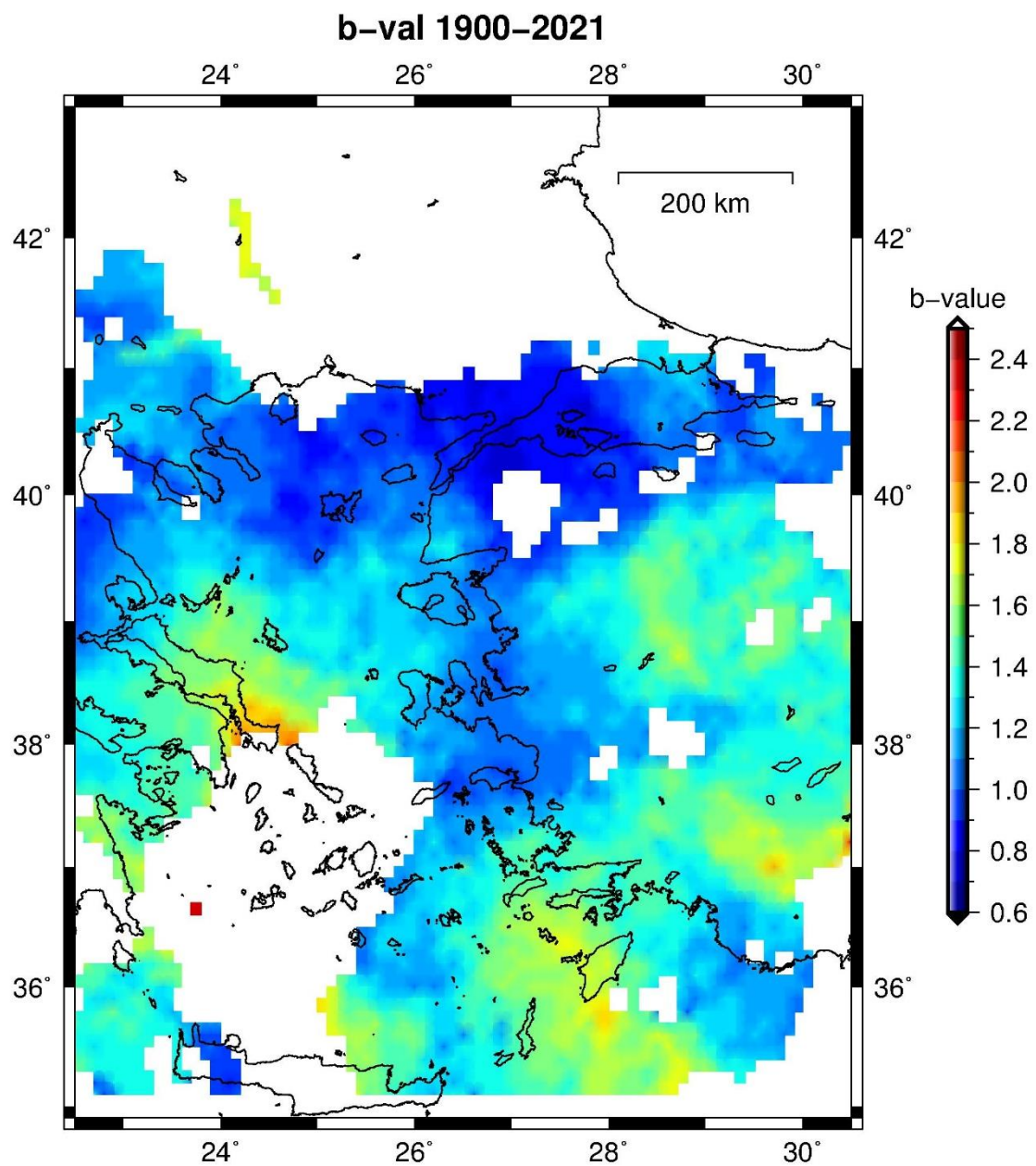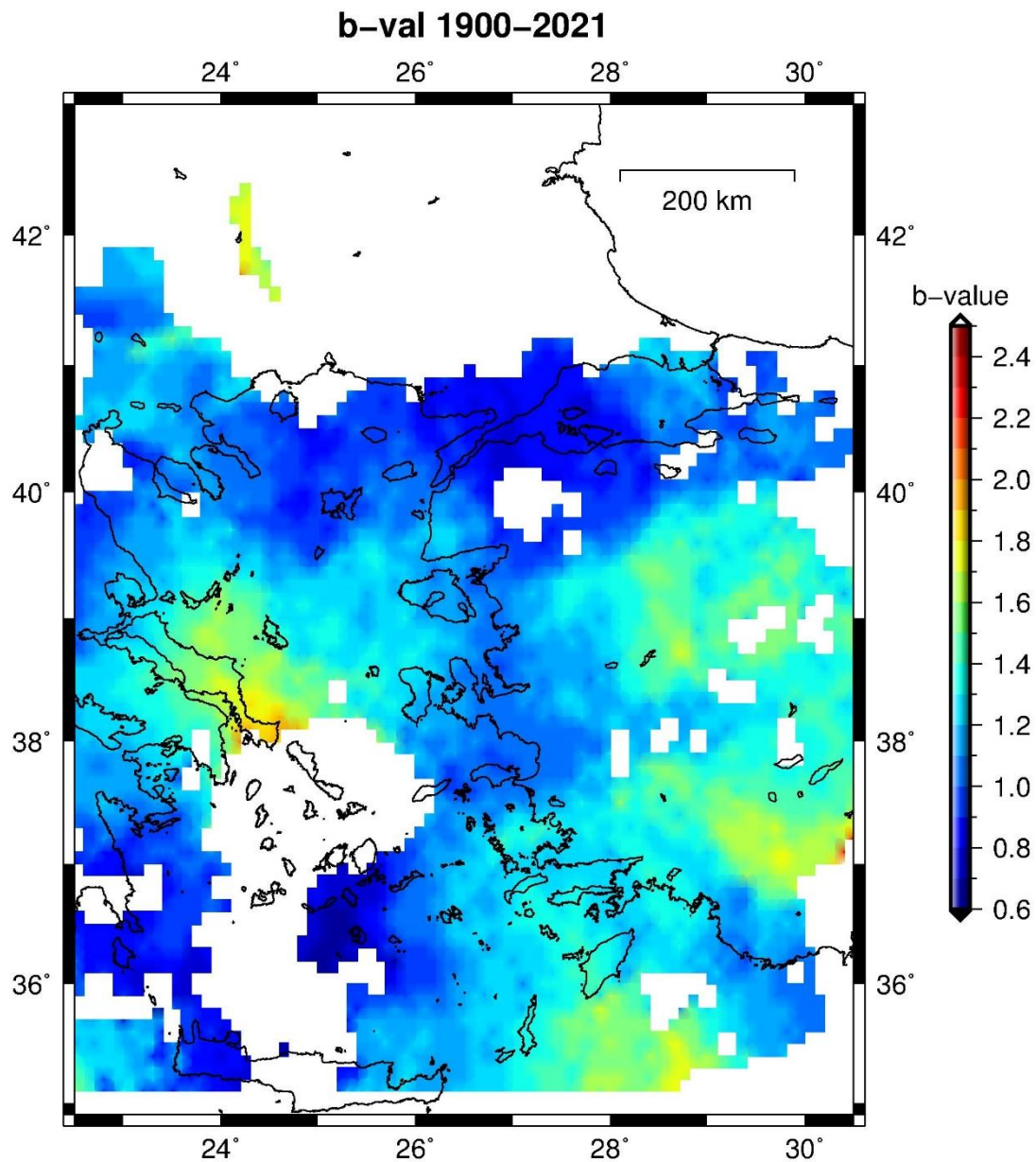**Figure 41: Spatial distribution of b-value for all (focal depths 0-200km) earthquakes that occurred during the period 1900-2021. The estimations are based on the complete events (M≥4.9) that occurred during the period 1900-2021. Circular regions are considered, centered at the nodes of a 0.1°x0.1° grid with radius R=80km and minimum required number of complete (M≥4.9) events within each circle, Nmin=30.**
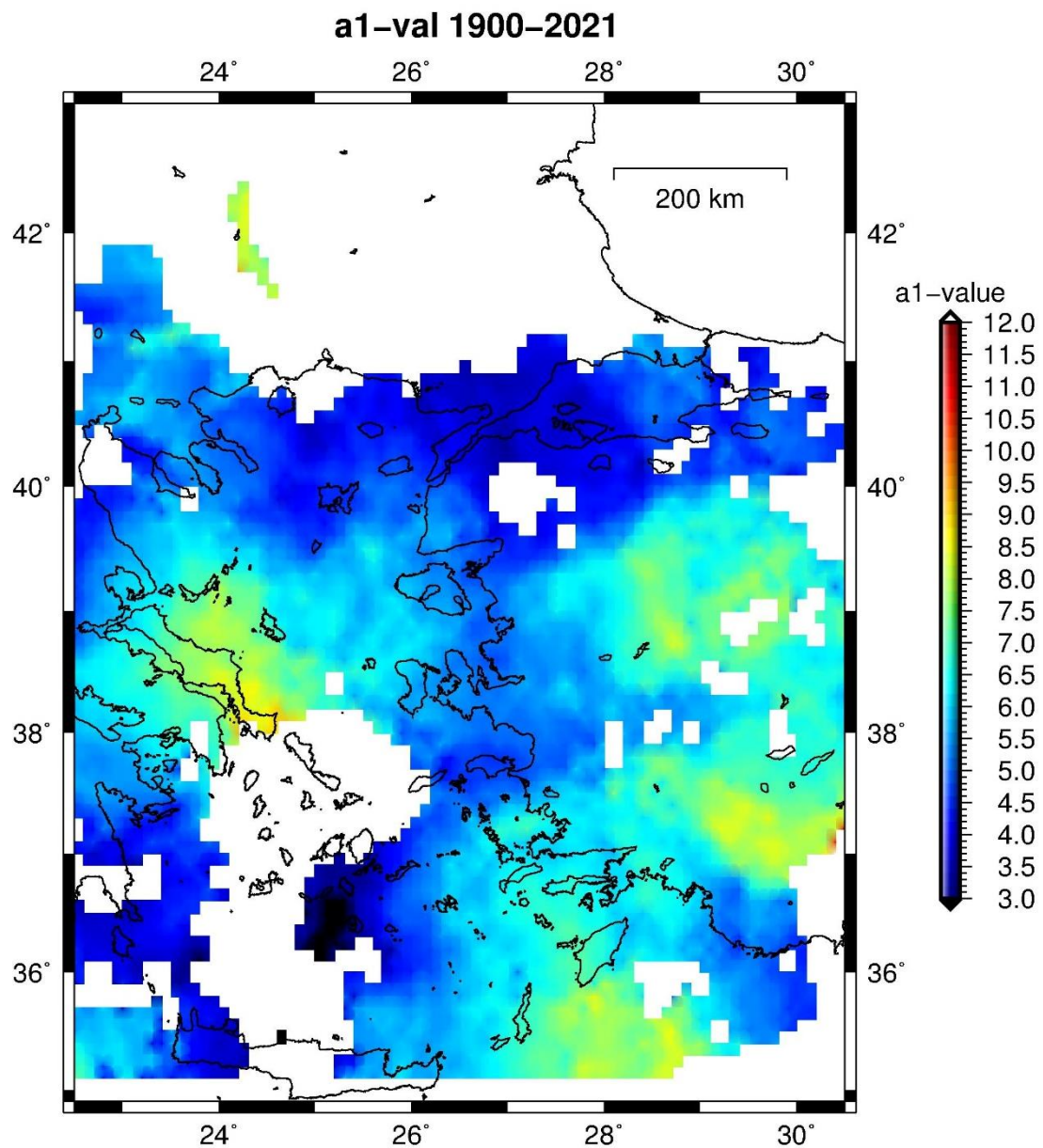
Figure 42: Spatial distribution of a_1-value for all (focal depths 0-200km) earthquakes. The estimations are based on the complete events (M≥4.9) that occurred during the period 1900-2021. Circular regions are considered, centered at the nodes of a 0.1°x0.1° grid with radius R=80km and minimum required number of complete (M≥4.9) events within each circle, Nmin=30.
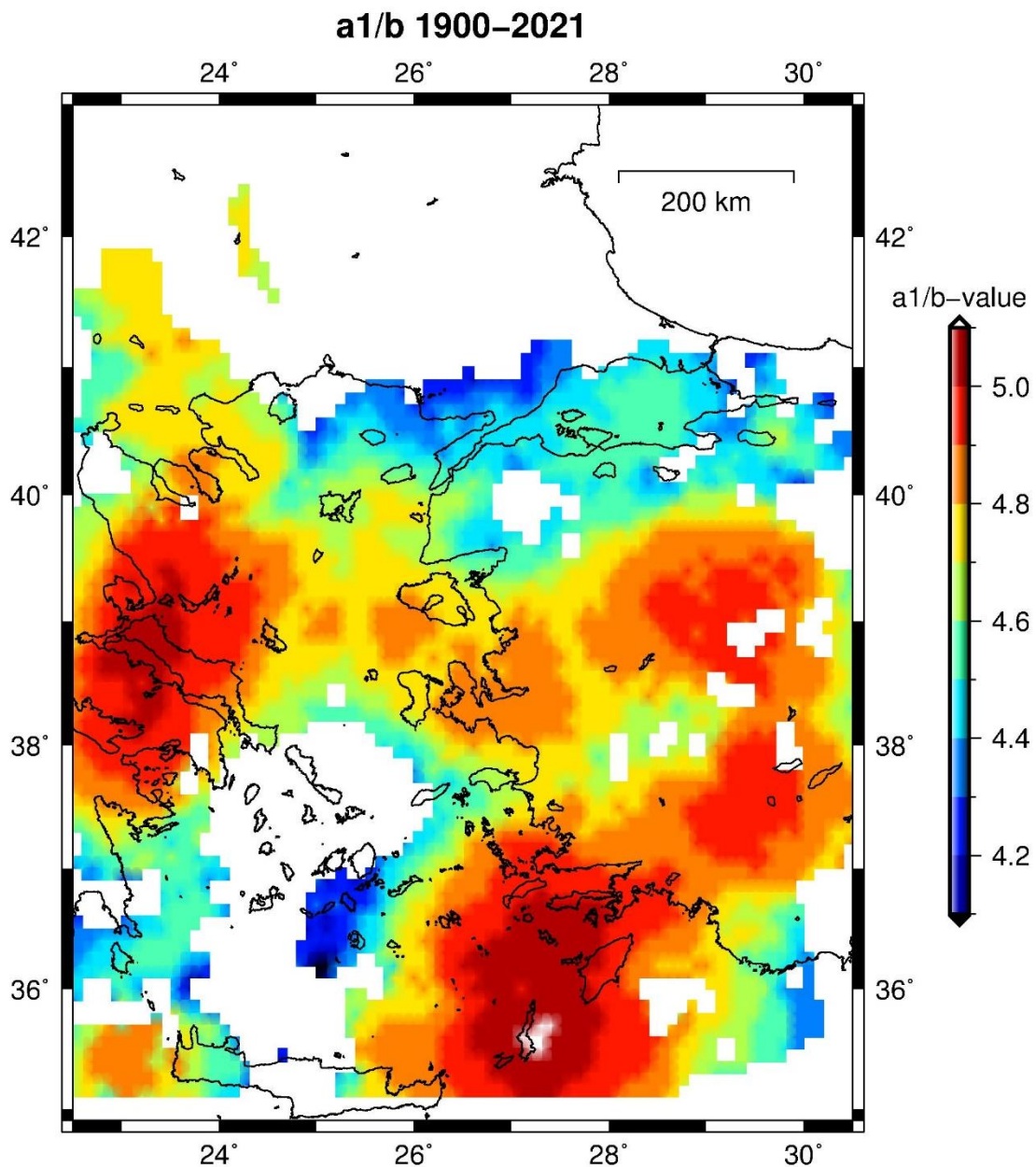
a1/b 1900–2021

Figure 43: Spatial distribution of a_1/b-value (most probable annual maximum magnitude) for all (focal depths 0-200km) earthquakes. The estimations are based on the complete events ($M{\geq}4.9$) that occurred during the period 1900-2021. Circular regions are considered, centered at the nodes of a 0.1°x0.1° grid with radius R=80km and minimum required number of complete ($M{\geq}4.9$) events within each circle, Nmin=30.
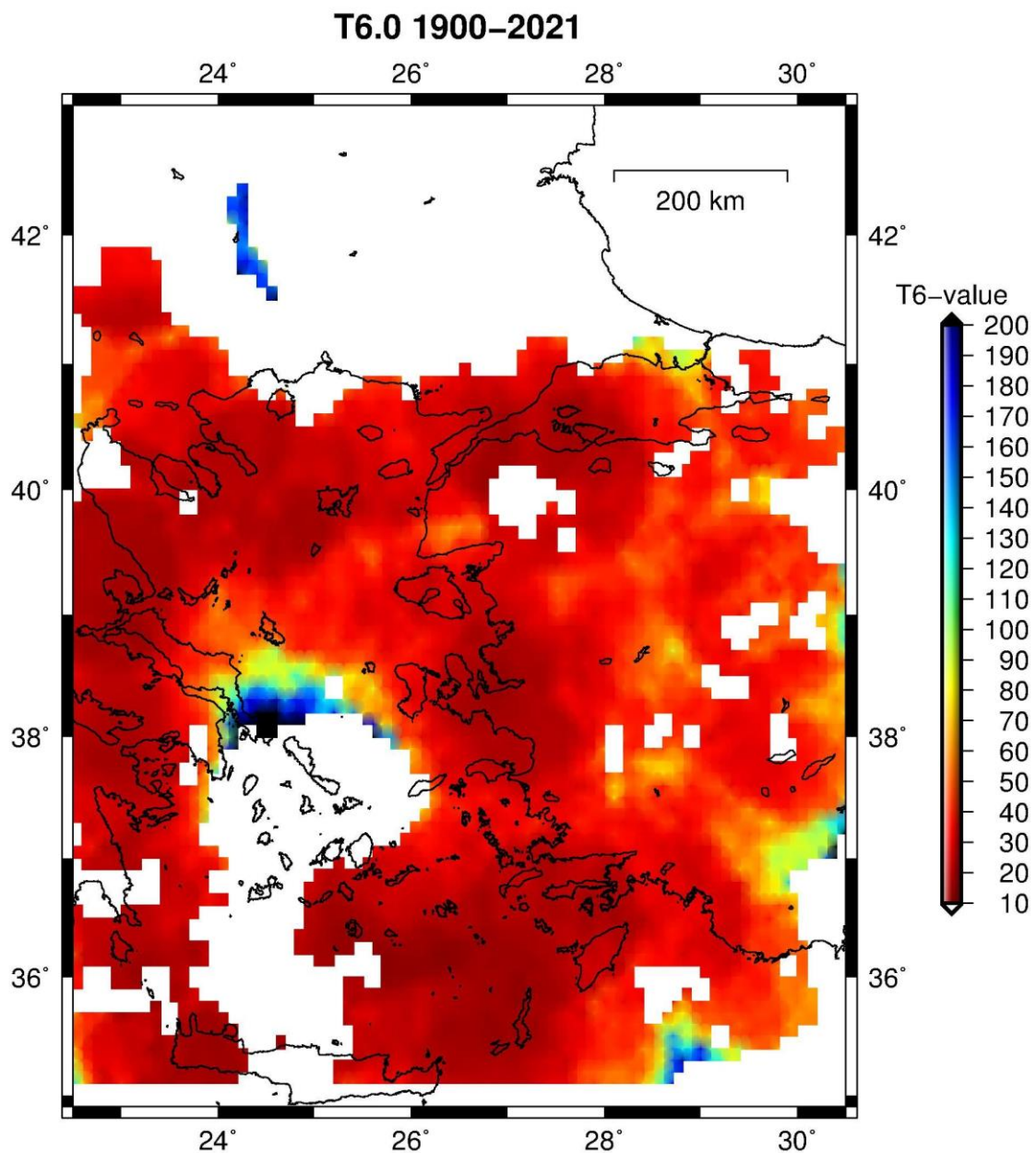
Figure 44: Spatial distribution of the mean return period for all (focal depths 0-200km) earthquakes of M≥6.0. The estimations are based on the complete events (M≥4.9) that occurred during the period 1900-2021. Circular regions are considered, centered at the nodes of a 0.1°x0.1° grid with radius R=80km and minimum required number of complete (M≥4.9) events within each circle, Nmin=30.
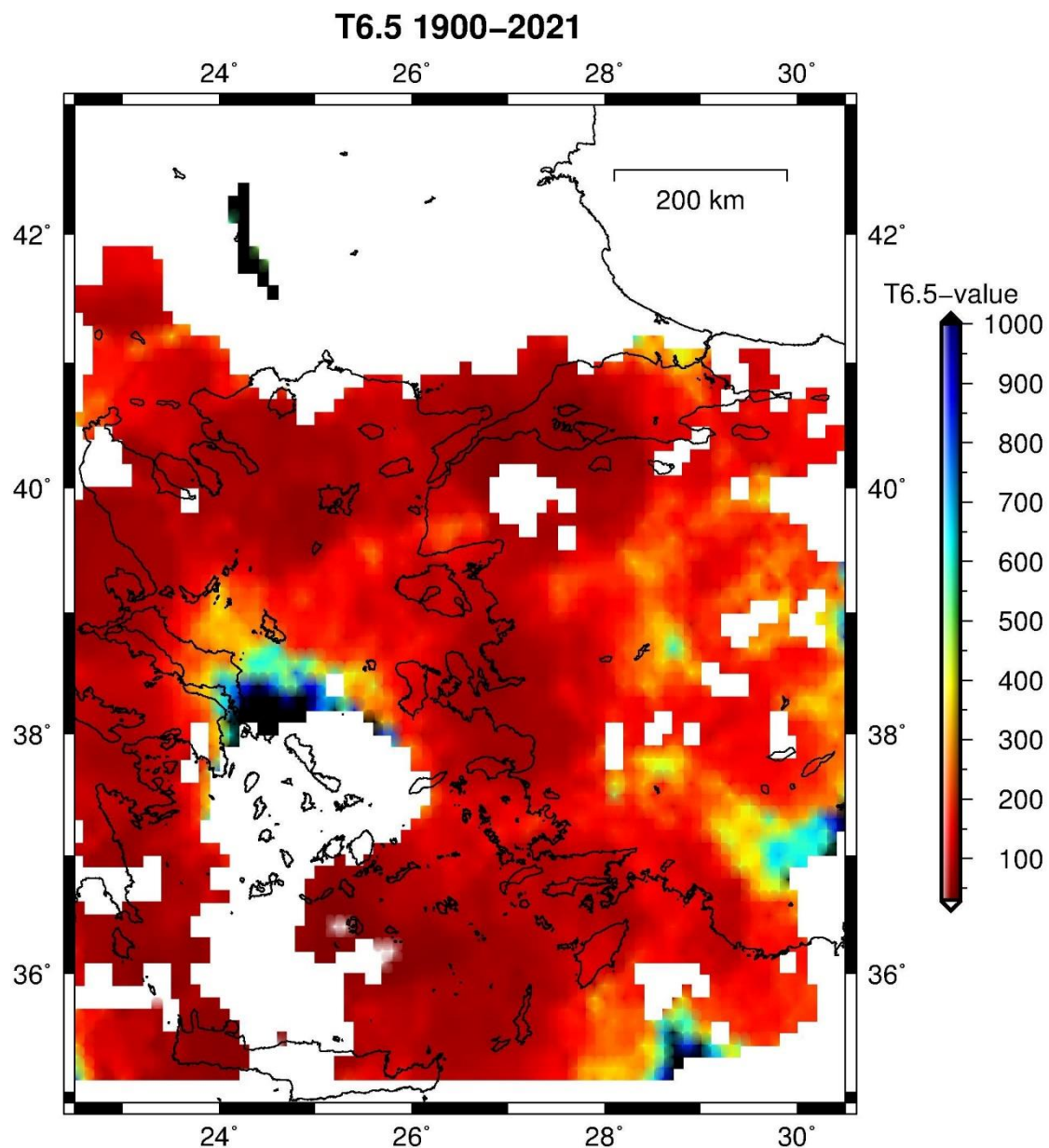
T6.5 1900−2021

Figure 45: Spatial distribution of the mean return period for all (focal depths 0-200km) earthquakes of M≥6.5. The estimations are based on the complete events (M≥4.9) that occurred during the period 1900-2021. Circular regions are considered, centered at the nodes of a 0.1°x0.1° grid with radius R=80km and minimum required number of complete (M≥4.9) events within each circle, Nmin=30.

M475 1900–2021
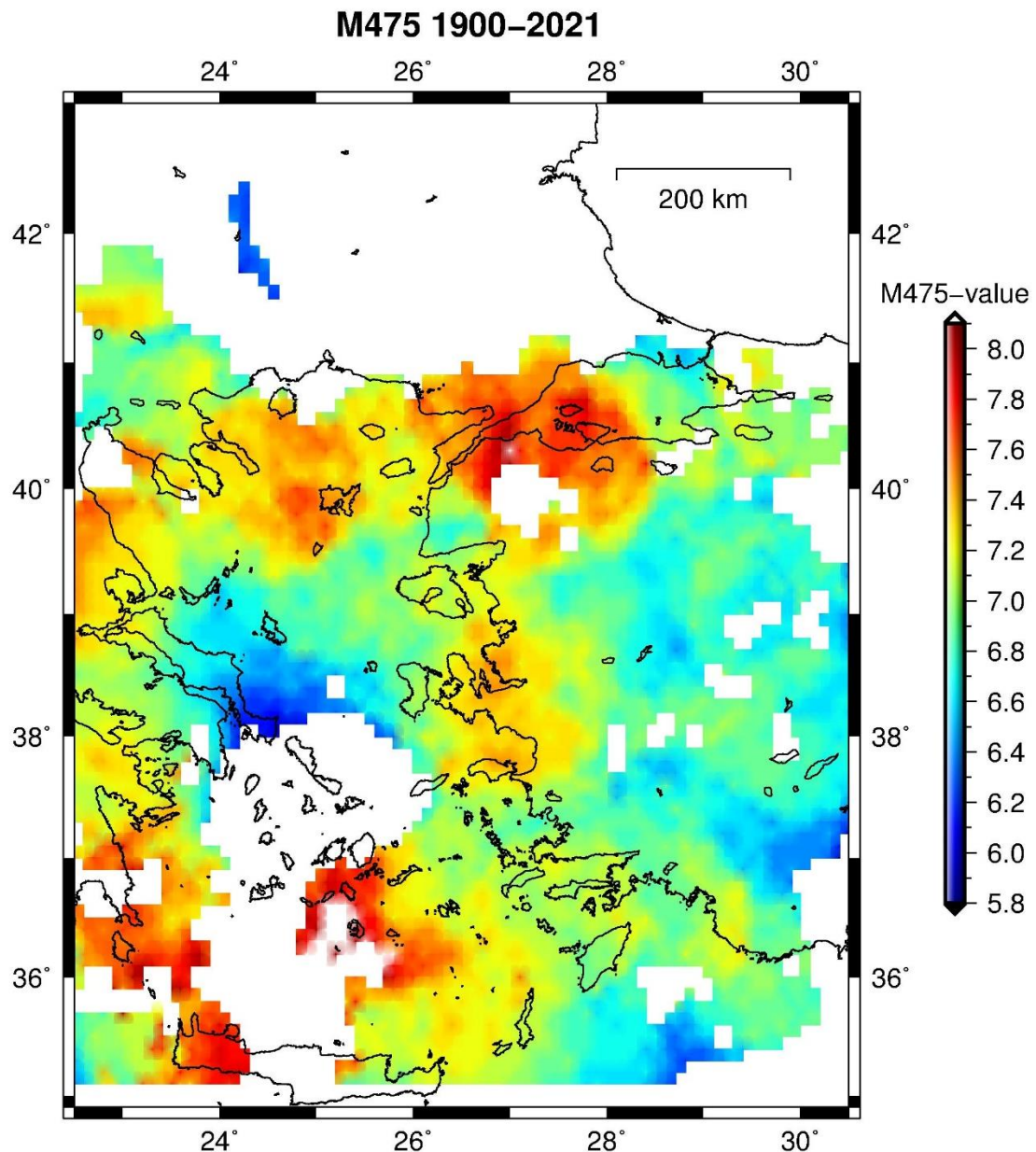
Figure 46: Spatial distribution of the probable maximum magnitude for a 475 years period (or the magnitude with 10% probability of exceedance within 50 years). The estimations are based on the complete events (all focal depths, M≥4.9) that occurred during the period 1900-2021. Circular regions are considered, centered at the nodes of a 0.1°x0.1° grid with radius R=80km and minimum required number of complete (M≥4.9) events within each circle, Nmin=30.

The values of the seismicity parameters used to produce the maps of figures 40-46 and based on earthquakes of the entire range of focal depths (0-200km) of the catalog are listed in the files of the accompanying this Deliverable WP2.2,e-Supplement **(1) "Catalog_Shallow&Intermediate_Depth_eqs.zip".**

3   PART 1: PROBABILISTIC SEISMIC HAZARD ASSESSMENT FOR CBA GREECE - TÜRKIYE

3.1 INTRODUCTION

Substantially every important decision concerning the evaluation of seismic loads on people and manmade facilities is made using some form of seismic hazard or seismic risk analysis. In some cases, these analyses are informally conducted, with probability and likelihood assessed intuitively with subjective expert opinion. In instances involving complicated assessments of effects derived from various geo-science and engineering disciplines, decision makers often prefer formal assessments of probabilities of earthquake occurrences and associated natural effects that may produce damage to facilities and injury or life-loss to people. Such formal assessments are usually most appropriate for recommendations on regional or national seismic design requirements, earthquake evaluation of important facilities whose loss would imply substantial financial hardship to owners, estimation of earthquake damage and losses for emergency preparedness purposes and decision making regarding seismic safety of critical facilities.

There are two main approaches to assess seismic hazard, the deterministic (DSHA) and the probabilistic (PSHA). Recent efforts have considered five types of analyses that reflect the current usage. In type I, purely deterministic seismic hazard analysis, one or more earthquakes are selected with only implicit consideration of their probabilities of occurrence. As an example, it could be mentioned, the assignment of a maximum credible earthquake with specified magnitude and distance or the identification of a "characteristic" earthquake on a specified fault segment with specified source parameters. Probabilistic concepts enter in this analysis only in a simple form, such as scatter about an average ground-motion empirical estimation curve (GMPE). The type II analysis, a semi-probabilistic seismic hazard analysis takes account of one or more specific earthquakes, but however the probability of occurrence is an explicit consideration in the selection of the earthquake. The type III analysis, a single model of probabilistic seismic hazard assessment (PSHA), differs sharply from type I and type II analysis techniques because in this case no specific earthquake is identified. In this case, a curve is produced that presents the annual probability that given levels of a ground-motion parameter will be exceeded at the site of structure. The type III is called single model PSHA because it employs only one model for the distribution of earthquake locations and magnitudes, and one attenuation model of the ground-motion parameter (Algermissen et al., 1982).

Due to the uncertainty concerning the appropriate model to use for the spatial distribution and occurrence rates of earthquakes and for the attenuation of ground-motion with distance, an appropriate procedure is to consider alternative models and to calculate the hazard curve for each of these models. The variability of results illustrates the range of uncertainty on hazard, and this is the type IV, multiple models of PSHA (EPRI, 1985;

Bernreuter et al., 1985). Combinations of techniques might be desirable in each situation. One useful hybrid method (type V) uses a type III and/or IV PSHA to characterize ground-motion probabilities and identify individual earthquakes that contribute the most to the seismic hazard. Then uses deterministic procedures to derive more detailed characteristics of the seismic hazard, including time histories of ground motion, which are available from a typical PSHA. This hybrid procedure can more effectively take advantage of recent advances in geological and seismological observations and physical modeling of the seismic source, wave propagation and site effects.

The main purpose of this study is to provide the PSHA ground motion intensity measures for Greece and Türkiye Cross Border Area (CBA), which is located from Alexandroupolis to the North up to Rhodos Island and SW coastal area of Türkiye.

The examined area (CBA Greece-Türkiye) is seismotectonically associated to the Hellenic Arc and North Anatolia fault and presents a high seismic activity. The area studied combines two seismotectonic regimes, the first of shallow crustal earthquakes with depths down to 40 km and the second of intermediate depth earthquakes located at the Benioff seismic zone of the southern Aegean affecting mostly the areas close to Rhodos Island and SW coastal regions of Türkiye. Strong earthquakes have hit several sites in this area from historical era till now (Papazachos and Papazachou, 1997) with a recent one located at the Northern coast of Samos Island in 2020 M7.0 (Cetin et al., 2020). For this reason, an accurate definition of seismic sources is indispensable to estimate seismic hazard at a site, which is threatened by earthquakes generated in these seismic sources. Analytical works concerning seismicity and active tectonics have been accomplished and CBA of Greece and Turkiye has been separated in seismogenic sources of the shallow and intermediate depth earthquakes (Papazachos and Papaioannou, 1993; Papazachos and Papazachou, 1997; Papaioannou and Papazachos, 2000; Vamvakaris et al., 2016; Woessner et al., 2015; Demircioğlu et al., 2018; Danciu et al., 2021).

The seismogenic source models and the seismicity parameters (the coefficients a and b of the Gutenberg-Richter relation, the area of each source, the maximum observed magnitude, and the annual rate of the earthquakes with M⊓5.0), which are going to be used in this analysis, are also given. All these parameters are useful for seismic hazard assessment in Greece - Türkiye CBA by application of the method proposed by Cornell (1968) and using the open-source code OpenQuake (Pagani et al., 2023). Using various geographical distributions of the seismogenic source models (Vamvakaris et al., 2016; Sesetyan et al., 2018; Danciu et al., 2021) in the study area and the seismicity parameters of each source, the PSHA of the Greek-Turkish CBR is carried out for Peak Ground Acceleration (PGA), Peak Ground Velocity (PGV) for various return periods (100, 475, and 950 years), for rock site conditions (VS30 ≥ 800 m/s). The pseudo acceleration (Sa) spectral values at three

distinct vibration periods (0.3, 0.6 and 1.0 sec) based on probabilistic analysis are evaluated, for three return periods 100, 475 and 950 years, as well.

3.2 OVERVIEW OF THE METHODOLOGY

The objective of PSHA is to provide a formal estimate of the earthquake threat at the area studied. Basically, the threat is expressed in terms of the amplitude of seismic motion (i.e. a peak ground acceleration, velocity, and values of the response spectrum of ground motion). A typical PSHA estimates the annual probabilities of exceedance as a function of single amplitude of strong ground shaking. A more complicated formulation of seismic hazard analysis includes vectorial representation of strong motion characteristics. Four basic elements are considered to assess seismic hazard at a specific site.

a. <u>Seismic sources characterization</u>. The seismic sources are identified based on geological, seismological and geophysical studies, in terms of their location, geometry and maximum earthquake magnitude observed in each source. The geographical distribution of the seismogenic sources in Greece and surrounding area has been presented (Papazachos and Papaioannou, 1993; Papazachos and Papazachou, 1997, Papaioannou and Papazachos, 2000; Vamvakaris et al., 2016; Woessner et al., 2015; Demircioğlu et al., (2018); Danciu et al., 2021). In a typical PSHA, though not indispensable, assumption for seismogenic sources is that the mean activity rate per square kilometer is constant within any zone. For faults, a common definition for a continuous fault zone is that the mean rate of activity per kilometer of fault length is constant. Also, the characteristics of the seismic magnitude distribution are usually assumed to be the same over any one source or faults.

b. <u>Earthquake recurrence.</u> Recurrence relationships characterize the frequency of occurrence of earthquakes of various sizes, from minimum magnitude of engineering significance to the maximum magnitude estimated for the source. Earthquake recurrence relationships must be developed for each identified seismic source that could significantly contribute to the seismic hazard at the site. The recurrence curves are usually described by either a truncated exponential recurrence model (Cornell and Vanmarcke, 1969) based on Gutenberg and Richter (1954) recurrence law, or a characteristic earthquake recurrence model (Youngs and Coopersmith, 1985). A Poisson probability model is usually assumed for probabilistic ground motion analyses. In the Poisson model, earthquake occurrence in time is assumed to be random and memory-less. The probability of an earthquake in each time-period is thus determined by the average frequency of earthquakes and is

independent of when the last earthquake occurred. It is noteworthy that recently some improved time and/or magnitude dependent models have been proposed (Papazachos and Papaioannou, 1997) for PSHA.

c. Ground Motion Predictive Equations (GMPE). GMPE describes the variation of the amplitude of a ground motion parameter as a function of earthquake magnitude and source –to –site distance. A great number of GMPEs have been developed for peak ground motion parameters (PGA, PGV), and for different structural periods of vibration (Sa). These relations are in terms of earthquake magnitude, rupture mechanism, various definitions of distance, faulting type and local site conditions. Attenuation relations have been proposed for different seismotectonic environments including crustal and subduction zone earthquakes. The same relationships have also been developed for different broad soil classes of subsurface conditions (e.g. rock, firm soil, and soft soil etc).

d. Probabilistic Seismic Hazard assessment (PSHA). The seismic source characterization and ground motion attenuation are combined in a probabilistic model to develop relationships between the amplitude of a ground motion parameter and the probability of its exceedance. These relationships are termed seismic hazard curves. Using the Total Probability theorem, the probability analysis integrates overall earthquake sizes and distances, and sums over all sources, to estimate the expected number of exceedances of the ground motion amplitude per unit time, which is an accurate estimate of the annual probability of exceedance.

The seismic source characterization of the area studied is determined by applying various seismic source models proposed from various studies. In PSHA, one calculates the expected number of occurrences as the sum of expected occurrences caused by many diverse earthquakes. The expectation of that sum always be the sum (Integral) of those expectations, even if future events are correlated in time space and size. There need not be any implicit or explicit assumption of Poissonian behavior, either in space or in time analysis. Virtually any model of future earthquake occurrence, including spatial temporal and size dependence can be accommodated. The analysis of PSHA is not limited to ground-motion amplitudes, whether characterized by scalars or vectors. A common application of PSHA derives annual probabilities of exceedance for a scalar representation of seismic shaking, e.g. peak ground values (acceleration, PGA, velocity, PGV) or the corresponding response spectral values for various natural periods. The mean return periods, in which the expected ground motion is calculated, are 100, 475 and 950 years. The actual 100, 475 and 950-year return periods have

approximately 39%, 10% and 5% probability of being exceeded in 50 years, respectively.

The GMPEs are applied for various parameters such as PGA, PGV, and pseudo acceleration (Sa). The basic formula which represents the attenuation of strong motion parameter in terms of magnitude, distance, and soil conditions, is given by:

$$\ln Y = F_E(\boldsymbol{M}, mech) + F_P(R, \boldsymbol{M}) + F_S(V_{S30}, R, \boldsymbol{M}, mech) + \varepsilon \cdot \sigma(\boldsymbol{M})$$

in which "ln" is the natural logarithm, and FE, FP, and FS are functions for the event ("E"), path ("P"), and site ("S") contributions to the motion. The standard normal variate ε is the fractional number of standard deviations σ of a predicted motion from the mean. As it can be deduced, it is important in any estimation of low or high probabilities in PSHA to make a statement about the degree of confidence in the results. A common way to examine uncertainty is to conduct sensitivity studies, varying the input parameters and model assumptions to see their impact upon the probabilities. Reviewing the sensitivity analysis of PSHA to changes in the parameter values can lead to quantitative conclusions regarding the uncertainty in analysis results. The basic process can be formalized and quantified in uncertainty analysis of the type in common use in PSHA. Such an uncertainty analysis, called a logic tree, considers a spectrum of values for each of the input parameters, a spectrum of functional forms for the GMPEs and a spectrum of model alternatives with respect to the seismic sources. The results of this type of uncertainty analyses and the weights associated with these are available, they can easily be processed to make them more amenable to inspection.

Concerning the site geological effects, if the site is a rock site, local soil amplification effects are not applicable, and the response spectrum is directly obtained from the PSHA using attenuation relationships for rock sites. For a site in a soil site, it is important to account for soil amplification effects. There are practically two approaches for incorporating soil geological conditions in PSHA. In the first, the site geological effects are directly incorporated in the PSHA using GMPEs applicable to the soil or rock condition at the site. In the second, peak ground or spectral values are predicted by using rock attenuation relationships and then carrying out site response

analyses to assess the modifying influence of the soil column on the ground motions. In this analysis, rock geological conditions in PSHA were considered. For GMPEs of PGA, PGV, and Sa the Vs30 parameter is adopted.

The methodology used to conduct PSHA was initially developed by Cornell (1968) and formulated as a computer code by McGuire (1976). Moreover, for Greece this computer code was modified and improved to take into account an anisotropic radiation model (Papazachos, 1992) of the attenuation of strong motion parameters by Margaris (1994) and Margaris and Papazachos (1994).

3.3 IMPLEMENTATION OF PSHA IN THE GREECE – TÜRKIYE CROSS BORDER AREA

The probabilistic assessment of seismic hazard (PSHA) in the Greece – Türkiye Cross Border Area (CBA) was jointly performed by the Greek and Turkish partners after the extent of the CBA had been jointly decided. The extent of CBA includes the four pilot sites of the project, namely Alexandroupoli, Cannakale, Samos and Izmir.

An important step in seismic hazard assessment is modeling the epistemic uncertainty associated to the seismic source models, the maximum earthquake magnitude and the ground motion models. This was achieved through a comprehensive logic-tree approach.

3.3.1 Selection of seismic source models for crustal earthquakes

The seismic source models for crustal earthquakes which were included in the seismic source logic-tree for the PSHA of the CBA were jointly selected, so that the most recent advances in seismic source modeling, coming from both countries, were considered. Therefore, two area source models, were selected, namely the one proposed by Vamvakaris et al. (2016) and the area source model used in Turkish Seismic Regulations (TBDY, 2018). Vamvakaris et al. (2016) model, shown in Figure 1, incorporate area sources as polygons with uniform distribution of seismicity within them, as well as, specific rupture planes. The area source model of TBDY (2018), shown in Figure 2, includes the seismicity parameters defined by Gutenberg Richter Distribution with a probabilistic approach for faulting mechanisms and hypocentral depths for each individual polygon.
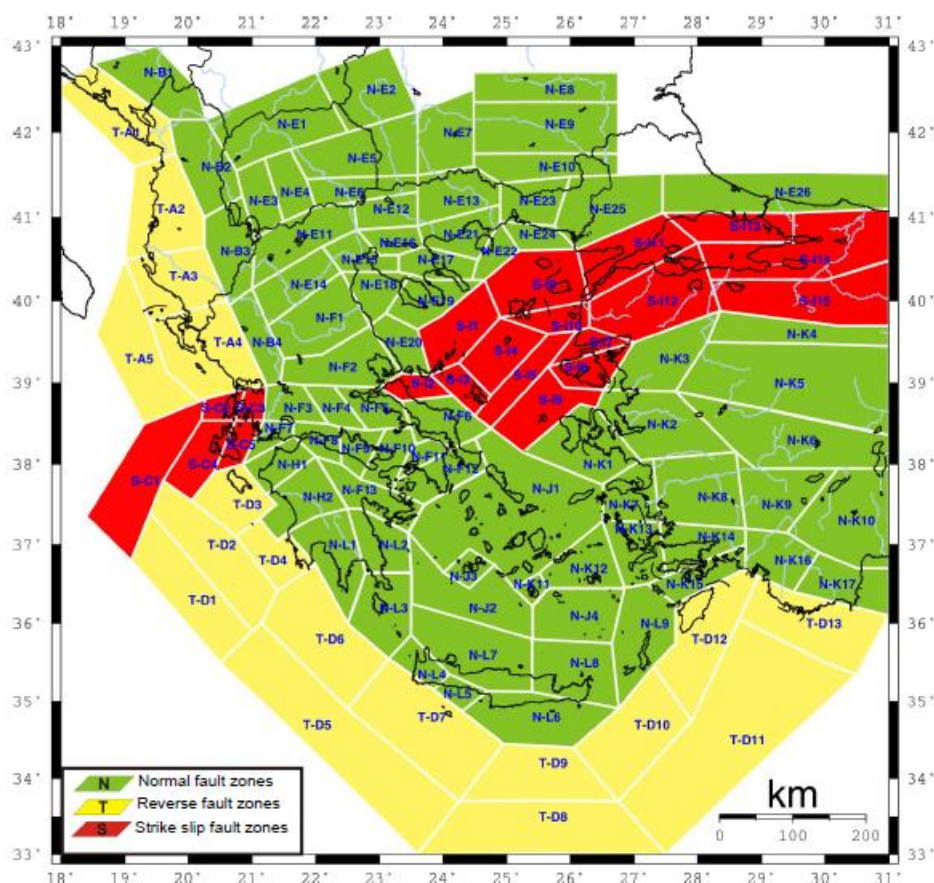
Figure 47: Area source model of Vamvakaris et al. (2016)

Following the common practice in recent PSHA studies (Woessner et al, 2013; Danciu et al., 2021), it was deemed by the working group that a fault-based seismic source model, should be incorporated in the relevant seismic source logic-tree, as well. Therefore, it was decided to adopt the approach followed for the development of the recent pan-European Seismic Hazard Model, ESHM20 (Danciu et al., 2021), combining the active faults with a smoothed gridded seismicity model. The active faults for ESHM20 were adopted, as they were developed upon the European Fault-Source Model 2020, an update of the European Database of Seismogenic Faults (EDSF) and several other recent active fault compilations in the Euro-Mediterranean regions (Basili et al., 2020). The crustal faults are represented by a down-dip planar geometry that defines its three-dimensional plane in the Earth's crust. In this representation, the trace of the fault upper edge is extruded downward basing on the dip and depth values.
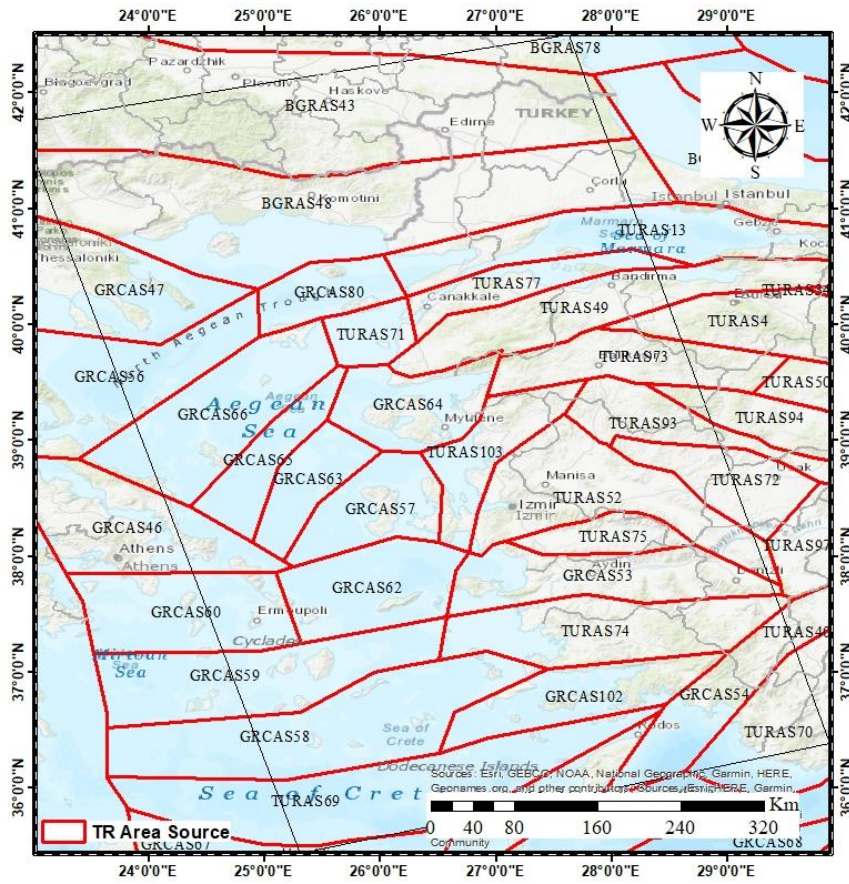
Figure 48. Area source model of TBDY (2018)

The smoothed gridded seismicity model of ESHM20 was modified for the PSHA of the CBA, taking into account the earthquake catalogue and the seismicity parameters which were computed for the CBA, within the framework of EReS. For each grid point (0.1°x0.1°) an a-value and a b-value, was calculated based on the seismicity of an area around it of 80 km radius, including at least 30 events. For the points where less than 30 events were detected, no calculation was made. The grid points were divided based on the TECTO zones proposed by ESHM20 and the mean a- and b-values were computed. The points for which specific calculation of a-value was possible (i.e. at least 30 events were detected within an area of 80 km radius around them) were assigned that a-value, normalized to the actual geographical area represented by it. On the other hand, the points of the grid for which no specific calculation of a-value was possible, were assigned the mean a-value of the corresponding TECTO zone. The b-value of each grid point was set equal to the mean b-value computed for the TECTO zone in which each point belongs. The smoothed seismicity is represented as point sources of a grid spanning across the entire CBA, which are grouped according to the corresponding area source of ESHM20 in which they are situated. All point sources within an ESHM20 area source

share source attribute such as style of faulting, depth, upper and lower seismogenic depth. As in ESHM20, in the vicinity of active faults, the background-smoothed seismicity is complementary to the seismic productivity together with the faults, whereas in regions with no faults, the smoothed seismicity is an alternative to an area source model. To avoid the double counting of the earthquake rate forecast due to active faults and background seismicity, a variable threshold magnitude was introduced. This concept requires a definition of fault proximity, which in this case is defined as a spatially symmetric buffer following the top-trace of the fault. The buffer zone considered by ESHM20 (Danciu et al., 2021) was adopted herein. The magnitude threshold was set to 5.9 and the main assumption is that events with M > 5.9 are associated with the faults. Within the fault buffer the occurrence rates of lower magnitude bins (<= 5.9) are represented by point sources, whereas the occurrence rates of the M>5.9 are associated with the fault. Outside the buffer, the Mmax of the smoothed seismicity model is the Mmax value attributed to the corresponding TECTO zone of ESHM20. The active faults, and smoothed gridded seismicity model adopted for the PSHA in the CBA is shown in Figure 3.
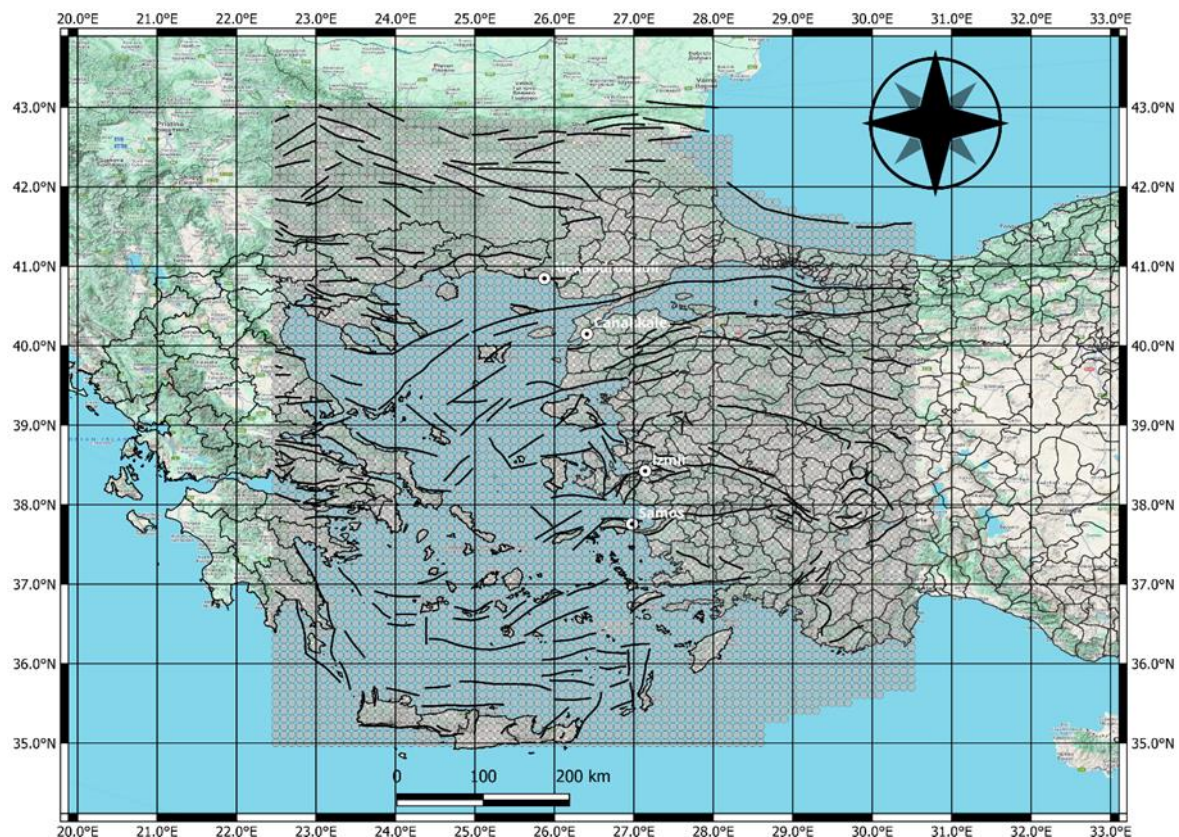
Figure 49: Active faults and smoothed gridded seismicity model adopted for the PSHA of the Greece – Türkiye CBA

Therefore, the seismic source logic-tree for crustal earthquakes consists of two source models, namely Vamvakaris et al. (2016) and ESHM20 Faults and smoothed seismicity. It was jointly decided to allocated the weights 0.375, and 0.625, respectively, to each one of them. Figure 4 presents the logic-tree of the seismic source model for crustal earthquakes.
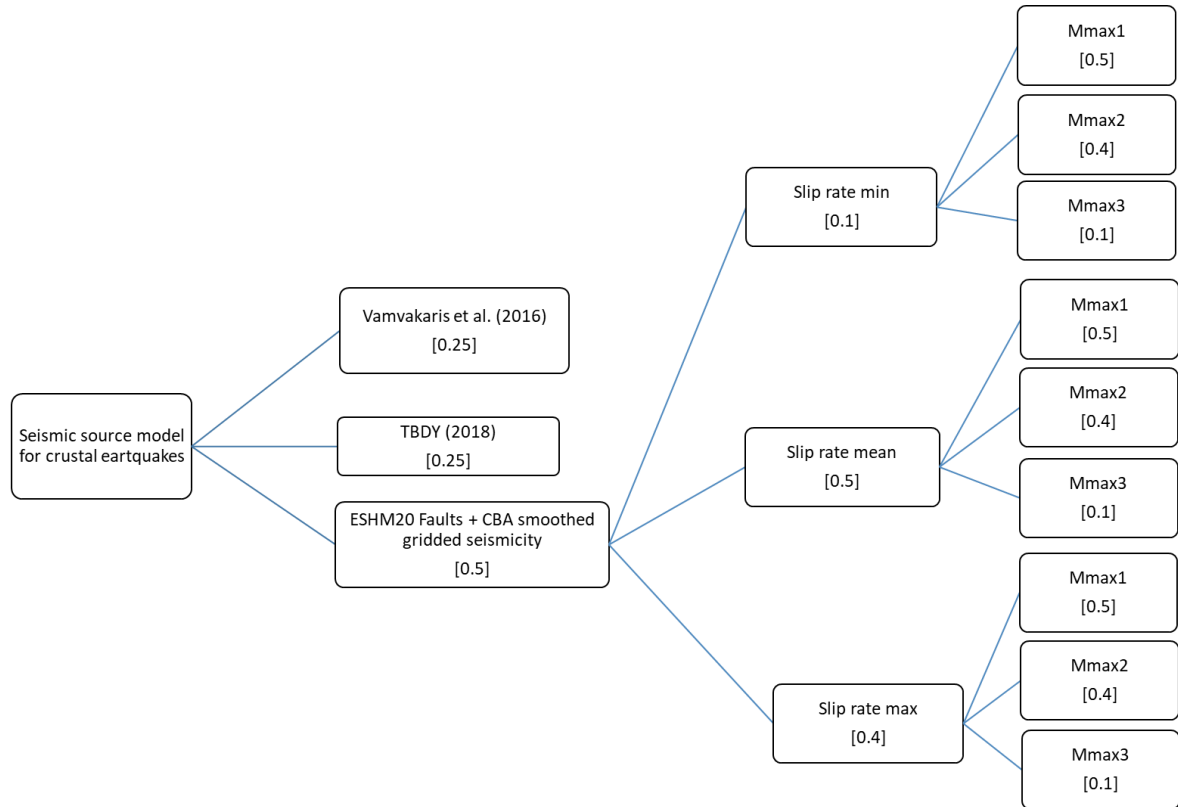
Figure 50: Logic-tree of the seismic source model for crustal earthquakes considered in the PSHA for the Greece – Türkiye CBA.

3.3.2 Selection of seismic source models for subduction earthquakes

The seismic source model for crustal earthquakes is supplemented by the source model for subduction earthquakes. For the PSHA in the Greece – Türkiye CBA it was jointly decided to consider the subduction sources (in-slab and interface) associated to the Hellenic Arc for ESHM20 (Danciu et al., 2021), as it was originally implemented, along with its accompanying uncertainties (Figure 5).
The combined source model jointly proposed herein is given in digital form in the **(2) e-Supplement_2_Combined_2_Model_Greece&Turkey_v3.zip.**
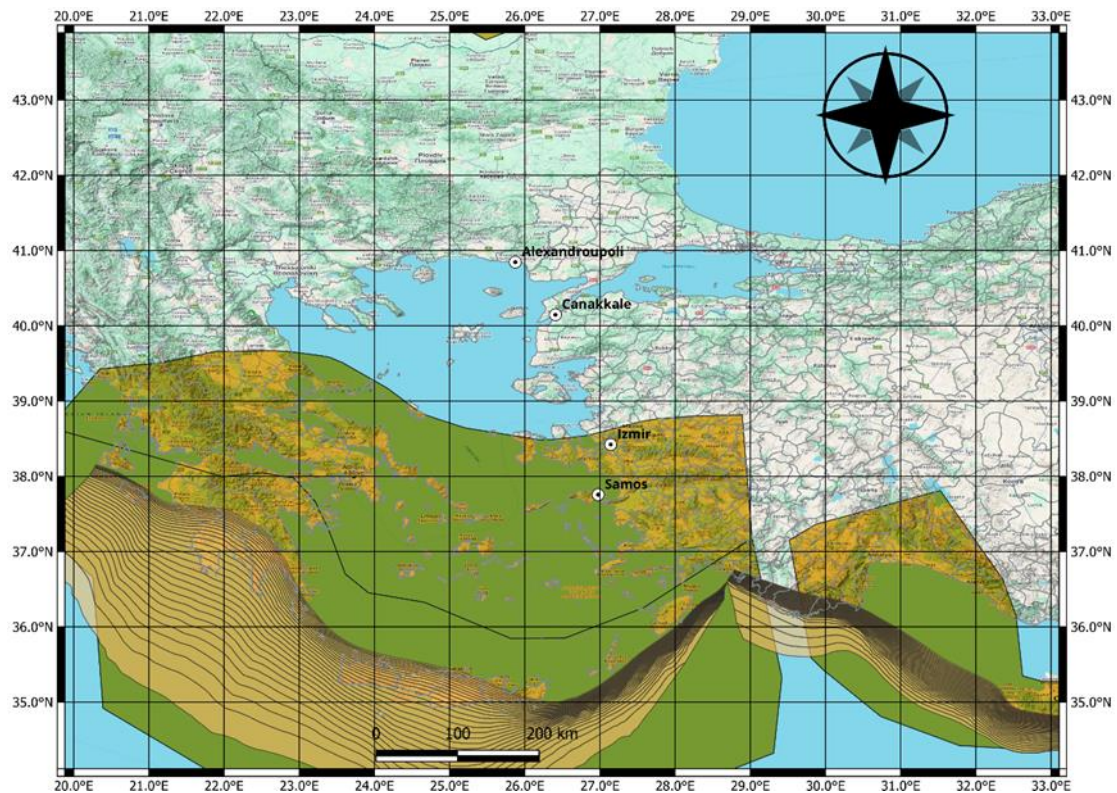
Figure 51: ESHM20 subduction sources which were adopted for the PSHA of the Greece – Türkiye CBA

3.3.3 Selection of Ground Motion Predictive Equations (GMPEs) for crustal and subduction earthquakes

The selection and weighting of GMPEs for crustal earthquakes in the CBA was based in the work of Theodoulidis et al. (2024). There, testing and ranking of pre-selected GMPEs was performed using strong motion data of the broader Greece – Türkiye CBA. Their final suggestion is shown in Table 1.

Table 4: Final ranking and weighting suggestion of GMPEs for crustal earthquakes in the Greece - Türkiye CBA, according to Theodoulidis et al. (2024)

A/A	GMPE	w_l-LLH	w_l-Residuals	Final w_l
1	Boore et al. (2021) [13] with bias	0.160	0.281	0.346
2	Chiou and Youngs (2014) [9]	0.160	0.270	0.337
3	Boore et al. (2021) [13] w/o bias	0.162	0.241	0.317
4	Chousianitis et al. (2018) [11]	0.272	0.121	-

The GMPE selection and weighting proposed by Theodoulidis et al. (2024) was adopted herein. Hence, the GMPEs of Boore et al. (2021) (with and without bias) and Chiou and Youngs (2014) were chosen, with weights 0.346, 0.317 and 0.337, respectively. The logic-tree of the ground motion model for crustal earthquakes is shown in Figure 6.

Boore et al. (2021) w/ bias
[0.346]

GMM for shallow
earthquakes

Boore et al. (2021) w/o bias
[0.317]

Chiou and Youngs (2014)
[0.337]
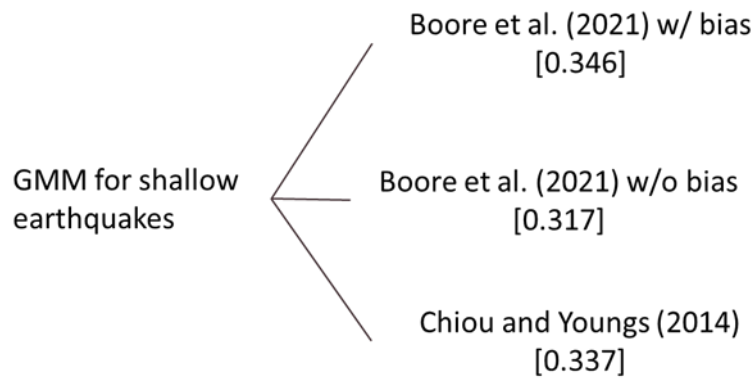
Figure 52: Logic-tree of the ground motion model for crustal earthquakes considered in the PSHA for the Greece – Türkiye CBA.

The selection and weighting of GMPEs for subduction (in-slab and interface) earthquakes was based on the similarity of seismotectonic environment between the CBA and the regions which provided strong motion data for the development of appropriated GMPEs. The Next Generation Attenuation Subduction (NGA-Sub) ground motion models (Parker et al. 2020; Kuehn et al. 2020; Gülerçe & Abrahamson, 2020) consist some of the most recent GMPEs for subduction earthquakes, calibrated against worldwide data. However, no data from the eastern Mediterranean were included in their calibration dataset. The latest GMPE developed with the aid of strong motion data from the Hellenic Arc for subduction earthquakes is the one of Skarlatoudis et al. (2013). Therefore, it was jointly decided to consider the GMPE of Skarlatoudis et al. (2013) with a weight equal to 0.4 and the GMPE of Parker et al. (2020) with a weight equal to 0.6 (Figure 7). The selection of the GMPE of Parker et al. (2020) against the rest of NGA-Sub models was based on its ability to predict PGV, which is an intensity measure for which PSHA outcomes are required for the Greece – Türkiye CBA.

Skarlatoudis et al. (2013)
[0.4]

GMM for subduction
earthquakes

Parker et al. (2020)
[0.6]

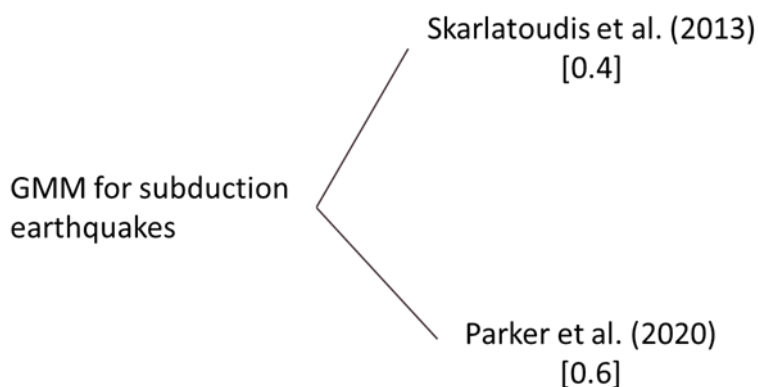**Figure 53: Logic-tree of the ground motion model for subduction earthquakes considered in the PSHA for the Greece – Türkiye CBA**

3.4 GROUND MOTION INTENSITY MEASURES ESTIMATED

The PSHA for the Greece – Türkiye CBA was performed for PGA, PGV, Sa (0.3s), Sa (0.6s) and Sa (1.0s) for return period equal to 100, 475 and 950 years, utilizing the seismic source and ground motion models described above. The investigation lefetime was set to 50 years; hence the corresponding probabilities of exceedance are 0.39, 0.1 and 0.051, resectively. The truncation level of the GMPEs was set to ±2.0 to avoid extremely large ground motion estimates. Rock site conditions were considered, therefore the VS30 value was set to 800 m/s. The analysis was performed through the software OpenQuake (Pagani et al., 2014), as jointly decided between the project partners.

3.5 PSHA results

The results of the PSHA for the Greece – Türkiye CBA are given in the form of seismic hazard maps for PGA, PGV, Sa (0.3 s), Sa (0.6 s) and Sa (1.0 s) and for three recurrence periods, TR, namely 100, 475 and 950 years. All the results are also given in tabular form, through an external spreadsheet file, which accompanies this report and is considered as an integral part of it.
Figures 8 and 9 present the seismic hazard curves, in terms of PGA and spectral acceleration at period equal to 1 sec (Sa (T=1.0 s)), respectively, for the four test sites of the project (Alexandroupoli, Cannakale, Izmir and Samos) as computed by using various seismic source models which were considered in this investigation. More specifically, the seismic hazard curves refer to the following seismic source models:
□   Vamvakaris et al. (2016) (see Figure 1)
□   TBDY (2018) (see Figure 2)
□   EReS SS model + ESHM20 faults, including the active faults of ESHM20 in combination with the smoothed gridded seismicity model which was developed herein (see Figure 3).
□   Final PSHA results, as computed by combining the seismic source models, as shown in Figure 4

Furthermore, the results of ESHM20, as presented in Danciu et al. (2021) are presented, as well, to compare.
Usually, for low return periods, small differences are observed between the estimates of the various source models. However, as the return period increases, the differences among the effects of the source models increase, as well. For two of the test sites, namely Alexandroupoli and Izmir, the active faults-based source model provides larger PGA and Sa (T=1.0 s) estimates than the uniform seismicity area source-based model, whereas for the rest of the test sites (Canakkale and Samos) the opposite occurs. This fact, along with the quite important observed differences in some cases, highlights the need for taking into account multiple source models (in terms of geometry and seismicity) to consider the epistemic uncertainty regarding the seismic source modeling.

For Alexandroupoli and Canakkale, the PSHA final estimates for PGA are in reasonable agreement with the ESHM20 results. On the other hand, the ESHM20 PGA results are quite larger than the final PSHA results reported herein for Izmir and Samos. Large differences are also apparent for the Sa (T=1.0 s) estimates, especially for Alexandroupoli. In general, the ESHM20 results provide higher ground motion estimates than the results reported herein. Those differences may by attributed to the different seismic source and ground motion models, which were incorporated in both cases, as well as, to the chosen truncation level of GMPEs, which was equal to ±3 in ESHM20 and equal to ±2 in the PSHA conducted for the Greece – Türkiye CBA.

Figures 8 – 24 present the final seismic hazard maps which were computed for the Greece – Türkiye CBA according to the approach presented in section 2.
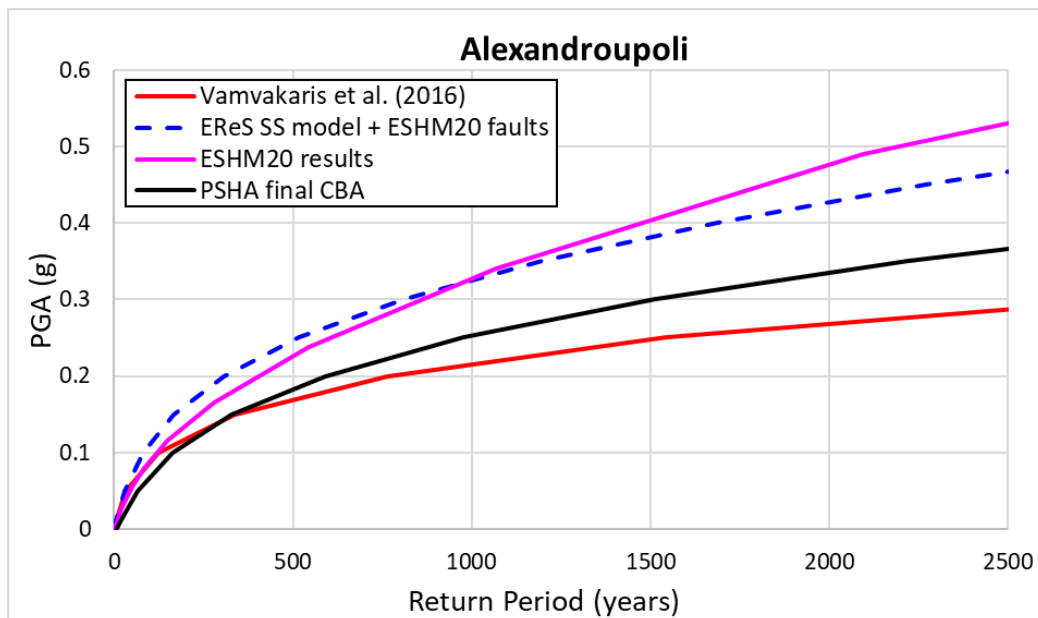
(a)
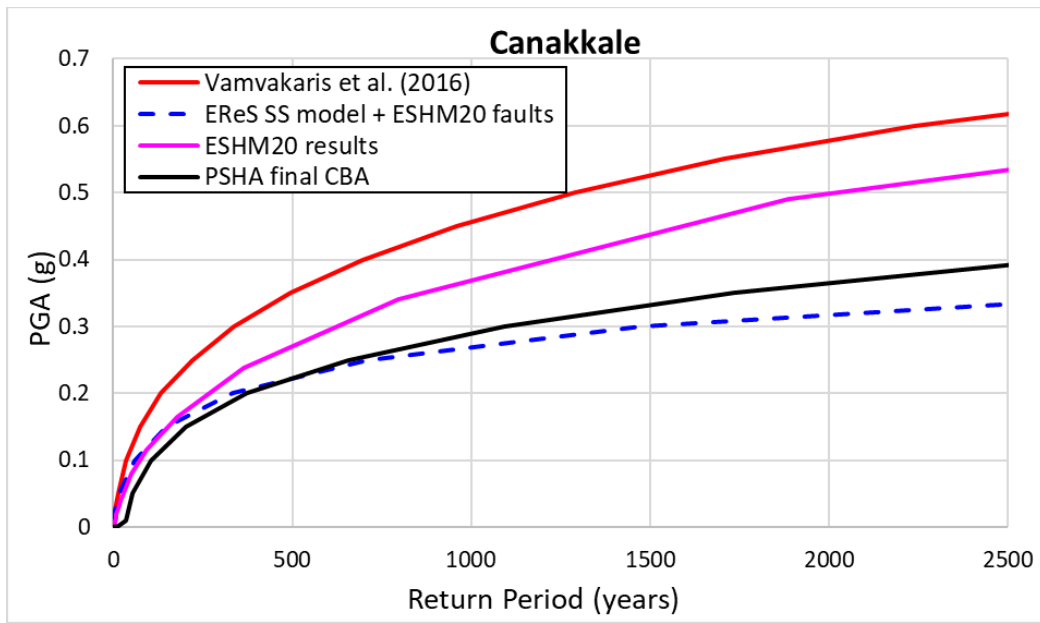
(b)
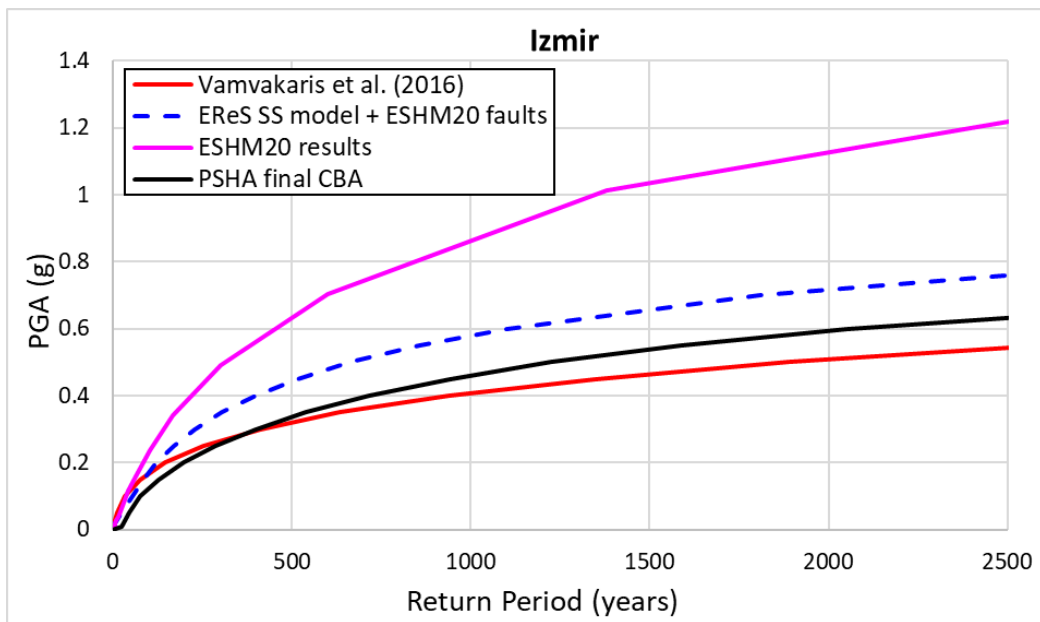
(c)
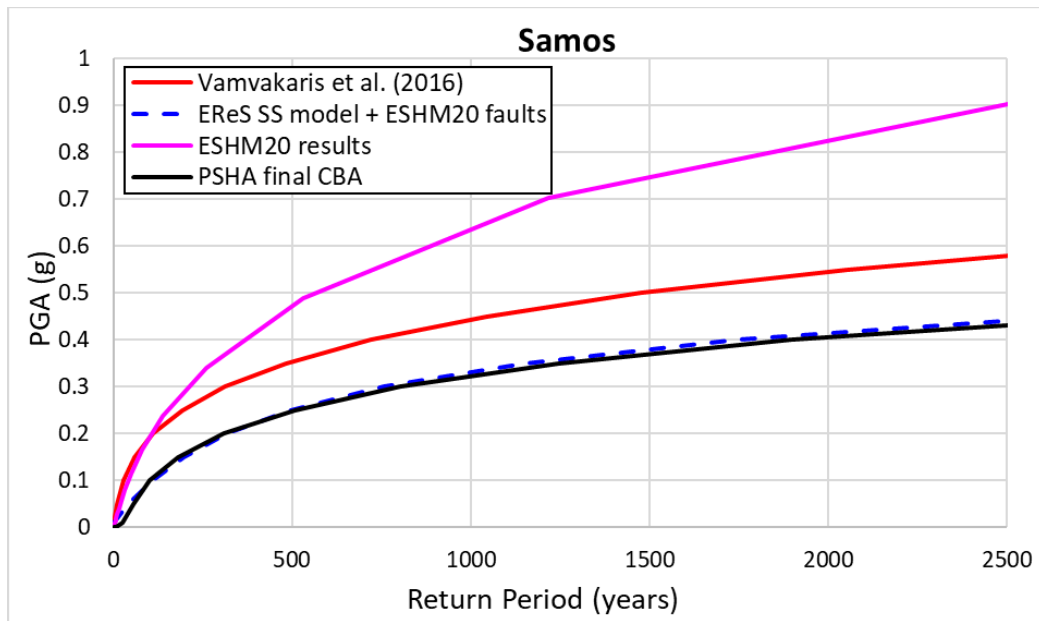
(d)

Figure 54: Comparison between PSHA results in terms of PGA for various seismic source models considered herein and the ESHM20 results for the four test-sites of CBA, (a) Alexandroupoli, (b) Cannakale, (c) Izmir and (d) Samos
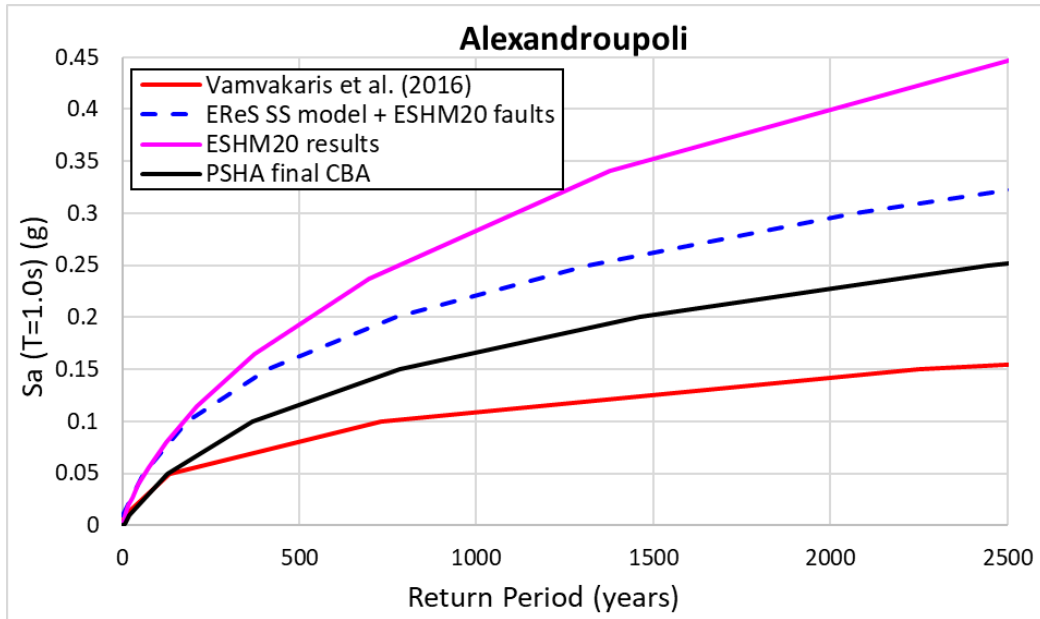
(a)
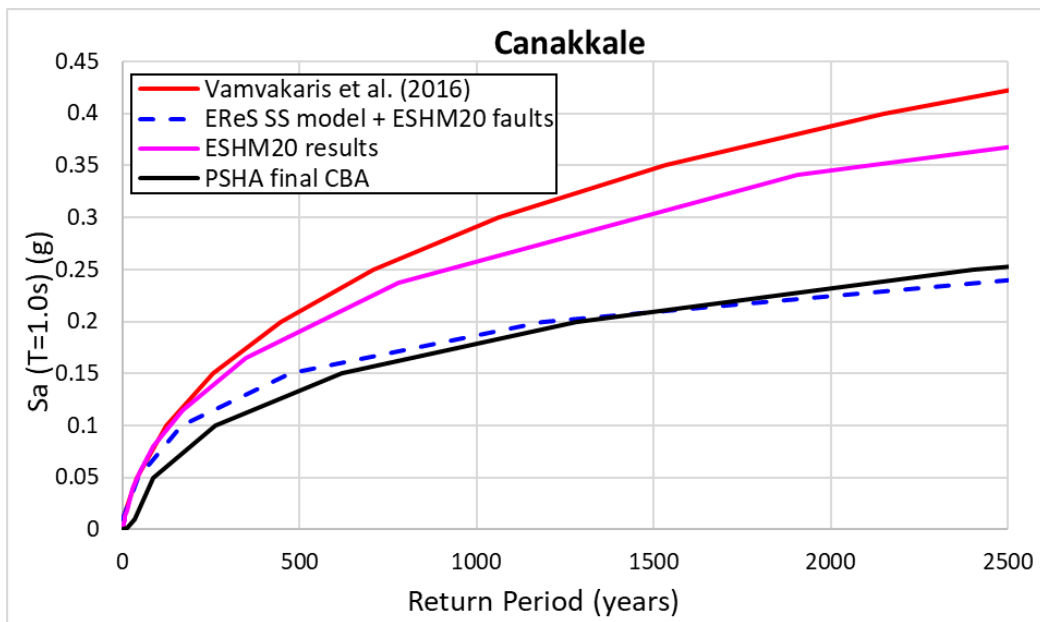
(b)
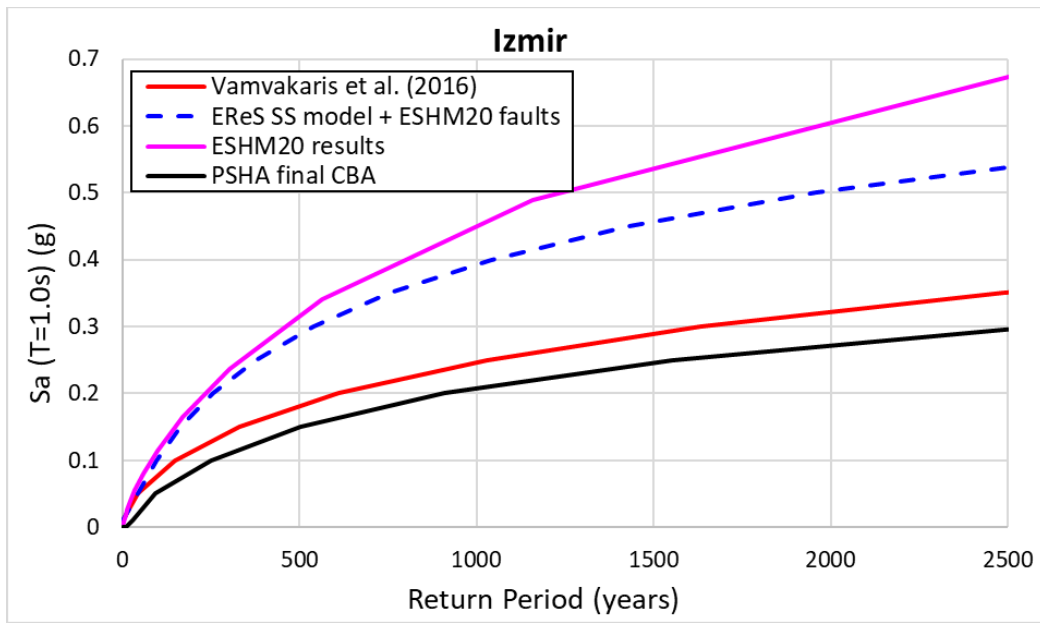
(c)
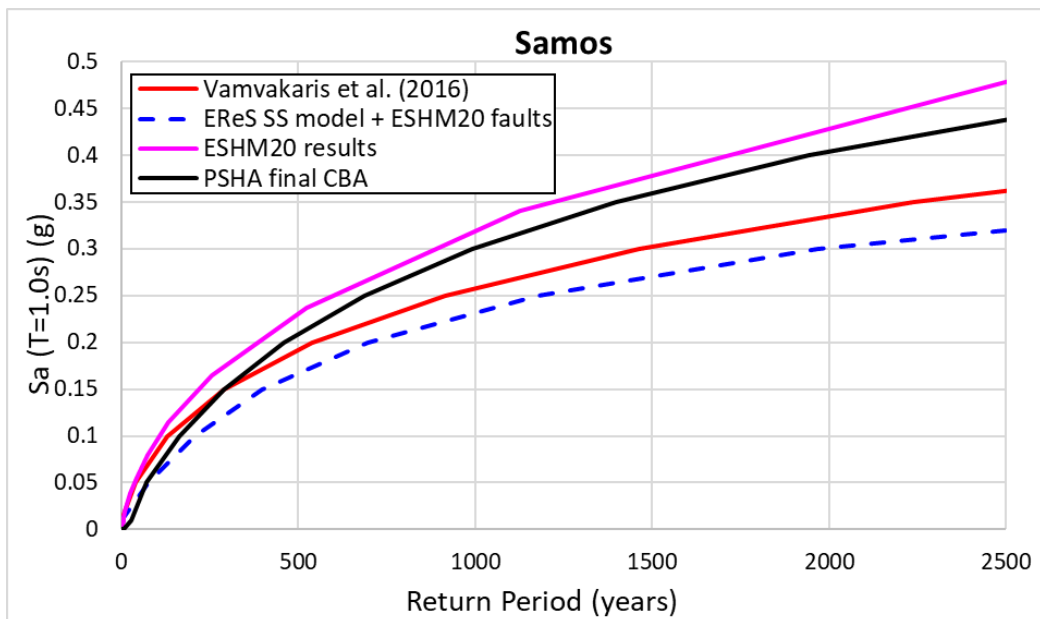
(d)

Figure 55: Comparison between PSHA results in terms of Sa (T=1.0 s) for various seismic source models considered herein and the ESHM20 results for the four test-sites of CBA, (a) Alexandroupoli, (b) Cannakale, (c) Izmir and (d) Samos
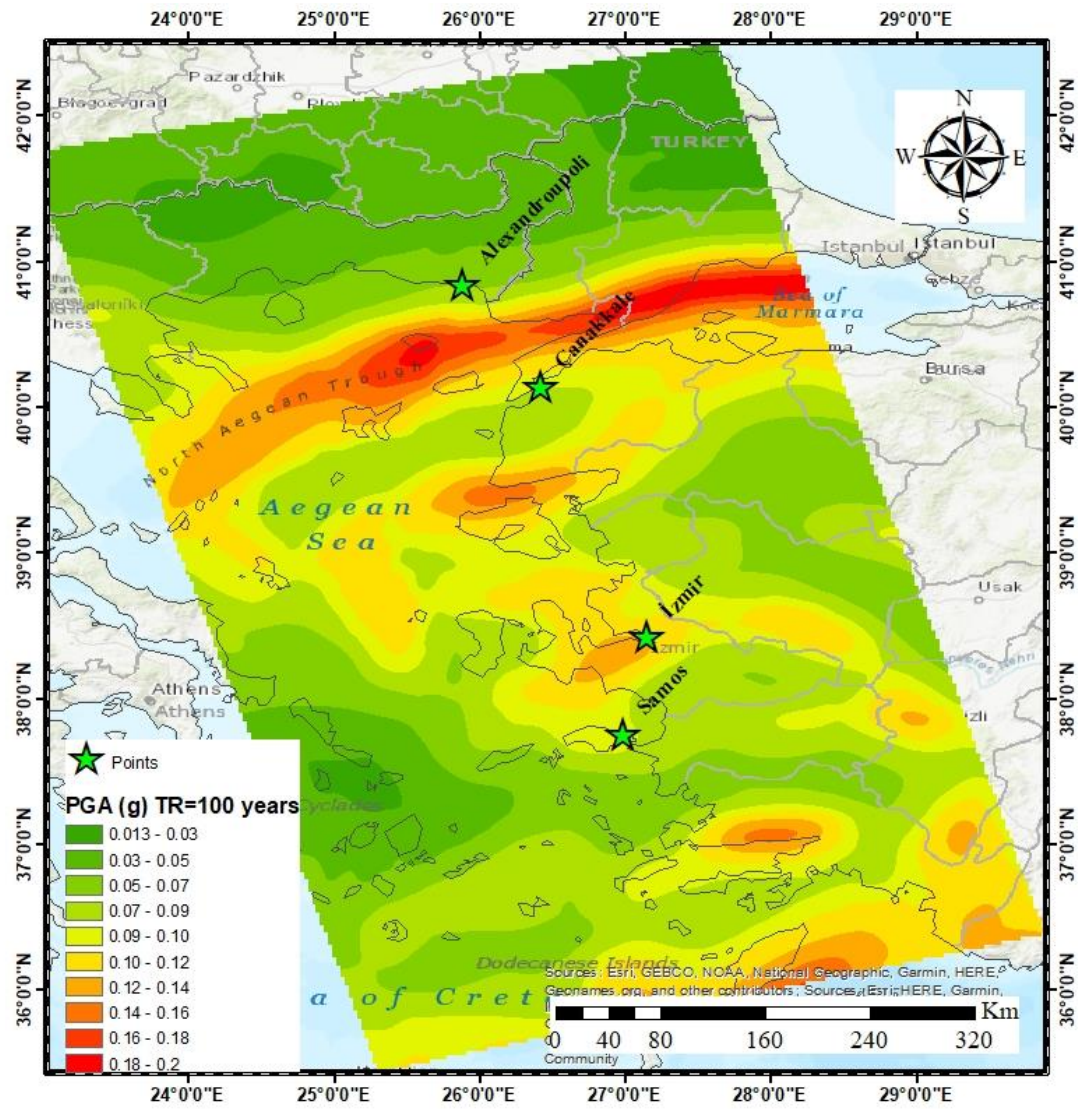
Figure 56: PSHA results for the Greece – Türkiye CBA and the Peak Ground Acceleration (PGA) for return period equal to 100 years
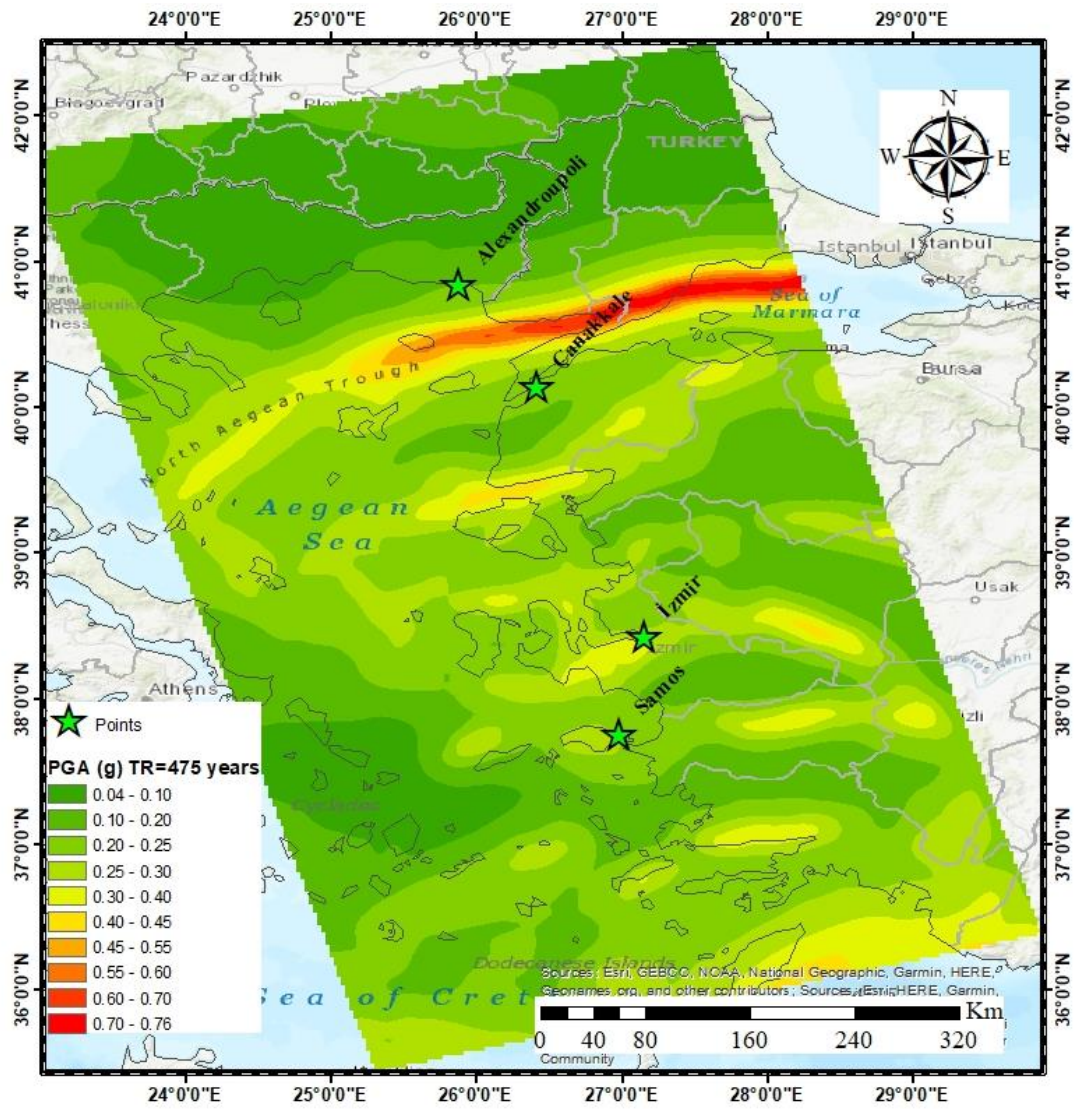
Figure 57: PSHA results for the Greece – Türkiye CBA and the Peak Ground Acceleration (PGA) for return period equal to 475 years
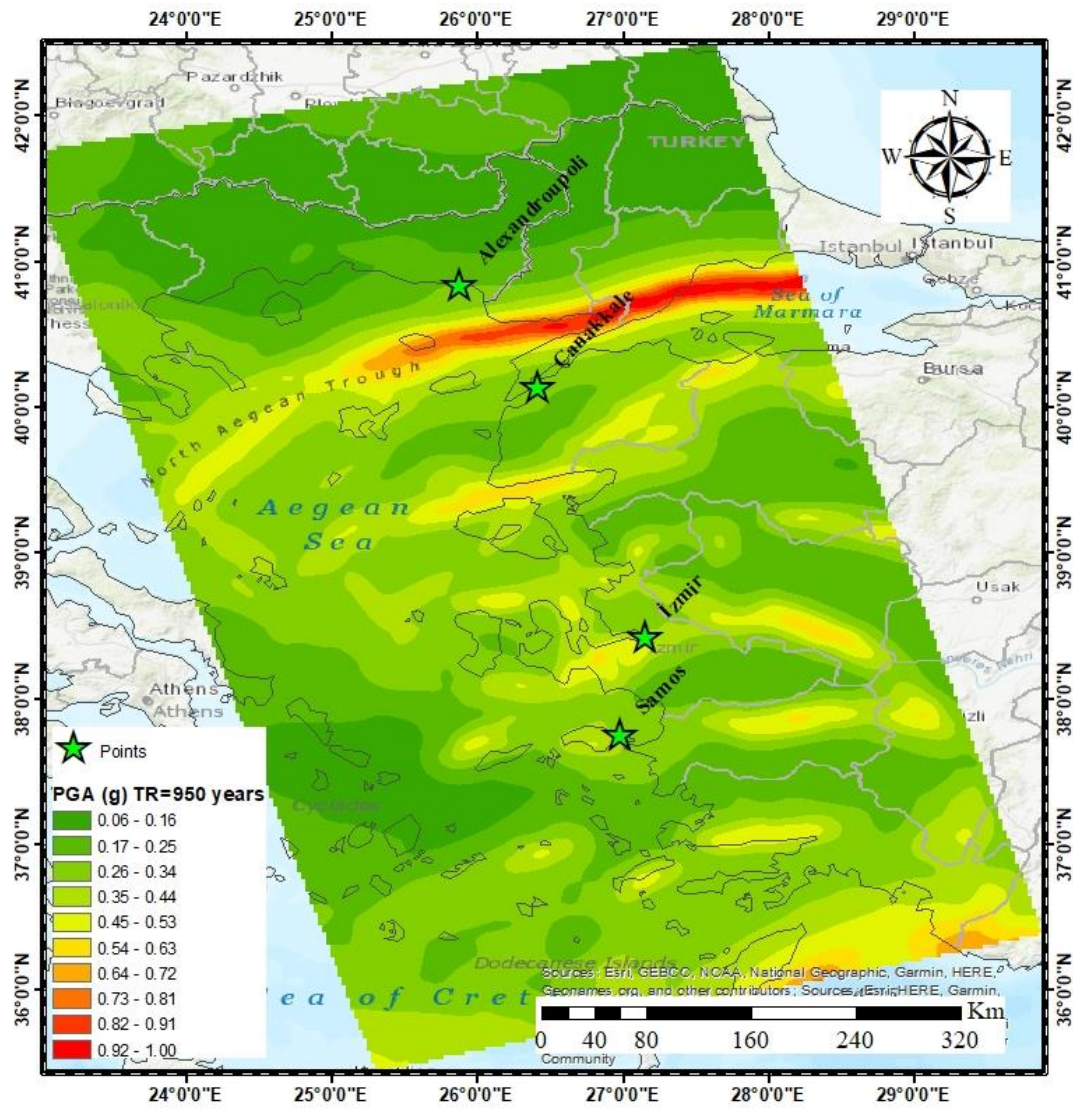
Figure 58: PSHA results for the Greece – Türkiye CBA and the Peak Ground Acceleration (PGA) for return period equal to 950 years
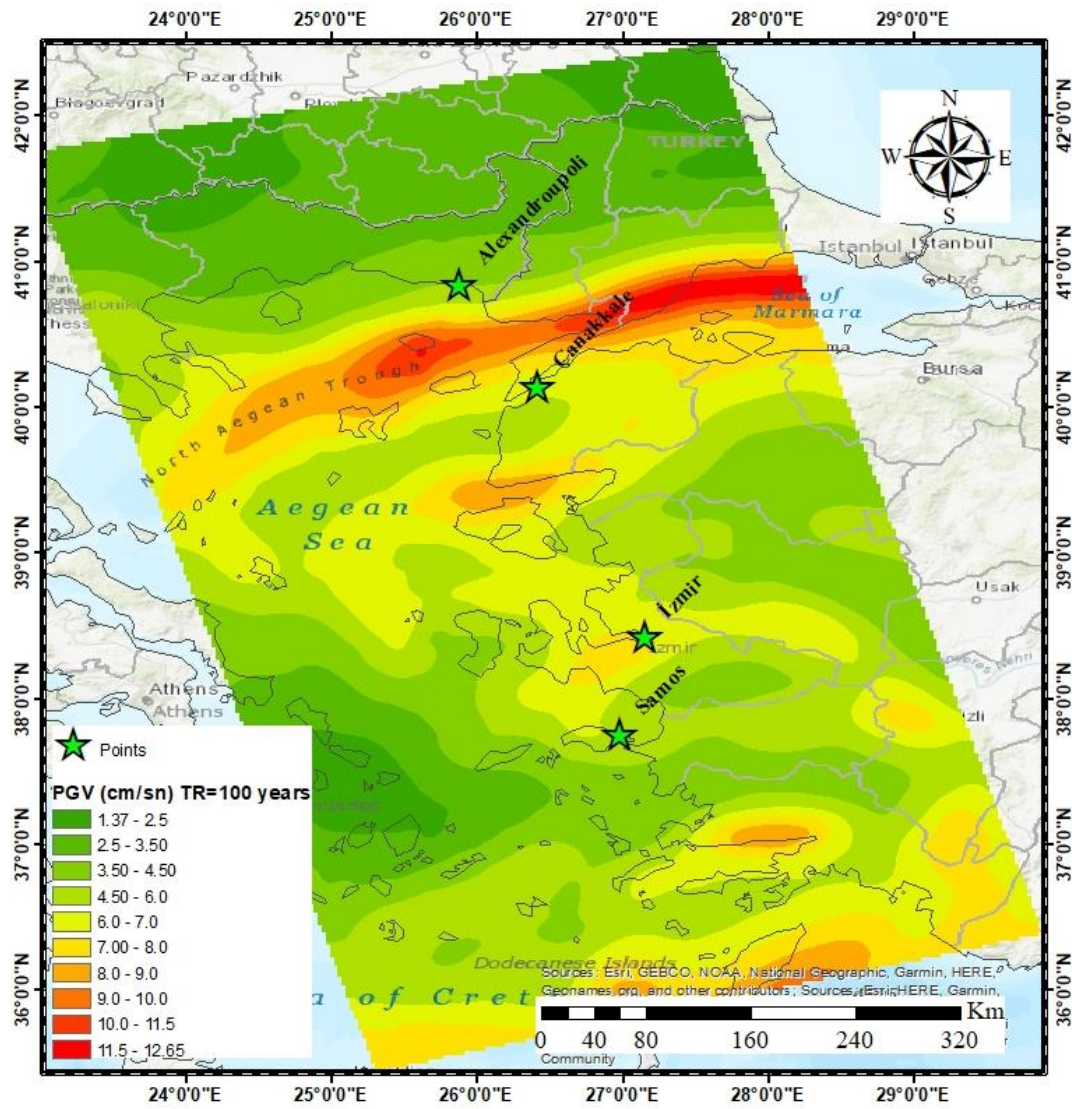
Figure 59: PSHA results for the Greece – Türkiye CBA and the Peak Ground Velocity (PGV) for return period equal to 100 years
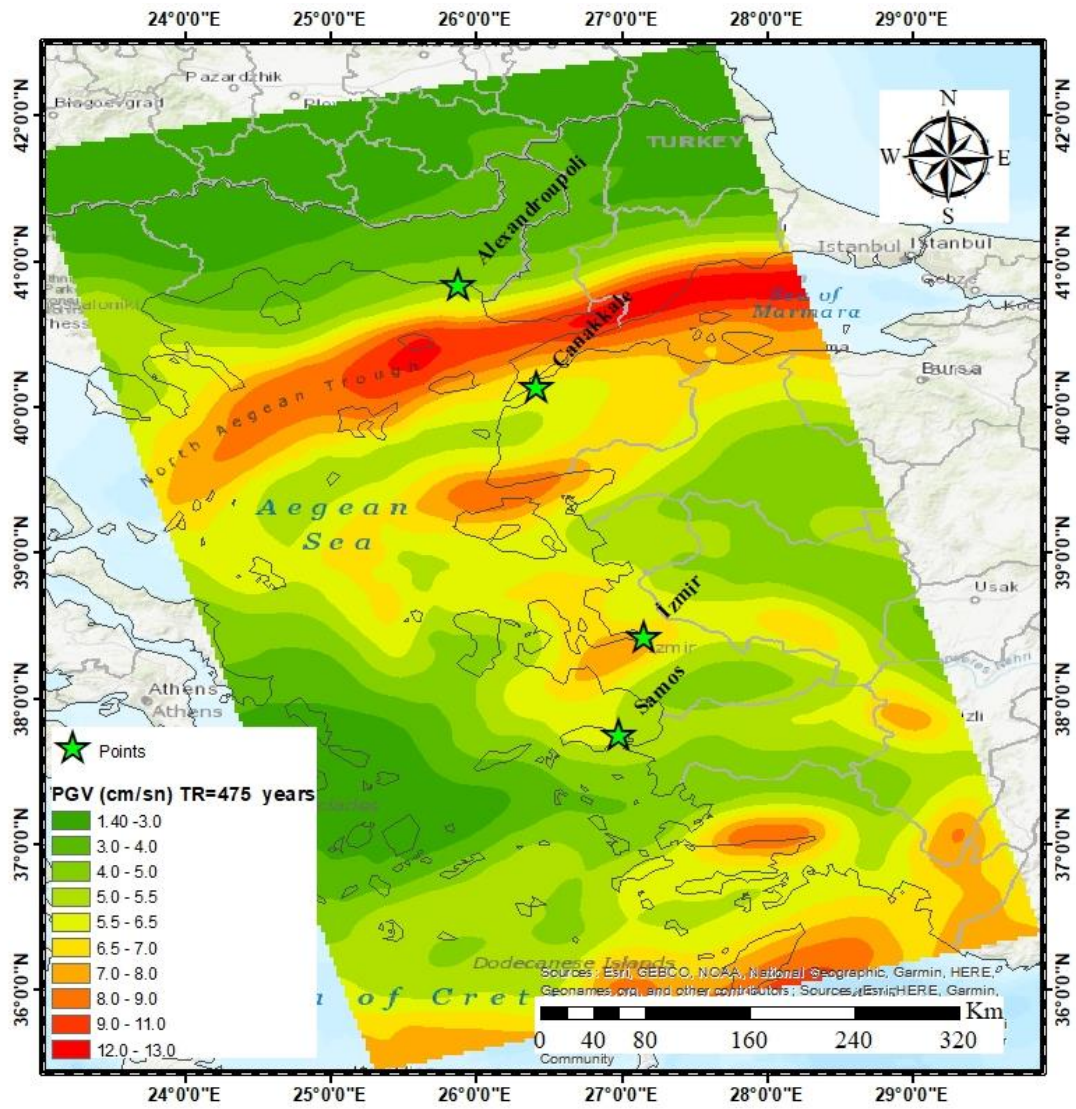
Figure 60: PSHA results for the Greece – Türkiye CBA and the Peak Ground Velocity (PGV) for return period equal to 475 years
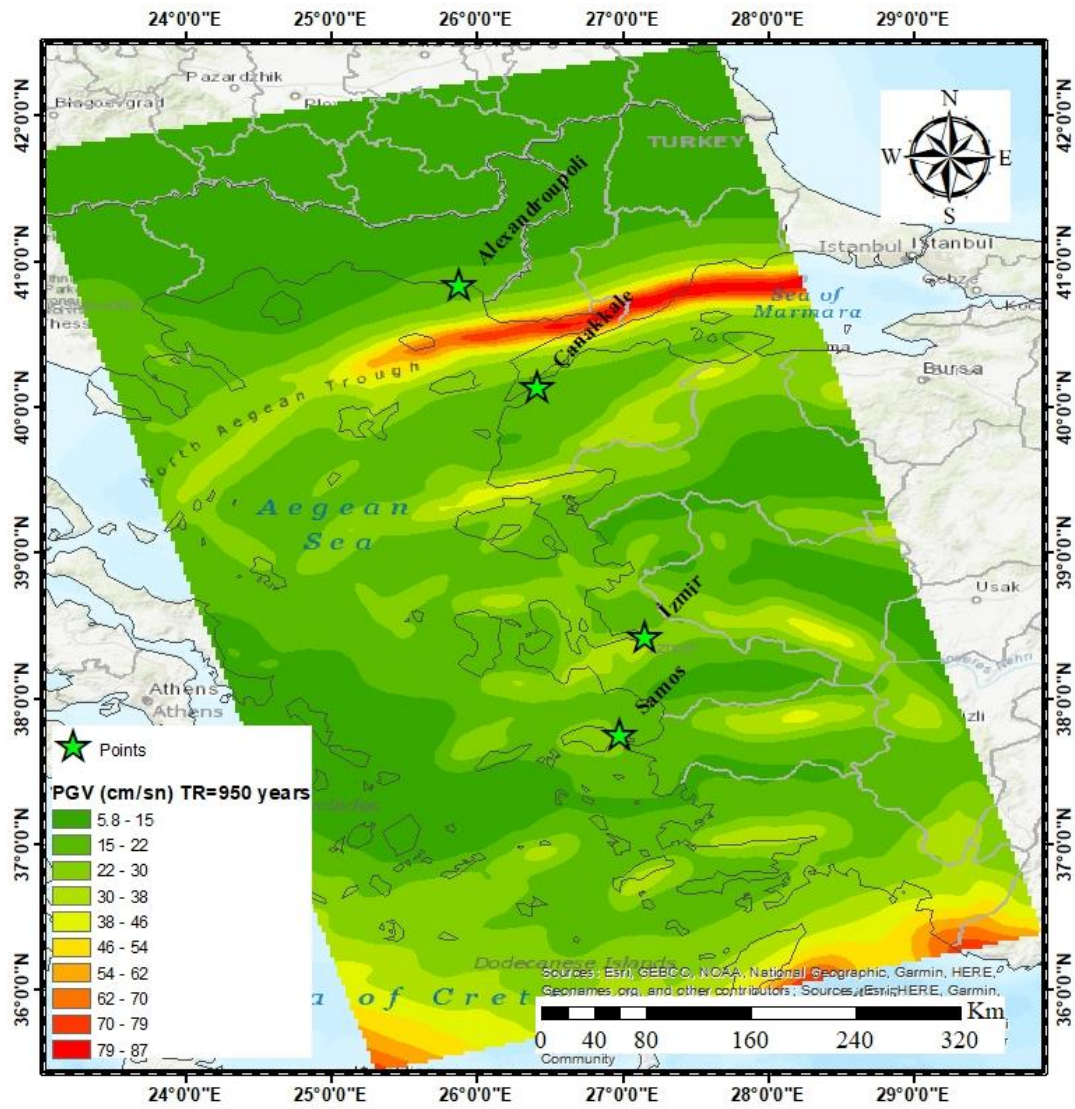
Figure 61: PSHA results for the Greece – Türkiye CBA and the Peak Ground Velocity (PGV) for return period equal to 950 years
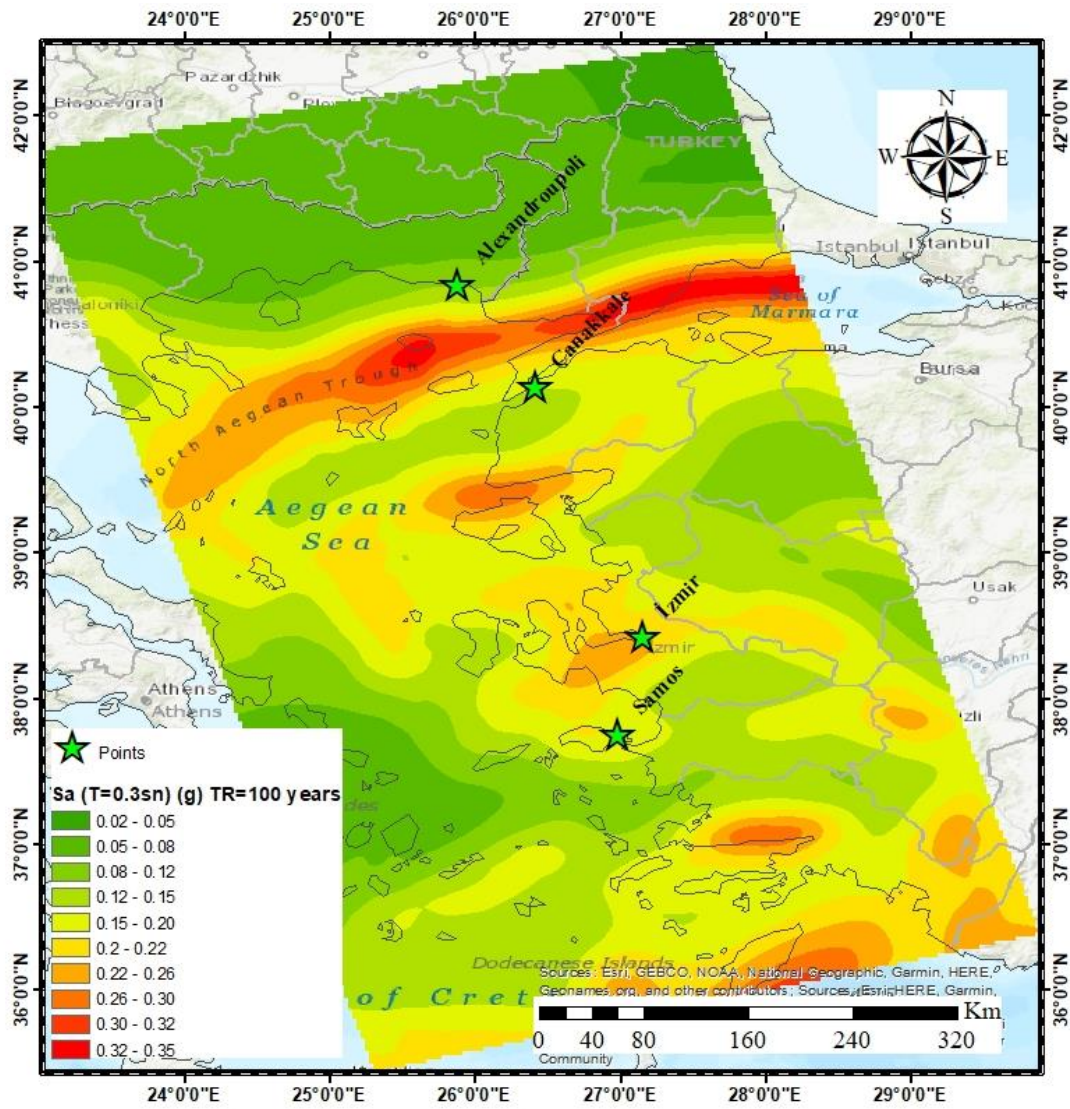
Figure 62: PSHA results for the Greece – Türkiye CBA and the Pseudo spectral acceleration for period equal to 0.3 sec, Sa (0.3s), for return period equal to 100 years
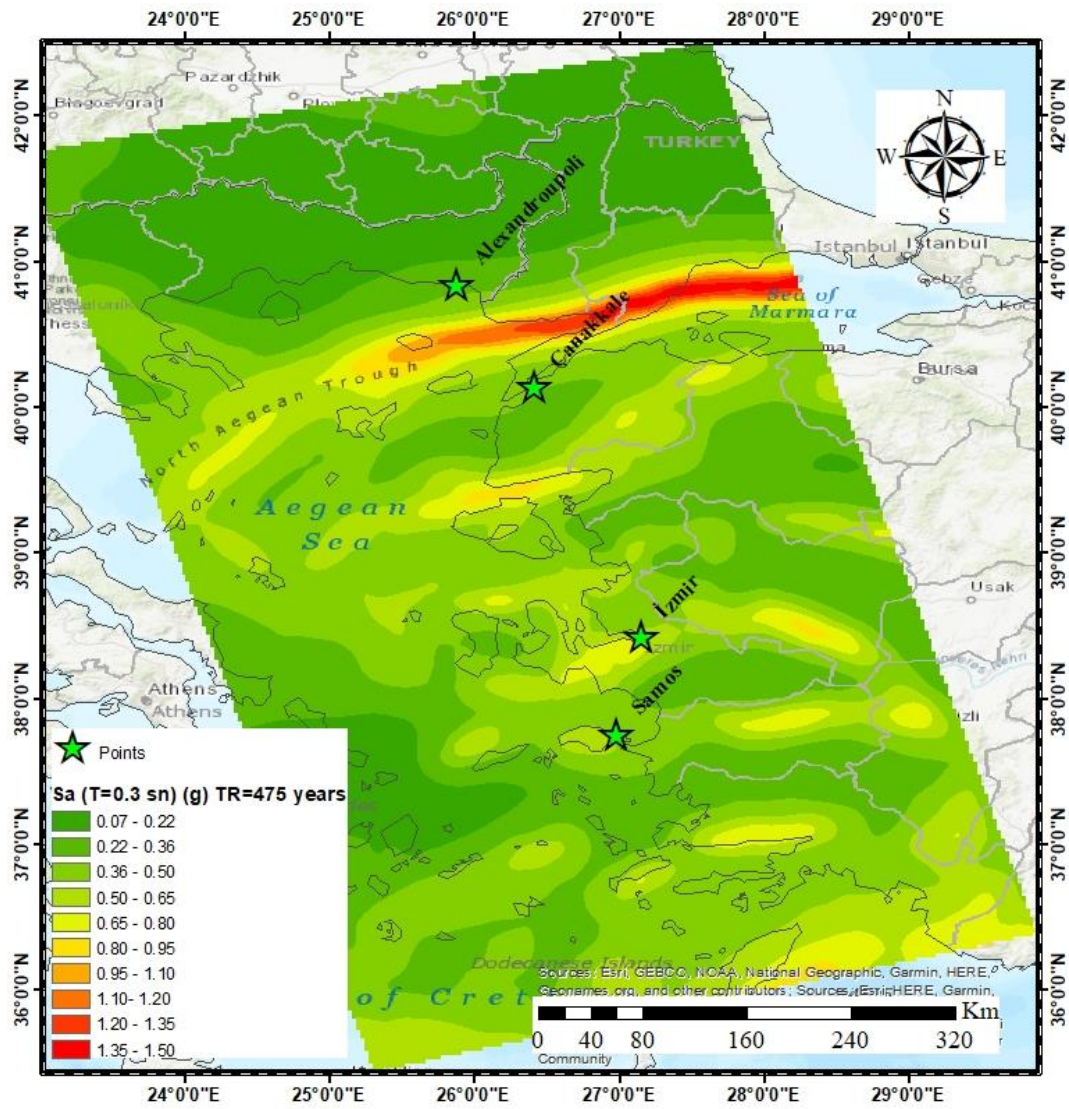
Figure 63: PSHA results for the Greece – Türkiye CBA and the Pseudo spectral acceleration for period equal to 0.3 sec, Sa (0.3s), for return period equal to 475 years
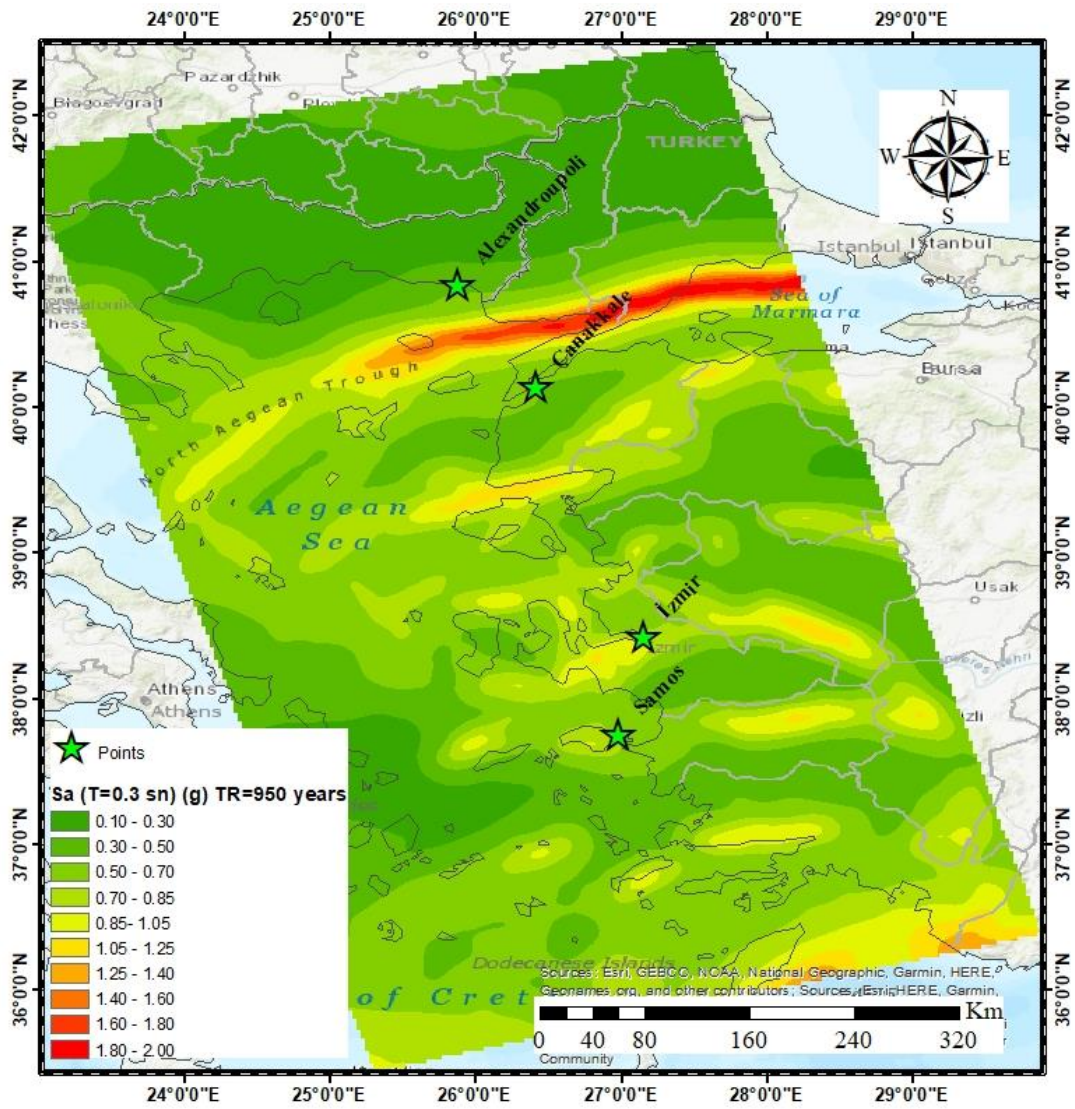
Figure 64: PSHA results for the Greece – Türkiye CBA and the Pseudo spectral acceleration for period equal to 0.3 sec, Sa (0.3s), for return period equal to 950 years
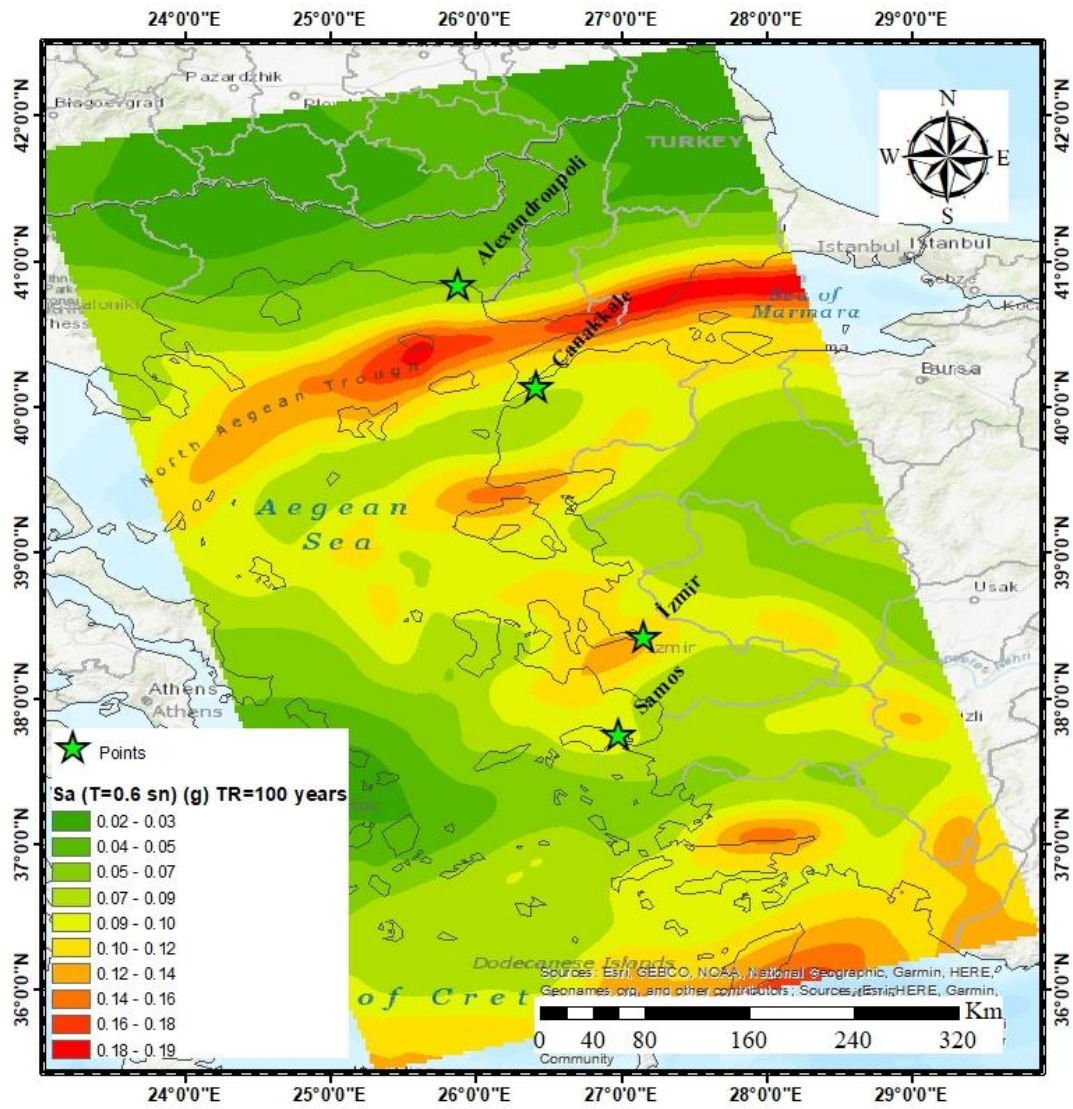
Figure 65: PSHA results for the Greece – Türkiye CBA and the Pseudo spectral acceleration for period equal to 0.6 sec, Sa (0.6s), for return period equal to 100 years
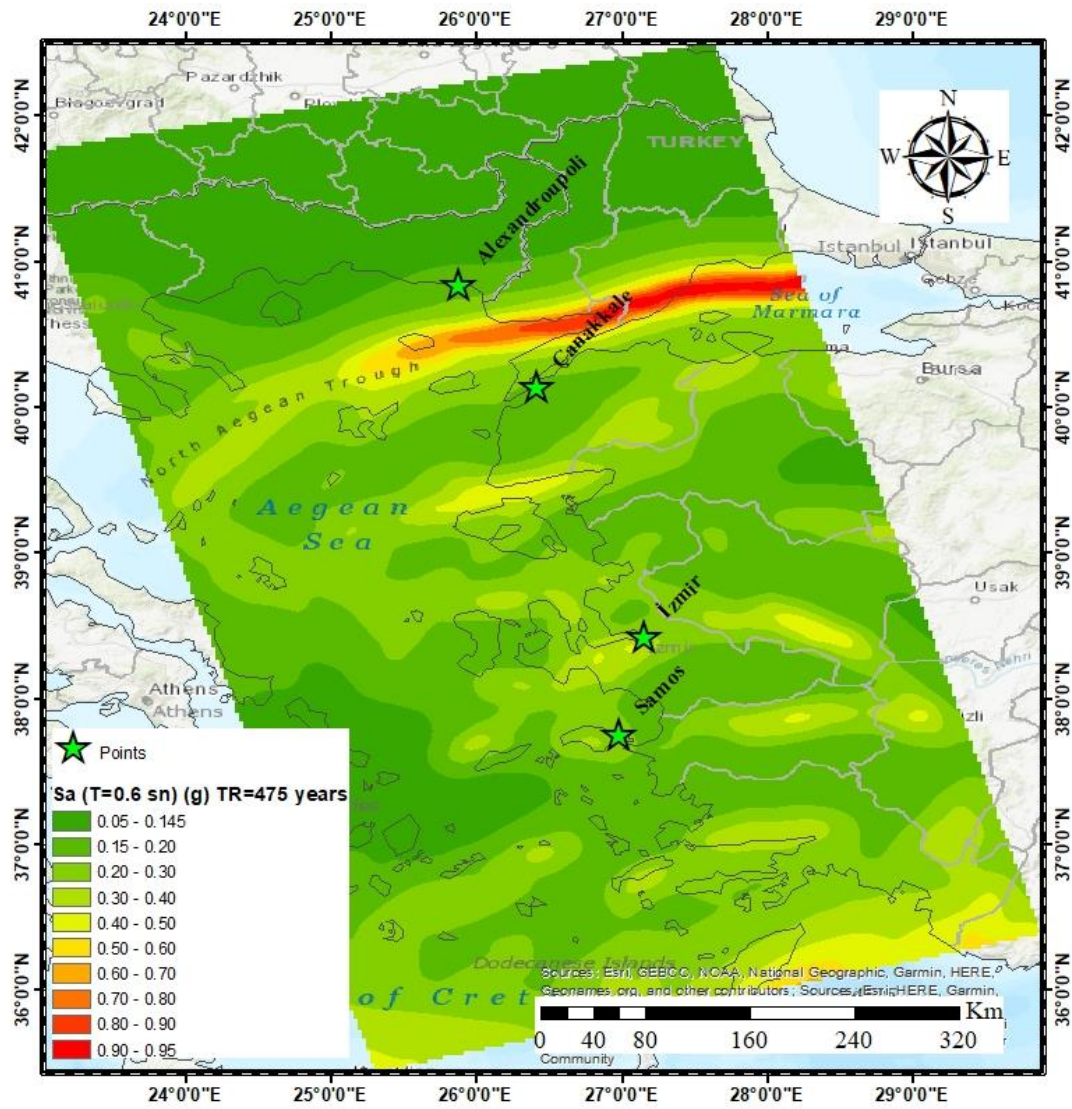
Figure 66: PSHA results for the Greece – Türkiye CBA and the Pseudo spectral acceleration for period equal to 0.6 sec, Sa (0.6s), for return period equal to 475 years
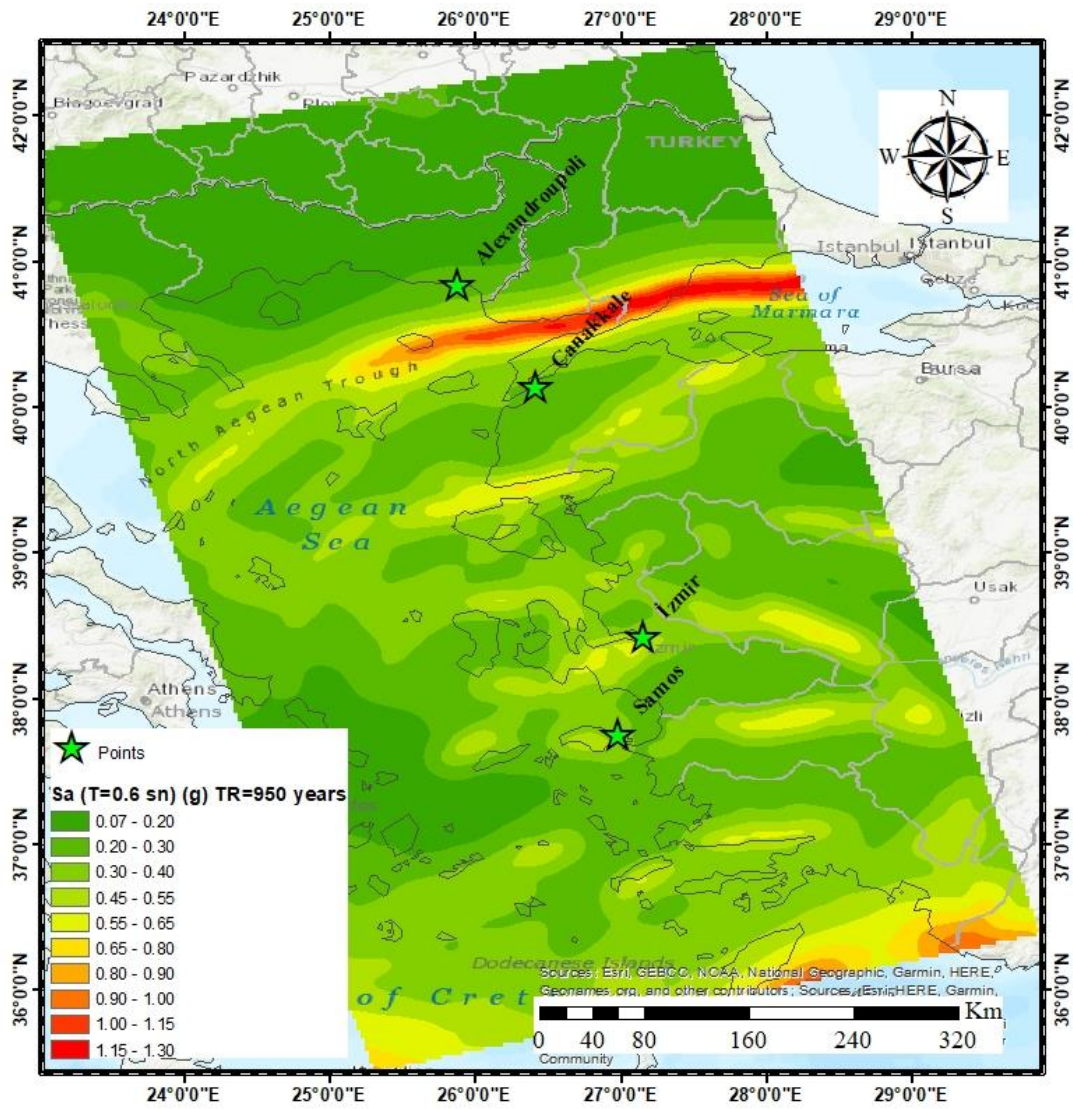
Figure 67: PSHA results for the Greece – Türkiye CBA and the Pseudo spectral acceleration for period equal to 0.6 sec, Sa (0.6s), for return period equal to 950 years
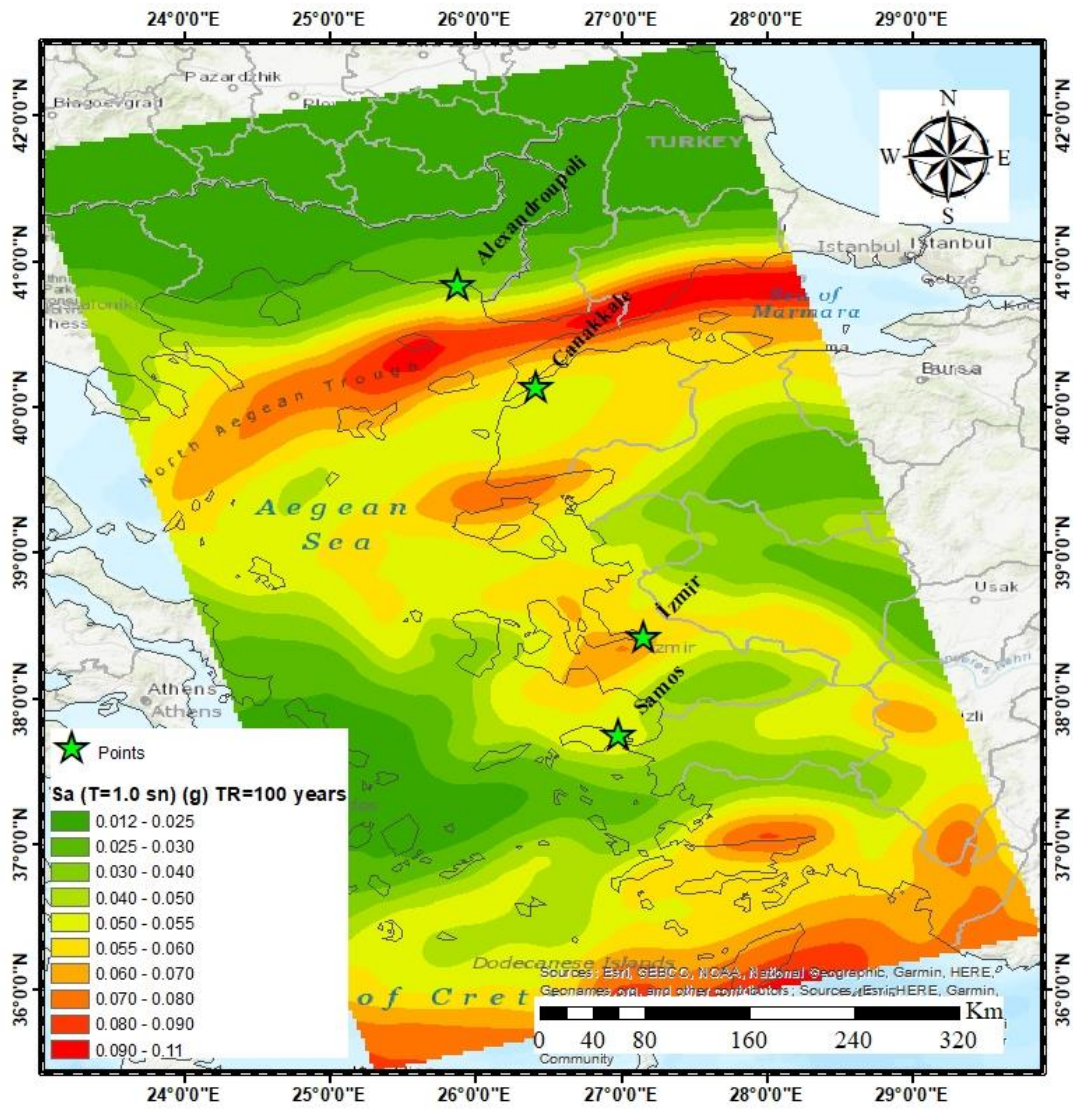
Figure 68: PSHA results for the Greece – Türkiye CBA and the Pseudo spectral acceleration for period equal to 1.0 sec, Sa (1.0s), for return period equal to 100 years
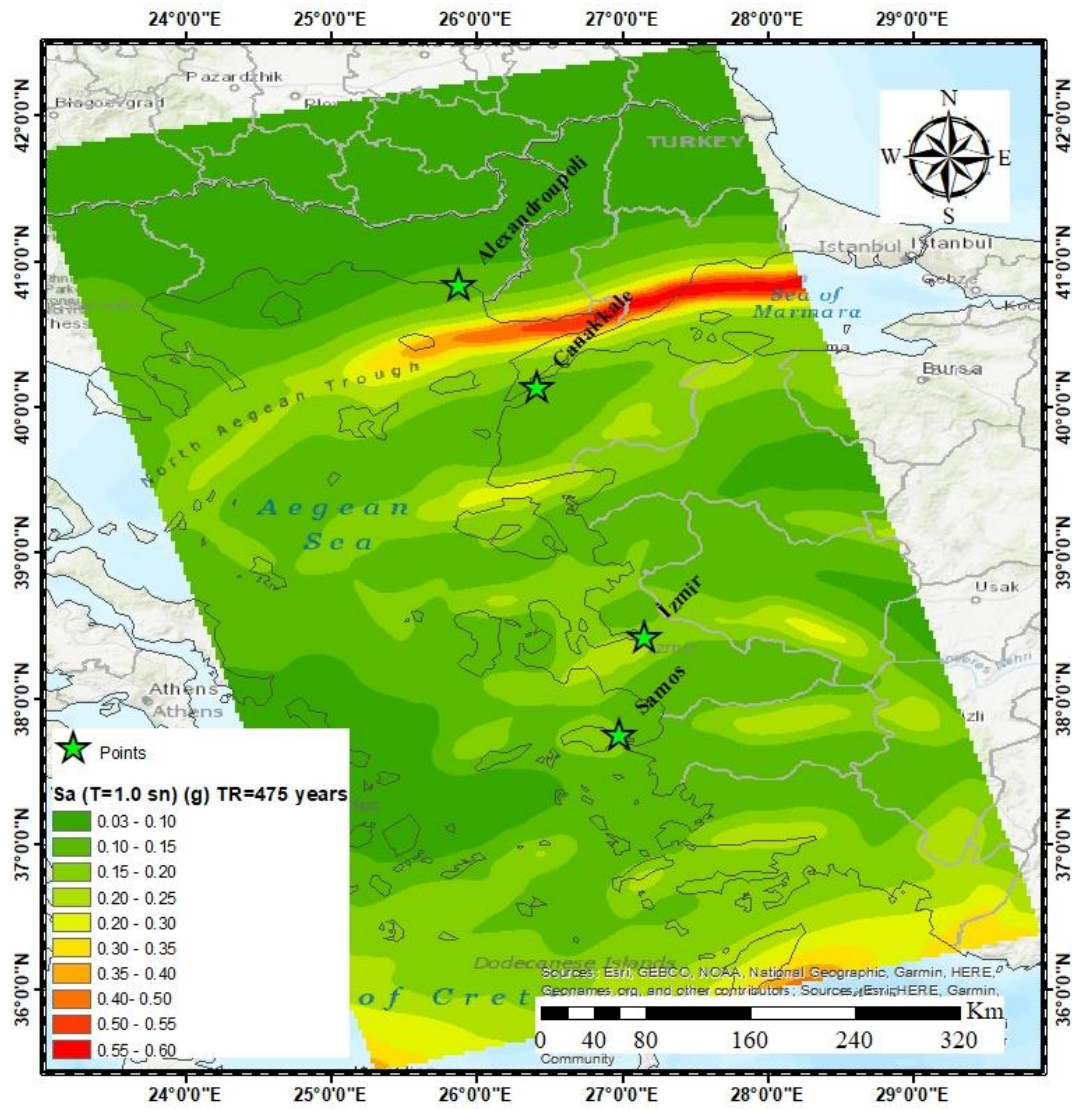
Figure 69: PSHA results for the Greece – Türkiye CBA and the Pseudo spectral acceleration for period equal to 1.0 sec, Sa (1.0s), for return period equal to 475 years
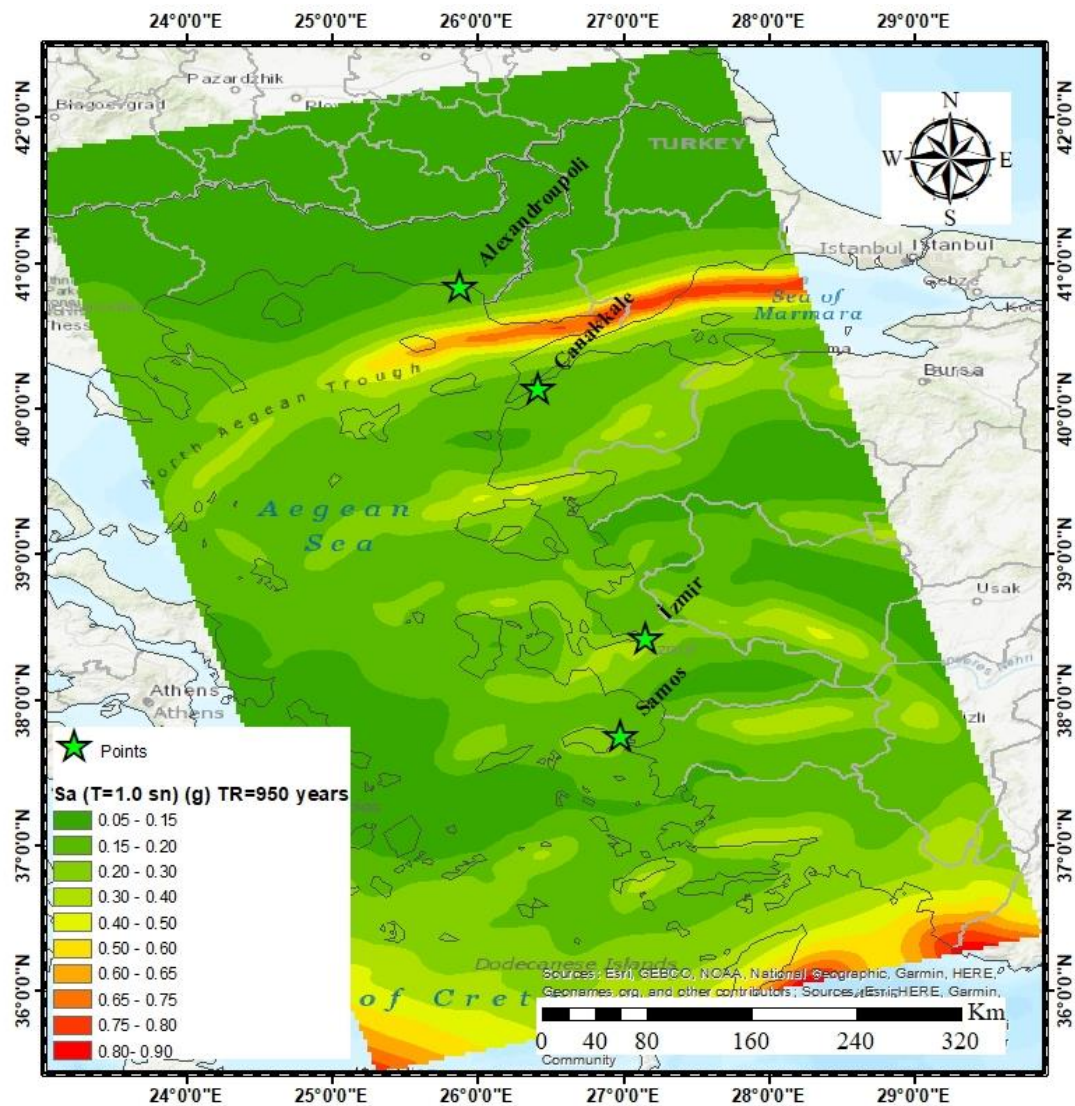
Figure 70: PSHA results for the Greece – Türkiye CBA and the Pseudo spectral acceleration for period equal to 1.0 sec, Sa (1.0s), for return period equal to 950 years

All results of PSHA in the Greece-Turkiye CBA are provided in digital form in the following e-Supplements:

(3) e-Supplement_3_output-2-hcurves-csv.zip

(4) e-Supplement_4_output-3-hmaps-csv.zip

3.6 DISCUSSION AND CONCLUSIONS

The differences between the utilized seismic source models, highlighted in Figures 8 and 9 for the pilot sites, are not negligible, even though the adopted source models were developed through earthquake catalogues and analyses which included the examined CBA. Hence, these differences justify the implementation of the logic-tree approach to account for the epistemic uncertainty.

The results presented in the maps of Figures 10 - 24 clearly reveal areas of high seismic hazard potential, mainly associated with the level of seismicity during the period covered by the earthquake catalog created and used in this study (see figure 3 of seismicity report).

In particular, the high values of ground motion intensity occurring in the NW, near the Greek-Bulgarian border, are associated with intense seismic activity in the surrounding area (e.g. 1904, M7.3; 1928, M7.0; 1931, M6.7).

The two branches of the North Anatolian fault (NAF), the main one crossing the Sea of Marmara and the North Aegean and the second one extending further south and parallel to the previous one are clearly formed. It is evident that high ground motion intensity values of these regions, observed in all the maps of Figures 10 - 24, are directly related to the strong seismic activity along these branches (e.g. 1905, M7.5; 1912, M7.6; 1944, M6.9; 1953, M6.7; 1999, M7.5).

High ground motion intensity values are also observed in the Evia region, which are probably due to the strong earthquakes that occurred in the region (1967, M6.7; 1981, M6.3; 2001, M6.5).

The effect of the recent high seismic activity near the island of Samos (2020, M7.0) that affected Izmir and the surrounding area is clearly visible in the above maps.

The relatively high PSHA values observed in the area to the E and SE of Izmir are associated with strong events that occurred in the area during the past century (e.g. 1925, M6.0; 1928, M6.5; 1969, M6. 5, etc.)

Also noteworthy are the relatively high ground motion amplitude values in the southeasternmost part of the map frame, which are related to strong events of the 20th century whose epicenters are located in this area (e.g. 1914, M7.0; 1926, M7.6, M6.9; 1948, M7.1; 1955, M6.9; 1957, M6.8, M7.2; 1978, M7.1; etc.).

The PSHA results presented herein could be considered as more localized seismic hazard estimates, compared to national and European seismic hazard models. The analysis included GMPEs which have been proven appropriate for the examined CBA (Theodoulidis et al., 2024), as well as, seismic source models which incorporate updated information regarding the seismicity and seismic fault characteristics of the study area.

4. PART 2: DETERNINISTIC SEISMIC HAZARD ASSESSMENT FOR THE CBA OF GREECE-TURKIYE

Introduction

The Deterministic Seismic Hazard Assessment (DSHA) at the two target pilot sites is focused in two Greek and two Turkish sites, along the cross-border area of Greece and Türkiye (Figure 71). Most specifically the two sites in Greece are the Alexandroupolis city in northeastern Greece mainland and the town of Vathy in Samos Island in eastern Aegean-Sea area, while the two Turkish sites are the Çanakkale and Izmir cities in north-western and mid-western Türkiye, respectively.

The DSHA maps for these four pilot sites, have been generated for the so-called near-field (< 50 km) seismic fault-sources per site, with a potential of generating high magnitude earthquakes (M> 6.5) and causing high Peak Ground Acceleration (PGA) values (e.g. > 0.1 g). The selection of each examined seismic source (active seismic faults) is analytically explained below, separately for each one of the four examined sites. Moreover, it's worth noting that the DSHA for these four sites has been implemented considering site condition proxy term based on the Vs30 parameter. More specifically, two types of DSHA maps have been produced; one based on the reference 'rock' ground motion, considering a constant Vs30 value of 760 m/s, corresponding to 'rock' site, and one for "cell" specific (0.005 x 0.005 degrees) Vs30 values, estimated by Stewart et al. 2014, based on the geology and slope gradient for five soil categories based on geologic age. In Figure 72 and Figure 73, these cell-specific Vs30 values in the cross-border areas between Izmir (Turkiey) and Vathy-Samos (Greece), as well as between Alexandroupolis (Greece) and Canakkale (Turkey), are presented.
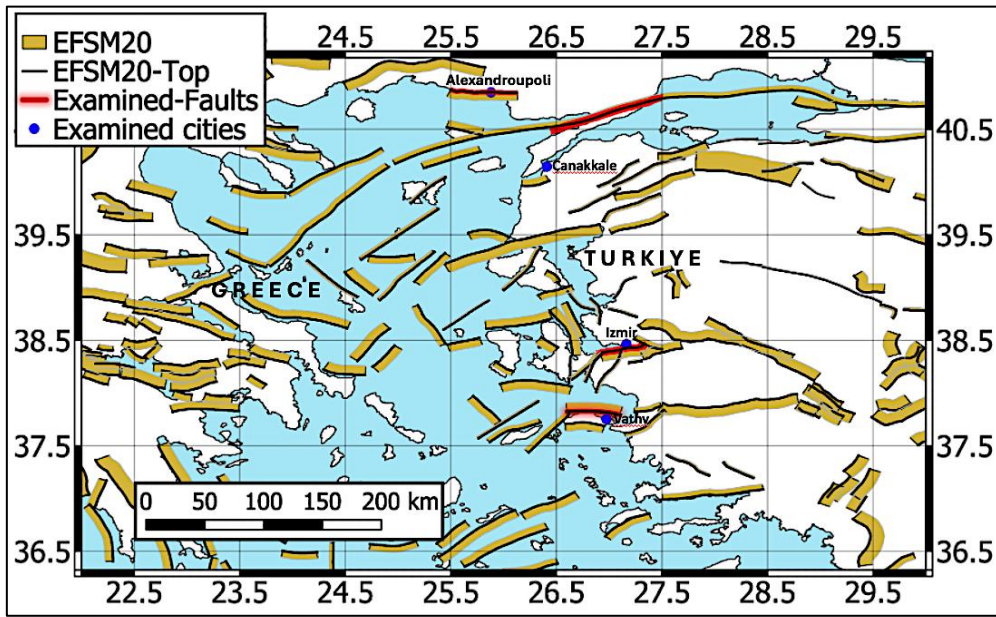
Figure 71. (a) A map of the CBA between Türkiye and Greece, where the European Fault-Source Model-2020 (EFSM20, Basili et al., 2022), is depicted. The four examined seismic faults (red lines), in the vicinity of the four pilot site of Alexandroupolis (Greece), Çanakkale (Türkiye), Izmir (Turkiey) and Vathy (Greece), are also depicted.
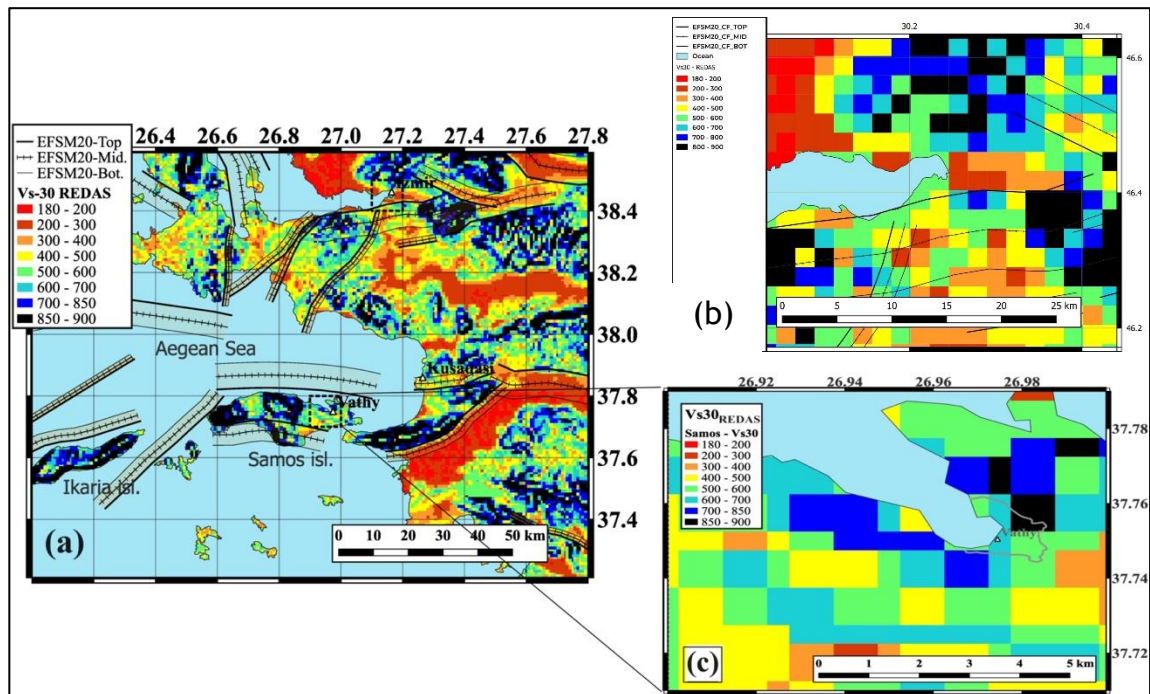
Figure 72. (a) Distribution of Vs30 values in the broader area of the Izmir and Vathy-Samos pilot sites, (b) Vs30 values focused on the Izmir pilot site (c) Vs30 values focused around the Vathy-Samos pilot site.
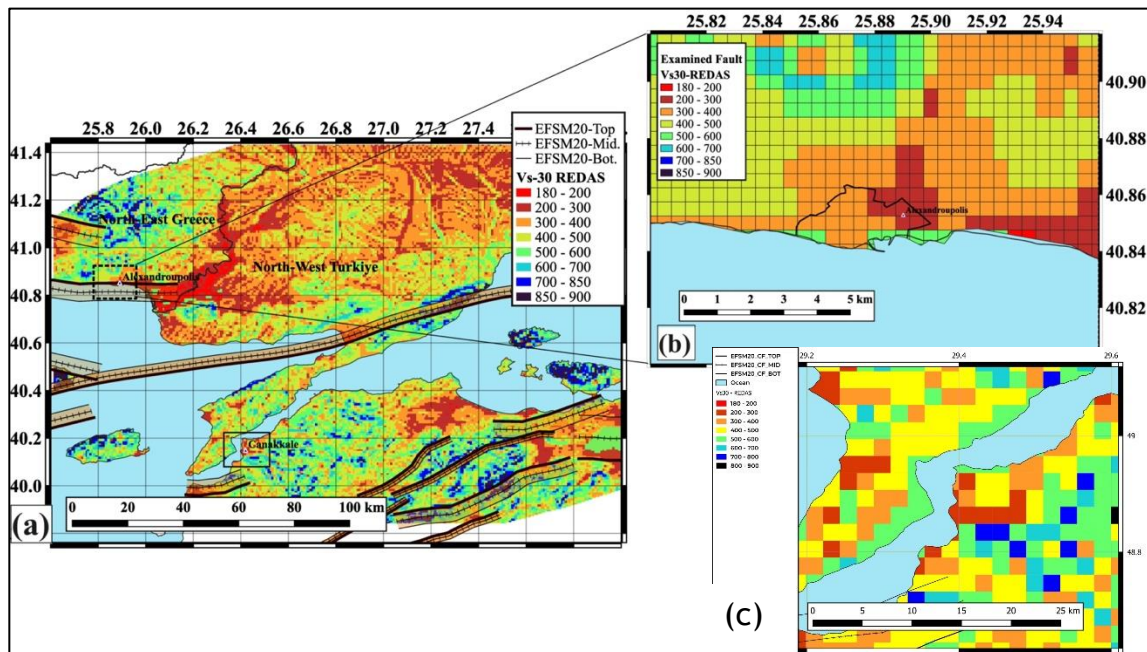
Figure 73. (a) Distribution of Vs30 values in the broader area of the Alexandroupoli and Canakkale pilot sites, (b) Vs30 values focused on the Alexandroupoli pilot site. (c) Vs30 values focused around the Canakkale pilot site.

Before any scenario is applied, validation of the REDA System is attempted in the next section, using the seismic fault of the Oct. 30, 2020, Samos earthquake (M7.0), occurred in the CBA and recorded by a big number of accelerometers in both countries.

Regarding the GMPEs proposed by Theodoulidis et al. (2024) for the CBA were adopted herein. Hence, the GMPEs of Boore et al. (2021) (with and without bias) and Chiou and Youngs (2014) were used in the REDAS software.

4.1   Validation to the M7.0 Samos Earthquake of Oct. 30, 2020, in the eastern Aegean Sea Greece-Turkey CBA)

In 30th of October,2020, an earthquake of moment magnitude M7.0 occurred in the northern coast of Samos Island, in western Aegean Sea, close to the cross-border area between Greece and Turkey. In Greek territory, in Samos Island, located ~14 km away from the epicenter, 2 fatalities and 19 injuries were caused (ITSAK Report, 2020 https://www.itsak.gr/uploads/news/earthquake_reports/EQ_Samos_20201030_report_v3.pdf), while in Türkiye, one 117 fatalities and 1034 injuries were caused mainly in Izmir Province, located ~70 km away from the epicenter. Serious damage, collapses and considerable economic losses were resulted,

mainly to residential buildings located in the district of Bayrakli and Bornova (Demirci et al. 2022).

Recently, several studies have been implemented, investigating the source properties of this earthquake event (among others: Lentas et al., 2021; Chousianitis and Konca, 2021, Foumelis et al., 2021, Plicka et al., 2022; Kiratzi et al., 2022). All these studies converge to a moment magnitude computation between 6.9 to 7.0. In Table 5, all the source fault parameters provided by these studies, are presented. Here attempting to empirically validate the REDAS software for its reliable computational potential, a simulation of the fault rupture of this earthquake (Samos, 2020), was implemented. The resulted Peak Ground Acceleration (PGA) and Velocity (PGV) values were compared to the observed ones at 29 sites in epicentral distances less than 100km, 2 in Samos Island (in Vathy city) and 27 in western Turkiey (Table 6, GEER, 2020).

Table 5. **Information of the rupture of the ~7.0 Samos earthquake, (2020/10/30-11:51:25, National Observatory of Athens, NOA), as provided by the referenced studies. All the studies, agree to a Normal (N) fault, while most of them consider a surface rupture up to ~1 km (0.5-2 km). The Latitude and Longitude values correspond to the epicenter of this earthquake. The presented Mw have been computed based on the corresponding provided seismic moment at each study. With "S.", "D.", "W." and "L", the average Strike, Dip, Width and subsurface length of the fault rupture, is given, while in "Dur" the duration of the main rupture is provided.**

Studies	Lat. (deg)	Long. (deg)	Depth (km)	Mw	S. (deg)	D. (deg)	W. (km)	L. (km)	Dur. (sec)
Sakkas 2021	37.8759	26.7235	13.0	6.932	277	50	19.7	35	~
Lentas et al 2021	37.8800	26.8600	9.8	7.024	276	34	20	35	15
Plicka et al 2022	37.9000	26.8170	12.0	7.031	270	50	20	35	~
Aktug et al 2021	37.8442	26.831	18.7	6.948	288	~	16	43	~
Chousianitis and Konca 2021	37.9020	26.7942	11.0	7.004	275	49	10	30	~
Ganas et al. 2021	37.9	26.817	5.1	6.957	276	37	15	40	
Ren et al. 2022	37.897	26.784	11.5	6.966	267	~	~	~	~
Kiratzi et al 2022	37.8919	26.8066	8.2	7.035	270	43	15	32	16

For the scenario event of the examined Samos 2020 earthquake, a unique fault with the input source parameters required by REDAS software, should be selected. For this reason, we chose to select one of the fault geometry "solutions" provided by the studies shown in Table 5, instead of selecting an average fault solution, since each individual fault solution is consistent with each own corresponding source properties provided in Table 5. In addition, an average fault geometry solution would probable not be fully consistent with average source properties of all relevant studies. Thus, taking into account that all studies conclude to more or less similar fault geometry, we have selected the model proposed by Kiratzi et al., (2022). It is noteworthy that Kiratzi et al., (2022) epicenter is the closest to the average of the epicenters of all studies (Figure 74).
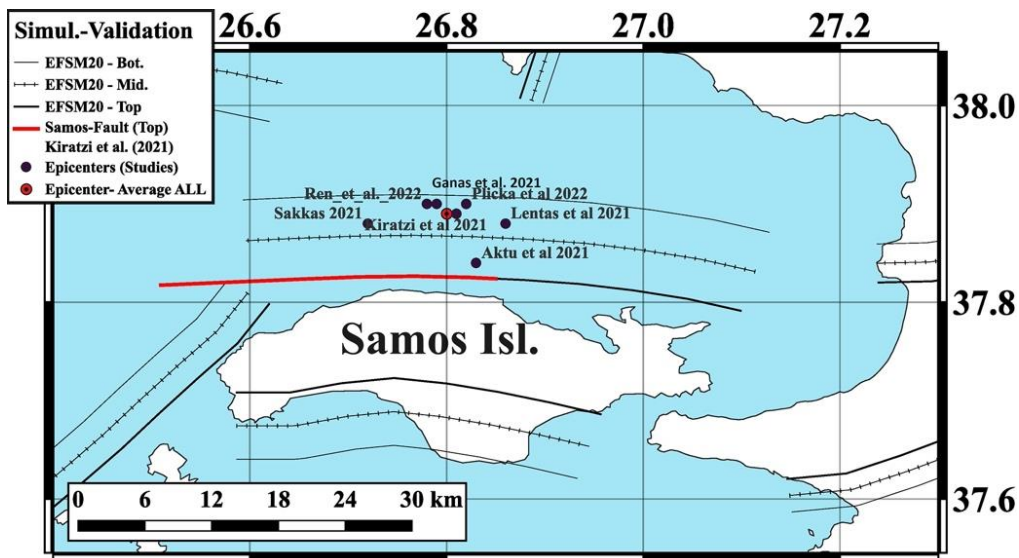
Figure 74. A map of the surface Fault (red line) of the Samos earthquake M7.0, as provided by Kiratzi et al., (2022), and used in this study for the validation of the REDAS software. The epicenters of the 7 studies in which the source properties of the Samos earthquake have been investigated (Table 1) are presented, while the arithmetic average epicenter of the 7 studies is also presented (in red).

Table 6. The recorder PGAs and PGVs for 29 sites in Türkiye (27) and Greece (2), as well as the corresponding values from the Samos 2020 scenario events implemented by the REDAS software, considering the specific Vs30 per cell as well as on rock for the site conditions (Vs30=760 m/s).

	Station	Lat.	Long.	R-JB (km)	Vs30-meas. (m/s)	Vs30-REDAS per cell (m/s)	PGA recorded (cm/s2)	PGA computed per cell (cm/s2)	PGA computed (on rock) (cm/s2)	PGV recorded (cm/s)	PGV computed per cell (cm/s)	PGV-computed (on rock) (cm/s)
1	SMG1	37.7561	26.9762	13.4	550	697	227.3	199.52	190.40	21.49	15.81	14.75
2	SAMA	37.7537	26.9806	13.8	840	900	166.31	169.79	186.63	17.37	12.57	14.43
3	905	37.86	27.265	36.4	369	452	179.31	103.10	77.72	8.93	8.84	5.81
4	911	37.7621	27.3909	48	307	464	66.66	75.49	57.53	4.54	6.56	4.40
5	918	37.3697	27.2643	62.4	630	295	38.19	70.18	42.12	5.99	7.16	3.37
6	919	37.5595	27.8355	91.6	986	497	21.4	31.67	24.99	1.22	3.18	2.25
7	920	37.5604	27.3749	54.8	894	328	30.69	77.74	49.36	3.00	7.54	3.85
8	3506	38.3944	27.0821	56.5	771	426	43.88	65.10	40.06	3.39	5.92	3.23
9	3511	38.4213	27.2563	66.2	827	893	41.29	35.5	32.89	5.98	2.77	2.76
10	3512	38.4009	27.1516	59.5	468	423	57.54	61.33	47.33	3.9	5.65	3.71
11	3513	38.4584	27.1671	66.1	196	600	106.28	44.50	38.94	17.11	3.83	3.16
12	3514	38.4762	27.1581	67.4	836	696	56.02	39.93	44.39	6.41	3.33	3.52
13	3516	38.3706	26.8907	49.9	460	459	48.36	72.18	38.98	4.84	6.33	3.16
14	3517	38.3756	27.1936	59.1	695	461	40.1	59.08	38.01	3.95	5.31	3.09
15	3518	38.4312	27.1435	62.3	298	258	106.1	74.84	54.63	11.33	7.89	4.20
16	3519	38.4525	27.1112	63.6	131	254	150.09	73.58	44.81	22.53	7.83	3.54
17	3520	38.478	27.2111	69.9	875	611	58.55	41.03	41.97	8.37	3.57	3.36

18	3521	38.4 679	27.076 4	64.1	145	600	110.84	46.23	40.89	16.17	3.95	3.29
19	3522	38.4 357	27.198 7	65.1	249	317	73.72	63.95	36.29	14.81	6.46	2.98
20	3523	38.3 282	26.770 6	45.1	414	410	80.32	85.73	40.49	5.73	7.65	3.26
21	3524	38.4 969	27.107 3	67.6	459	545	68.34	45.58	39.78	5.90	4.05	3.21
22	3526	38.5 782	26.979 5	74.1	205	203	88.77	68.05	61.23	10.82	7.95	4.65
23	3527	38.6 39	26.512 8	80.4	207	448	80.93	40.26	37.85	8.85	3.95	3.09
24	3528	38.3 039	26.372 6	44.9	532	600	149.31	70.14	33.61	8.36	5.66	2.81
25	3533	38.2 572	27.130 2	44.8	415	308	73.64	99.76	30.03	5.95	9.58	2.58
26	3534	38.6 624	26.758 6	81.8	328	575	92.48	34.29	61.46	5.09	3.18	4.67
27	3536	38.1 968	26.838 4	30.2	1141	320	79.14	145.04	61.66	8.71	13.57	4.68
28	4501	38.6 126	27.381 4	90.3	340	468	40	33.30	29.33	7.06	3.37	2.53
29	4814	37.3 991	27.656 7	85.3	694	527	25.33	34.06	92.27	1.63	3.27	6.87

The fault geometry proposed by Kiratzi et al., (2022) and examined herein, has its fault right upper corner (in the map projection) at the point with coordinates: [37.824 , 26.85], while the top center of the fault is at the point with coordinates [37.82, 26. 62]. Based on these points of the fault surface projection, as well as on the fault length of 32 km, given by Kiratzi et al., (2022)), and considering the fault geometry as provided by the European Fault-Source Model of 2020 (EFSM20), the surface fault geometry has been rebuilt for the needs of this study (Figure 74). Its coordinates are analytically given in Appendix A and are directly used as input to the REDAS software for the validation of the Samos 2020 mainshock.

In Figure 75a and Figure 75b, the PGA results extracted by the simulation implemented by the REDAS software are presented in maps, in comparison with the observed PGA values (in colored circles) in the 29 specific sites (Table 2). In Figure 76a, the observed PGA values are depicted versus the Joyner-Boore fault distance (R_{JB}), presenting the expected trend of the PGA to be decreased with distance. In Figure 76b, the ratio of PGA between the observed and the estimated by REDAS software (Figure 75b, Table 1), based on the specific Vs30 values (per cell, Figure 72), is presented in comparison

with the corresponding ratio of the real (measured) over estimated ("per cell")Vs30 values (Table 1). From this figure it is obvious that the lower the Vs30 ratio the higher the underestimation of the simulated PGA values and vice versa, while when the real (measured) and simulated Vs30 are similar, that is their ratio is around 1, the latter are closer to the observed ones. This is numerically confirmed by the least square analysis (in logarithmic scale) between the two examined ratios, where the coefficient, a, of the linear equation (logY=a + blogX in the legend in Figure 76b) is close to zero (a~0.045), indicating that for Vs30(real)/Vs30(p.c.)=1, the simulated PGA(sim.), is similar to the observed PGA(real). Moreover, the low standard deviation of the least square analysis, (std~32%), indicates that this trend between Vs30(real)/Vs30(p.c.) and PGA (real)/ PGA(sim.), is consistent and the simulated PGA values are in good agreement with the observed ones, albeit they may differ a lot when the estimated Vs30 values diverge from the observed ones.

In Figure 76c, the ratio between the observed PGA (real) over the extracted by REDAS values referred to 'rock' site (Vs30=760 m/s) as a function of measured Vs30, similarly indicates that for a reliable PGA estimation, a suitable selection of the Vs30 values is necessary. It's worth noting also, that for "rock" sites, for which Vs30 values are close to 760m/s, the simulated PGAs have been satisfactorily estimated by REDAS. Certainly, further testing on these topic is needed based on data of additional earthquakes in the CBA and more specifically recorded on 'rock' site conditions.
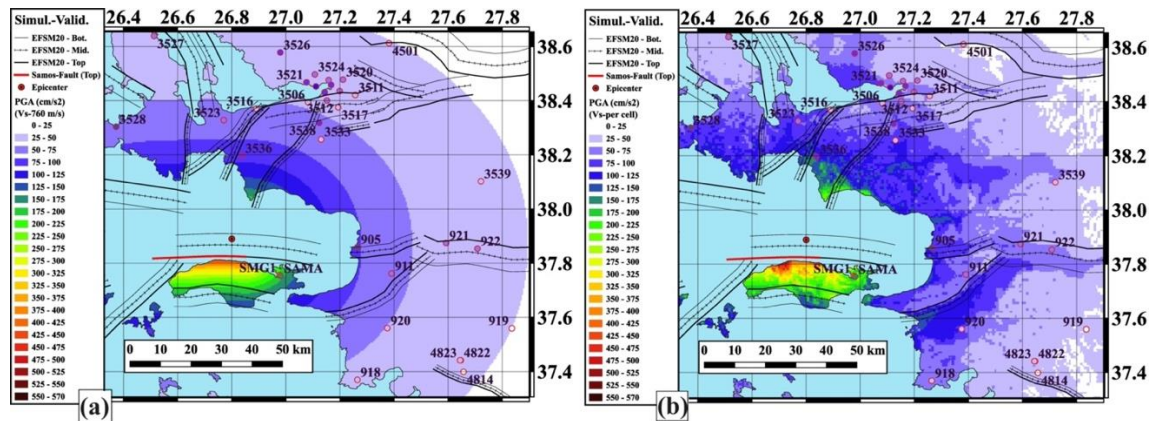
Figure 75. (a) The PGA (in cm/s2) at each geographic cell of (0.005 x 0.005, degrees), as computed by the Rupture simulation of the Samos-earthquake 2020 (in red line, Figure 71), for Vs30 = 760 m/s, to each cell (rock site condition). The adjacent faults to the examined Samos-2020 fault, into the broader Greece-Türkiye area, provided by the European Fault-Source Model of 2020 (EFSM20), are also depicted. (b) Similar to Figure 75a, but for specific Vs30 values of each site specific "cell" (Figure 72a,c). The observed (real), PGA, are also presented in the same color scale (Table 6).
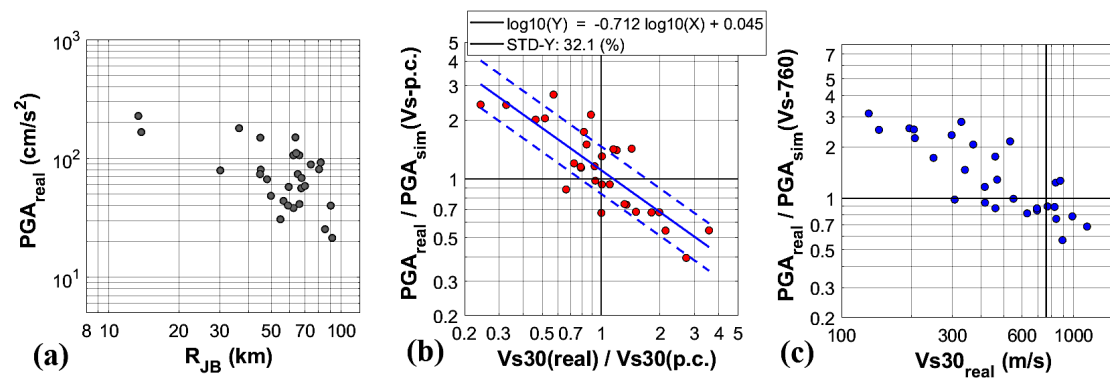
Figure 76. (a) The observed (real) PGA, at the 29 sites (Table 6). computed by REDAS software, for the Rupture simulation of the "Samos-2020" Fault (Table 5, Appendix A, Figure 75, Figure 76b). (b) The ratio between the observed (real) PGAs and the one computed by the simulation (Figure 76b) of the specific Vs30 values, versus the ration between the real (measured) Vs30 values (Table 6) at the 29 sites, and the cell-specific ones (per cell, Figure 72a,c). (c) The ratio between the observed (real) PGAs and the one computed by the simulation (Figure 76b) of the specific Vs30 values (Figure 72a,c), *vs* the real Vs30 values.

In Figure 77, results of PGV extracted by corresponding simulation implemented by the REDAS software are presented in maps, in comparison with the observed PGV values (in colored circles) in the 29 specific sites (Table 6). In Figure 78a, the observed PGV values are depicted versus the Joyner-Boore (R_{JB}) distance, presenting the expected trend of the PGV to be decreased with distance, but exhibiting a greater scattering than in PGA, probably due to higher impact of the Vs30 proxy site effect on PGV compared to PGA (see Figure 76a). In Figure 78b, the ratio of PGV between the observed and the estimated by REDAS software (Figure 77b, Table 1) based on the specific Vs30 values (per cell, Figure 72a,c), is presented in comparison with the corresponding ratio of the real (measured) over estimated ("per cell")Vs30 values (Table 1). Also in this case, it seems that a correlation between Vs30(real)/Vs30(p.c.) and PGV(real)/ PGV(sim.) ratio (in logarithm scale) is observed, which however presents higher standard deviation (std ~48%). The latter also indicates that the site term can particularly affect the PGV values in higher level than the PGA values. The same trend in apparent in Figure 78c, for the observed PGV (real), with respect to the estimated one on 'rock' conditions (Vs30~760m/s). In this case scattering is also greater than the corresponding one presented for PGAs in Figure 76c.
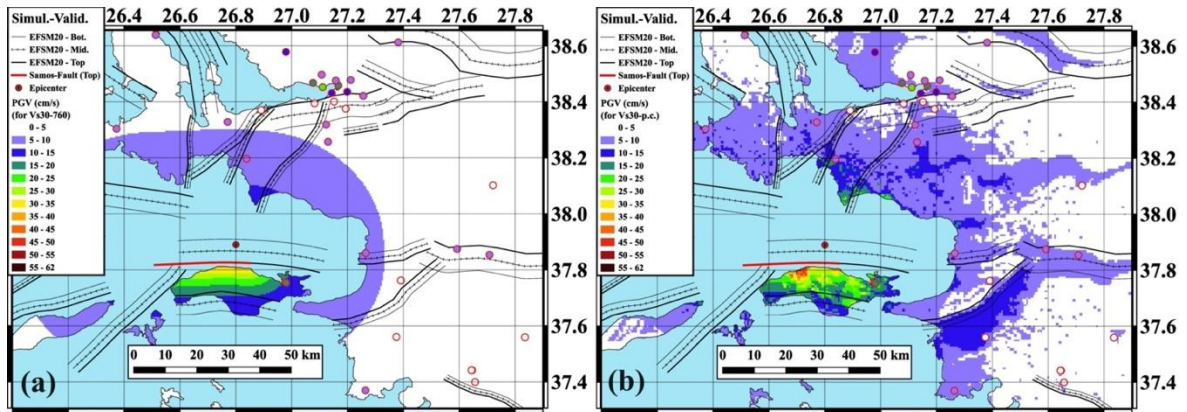
Figure 77. (a, b) Similar Figure-Maps to Figure 75a, b, but for simulated PGV(cm/s) values of the Samos 2020, earthquake.
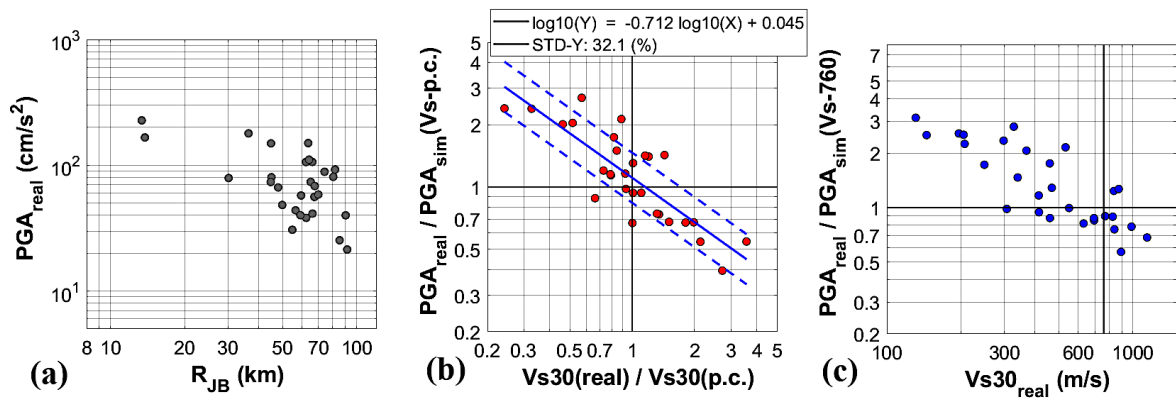

Figure 78. (a, b and c) Similar to Figure 76a, b, c, but for the simulated PGV (cm/s) values of the Samos 2020, earthquake.

4.2 Vathy, Samos Island, (scenario of Northern Samos fault)

Vathy town located in the northern part of Samos Island, which is in central-eastern part of the Aegean Sea. This is a well-studied area in terms of the geological active shallow faults, based on several individual studies in the past. All those studies have been concentrated and taken into account in the Greek Database of Seismogenic Sources (GreDass) project, conducted and updated by Sboras et al., (2009), Pavlides et al., (2010) and Caputo and Pavlides, (2013), as well as in a corresponding project under the National Observatory of Athens (NOA-Faults), conducted and updated by Ganas et al., (2013) and Ganas et al., (2018). Here, for the Vathy town, selection of a "Near-Field" seismic source, is based on the European Fault-Source Model (EFSM20, Basili et al. 2022), included in the 2020 updated version of the European Seismic Hazard Model (ESHM20, Danciu et al., 2021), which, for this specific area, has been directly based on the Seismogenic Sources of GreDass and NOA- Faults.

More specifically, as a "Near-Field" Seismic Source to Vathy town, the fault located to the north coast of Samos Island (named: "Samos-North" Fault, Figure 71), as outlined in the EFSM20 database, has been selected for the DSHA. It's worth noting that this fault has been recently activated, on 30th of October 2020, generating an earthquake of M7.0 (among others: Chousianitis and Konca, 2021, Foumelis et al., 2021, Kiratzi et al., 2022 and Plicka et al., 2022). The characteristics of this seismic fault, as provided by EFSM20, corresponds to a 44.3 km subsurface fault length, with an average of 17.3 km width, located along the North-coast of Samos Island, with a strike direction of 274 degrees. The average width of this fault is determined as 17.3 km, with a minimum and maximum values varying from 15.4 to 20.5 km, while its dip ranges from 45 to 70 degrees, with an average of 57 degrees. It's minimum and maximum depth are defined from 0 km to 14.5 km, while the rupture mechanism is declared as Normal fault ("N"-Fault). Finally, the average maximum moment Magnitude which is related to a potential earthquake event is defined to 6.73, ranging between 6.51 to 7.04 for ± 1 standard deviation (std) range covering the 95% of the maximum possibility, and between 6.46 to 7.14 for $\pm$ 2stds, covering the 98% of its maximum potential.

In this study, seeking to investigate a relevantly conservative fault-rupture scenario, an earthquake of a maximum magnitude 7.04, identical to the upper limit of the maximum potential magnitude for the 95% of possibility, as mentioned above, was selected to be examined. For this reason, the Fault characteristics, necessary for the Rupture-scenario at the DSHA, were re-determined based on this maximum moment magnitude (7.04)

and considering the suggested geometric and dynamic characteristics provided by EFSM20, mentioned above. More specifically, for an earthquake of magnitude 7.04, that is a sub-surface fault length corresponding to 43.7 km (Wells and Coppersmith, 1994), is very close to the recently activated one of 44.3 km, as is declared in the ESFM20. For this reason and keeping the geometry of the surface fault in ESFM20 (Figure 71) the surface trace of the adopted herein, fault of 43.7 km, is symmetrically distributed along the 44.3 km of the main fault trace, by skipping 0.3 km on each side of the 44.3 km fault. The surface trace of the adopted for the scenario fault is given with specific coordinated in Appendix B, while its width, strike and slip are kept those provided by the ESFM20 (Table 7). The epicenter and its depth are also given in Table 7, positioned in the center of the fault, by considering that the depth ranges from 0 km to 14.5 km, and the rupture reaches up to the surface (top = 0 km).

Table 7. Information of 4 Seismic Faults, investigated in this study, for the Vathy, Alexandroupolis, Canakkale and Izmir pilot sites. Information are taken from the European Fault-Source Model (EFSM20, Basili et al., 2022), and the Active Fault Database of Türkiye (AFDT, Emre et al., 2018).

	Examined Faults for event scenarios for the 4 pilot sites in the CBA			
Fault-ID in ESFM20	#08-GRCS912	#08-GRCS160	-	-
Fault-ID in AFDT	-	-	1-37	38
Sites affected per fault	Vathy	Alexandroupolis	Canakkale and Alexandroupolis	Izmir
Mw	7.04	6.96	7.35	6.6
Mechanism	Normal	Normal	Strike Slip	Normal
Strike (deg)	274	094	255	250
Dip (deg)	57	60	82.5	65
Width (km)	17.03	16.2	19	13
Top (km)	0	0	0	0
Epicenter - Lat. (deg)	37.8656	40.814334	40.645883	38.3997
Epicenter - Long. (deg)	26.8504	25.812298	26.973885	27.0603
Hypocentral-Depth (km)	7.25	7.00	9.5	12

Results for the pilot site of Vathy-Samos

For the DSHA apart from the properties of the selected fault scenarios, for the REDAS event scenarios, Ground Motion Models are incorporated and used, as proposed by Theodoulidis et al. 2024.
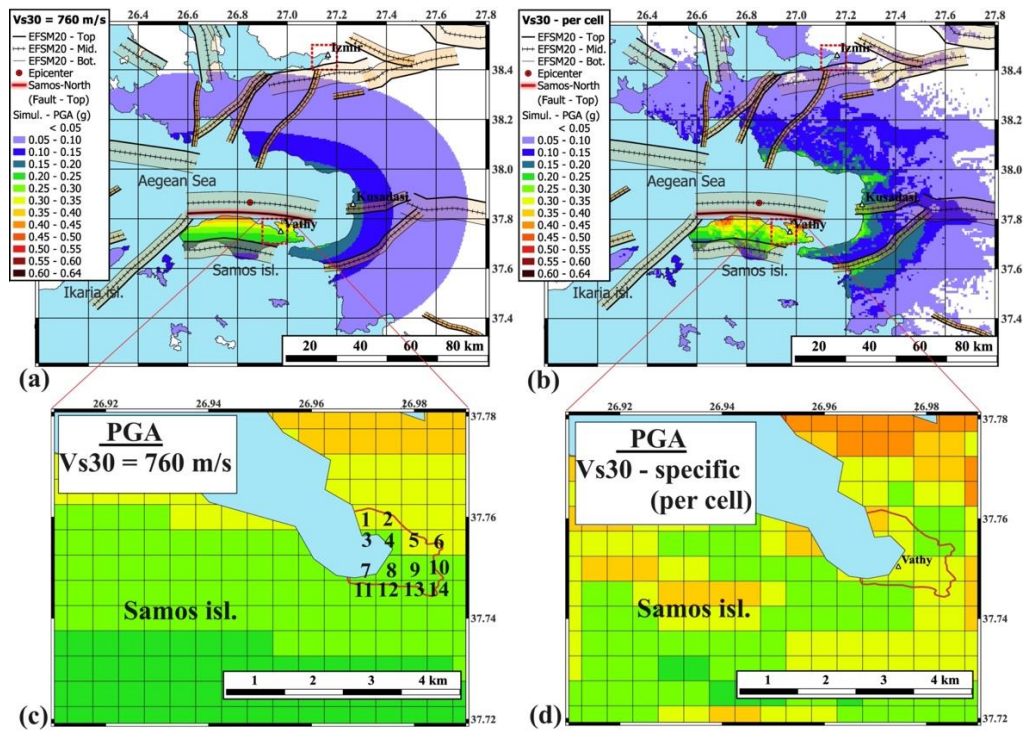
Figure 79. (a) Distribution of PGA (in g) at each geographic cell (0.005 x 0.005, degrees size), computed by the causative event scenario of the Northern Samos Fault (Appendix B, in red line), for engineering bedrock (Vs30 = 760 m/s). The adjacent faults to the Northern Samos Fault in the broader Greece-Türkiye CBA provided by the EFSM20, are also depicted.
(b) Similar to Figure 79a, but for specific Vs30 values of each site specific "cell" (Figure 72a,c) (c) The same PGA values presented in Figure 79a, focused on the area very close to the Vathy town pilot site, as it is extended within the red line. The cells included (at least their ~25%) into the examined site, are numbered. (d) Similar to Figure 79c, but including the PGA values of Figure 79b.
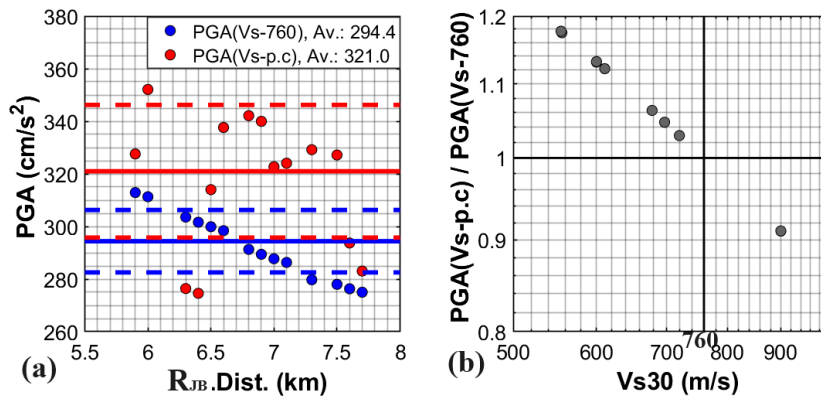
Figure 80. (a) PGA computed by the REDAS software, for the Scenario event of Samos Fault (Table 7, Appendix B, Figure 79a,b), for engineering bedrock Vs30=760 m/s (blue points), and for the cell-specific Vs30 values (Figure 72a,c). These 14 PGA values (blue and red points) correspond to the 14 numbered site specific "cells" of Vathy town depicted in Figure 79c and Figure 79d, respectively. (b) The ratio between the PGAs, of the specific Vs30 values (blue points in Figure 80a) over the corresponding ones of constant engineering bedrockVs30=760 m/s values (red points in Figure 80a) versus the corresponding Vs30 value of each cell.
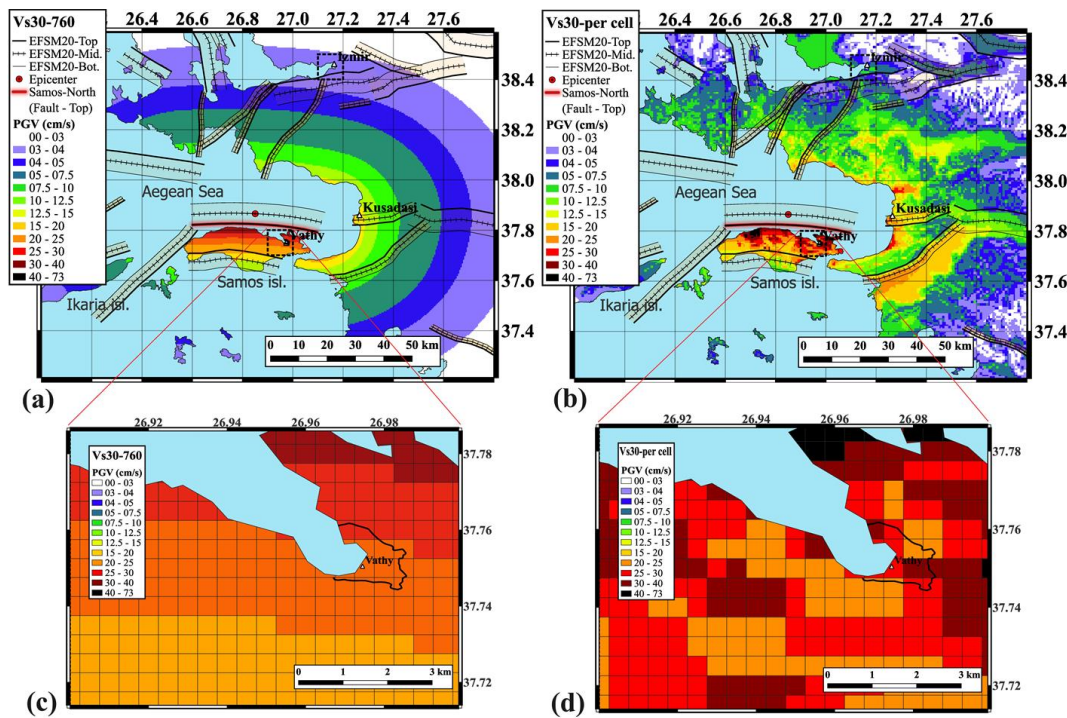

Figure 81. (a) Distribution of PGV(in cm/s) at each geographic cell (0.005 x 0.005 degrees size), computed by the causative event scenario of the Northern Samos Fault(Appendix B, in red line), for engineering bedrock (Vs30 = 760 m/s). The adjacent faults to the Northern Samos Fault in the broader Greece-Türkiye CBA provided by the EFSM20, are also depicted. (b) Similar to Figure 81a, but for specific Vs30 values of each site specific "cell" (Figure 72a,c) as determined by (Stewart et al. 2014) (c) The same PGV values presented in Figure 81a, focused on the area very close to the Vathy town pilot site, as it is extended within the black line. (d) Similar to Figure 81c but including the PGV values of Figure 5b.
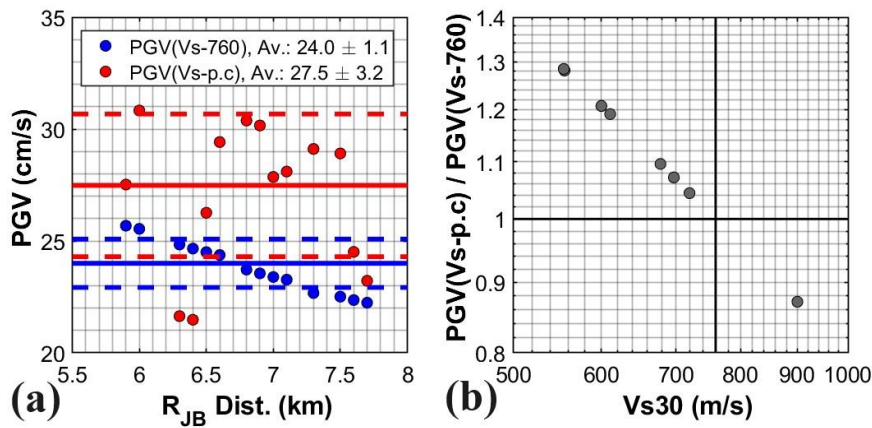
Figure 82. (a) PGV computed by the REDAS software, for the scenario event of Samos Fault (Table 7, Appendix B, Figure 81a,b), for engineering bedrock Vs30=760 m/s (blue points), and for the cell-specific Vs30 values (Figure 72a,c) as has been determined by (Stewart et al. 2014). (b) The ratio between the PGAs, of the specific Vs30 values (red points in Figure 82a) over the corresponding ones of engineering bedrock, Vs30=760 m/s values (blue points in Figure 82a) versus the corresponding Vs30 value of each cell.
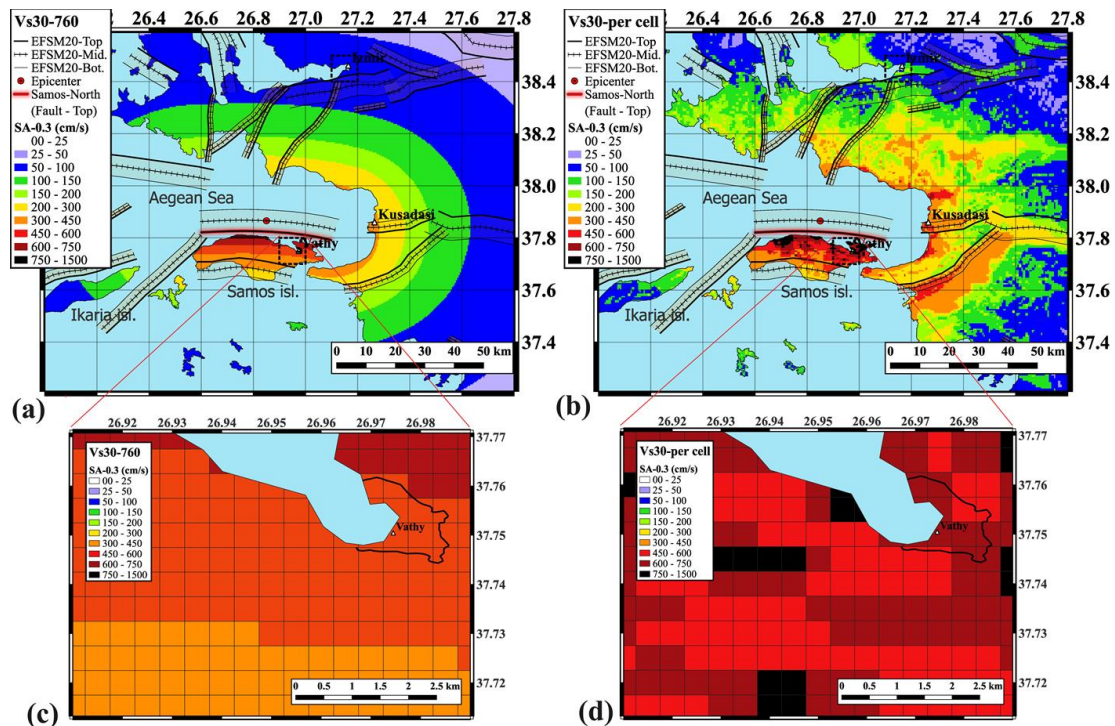

Figure 83. (a) Distribution of Sa[0.3s](in cm/s) at each geographic cell (0.005 x 0.005 degrees size), computed by the causative event scenario of the Northern Samos Fault(in red line), for engineering bedrock (Vs30 = 760 m/s). The adjacent faults to the Northern Samos Fault in the broader Greece-Türkiye CBA provided by the EFSM20, are also depicted. (b) Similar to Figure 83a, but for specific Vs30 values of each site specific "cell" (Figure 72a,c) as determined by (Stewart et al. 2014) (c) The same Sa[0.3s] values presented in Figure 83a, focused on the area very close to the Vathy town pilot site, as it is extended within the black line (d) Similar to Figure 83c but including the Sa values of Figure 83b.
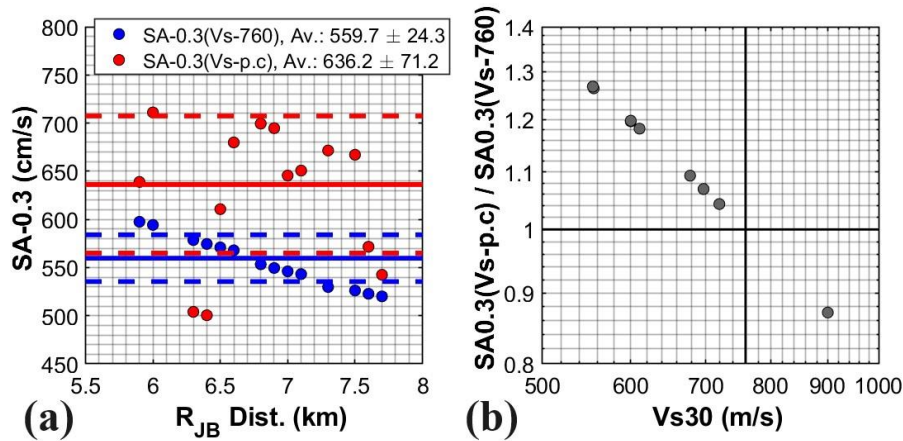
Figure 84. (a) Sa[0.3s] computed by the REDAS software, for the scenario event of Samos Fault (Table 7, Appendix B, Figure 83a,b), for engineering bedrock Vs30=760 m/s (blue points), and for the cell-specific Vs30 values (Figure 72a,c) as has been determined by (Stewart et al. 2014). (b) The ratio between the Sa[0.3s], of the cell-specific Vs30 values (red points in Figure 84a over the corresponding ones of engineering bedrock, Vs30=760 m/s values (blue points in Figure 84a) versus the corresponding Vs30 value of each cell.
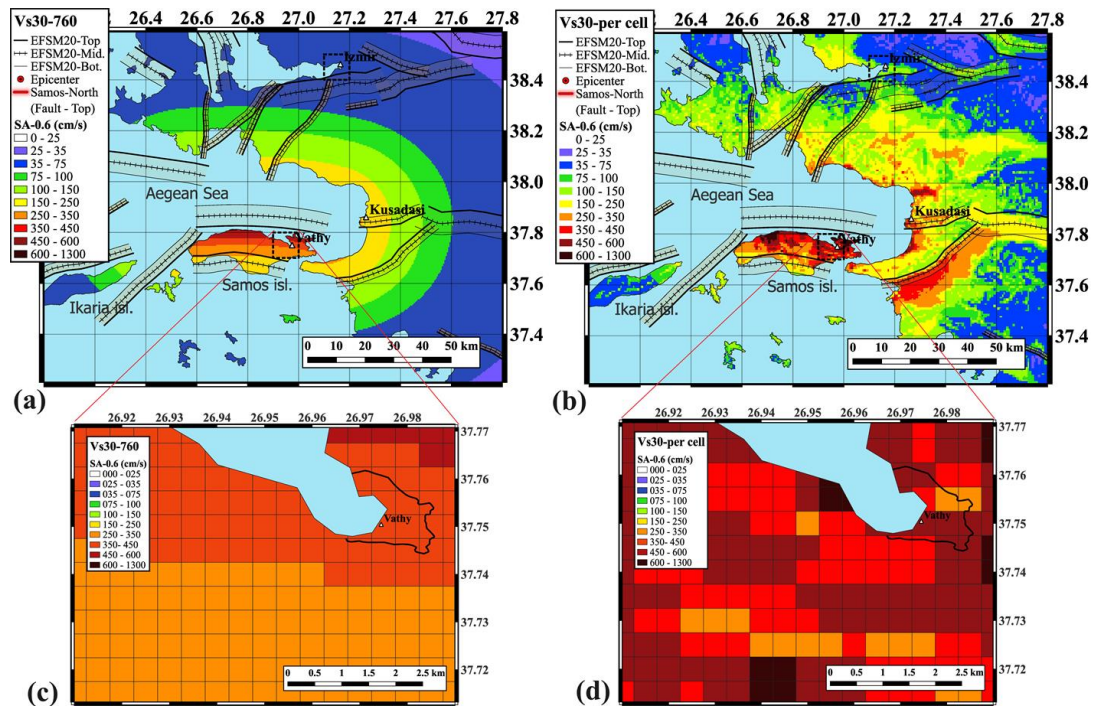
Figure 85. (a) Distribution of Sa[0.6s](in cm/s) at each geographic cell (0.005 x 0.005 degrees size), computed by the causative event scenario of the Northern Samos Fault(in red line), for engineering bedrock (Vs30 = 760 m/s). The adjacent faults to the Northern Samos Fault in the broader Greece-Türkiye CBA provided by the EFSM20, are also depicted. (b) Similar to Figure 85a, but for specific Vs30 values of each site specific "cell" (Figure 72a,c) as determined by (Stewart et al. 2014) (c) The same Sa[0.6s] values presented in Figure 85a, focused on the area very close to the Vathy town pilot site, as it is extended within the black line (d) Similar to Figure 85c but including the Sa values of Figure 9b.

Figure 86. (a) Sa[0.6s] computed by the REDAS software, for the scenario event of Samos Fault (Table 7, Appendix B, Figure 85a,b), for engineering bedrock Vs30=760 m/s (blue points), and for the specific Vs30 values (Figure 72a,c) as has been determined by (Stewart et al. 2014). (b) The ratio between the Sa[0.6s], of the specific Vs30 values (red points in Figure 86b over the corresponding ones of engineering bedrock, Vs30=760 m/s values (blue points in Figure 86a) versus the corresponding Vs30 value of each cell.
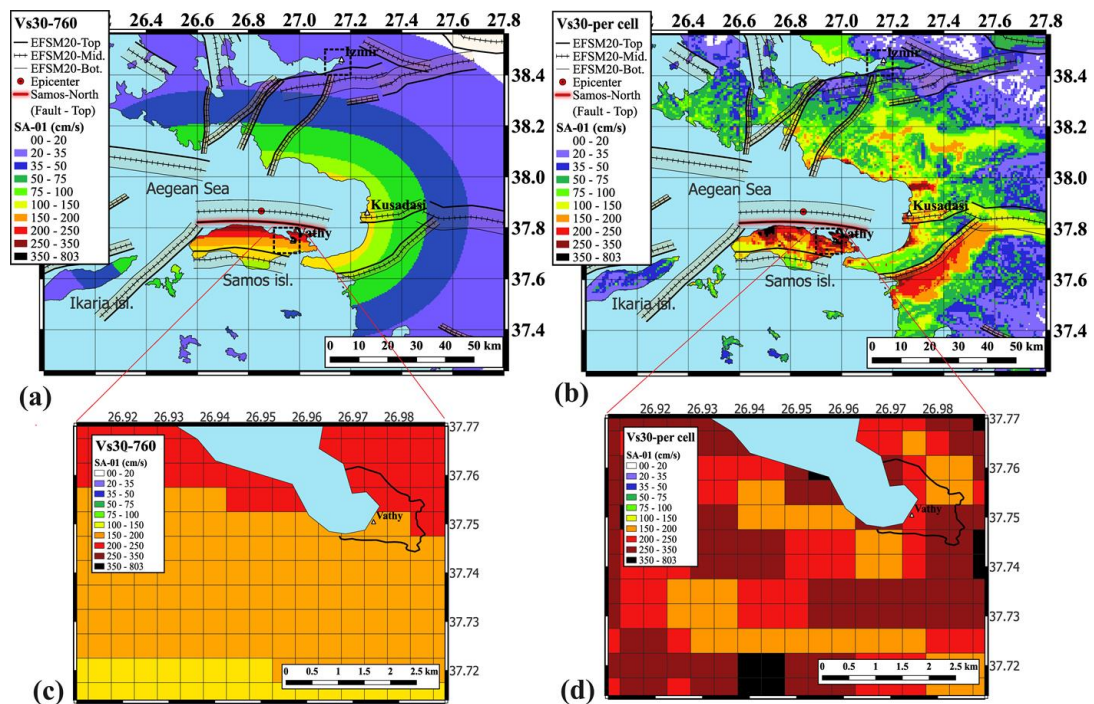
Figure 87. (a) Distribution of Sa[1.0](in cm/s) at each geographic cell (0.005 x 0.005 degrees size), computed by the causative event scenario of the Northern Samos Fault(in red line), for engineering bedrock (Vs30 = 760 m/s). The adjacent faults to the Northern Samos Fault in the broader Greece-Türkiye CBA provided by the EFSM20, are also depicted. (b) Similar to Figure 87a, but for cell-specific Vs30 values (Figure 72a,c), as determined by (Stewart et al. 2014) (c) The same Sa[0.6s] values presented in Figure 87a, focused on the area very close to the Vathy town pilot site, as it is extended within the black line (d) Similar to Figure 87c but including the Sa values of Figure 87b.
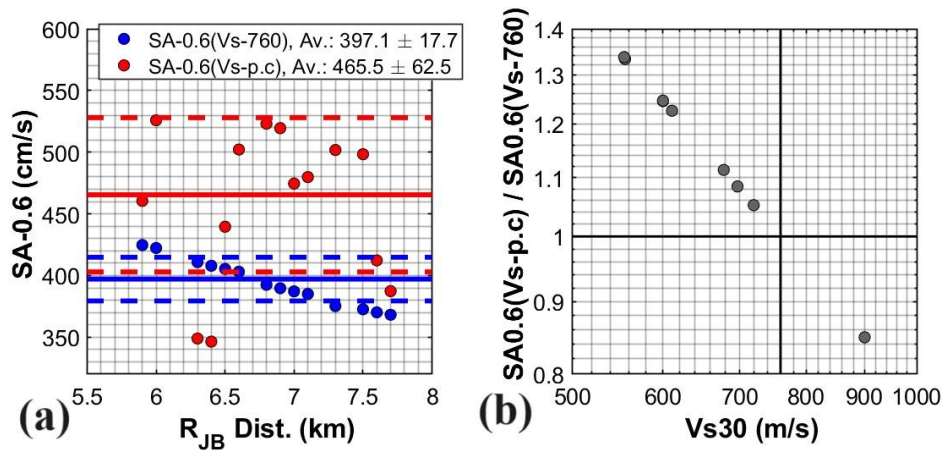
Figure 88. (a) Sa[0.6s] computed by the REDAS software, for the scenario event of Samos Fault (Table 7, Appendix B, Figure 87a,b), for engineering bedrock Vs30=760 m/s (blue points), and for the cell-specific Vs30 values (Figure 72a,c) as has been determined by (Stewart et al. 2014). (b) The ratio between the Sa[1.0s], of the specific Vs30 values (red points in Figure 88a over the corresponding ones of engineering bedrock, Vs30=760 m/s values (blue points in Figure 88a) versus the corresponding Vs30 value of each cell.
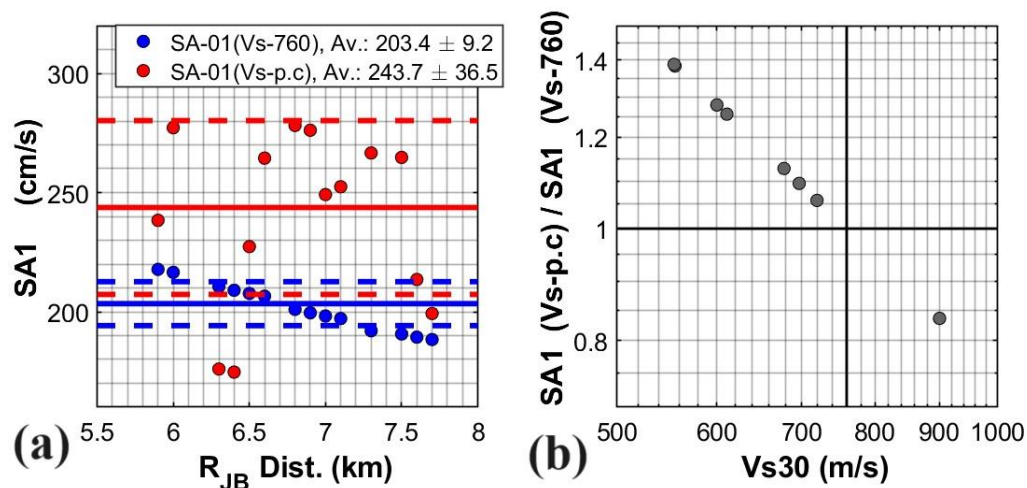
4.3 The pilot site Alexandroupoli [seismic scenario of Maronia-Alexandroupoli fault]

Alexandroupoli city is in the north-eastern part of Greece, in the northern Aegean Sea (Figure 71). This area is generally characterized by a low seismicity, where few large earthquakes is known to be occurred in the broader area. This area is also included to the well-studied areas, in terms of the geological active shallow faults, by the Greek Database of Seismogenic Sources (GreDass) project, conducted and updated by Sboras et al., (2009), Pavlides et al., (2010) and Caputo and Pavlides, (2013), as well as in a corresponding project under the National Observatory of Athens (NOA-Faults), conducted and updated by Ganas et al., (2013) and Ganas et al., (2018). Here, for the Alexandroupoli city, the selection of the "Near-Field" seismic source, is based directly on the European Fault-Source Model (EFSM20, Basili et al. 2022), included in the 2020 updated version of the European Seismic Hazard Model (ESHM20, Danciu et al., 2021), which, for this specific area, has been based on the Seismogenic Sources of GreDass and NOA-Faults.

More specifically, as a "Near-Field" Seismic Source to Alexandroupoli city, the fault located to its southern part, along the coastline (named: "Maronia-Alexandroupoli" Fault, Figure 71), as outlined in the EFSM20 database, has been selected for the DSHA. It's worth noting that the activation of this fault into the past years, is not known. The characteristics of this fault, as provided

by EFSM20, corresponds to a 53.7 km subsurface fault length, with a strike direction of 94 degrees. The average width of this fault is determined as 16.2 km, with a minimum and maximum values varying from 14.5 to 19.8 km, while its Dip ranges from 45 to 75 degrees, with an average of 60 degrees. It's minimum and maximum Depth are defined from 0 km to 14 km, while the rupture mechanism is declared as Normal ("N"-Fault). Finally, the average maximum moment Magnitude which is related to a potential earthquake event is defined to 6.65, ranging between 6.43 to 6.96 for ± 1 standard deviation (std) range covering the 95% of the maximum possibility, and between 6.38 to 7.06 for $\pm$ 2stds, covering the 98% of its maximum potential.

Here, seeking to investigate a relevantly conservative fault-rupture scenario, an earthquake of a maximum magnitude 6.96, identical to the upper limit of the maximum potential magnitude for the 95% of possibility, was selected to be examined. For this reason, the Fault characteristics, necessary for the Rupture-scenario at the DSHA, were re-determined based on this maximum moment magnitude (6.96) and considering the suggested geometric and dynamic characteristics provided by EFSM20, mentioned above. More specifically, for an earthquake of magnitude 6.96, the corresponding sub-surface fault length is 39.7 km (Wells and Coppersmith, 1994). Based on this length, and taking into account the geometry of the surface fault in ESFM20 (Figure 71), the surface trace of the adopted herein, fault of 39.7km, is symmetrically distributed along the 53.7 km of the main fault trace given in ESGM20, by skipping 7 km on each side of the 53.7 km fault. The surface trace of the adopted for the scenario fault is given with specific coordinated in Appendix C, while its width, strike and slip are kept those provided by the ESFM20 (Table 7). The epicenter and its depth are also given in Table 7, positioned in the center of the fault, by considering that the depth ranges from 0 km to 14 km, and the rupture reaches up to the surface (top = 0 km).

Results for the pilot site of Alexandroupolis
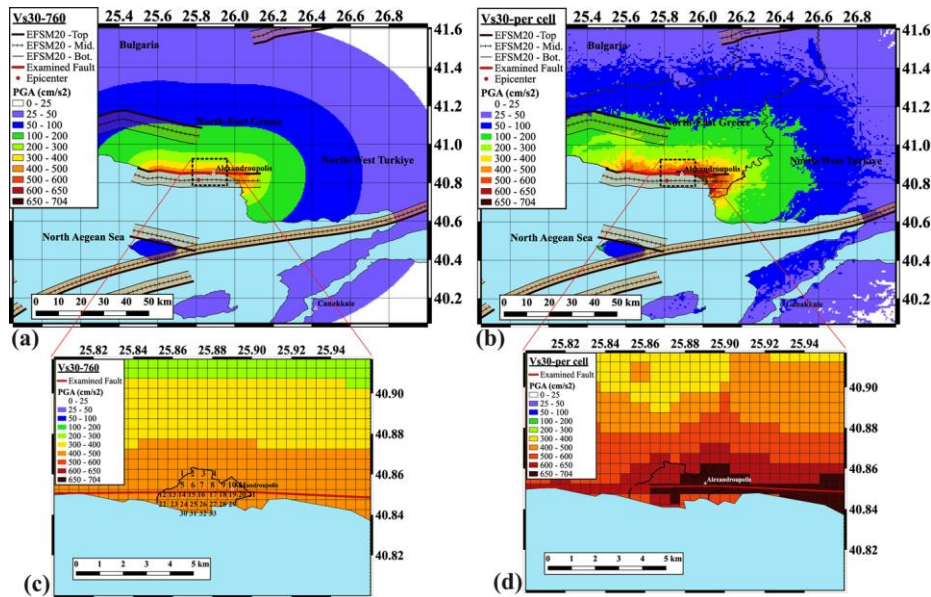
Figure 89. (a) Distribution of PGA(in cm/s/s) at each geographic cell (0.005 x 0.005, degrees size), computed by the causative event scenario of the Maronia-Alexandroupoli Fault (in red line), for engineering bedrock (Vs30 = 760 m/s). The adjacent faults to the Maronia-Alexandroupoli Fault in the broader Greece-Türkiye CBA provided by the EFSM20, are also depicted. (b) Similar to Figure 89a, but for cell-specific Vs30 values (Figure 73a,b) of each site, as determined by (Stewart et al. 2014) (c) The same PGA values presented in Figure 89a, focused on the area very close to the Alexandroupoli pilot site, as it is extended within the black line. The cells included (at least their ~25%) into the examined site, are numbered. (d) Similar to Figure 89c but including the PGA values of Figure 89b.
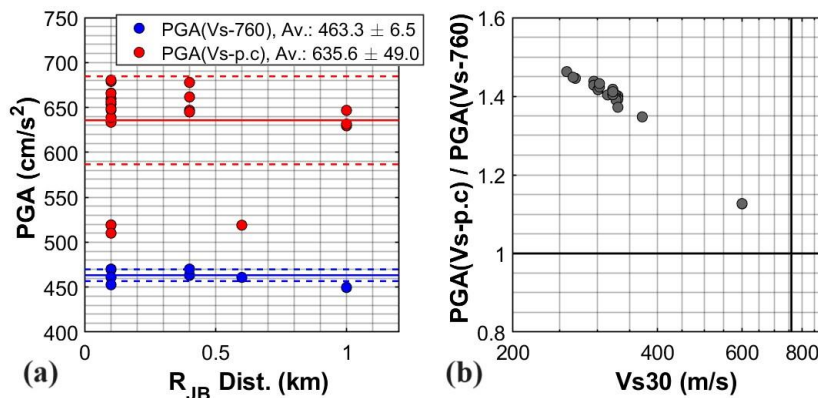
Figure 90. (a) PGA (in cm/s/s) computed by the REDAS software, for the Scenario event of Maronia-Alexandroupoli (Table 7, Appendix C, Figure 90a,b), for engineering bedrock Vs30=760 m/s (blue points), and for the cell-specific Vs30 values (Figure 73a,b) as have been determined by (Stewart et al. 2014). These PGA values (blue and red points) correspond to the "cells" of Alexandroupoli city depicted in Figure 89c and Figure 89c d, respectively. (b) The ratio between the PGAs, of the specific Vs30 values (red points in Figure 90a) over the corresponding ones of engineering bedrockVs30=760 m/s values (blue points in Figure 90a) versus the corresponding Vs30 value of each cell.
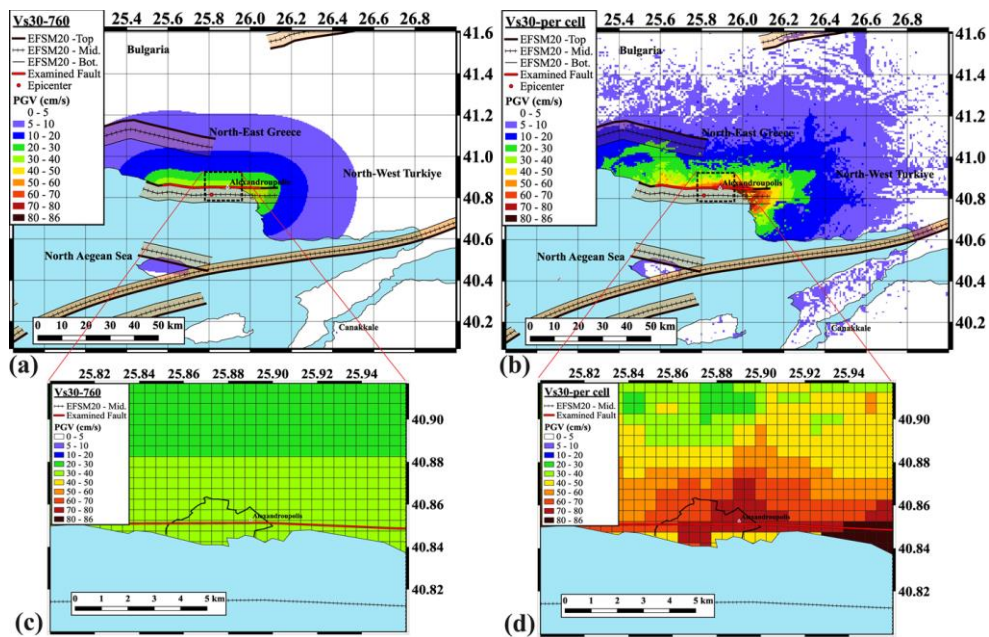
Figure 91. (a) Distribution of PGV(in cm/s) at each geographic cell (0.005 x 0.005, degrees size), computed by the causative event scenario of the Maronia-Alexandroupoli Fault (in red line), for engineering bedrock (Vs30 = 760 m/s). The adjacent faults to the Maronia-Alexandroupoli Fault in the broader Greece-Türkiye CBA provided by the EFSM20, are also depicted. (b) Similar to Figure 91a, but for the cell-specific Vs30 values (Figure 73a,b) as determined by Stewart et al. (2014) (c) The same PGV values presented in Figure 91a, focused on the area very close to the Alexandroupoli pilot site, as it is extended within the black line. (d) Similar to Figure 91c but including the PGV values of Figure 91b.
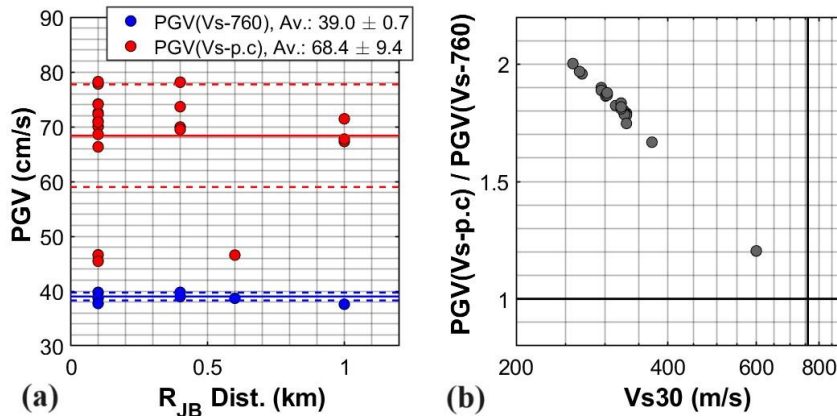
Figure 92. (a) PGV (in cm/s) computed by the REDAS software, for the Scenario event of Maronia-Alexandroupoli (Table 7, Appendix C, Figure 91a,b), for engineering bedrock Vs30=760 m/s (blue points), and for the cell-specific Vs30 values (Figure 73a,b) as have been determined by (Stewart et al. 2014). These PGV values (blue and red points) correspond to the "cells" of Alexandroupoli city depicted in Figure 91c and Figure 91d, respectively. (b) The ratio between the PGAs, of the specific Vs30 values (red points in Figure 92a) over the corresponding ones of engineering bedrockVs30=760 m/s values (blue points in Figure 92a) versus the corresponding Vs30 value of each cell.
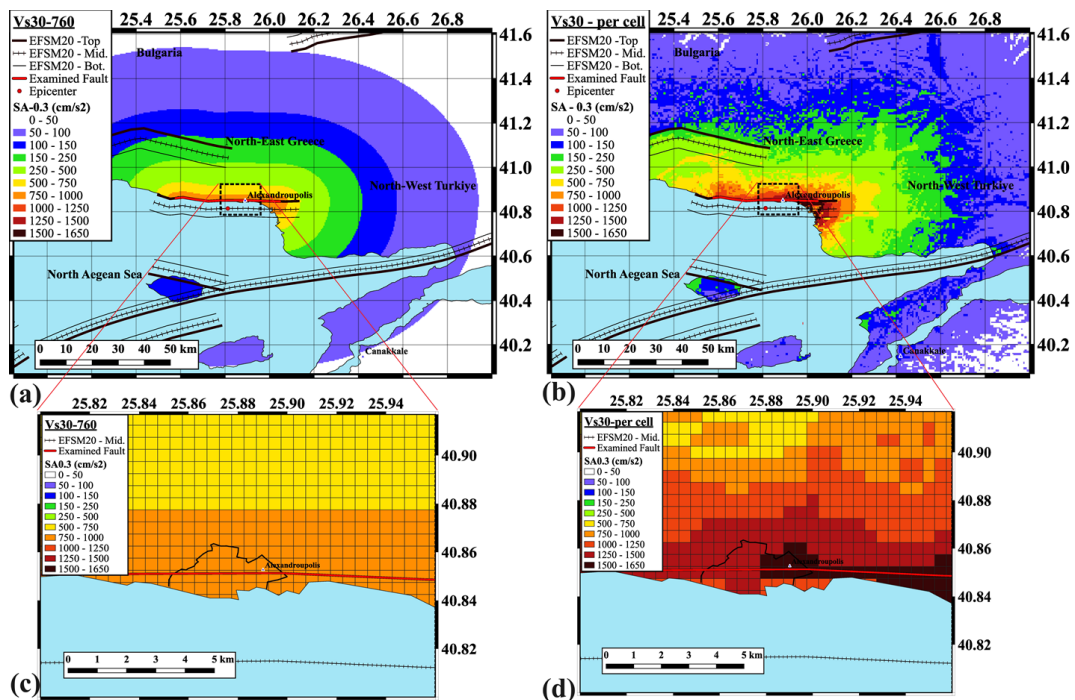
Figure 93. (a) Distribution of Sa[0.3s](in cm/s/s) at each geographic cell (0.005 x 0.005, degrees size), computed by the causative event scenario of the Maronia-Alexandroupoli fault (in red line), for engineering bedrock (Vs30 = 760 m/s). The adjacent faults to the Maronia-Alexandroupoli fault in the broader Greece-Türkiye CBA provided by the EFSM20, are also depicted. (b) Similar to Figure 93a, but for the cell-specific Vs30 values (Figure 73a,b) as determined by (Stewart et al. 2014) (c) The same PGA values presented in Figure 93a, focused on the area very close to Alexandroupoli pilot site, as it is extended within the black line. (d) Similar to Figure 93c but including the PGA values of Figure 93b.
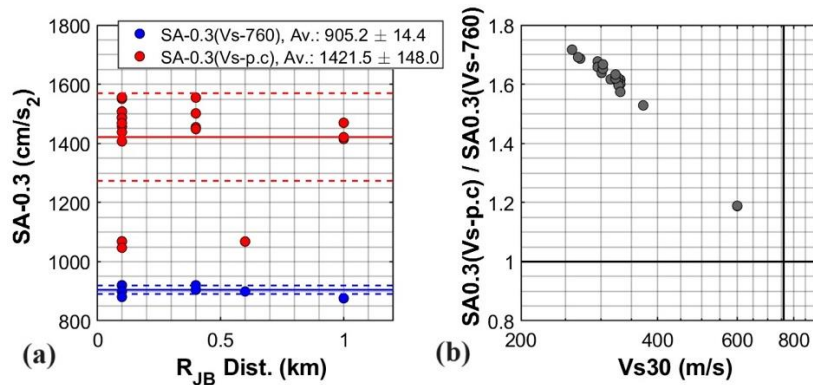

Figure 94. (a) Sa[0.3s] (in cm/s/s) computed by the REDAS software, for the scenario event of Maronia-Alexandroupoli (Table 7, Appendix C, Figure 93a,b), for engineering bedrock Vs30=760 m/s (blue points), and for the cell-specific Vs30 values (Figure 73a,b) as have been determined by (Stewart et al. 2014). These PGA values (blue and red points) correspond to the "cells" of Alexandroupoli city depicted in Figure 93c and Figure 93d, respectively. (b) The ratio between the PGAs, of the specific Vs30 values (red points in Figure 94a) over the corresponding ones of engineering bedrockVs30=760 m/s values (blue points in Figure 94a) versus the corresponding Vs30 value of each cell.
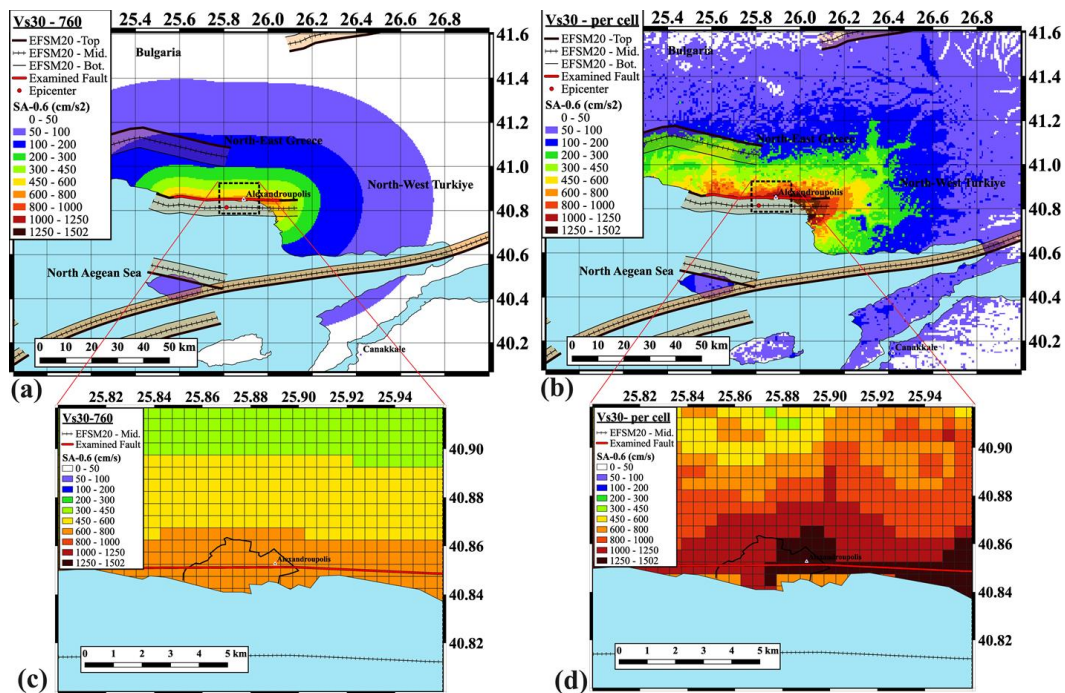
Figure 95. (a) Distribution of Sa[0.6s](in cm/s/s) at each geographic cell (0.005 x 0.005, degrees size), computed by the causative event scenario of the Maronia-Alexandroupoli fault (in red line), for engineering bedrock (Vs30 = 760 m/s). The adjacent faults to the Maronia-Alexandroupoli fault in the broader Greece-Türkiye CBA provided by the EFSM20, are also depicted. (b) Similar to Figure 95a, but for the cell-specific Vs30 values (Figure 73a,b), as determined by (Stewart et al. 2014) (c) The same Sa[0.6s] values presented in Figure 95a, focused on the area very close to Alexandroupoli pilot site, as it is extended within the black line (d) Similar to Figure 20c but including the PGA values of Figure 95b.


Figure 96. (a) Sa[0.6s](in cm/s/s) computed by the REDAS software, for the scenario event of Maronia-Alexandroupoli (Table 7, Appendix C, Figure 95a,b), for engineering bedrock Vs30=760 m/s (blue points), and for the cell-specific Vs30 values (Figure 73a,b). cThese Sa[0.6s] values (blue and red points) correspond to the "cells" of Alexandroupoli city depicted in Figure 95c and Figure 95d, respectively. (b) The ratio between the Sa[0.6s], of the specific Vs30 values (red points in Figure 96a) over the corresponding ones of engineering bedrockVs30=760 m/s values (blue points in Figure 96a) versus the corresponding Vs30 value of each cell.
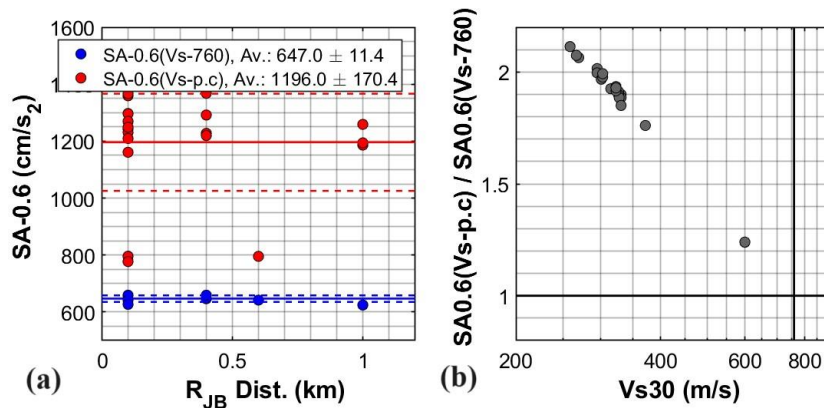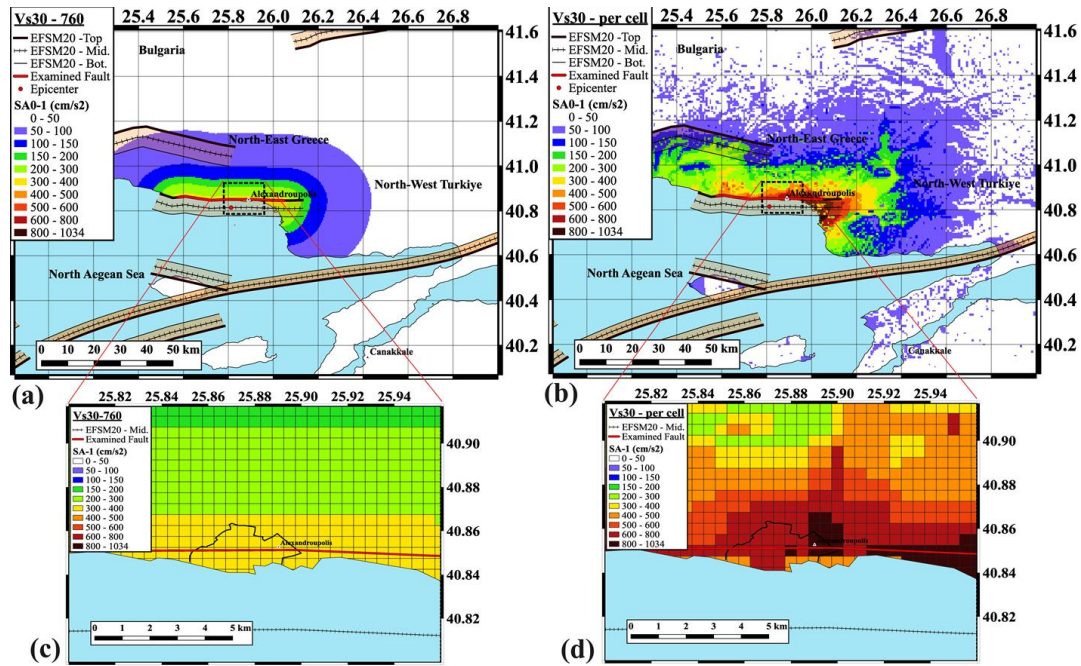
Figure 97. (a) Distribution of Sa[1.0s](in cm/s/s) at each geographic cell (0.005 x 0.005, degrees size), computed by the causative event scenario of the Maronia-Alexandroupoli fault (in red line), for engineering bedrock (Vs30 = 760 m/s). The adjacent faults to the Maronia-Alexandroupoli fault in the broader Greece-Türkiye CBA provided by the EFSM20, are also depicted. (b) Similar to Figure 97a, but for specific Vs30 values of each site specific "cell" as determined by (Stewart et al. 2014) (c) The same Sa[1.0s] values presented in Figure 97a, focused on the area very close to Alexandroupoli pilot site, as it is extended within the black line (d) Similar to Figure 97c but including the Sa[1.0s] values of Figure 97b.
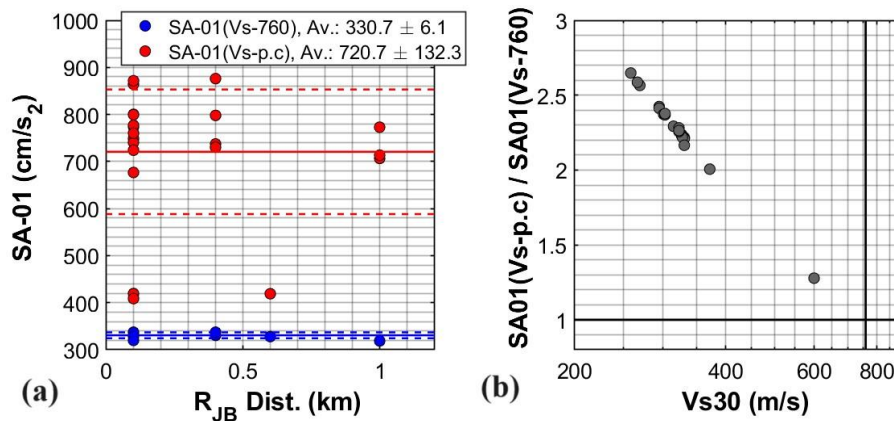

Figure 98. (a) Sa[1.0s](in cm/s/s) computed by the REDAS software, for the scenario event of Maronia-Alexandroupoli (Table 7, Appendix C, Figure 97a,b), for engineering bedrock Vs30=760 m/s (blue points), and for the specific Vs30 values (Figure 73a,b). These Sa[1.0s] values (blue and red points) correspond to the "cells" of Alexandroupoli city depicted in Figure 97c and Figure 97d, respectively. (b) The ratio between the Sa[1.0s], of the specific Vs30 values (red points in Figure 98a) over the corresponding ones of engineering bedrock Vs30=760 m/s values (blue points in Figure 98a) versus the corresponding Vs30 value of each cell.

4.4   The pilot site Alexandroupoli (scenario of the NAF-Ganos fault)

Regarding the city of Alexandroupoli, except for the near-field "Maronia-Alexandroupolis Fault" (Figure 90) examined in the Section-3 here, another one Fault was examined. This fault is name as "Ganos" and constitutes a large segment of the North Anatolian Fault (NAF) (Figure 71), located in wester Turkiey, in western part of Marmaras Sea. This "two-faults examination strategy" was chosen for Alexandroupolis city, since except for the very near field fault of "Maronia-Alexandroupolis, the "Ganos-NAF", is located in only ~65 km away from the city and its seismic potential is declared high enough with respect to all the other faults located around Alexandroupolis city in these epicentral distances (0-80 km). Most specifically, based on the Active Fault Database of Türkiye (AFDT, Emre et al., 2018), the seismic potential of this Fault, corresponds to an earthquake of a moment Magnitude, 7.35. Moreover, this fault has been also characterized by the Greek Database of Seismogenic Sources (GreDass), named as "South-NAT, Ganos", with a similar seismic potential of 7.5.

Analytically, the "Ganos-NAF", as given by the Active Fault Database of Türkiye (AFDT, Emre et al., 2018), corresponds to a ~90 km subsurface fault length, while summarizing all the corresponding part of this Fault , a total of ~104 km is resulted. The average width is ~19 km, and the Strike ranges from 247 to 74 degrees. Its average Dip ranges from 75 to 90 degrees, while its maximum depth reach up to 18-20 km. The rupture mechanism is clearly declared as Strike-Slip ("SS"-Fault).

Here, seeking to investigate this high seismic potential fault, the following rupture scenario was considered for a maximum moment magnitude of 7.35. The average Fault characteristics, were re-determined based on this maximum moment magnitude (7.35), considering the suggested geometric and dynamic characteristics provided by the Active Fault Database of Türkiye (AFDT, Emre et al., 2018). More specifically, for an earthquake of magnitude 7.34, the sub-surface fault length corresponding to 97 km (Wells and Coppersmith, 1994), which is in between the characteristic range of 90-104 km mentioned above. Based on this length (97 km), the fault was "re-traced" following the geometry proposed by the Active Fault Database of Türkiye (AFDT, Emre et al., 2018), starting from the left corner of the Fault, which is the closest part to Alexandroupoli city (and to Canakkale city, which is the other city examined fro this fault below).

The surface trace of the adopted for the scenario fault is given with specific coordinated in Appendix D, while its width, strike and slip are kept as the average of the ranges provided by the ESFM20 (Table 7) and mentioned above.

The epicenter and its depth are also given in Table 7, positioned in the center of the fault, by considering that the depth ranges from 0 km to 19 km, and the rupture reaches up to the surface (top = 0 km)

Results for the pilot site of Alexandroupolis
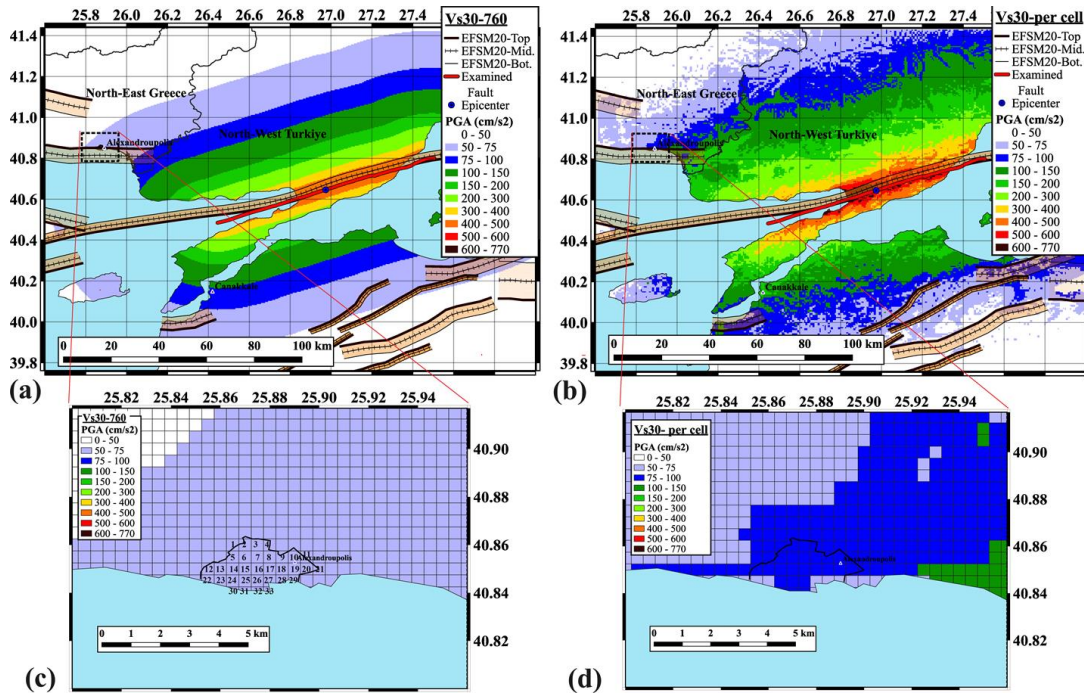
Figure 99. (a) Distribution of PGA(in cm/s/s) at each geographic cell (0.005 x 0.005, degrees size), computed by the causative event scenario of the NAF-Ganos fault (in red line), for engineering bedrock (Vs30 = 760 m/s). The adjacent faults to the NAF-Ganos fault in the broader Greece-Türkiye CBA provided by the EFSM20, are also depicted. (b) Similar to Figure 99a, but for specific Vs30 values of each site specific "cell" (Figure 73a,b) as determined by (Stewart et al. 2014) (c) The same PGA values presented in Figure 99a, focused on the area very close to the Alexandroupoli pilot site, as it is extended within the black line. The cells included (at least their ~25%) into the examined site, are numbered. (d) Similar to Figure 99c but including the PGA values of Figure 99b.
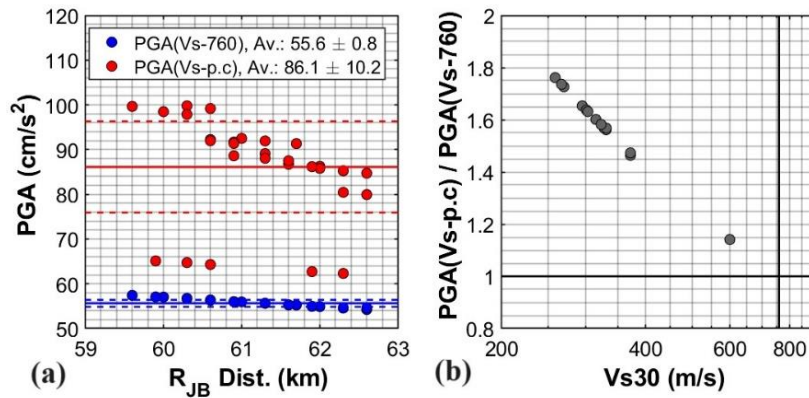
Figure 100. (a) PGA (in cm/s/s) computed by the REDAS software, for the scenario event of NAF-Ganos (Table 7, Appendix D, Figure 99a,b) for engineering bedrock Vs30=760 m/s (blue points), and for the specific Vs30 values (Figure 73a,b). These PGA values (blue and red points) correspond to the "cells" of Alexandroupoli city depicted in Figure 99c and Figure 99d, respectively (b) The ratio between the PGAs, of the specific Vs30 values (red points in Figure 100a) over the corresponding ones of engineering bedrockVs30=760 m/s values (blue points in Figure 100a) versus the corresponding Vs30 value of each cell.
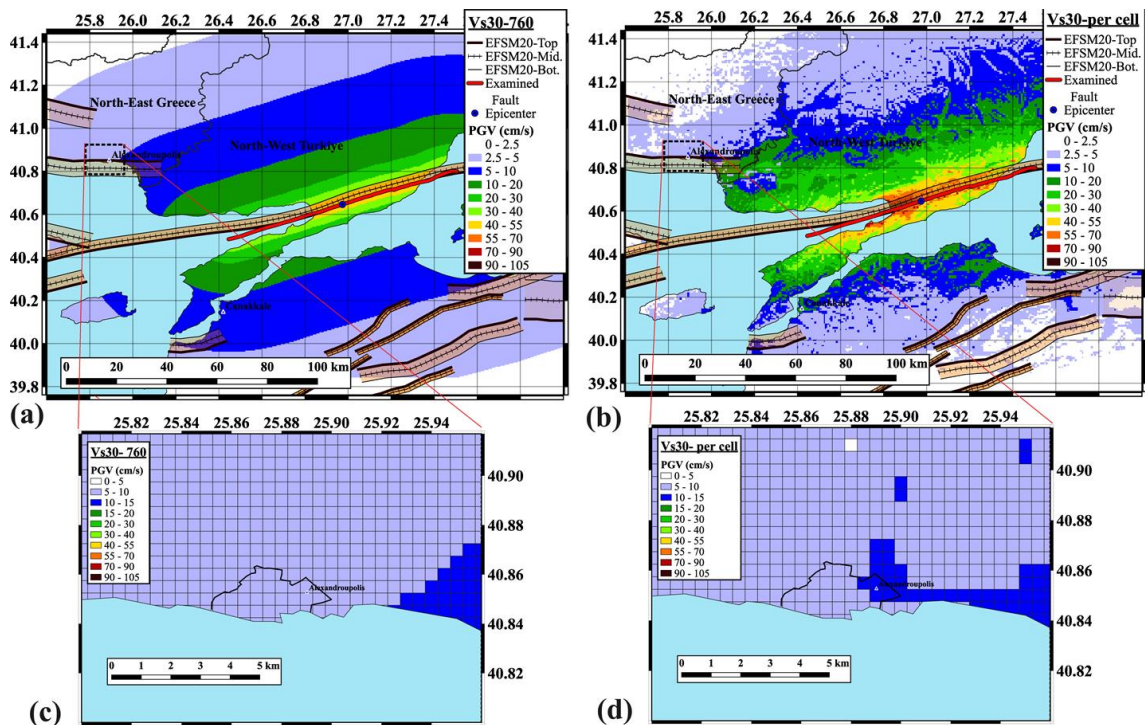
Figure 101. (a) Distribution of PGV(in cm/s) at each geographic cell (0.005 x 0.005, degrees size), computed by the causative event scenario of the NAF-Ganos fault (in red line), for engineering bedrock (Vs30 = 760 m/s). The adjacent faults to the NAF-Ganos fault in the broader Greece-Türkiye CBA provided by the EFSM20, are also depicted. (b) Similar to Figure 101a, but for the cell-specific Vs30 values (Figure 73a,b) (c) The same PGA values presented in Figure 101a, focused on the area very close to the Alexandroupoli pilot site, as it is extended within the black line. (d) Similar to Figure 101c but including the PGV values of Figure 101b.
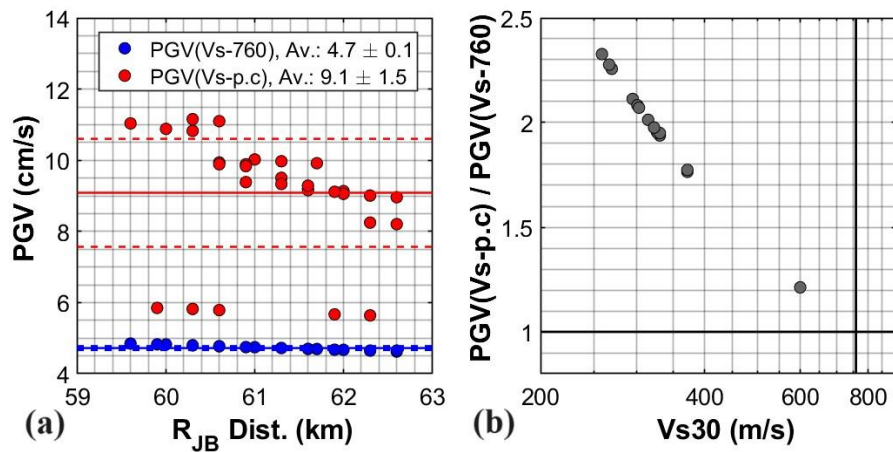
Figure 102. (a) PGV (in cm/s) computed by the REDAS software, for the scenario event of NAF-Ganos (Table 7, Appendix D, Figure 101a,b) for engineering bedrock Vs30=760 m/s (blue points), and for the cell-specific Vs30 values (Figure 73a,b). These PGV values (blue and red points) correspond to the "cells" of Alexandroupoli city depicted in Figure 101c and Figure 101d, respectively (b) The ratio between the PGVs, of the specific Vs30 values (red points in Figure 102a) over the corresponding ones of engineering bedrockVs30=760 m/s values (blue points in Figure 102a) versus the corresponding Vs30 value of each cell.
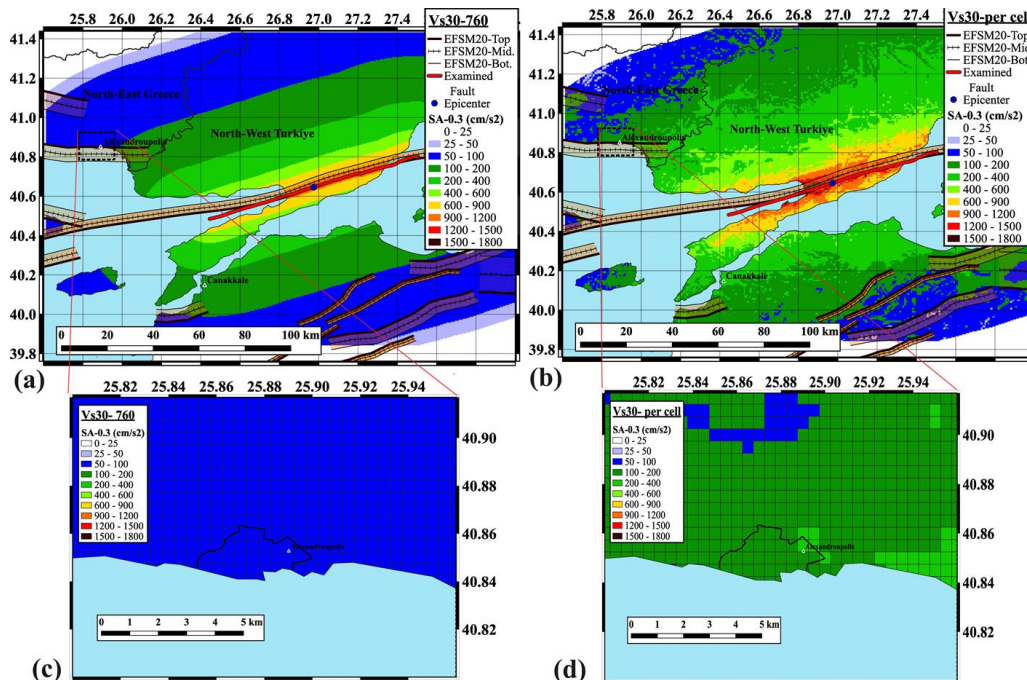

Figure 103. (a) Distribution of Sa[0.3s](in cm/s/s) at each geographic cell (0.005 x 0.005 degrees size), computed by the causative event scenario of the NAF-Ganos fault (in red line), for engineering bedrock (Vs30=760 m/s). The adjacent faults to the NAF-Ganos in the broader Greece-Türkiye CBA provided by the EFSM20, are also depicted. (b) Similar to Figure 103a, but for the cell-specific Vs30 values (Figure 73a,b) (c) The same Sa[0.3s] values presented in Figure 28a, focused on the area very close to the Alexandroupoli pilot site, as it is extended within the black line. (d) Similar to Figure 103c but including the Sa[0.3s] values of Figure 103b.
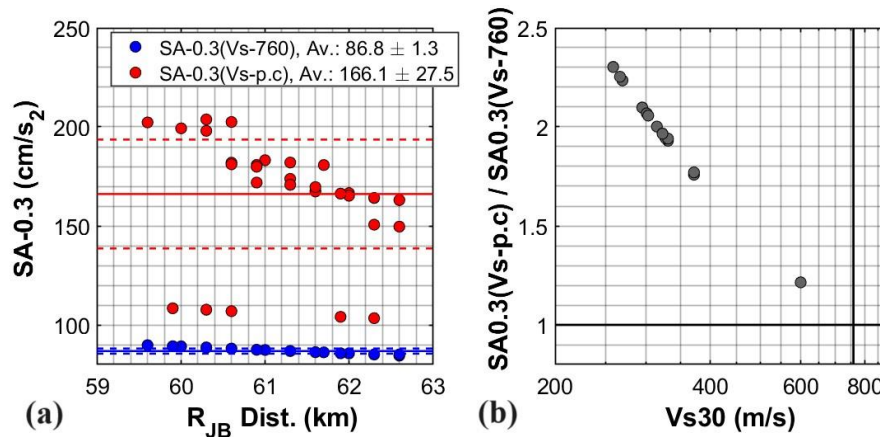
Figure 104. (a) Sa[0.3s] (in cm/s/s) computed by the REDAS software, for the scenario event of NAF-Ganos (Table 7, Appendix D, Figure 103a,b) for engineering bedrock Vs30=760 m/s (blue points), and for the cell-specific Vs30 values (Figure 73a,b). These Sa[0.3s] values (blue and red points) correspond to the "cells" of Alexandroupoli city depicted in Figure 103c and Figure 103d, respectively (b) The ratio between the Sa[0.3s] of the specific Vs30 values (red points in Figure 104a) over the corresponding ones of engineering bedrockVs30=760 m/s values (blue points in Figure 104a) versus the corresponding Vs30 value of each cell.
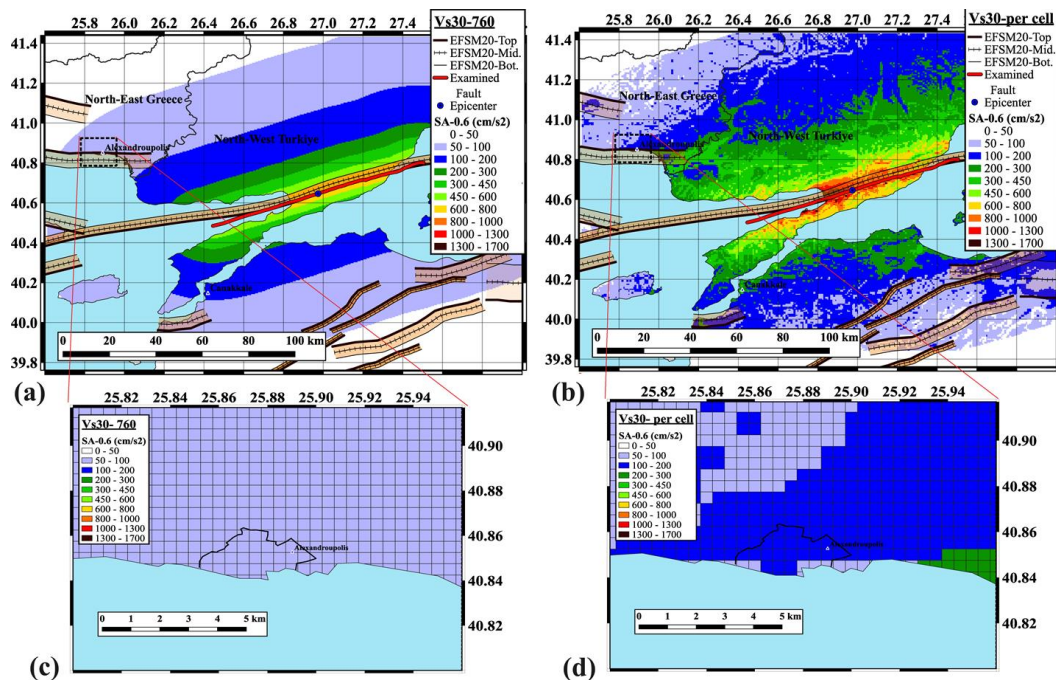

Figure 105. (a) Distribution of Sa[0.6s](in cm/s/s) at each geographic cell (0.005 x 0.005 degrees size), computed by the causative event scenario of the NAF-Ganos fault (in red line), for engineering bedrock (Vs30=760 m/s). The adjacent faults to the NAF-Ganos in the broader Greece-Türkiye CBA provided by the EFSM20, are also depicted. (b) Similar to Figure 105a, but for the cell-specific Vs30 values (Figure 73a,b) (c) The same Sa[0.3s] values presented in Figure 105a, focused on the area very close to the Alexandroupoli pilot

site, as it is extended within the black line (d) Similar to Figure 105c but including the Sa[0.6s] values of Figure 105b.


Figure 106. (a) Sa[0.6s] (in cm/s/s) computed by the REDAS software, for the scenario event of NAF-Ganos (Table 7, Appendix D, Figure 105a,b) for engineering bedrock Vs30=760 m/s (blue points), and for the cell-specific Vs30 values (Figure 73a,b). These Sa[0.6s] values (blue and red points) correspond to the "cells" of Alexandroupoli city depicted in Figure 105c and Figure 105d, respectively (b) The ratio between the Sa[0.6s] of the specific Vs30 values (red points in Figure 106a) over the corresponding ones of engineering bedrockVs30=760 m/s values (blue points in Figure 106a) versus the corresponding Vs30 value of each cell.
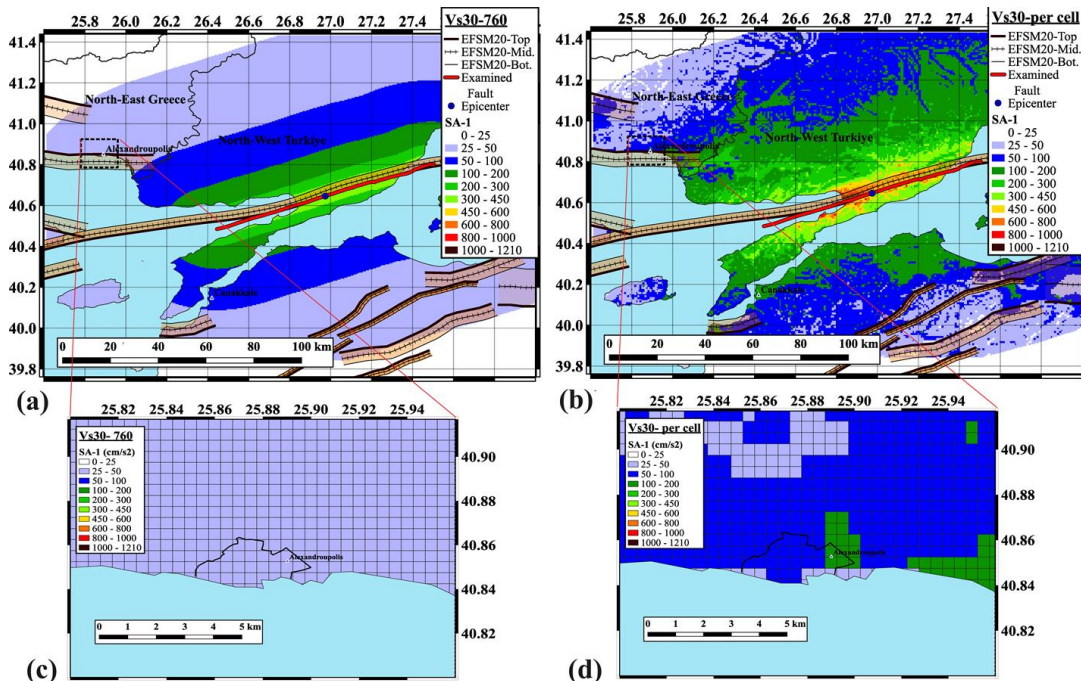
Figure 107. (a) Distribution of Sa[1.0s] (in cm/s/s) at each geographic cell (0.005 x 0.005 degrees size), computed by the causative event scenario of the NAF-Ganos fault (in red line), for engineering bedrock (Vs30=760 m/s). The adjacent faults to the NAF-Ganos in the broader Greece-Türkiye CBA provided by the EFSM20, are also depicted. (b) Similar to Figure 107a, but for the cell-specific Vs30 values (Figure 73a,b). (c) The same Sa[1.0s]

values presented in Figure 107a, focused on the area very close to the Alexandroupoli pilot site, as it is extended within the black line (d) Similar to Figure 107c but including the Sa[0.6s] values of Figure 107b.
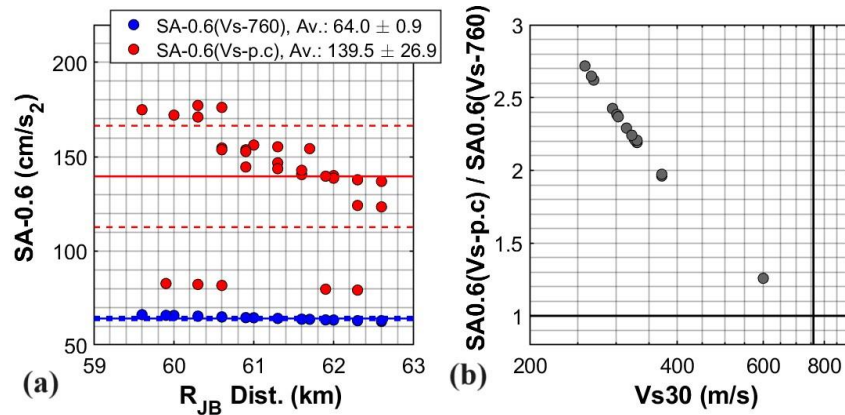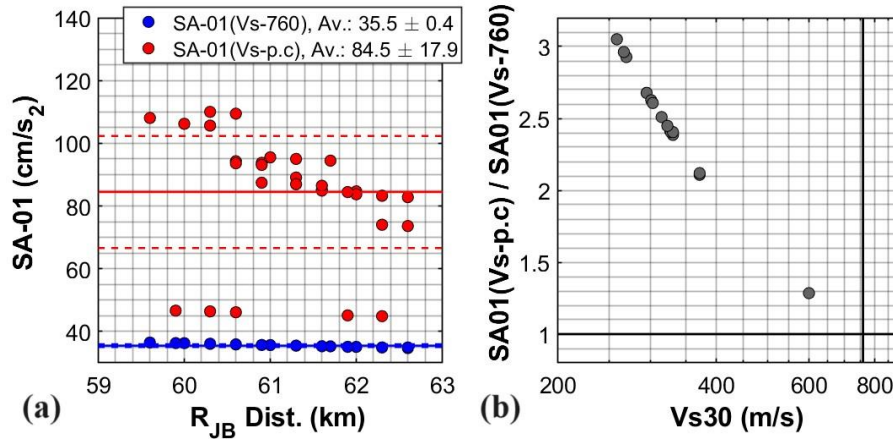

Figure 108. (a) Sa[1.0s] (in cm/s/s) computed by the REDAS software, for the scenario event of NAF-Ganos (Table 7, Appendix D, Figure 107a,b) for engineering bedrock Vs30=760 m/s (blue points), and for the cell-specific Vs30 values (Figure 73a,b). These Sa[1.0s] values (blue and red points) correspond to the "cells" of Alexandroupoli city depicted in Figure 107c and Figure 107d, respectively (b) The ratio between the Sa[1.0s] of the specific Vs30 values (red points in Figure 108a) over the corresponding ones of engineering bedrockVs30=760 m/s values (blue points in Figure 108a) versus the corresponding Vs30 value of each cell.

4.5 The pilot site Canakkale (scenario of the NAF-Ganos fault)

Çanakkale is a province in the Marmara Region, located in the northwest of Türkiye, on the Gallipoli Peninsula and the Biga Peninsula, which is an extension of Anatolia, between 25º-35º and 27º-45º Eastern Longitudes and 39º-30º and 40º-42º Northern Latitudes. Its coastline length is 671 km and its total surface area is 9,817 km2, and it ranks 30th in Turkey in terms of surface area is taking.

The territory of Çanakkale Province has a rugged structure, which is generally formed by the division of areas covered with mountains and hills by valleys. The highest mountain of the province is Kazdağı (1767 m.), located on the border of Balıkesir, and other elevations are located around this mountain. 500 - 1000 m extending in the North-East and South-West directions in the Biga region. The elevations between create a wavy appearance. The north of Edremit Bay is where the highest of these mountains and hills are located.

The high mountainous areas, which are widely spread in the SW of the Biga Peninsula, were generally shaped by pre-Neogene basement rock assemblages and Neogene aged volcanism. The most common geomorphological unit in the Çanakkale region is structurally controlled plateaus, which can be found at various elevation levels and have a stepped appearance in some parts due to erosion surfaces of different ages. The plateaus, which generally developed on Neogene aged rock communities, were deeply incised and disintegrated by streams.

Alluvial plains and valley floors outside the Dardanelles region generally extend in the NE-SW direction in accordance with the tectonic controlled main orographic structure of the region. The alluvial fill plains outside the coastal plains and deltas generally correspond to valley floors.

Erosion processes are effective on plateaus and mountainous areas. In these areas, slope erosion is effective in areas where splitting is high, rock types that are not resistant to abrasion surface, and the slope is high. Superficial erosion caused by surface flooding is observed on low-slope plateaus and glacier surfaces.

Within the borders of Çanakkale province, there are Saroz-Gaziköy Fault, Anafarta Faults, Etili Fault, Çan-Biga Fault Zone, Sarıköy Fault, Yenice-Gönen Fault, Akşam Fault, Pazarköy Fault and Edremit Fault. The activity of these faults has been proven by earthquakes and instrumental data.

Following the 5.5 magnitude earthquake event that occurred in Ayvacık District of Çanakkale Province on 06.02.2017, 1071 buildings were classified as severely damaged and 575 people were accepted as affected. Following the 5.3 magnitude earthquake disaster in Ayvacık District on 20.02.2019, 149 buildings were classified as severely damaged and 30 people were considered as affected.

Earthquakes affected Çanakkale province since 1900 (instrumental period) until today are briefly explained below:

- Saroz-Gaziköy (09.08.1912): This earthquake centered in Şarköy-Mürefte has a magnitude of 7.3. 850 houses in Mürefte and 1085 houses in Şarköy totally collapsed. A large part of Gallipoli was also destroyed in this earthquake.
- Saroz-Gaziköy (10.08.1912): This earthquake centered in Şarköy-Mürefte has a magnitude of 6.3. It was at a depth of 15 km, centered at Latitude: 40.6, Longitude: 27.10.
- Çan (13.09.1912): This earthquake, which occurred on the Çan-Lapseki district border, had a magnitude of 6.9.
- Ayvalÿk (18.11.1919): This earthquake centered in Ayvalık has a magnitude of 7.0
- Çanakkale-Truva (02.05.1928): This earthquake centered in the Aegean Sea off the coast of Troy has a magnitude of 6.0.
- Biga-Karabiga (04.01.1935): This earthquake, which occurred off the coast of Karabiga in the Sea of Marmara, had a magnitude of 6.4.
- Edremit Bay (06.10.1944): This earthquake, which occurred in the Edremit Bay off the coast of Altÿnoluk, had a magnitude of 6.8.
- Yenice (18.03.1953): This earthquake centered in Yenice has a magnitude of 7.2. As a result of this earthquake. It was determined that damage and destruction occurred in an area of 30000 km^2. More than 8000 buildings were destroyed or severely damaged. 211 schools, 176 official buildings, 27 mosques were destroyed, and a total of 250 people lost their lives.
- Gulf of Saros (27.03.1975): This earthquake, which occurred in the Gulf of Saros, had a magnitude of 5.7. 17 damaged buildings in Ilgarlı village and 30 houses in Pazarlı were destroyed. In Yeniköy, 50 houses suffered severe damage and 87 houses received moderate damage. 7 houses in Ocaklı village have become uninhabitable. The mosque and 75 houses in Güneyli Village have become uninhabitable.
- Aegean Sea Earthquake Off Gökçeada: An earthquake occurred off Gökçeada (Aegean Sea) on May 24, 2014. According to the data received from AFAD Türkiye Earthquake Data Center (TDVM), the magnitude of the earthquake was calculated as 6.5. The duration of the earthquake was 42 seconds. It was measured as . After the earthquake in question, 405 aftershocks with magnitudes ranging from 1.1 to 5.3 occurred in the first 48 hours.
- Ayvacık Earthquake: According to the data received from AFAD Turkey Earthquake Data Center (TDVM) on February 6, 2017, a 5.3 magnitude earthquake occurred with the epicenter in Ayvacık. 1071 buildings were severely damaged.
- Ayvacık Earthquake: According to the data received from AFAD Turkey Earthquake Data Center (TDVM) on February 20, 2019, a 5.0 magnitude earthquake occurred with the epicenter in Ayvacık.

In this study, a scenario earthquake event affecting the Çanakkale province has been considered. The Ganos and Saros segments of the North Anatolian Fault (NAF) have been considered in the scenario event. The maximum magnitude of 7.4 earthquake has been considered with the rupture of two above segments with the 132km rupture length.

Results for the pilot site Canakkale

The REDAS hazard module harmonized CBA Ground Motion Models (Papatheodorou et al. 2024, Theodoulidis et al. 2024) were used in the DSHA.

The analysis results have been shared in the below from Figure 39 to Figure 48 in PGA, PGV and Sa distributions in the periods of 0.3s, 0.6s and 1.0s and related graphs.
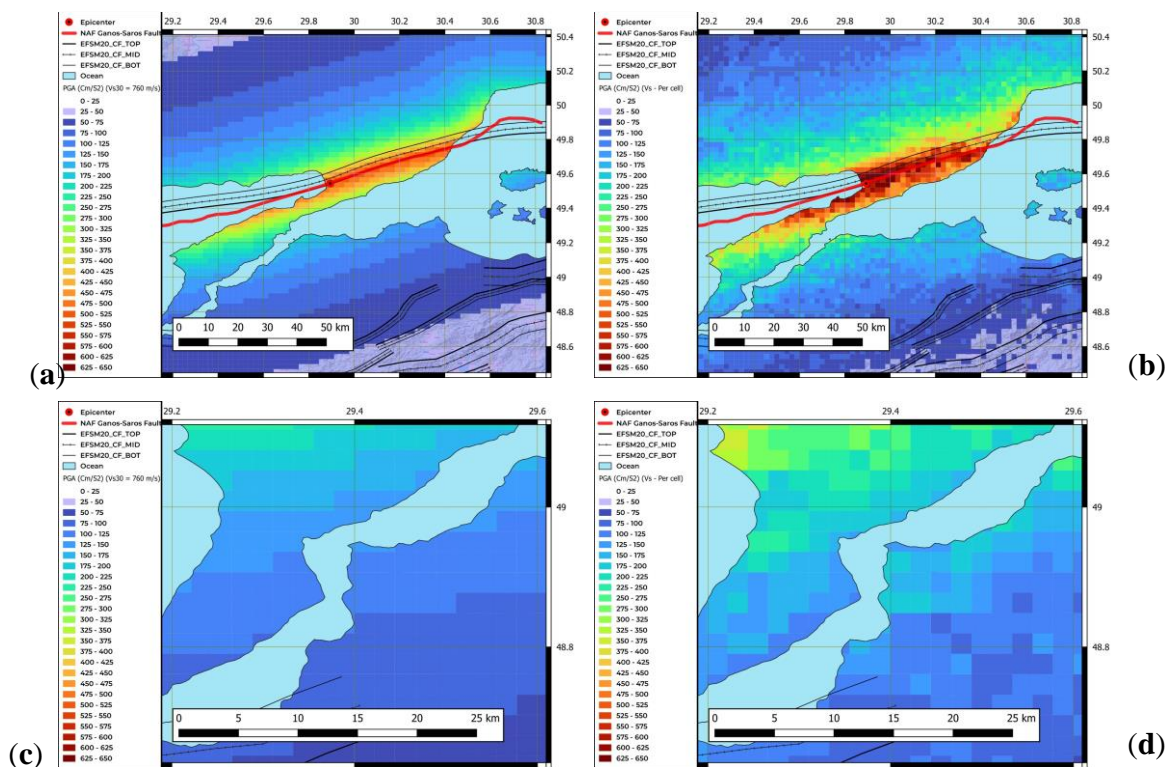
Figure 109. (a) Distribution of PGA(in cm/s/s) at each geographic cell (0.005 x 0.005, degrees size), computed by the causative event scenario of the NAF-Ganos fault (in red line), for engineering bedrock (Vs30 = 760 m/s). The adjacent faults to the NAF-Ganos fault in the broader Greece-Türkiye CBA provided by the EFSM20, are also depicted. **(b)** Similar

to

(a) (b) (c) (d)

Figure 109a, but for specific Vs30 values of each site specific "cell" (Figure 73a,c) (c) The same PGA values presented in

(a) (b) (c) (d)

Figure 109a, focused on the area very close to the Canakkale pilot site, as it is extended within the black line. The cells included (at least their ~25%) into the examined site, are

numbered. (d) Similar to

Figure 109c but including the PGA values of

Figure 109b.

(a)

(b)

Figure 110. (a) PGA (in cm/s/s) computed by the REDAS software, for the scenario event of NAF-Ganos (Table 7, Appendix D,

(a)

(b)

(c)

(d)
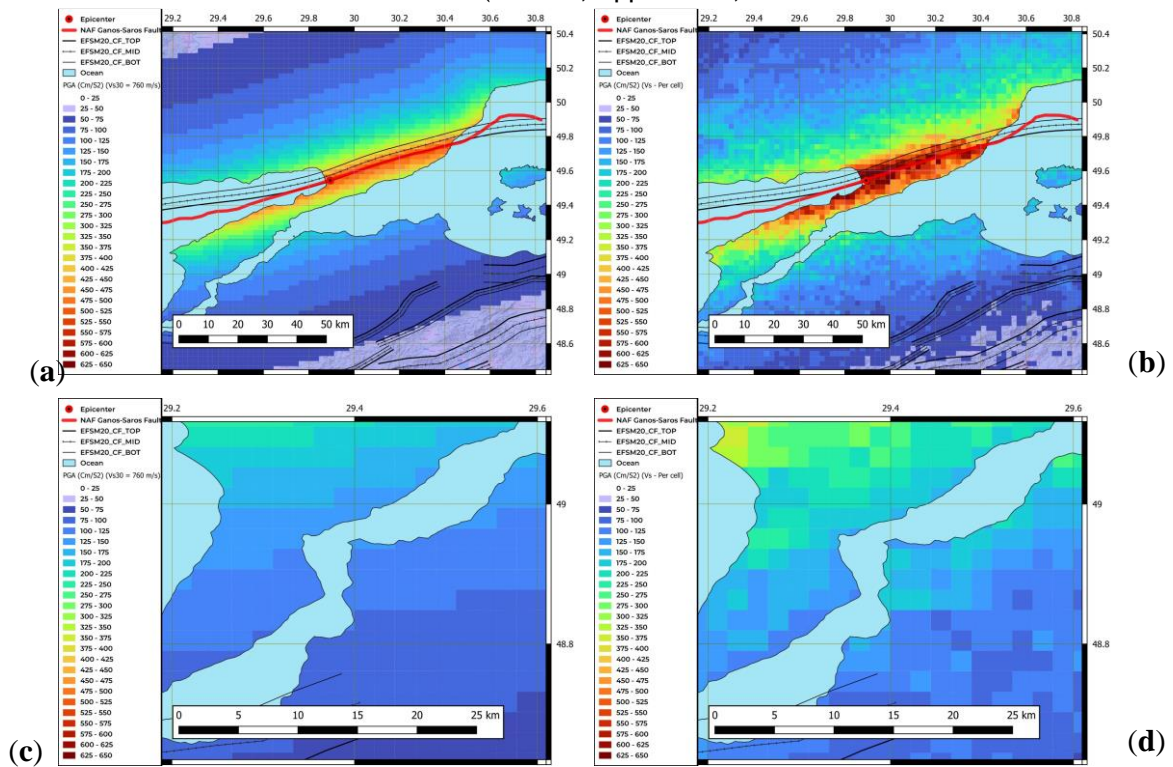
Figure 109a,b) for engineering bedrock Vs30=760 m/s (blue points), and for the specific Vs30 values (Figure 73a,b). These PGA values (blue and red points) correspond to the

"cells" of Canakkale city depicted in

Figure 109c and

Figure 109d, respectively (b) The ratio between the PGAs, of the specific Vs30 values (red points in

(a)   (b)

Figure 110a) over the corresponding ones of engineering bedrockVs30=760 m/s values (blue points in

(a)   (b)

Figure 110a) versus the corresponding Vs30 value of each cell.

(a)   (b)

(c)   (d)

Figure 111. (a) Distribution of PGV (in cm/s) at each geographic cell (0.005 x 0.005, degrees size), computed by the causative event scenario of the NAF-Ganos fault (in red

line), for engineering bedrock (Vs30 = 760 m/s). The adjacent faults to the NAF-Ganos fault in the broader Greece-Türkiye CBA provided by th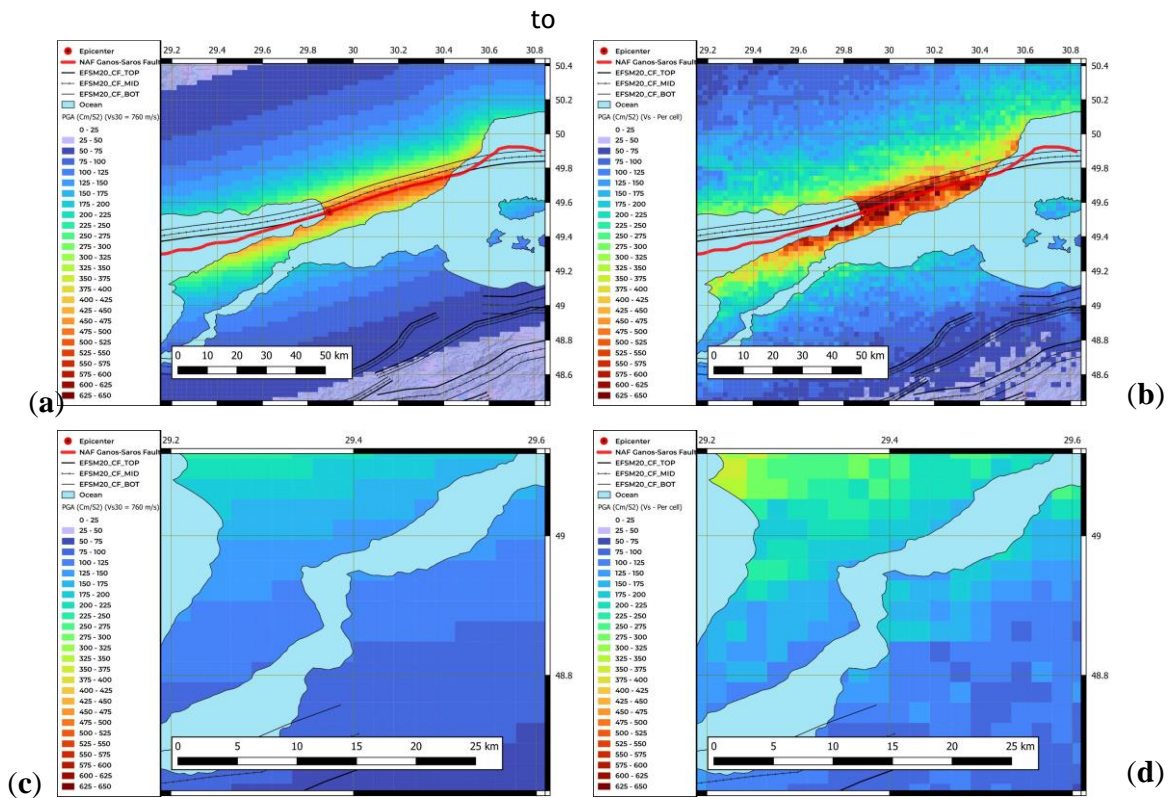e EFSM20, are also depicted. (b) Similar to Figure 111a, but for specific Vs30 values of each site specific "cell" (Figu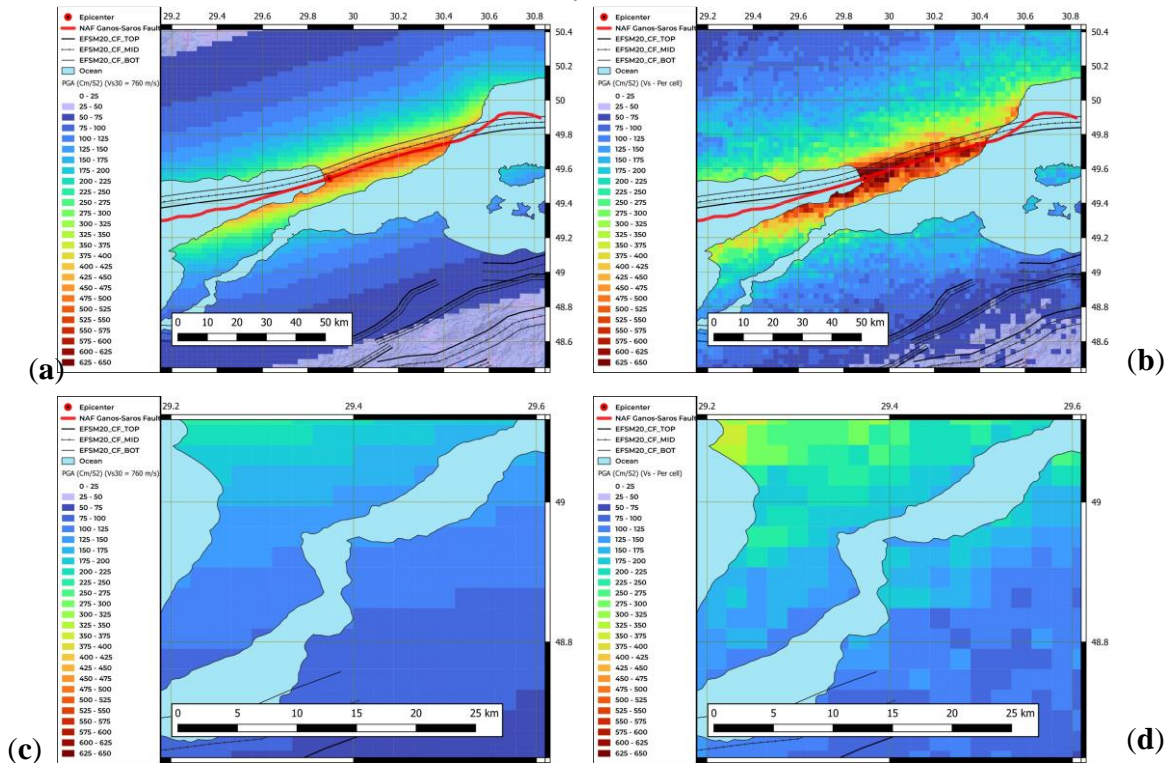re 73a,c) (c) The same PGV values presented in Figure 111a, focused on the area very close to the Canakkale pilot site, as it is extended within the black line. The cells included (at least their ~25%) into the examined site, are numbered. (d) Similar to Figure 111c but including the PGV values of Figure 111b.
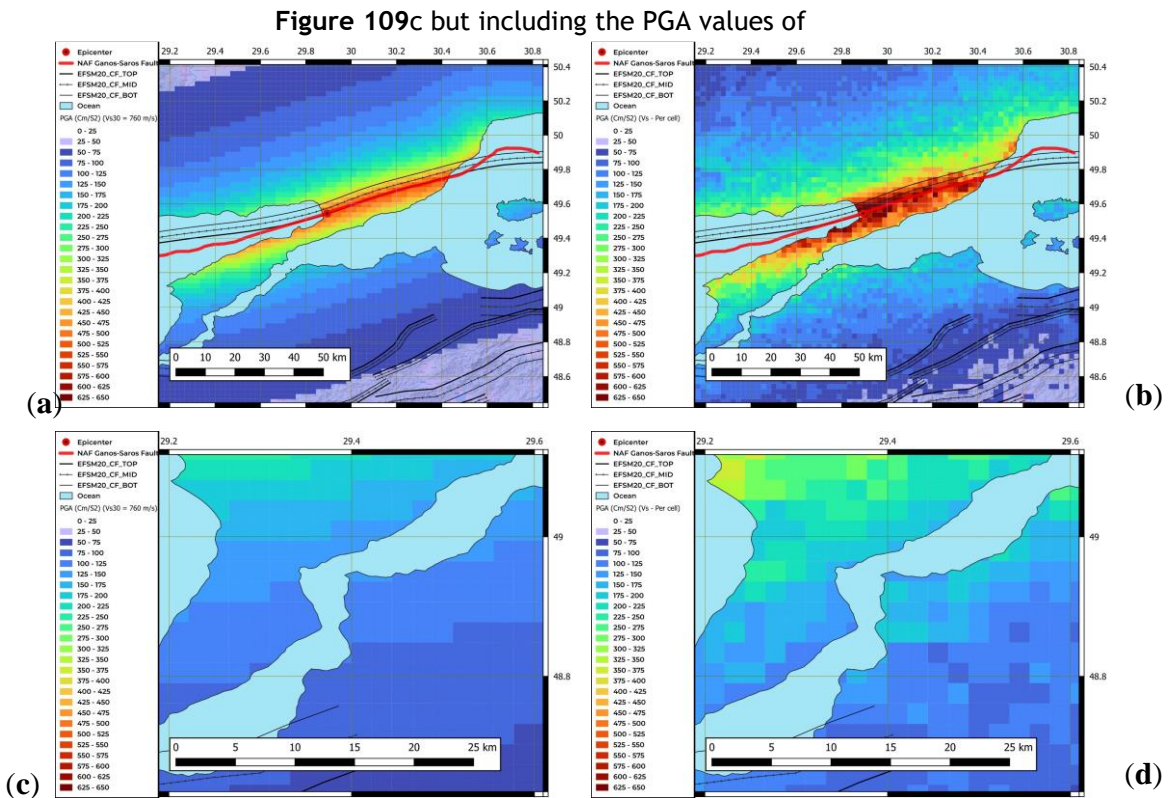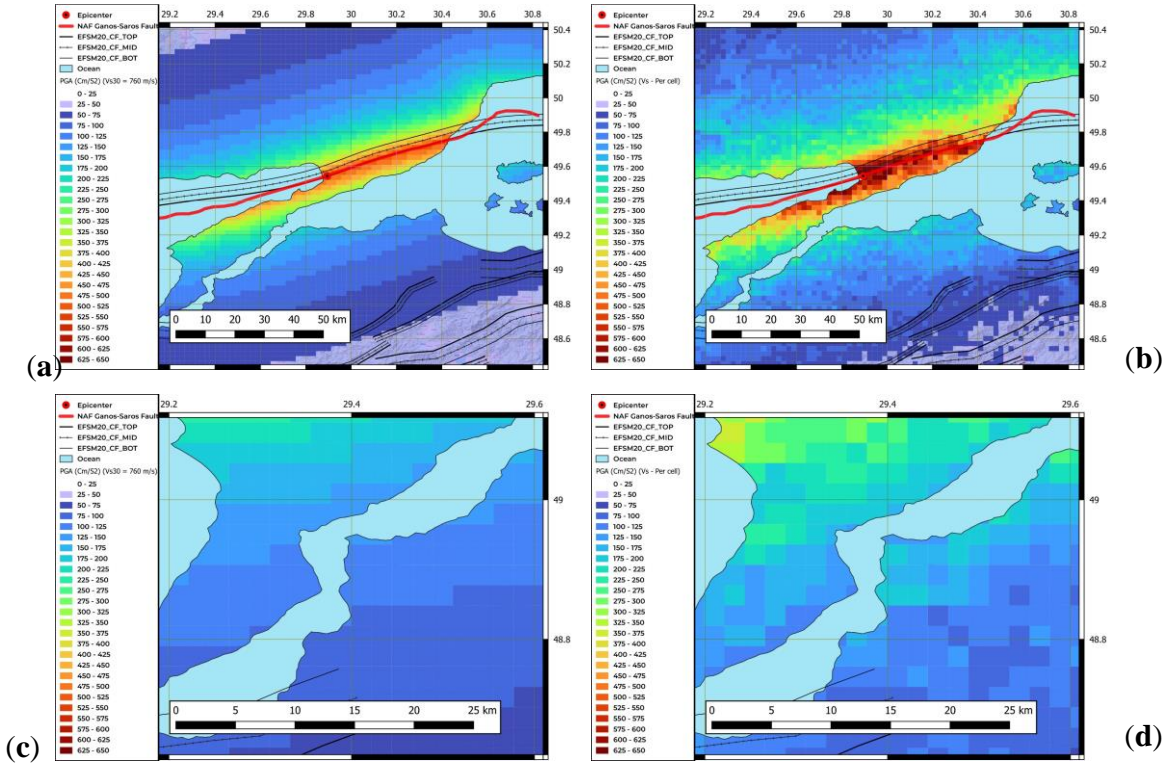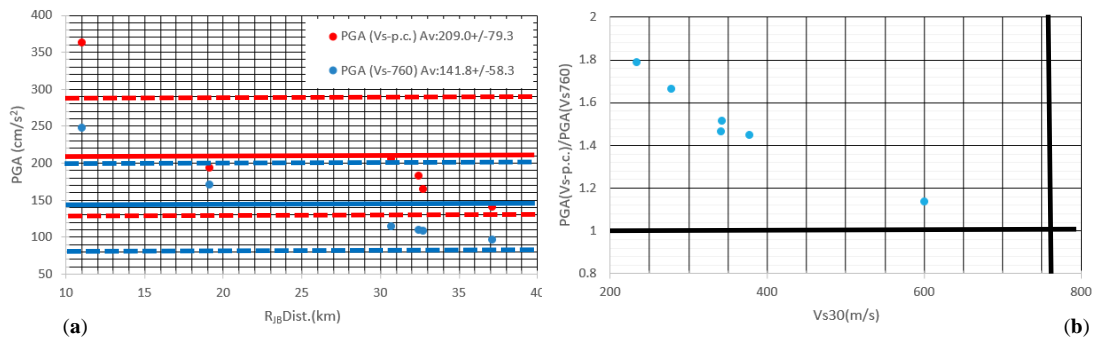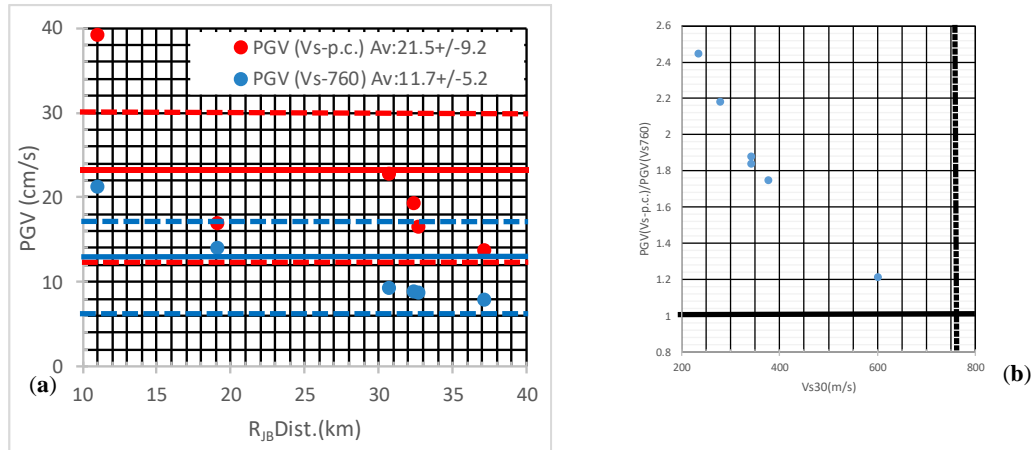

Figure 112. (a) PGV (in cm/s) computed by the REDAS software, for the scenario event of NAF-Ganos (Table 7, Appendix D, Figure 111a,b) for engineering bedrock Vs30=760 m/s (blue points), and for the specific Vs30 values (Figure 73a,b). These PGV values (blue and red points) correspond to the "cells" of Canakkale city depicted in Figure 111c and Figure 111d, respectively (b) The ratio between the PGVs, of the specific Vs30 values (red points in Figure 112a) over the corresponding ones of engineering bedrockVs30=760 m/s values (blue points in Figure 112a) versus the corresponding Vs30 value of each cell.

Figure 113. (a) Distribution of SA[0.3 s] (in cm/s/s) at each geographic cell (0.005 x 0.005, degrees size), computed by the causative event scenario of the NAF-Ganos fault (in red

line), for engineering bedrock (Vs30 = 760 m/s). The adjacent faults to the NAF-Ganos fault in the broader Greece-Türkiye CBA provided by the EFSM20, are also depicted. (b) Similar to Figure 113a, but for specific Vs30 values of each site specific "cell" (Figure 73a,c) (c) The same SA[0.1 s] values presented in Figure 113a, focused on the area very close to the Canakkale pilot site, as it is extended within the black line. The cells included (at least their ~25%) into the examined site, are numbered. (d) Similar to Figure 113c but including the SA[0.1 s] values of Figure 113b.

**Figure 114. (**a) SA[0.3 s] (in cm/s/s) computed by the REDAS software, for the scenario event of NAF-Ganos (Table 7, Appendix D, Figure 113a,b) for engineering bedrock Vs30=760 m/s (blue points), and for the specific Vs30 values (Figure 73a,b). These SA[0.1 s] values (blue and red points) correspond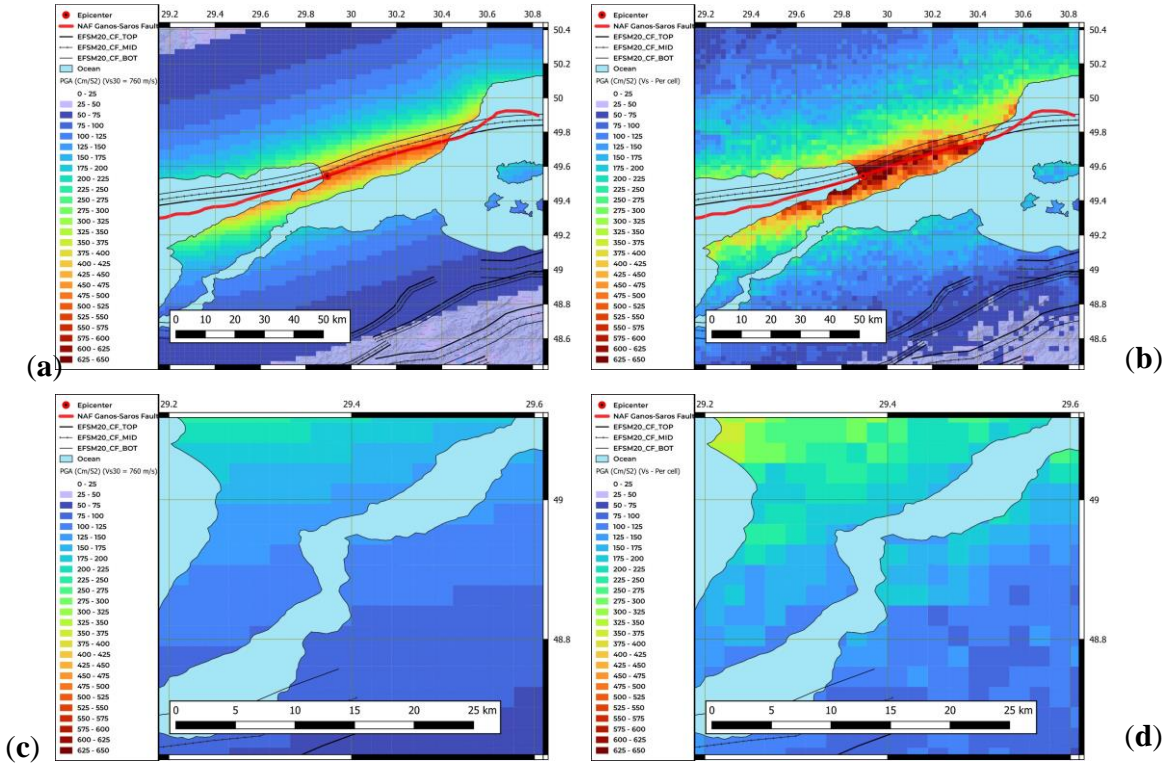 to the "cells" of Canakkale c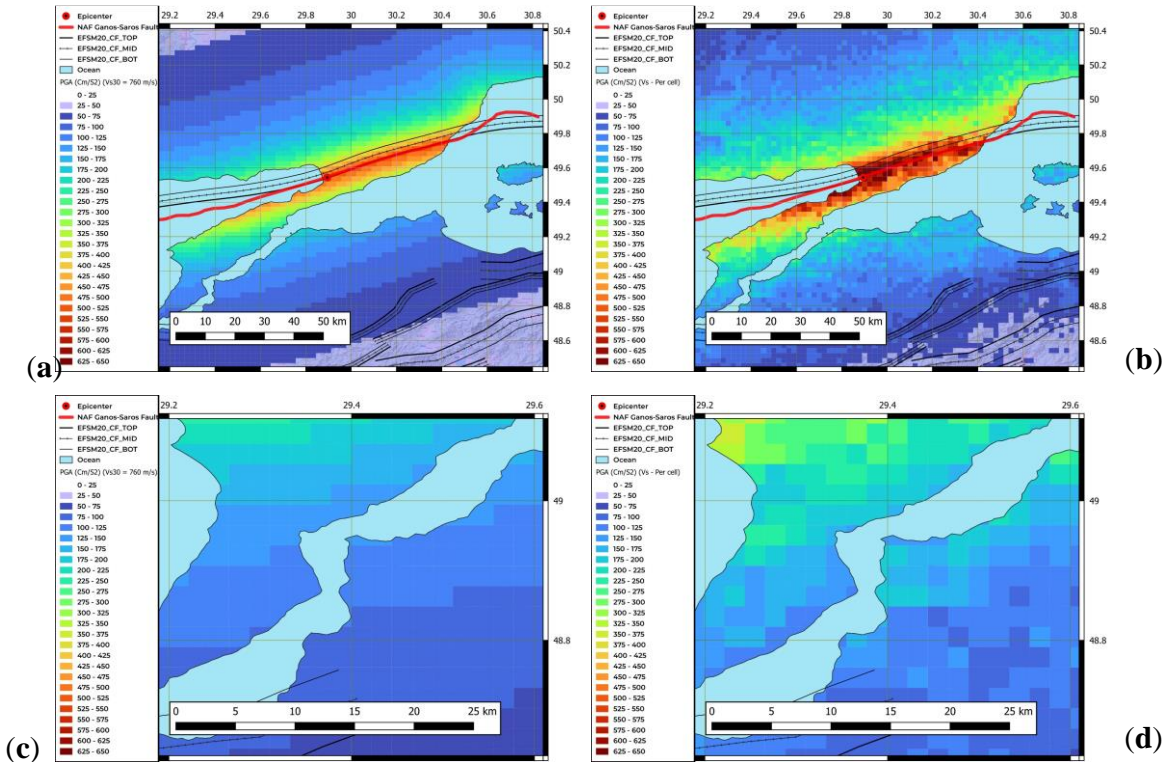ity depicted in Figure 113c and Figure 113d, respectively (b) The ratio between the SA[0.1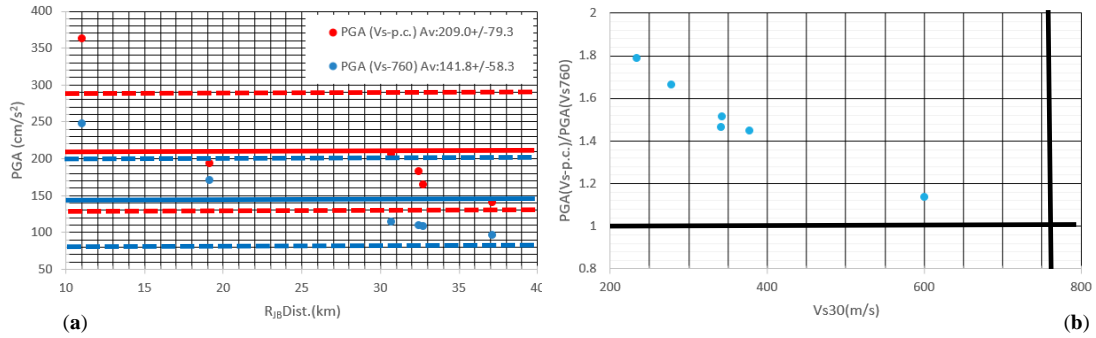 s], of the specific Vs30 values (red points in Figure 114a) over the corresponding ones of engineering bedrockVs30=760 m/s values (blue points in Figure 114a) versus the corresponding Vs30 value of each cell.
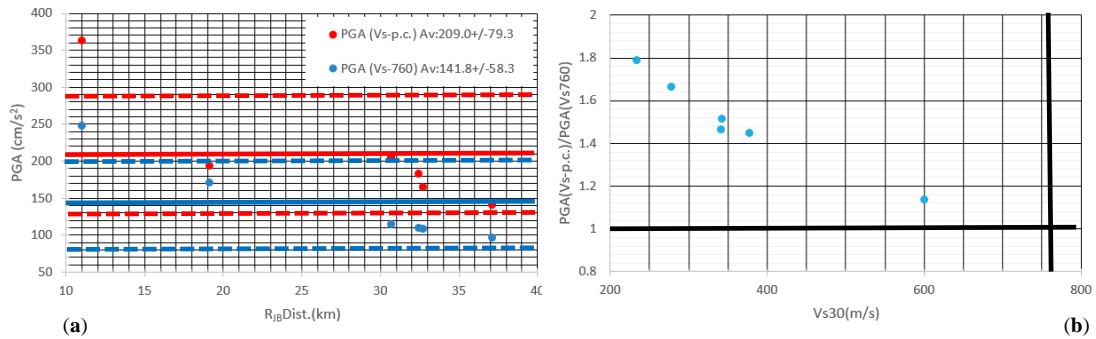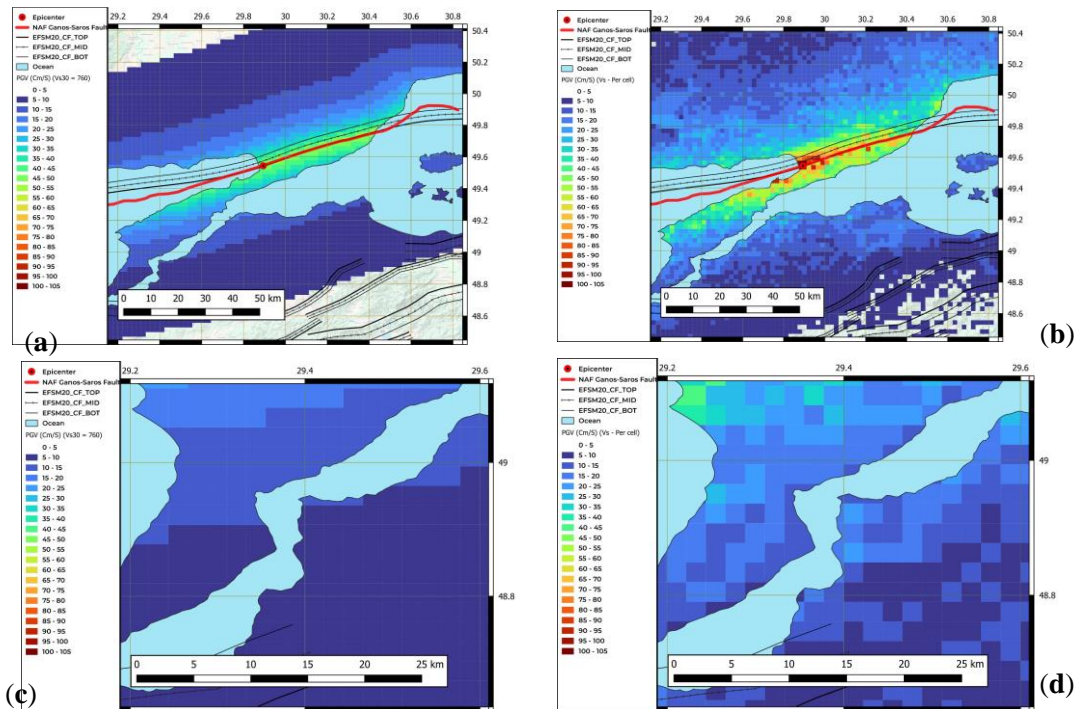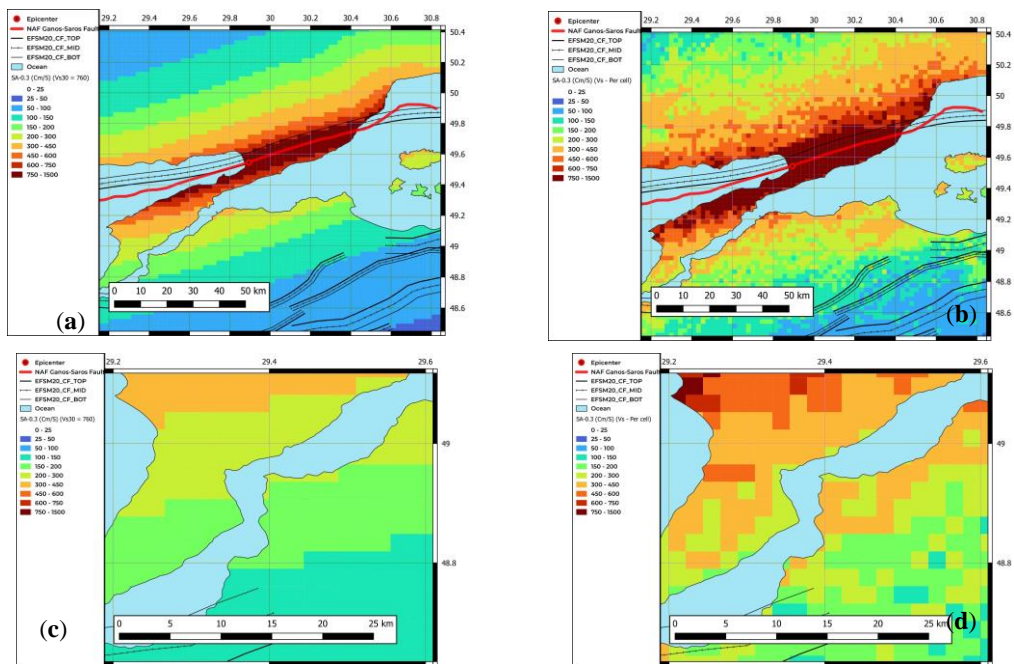

Figure 115. (a) Distribution of SA[0.6 s] (in cm/s/s) at each geographic cell (0.005 x 0.005, degrees size), computed by the causative event scenario of the NAF-Ganos fault (in red

line), for engineering bedrock (Vs30 = 760 m/s). The adjacent faults to the NAF-Ganos fault in the broader Greece-Türkiye CBA provided by the EFSM20, are also depicted. (b) Similar to Figure 115a, but for specific Vs30 values of each site specific "cell" (Figure 73a,c) (c) The same SA[0.6 s] values presented in Figure 115a, focused on the area very close to the Canakkale pilot site, as it is extended within the black line. The cells included (at least their ~25%) into the examined site, are numbered. (d) Similar to Figure 115c but including the SA[0.6 s] values of Figure 115b.
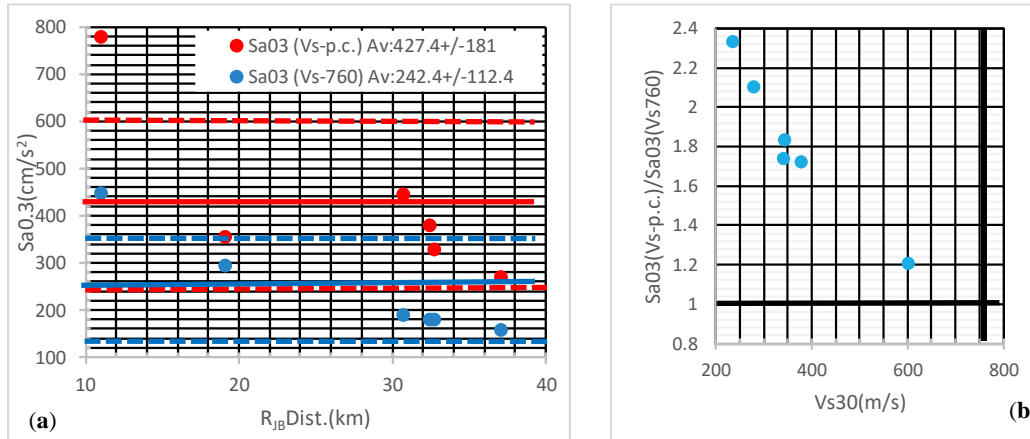

(a)

(b)

Figure 116. (a) SA[0.6 s] (in cm/s/s) computed by the REDAS software, for the scenario event of NAF-Ganos (Table 7, Appendix D, Figure 115a,b) for engineering bedrock Vs30=760 m/s (blue points), and for the specific Vs30 values (Figure 73a,b). These SA[0.6 s] values (blue and red points) correspond to the "cells" of Canakkale city depicted in Figure 115c and Figure 115d, respectively (b) The ratio between the SA[0.6 s], of the specific Vs30 values (red points in

(a)

(b)
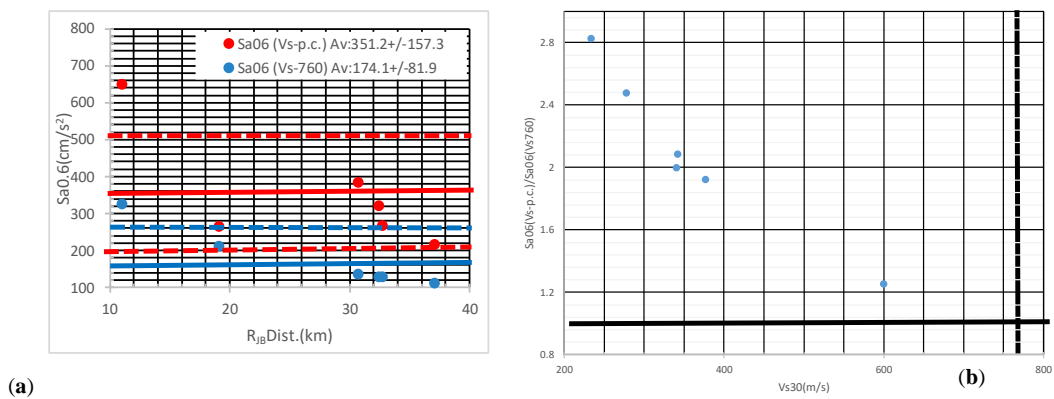
Figure 116a) over the corresponding ones of engineering bedrockVs30=760 m/s values (blue points in
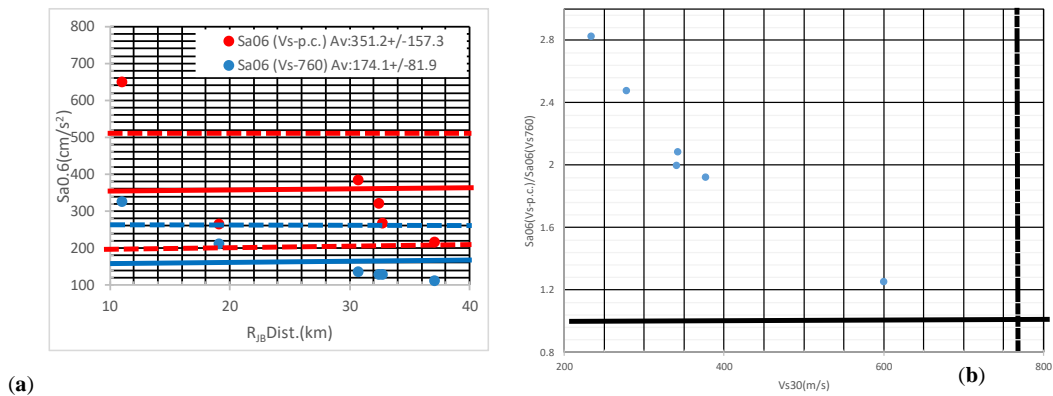
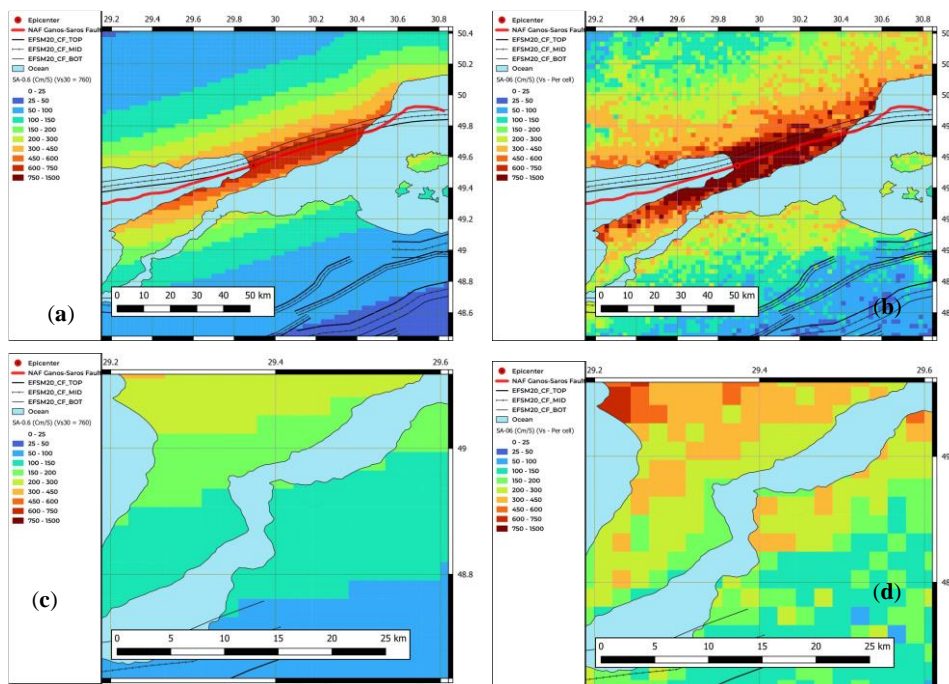**Figure 116**a) versus the corresponding Vs30 value of each cell.
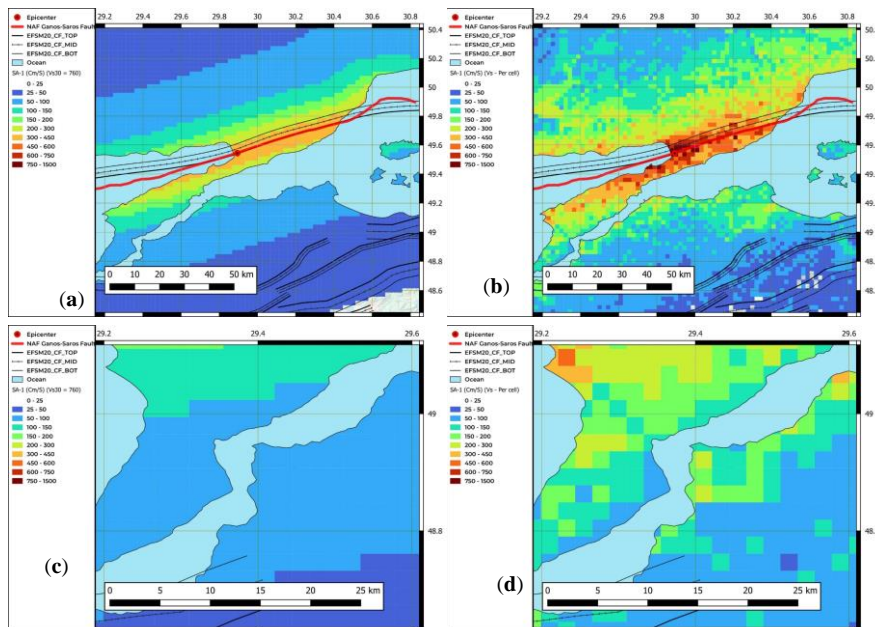
Figure 117. (a) Distribution of SA[1 s] (in cm/s/s) at each geographic cell (0.005 x 0.005, degrees size), computed by the causative event scenario of the NAF-Ganos fault (in red line), for engineering bedrock (Vs30 = 760 m/s). The adjacent faults to the NAF-Ganos fault in the broader Greece-Türkiye CBA provided by the EFSM20, are also depicted. (b) Similar to Figure 117a, but for specific Vs30 values of each site specific "cell" (Figure 73a,c) (c) The same SA[1 s] values presented in Figure 117a, focused on the area very close to the Canakkale pilot site, as it is extended within the black line. The cells included (at least their ~25%) into the examined site, are numbered. (d) Similar to Figure 117c but including the SA[1 s] values of Figure 117b.
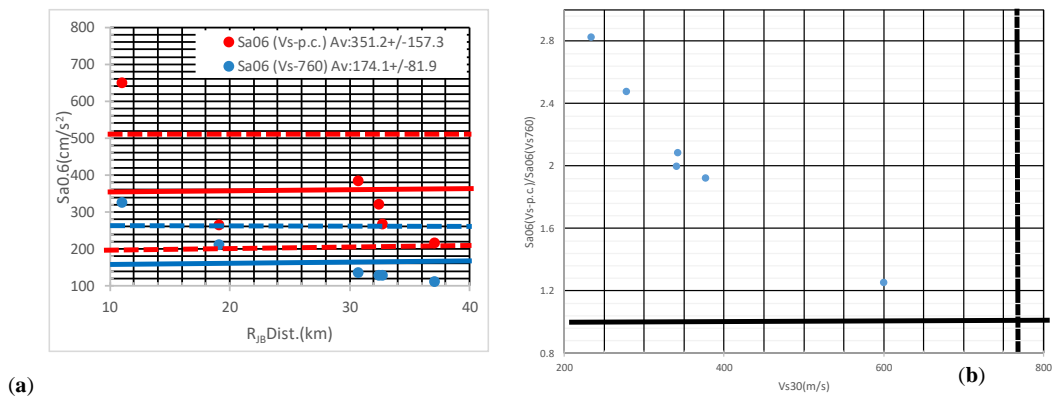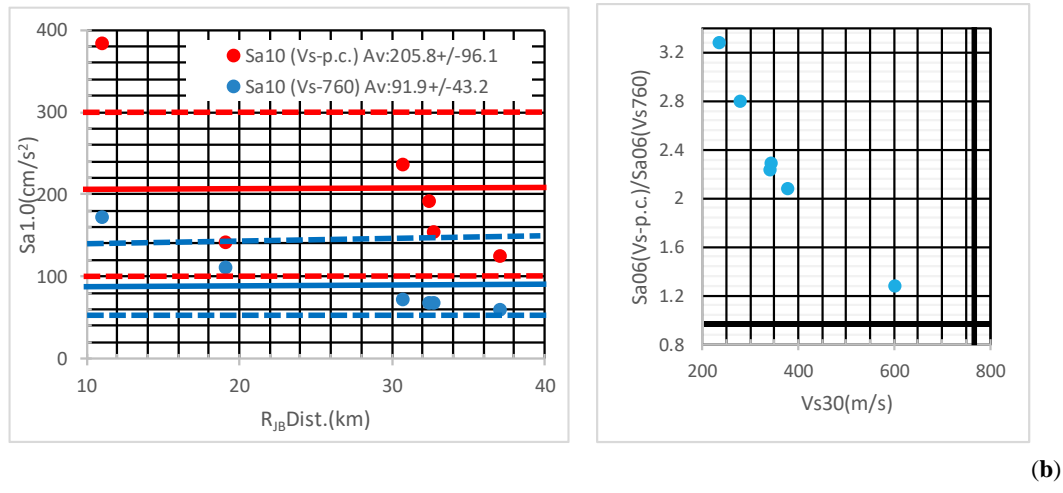
Figure 118. (a) SA[1 s] (in cm/s/s) computed by the REDAS software, for the scenario event of NAF-Ganos (Table 7, Appendix D, Figure 117a,b) for engineering bedrock Vs30=760 m/s (blue points), and for the specific Vs30 values (Figure 73a,b). These SA[1 s] values (blue and red points) correspond to the "cells" of Canakkale city depicted in Figure 117c and Figure 117d, respectively (b) The ratio between the SA[1 s], of the specific Vs30 values (red points in Figure 118a) over the corresponding ones of engineering bedrockVs30=760 m/s values (blue points in Figure 118a) versus the corresponding Vs30 value of each cell.

4.6   The pilot site Izmir (scenario of the Izmir fault)

Located in the Aegean Region, Izmir province is located around the Gulf of Izmir in the west of the Anatolian Peninsula, surrounded by the Aegean Sea in the west, Balıkesir Province in the north, Manisa Province in the east and Aydın Province in the south. It is located between the northern latitudes of 37°45' and 39°15' and between the eastern longitudes of 26°15' and 28°20'. It is a port city with altitude of 2 m. There are 30 districts and 1295 neighborhoods throughout the province.

The North-South length of the province is approximately 200.00 km, and the East-West width is 180.00 km. The coastline length is 629 km. With its surface area of 11,922.207 km2, Izmir ranks 3rd among 8 provinces in the Aegean Region and 23rd among 81 provinces in Turkey.

Additionally, it ranks 3rd in Türkiye after Istanbul and Ankara with a population of 4,394,694 people (TUIK, 2020). Population density (number of people per square kilometer) is 366 people/km^2, ranking 1st in the Aegean Region and 3rd in Turkey.

Izmir metropolitan is surrounded by the slopes of Aydın Mountains, Kıran Mountain, Bozdağlar, Akdağ, Yamanlar Mountain, Teke Mountain, Nif Mountain, Yunt Mountain and Madra Mountain, from south to north. Between the Aydın Mountains and Bozdağlar, the Küçük Menderes Plain, known as the Küçük Menderes Graben, is located. Küçük Menderes Plain starts almost from the Beydağ settlement area in the east, approximately 10-15 km away. It extends in width to Torbalı and Selçuk. Metamorphic rocks, especially schist,

phyllite, marble, and sedimentary units such as sandstone, mudstone and limestone crop out in the area (Konak, 2002).

Bornova Plain was formed in the east of the gulf by the alluviums brought by the streams descending from the nearby slopes and the alluviums carried by the drainage area filling the sea, and Kemalpaşa Plain is located in the east. Between the Bornova Plain and the Kemalpaşa Plain is the Belkahve Pass, whose height reaches up to 250 m.

Rock communities belonging to both the Palaeotectonic and Neotectonic periods are exposed within the borders of Izmir Province. In particular, the metamorphic rocks of the Menderes Massif, which formed the pre-Miocene foundation of the basins, cover large areas around Kiraz-Ödemiş-Tire-Torbalı.

The Yuntdağı uplift, which crops out between Soma and Bayraklı, is a Miocene aged volcanic mountain extending in the NE-SW direction. The Yuntdağı volcanics, which are located along large-scale fault zones that developed in the NE-SW direction during the Miocene period, contain outlet centers that cut the Late Cretaceous-Paleocene aged Bornova Flysch Zone (Bornova Complex) rocks (Sözbilir et al., 2003; Uzel and Sözbilir, 2008; Özkaymak et al., 2008).

Izmir Province and its immediate surroundings correspond to a back-arc area expanding in the NS direction. The subduction of the African plate under the Aegean microplate and the movement of the Anatolian microplate towards W-SW along the North Anatolian Fault Zone enable regional deformation to take shape. As a result, in addition to the 21 faults within Izmir Province that have the potential to produce earthquakes of 6.0-7.2 magnitude, there are also many active faults under the Aegean Sea, which borders the province from the west.

Based on geological and seismological data, there are many faults that will affect the province of Izmir. According to the Active Fault Map of Turkey within the borders of Izmir Province, there are a total of 21 faults classified as Holocene Faults/Quaternary Faults (17) and Neotectonic period lineaments (4). These consist of detachment faults that extend between the rock communities of the Miocene period and the basement rocks of the pre-Miocene period, and the normal faults with dip/oblique slip and strike-slip faults that developed after the Miocene.

Strike-slip faults control post-Miocene tectonics on the Izmir-Manisa line. Similarly, normal faults with dip/oblique slip have developed as edge faults limiting the elevations within the Gediz Basin (such as Nif Mountain, Spil Mountain, Çaldağı, Bozdağ, etc.). In addition to 21 faults within Izmir Province that have the potential to produce earthquakes of 6-7.2 magnitude, there are also many active faults under the Aegean Sea, which borders the province from the west. (Özkaymak and Sözbilir, 2008; Sözbilir et al., 2011).

Izmir Province is located in Western Anatolia, one of the most seismically active regions of the world (ÿengör et al., 1985; Taymaz et al., 1991; Seyitoÿlu and Scott, 1991; Pavlides, 1996; Papazachos and Papazachou, 1997; Altunel, 1999; Koçyiÿit et al., 1999; Akyüz and Altunel, 2001; Pavlides and Caputo,

2008; Akyol et al., 2006). Geological and seismological studies carried out to date show that Izmir and the surrounding area is dominated by NE-SW trending strike-slip and NW-SE, NE-SW and EW trending dip/oblique-slip normal faulting. These active structures work together and are responsible for many large earthquakes that occurred in the region in both historical and instrumental periods (Taymaz et al., 1991; Emre et al., 2005; Akyol et al., 2006; Zhu et al., 2006; Aktar et al., 2006; Tan et al., 2008; Özkaymak et al., 2012).

As it is known, in the instrumental period, the 1928 Torbalı earthquake and the 30 October 2020 Samos earthquakes in Izmir Province and its surroundings were important destructive earthquakes that caused loss of life and property. However, in historical earthquake catalogs and some historical records, there is information that the settlements in this region were affected by major earthquakes and major destructions occurred (e.g. Ergin et al., 1967; Shebalin et al., 1974; Soysal et al., 1981; Ambraseys and Finkel, 1995; Ambraseys, 1988 and 2009; Ambraseys and Jackson, 1998; Guidoboni et al., 1994; Papazachos and Papazachou, 1997).

In this study, a scenario earthquake event affecting the Izmir metropolitan province has been considered. The Izmir fault with a length of 38km has been considered in the scenario event. The maximum magnitude of 6.6 earthquake has been considered with the rupture of Izmir fault.

Results for the pilot site Izmir

The REDAS hazard module harmonized CBA Ground Motion Models (Papatheodorou et al. 2024, Theodoulidis et al. 2024) were used in the DSHA for Izmir metropolitan city.

The analysis results have been shared in the below from Figure 49 to Figure 58, in PGA, PGV and Sa distributions in the periods of 0.3s, 0.6s and 1.0s and related graphs.
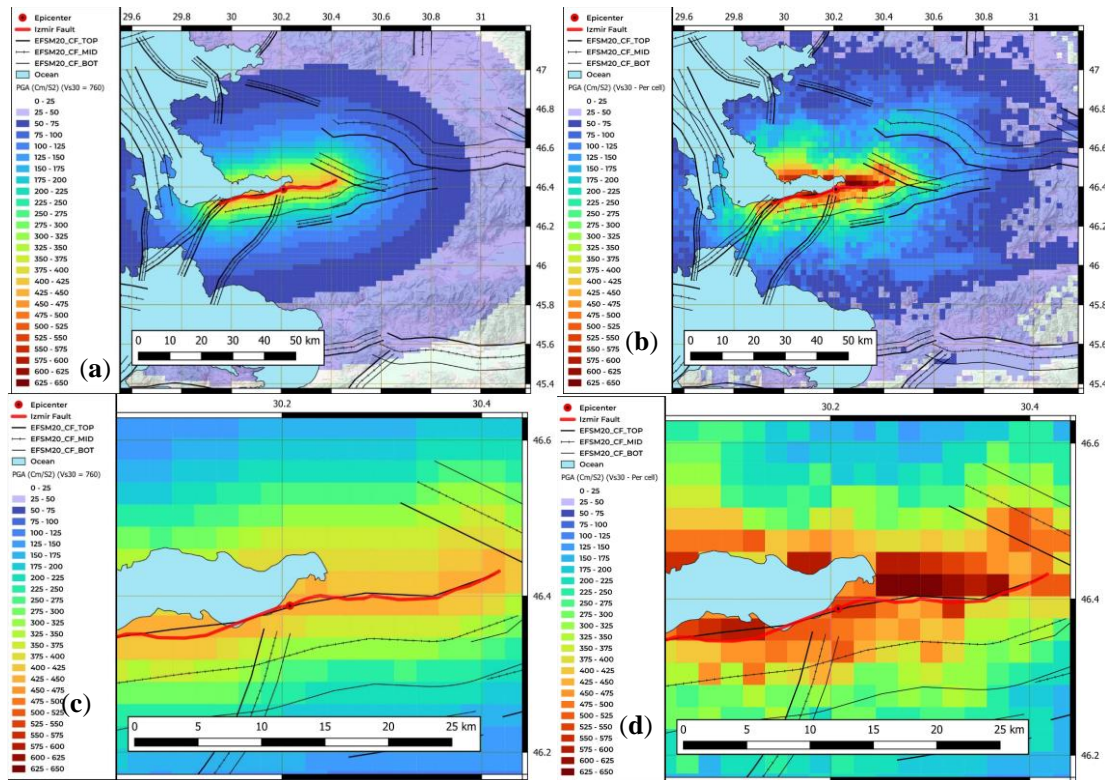
Figure 119. (a) Distribution of PGA(in cm/s/s) at each geographic cell (0.005 x 0.005, degrees size), computed by the causative event scenario of the Izmir-fault (in red line), for engineering bedrock (Vs30 = 760 m/s). The adjacent faults to the Izmir-Ganos fault in the broader Greece-Türkiye CBA provided by the EFSM20, are also depicted. (b) Similar to Figure 119a, but for specific Vs30 values of each site specific "cell" (Figure 72a,b) (c) The same PGA values presented in Figure 119a, focused on the area very close to the Izmir pilot site, as it is extended within the black line. The cells included (at least their ~25%) into the examined site, are numbered. (d) Similar to Figure 119c but including the PGA values of Figure 119b.
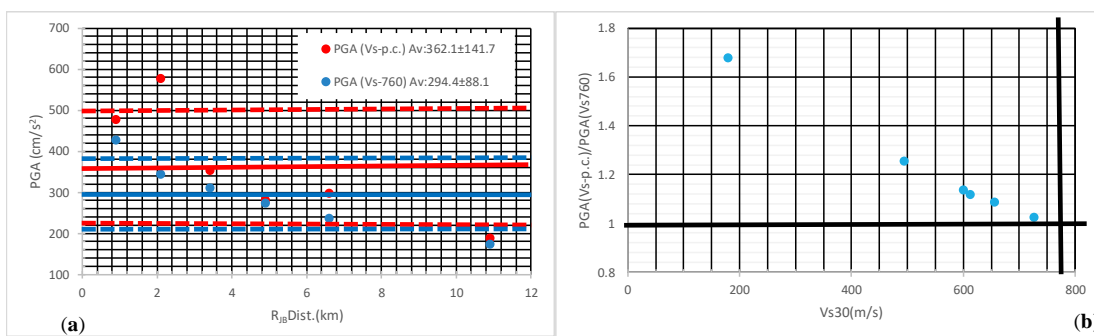
Figure 120. (a) PGA (in cm/s/s) computed by the REDAS software, for the scenario event of Izmir Fault (Table 7, Appendix E, Figure 119a,b) for engineering bedrock Vs30=760 m/s (blue points), and for the specific Vs30 values (Figure 72a,b). These PGA values (blue and red points) correspond to the "cells" of Izmir city depicted in Figure 119c and Figure 119d, respectively (b) The ratio between the PGAs, of the specific Vs30 values (red points in Figure 120a) over the corresponding ones of engineering bedrockVs30=760 m/s values (blue points in Figure 120a) versus the corresponding Vs30 value of each cell.
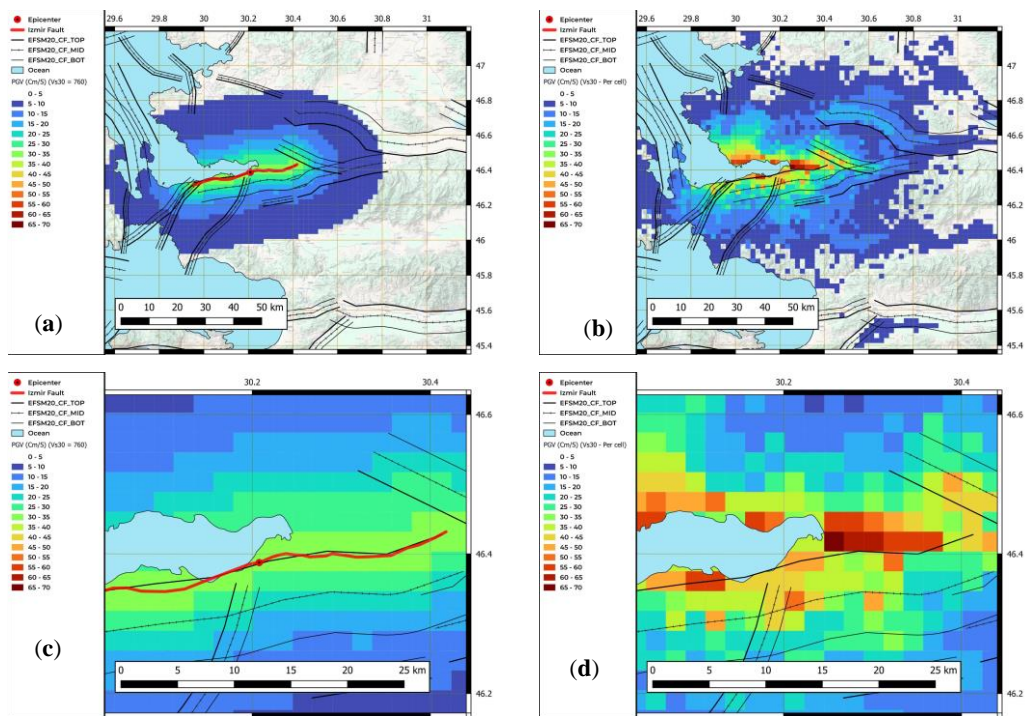
Figure 121. (a) Distribution of PGV (in cm/s) at each geographic cell (0.005 x 0.005, degrees size), computed by the causative event scenario of the Izmir-fault (in red line), for engineering bedrock (Vs30 = 760 m/s). The adjacent faults to the Izmir-fault in the broader Greece-Türkiye CBA provided by the EFSM20, are also depicted. (b) Similar to Figure 121a, but for specific Vs30 values of each site specific "cell" (Figure 72a,b) (c) The same PGV values presented in Figure 121a, focused on the area very close to the Izmir pilot site, as it is extended within the black line. The cells included (at least their ~25%) into the examined site, are numbered. (d) Similar to Figure 121c but including the PGV values of Figure 121b.
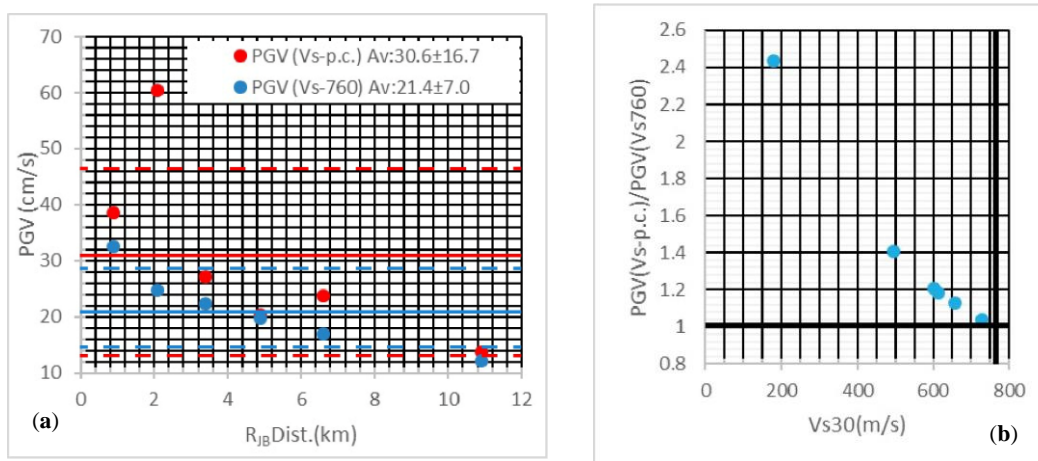
Figure 122. (a) PGV (in cm/s) computed by the REDAS software, for the scenario event of Izmir (Table 7, Appendix E, Figure 121a,b) for engineering bedrock Vs30=760 m/s (blue points), and for the specific Vs30 values (Figure 72a,b). These PGV values (blue and red points) correspond to the "cells" of Izmir city depicted in Figure 121c and Figure 121d, respectively (b) The ratio between the PGVs, of the specific Vs30 values (red points in Figure 122a) over the corresponding ones of engineering bedrockVs30=760 m/s values (blue points in Figure 122a) versus the corresponding Vs30 value of each cell.

Figure 123. (a) Distribution of SA[0.3 s] (in cm/s/s) at each geographic cell (0.005 x 0.005, degrees size), computed by the causative event scenario of the Izmir-Fault (in red line), for engineering bedrock (Vs30 = 760 m/s). The adjacent faults to the Izmir-Fault in the broader Greece-Türkiye CBA provided by the EFSM20, are also depicted. (b) Similar to Figure 123a, but for specific Vs30 values of each site specific "cell" (Figure 72a,b) (c) The same SA[0.1 s] values presented in Figure 123a, focused on the area very close to the Izmir pilot site, as it is extended within the black line. The cells included (at least their ~25%) into the examined site, are numbered. (d) Similar to Figure 123c but including the SA[0.1 s] values of Figure 123b.

Figure 124. (a) SA[0.3 s] (in cm/s/s) computed by the REDAS software, for the scenario event of Izmir (Table 7, Appendix E, Figure 123a,b) for engineering bedrock Vs30=760 m/s (blue points), and for the specific Vs30 values (Figure 72a,b). These SA[0.1 s] values (blue and red points) correspond to the "cells" of Izmir city depicted in Figure 123c and Figure 123d, respectively (b) The ratio between the SA[0.1 s], of the specific Vs30 values (red points in Figure 124a) over the corresponding ones of engineering bedrockVs30=760 m/s values (blue points in Figure 124a) versus the corresponding Vs30 value of each cell.
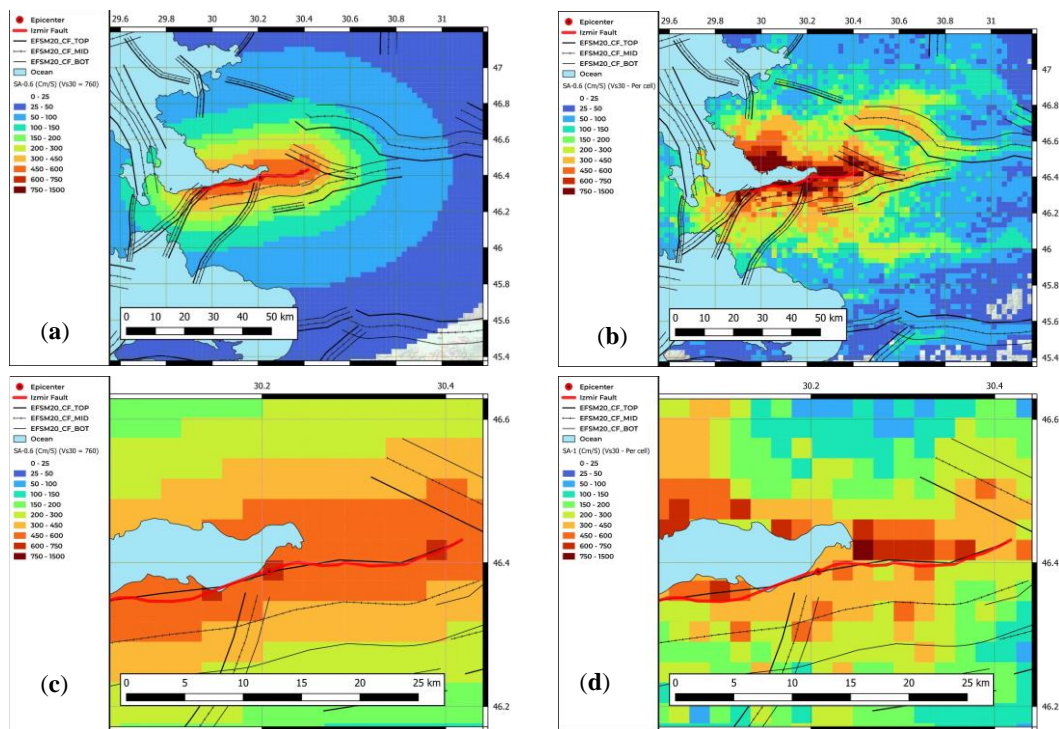
Figure 125. (a) Distribution of SA[0.6 s] (in cm/s/s) at each geographic cell (0.005 x 0.005, degrees size), computed by the causative event scenario of the Izmir fault (in red line), for engineering bedrock (Vs30 = 760 m/s). The adjacent faults to the Izmir fault in the broader Greece-Türkiye CBA provided by the EFSM20, are also depicted. (b) Similar to Figure 125a, but for specific Vs30 values of each site specific "cell" (Figure 72a,b) (c) The same SA[0.6 s] values presented in Figure 125a, focused on the area very close to the Izmir pilot site, as it is extended within the black line. The cells included (at least their ~25%) into the examined site, are numbered. (d) Similar to Figure 125c but including the SA[0.6 s] values of Figure 125b.

Figure 126. (a) SA[0.6 s] (in cm/s/s) computed by the REDAS software, for the scenario event of Izmir (Table 7, Appendix E, Figure 125a,b) for engineering bedrock Vs30=760 m/s (blue points), and for the specific Vs30 values (Figure 72a,b). These SA[0.6 s] values (blue and red points) correspond to the "cells" of Izmir city depicted in Figure 125c and Figure 125d, respectively (b) The ratio between the SA[0.6 s], of the specific Vs30 values (red points in Figure 126a) over the corresponding ones of engineering bedrockVs30=760 m/s values (blue points in Figure 126a) versus the corresponding Vs30 value of each cell.
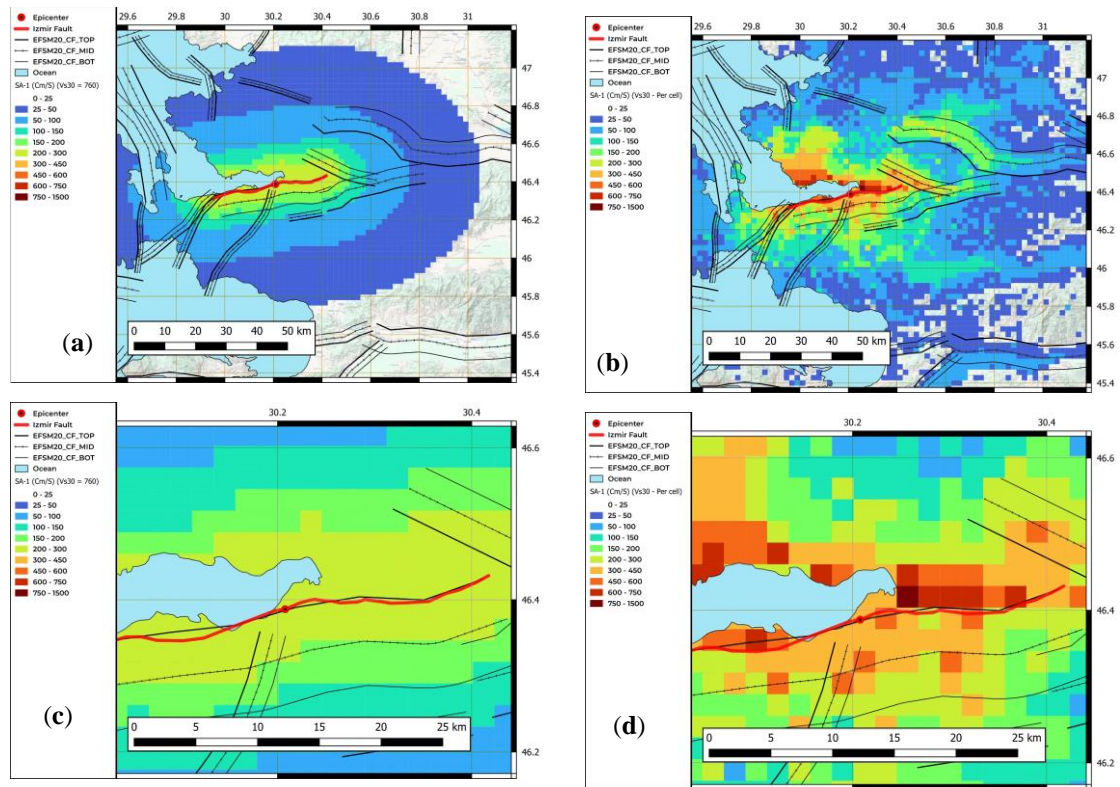
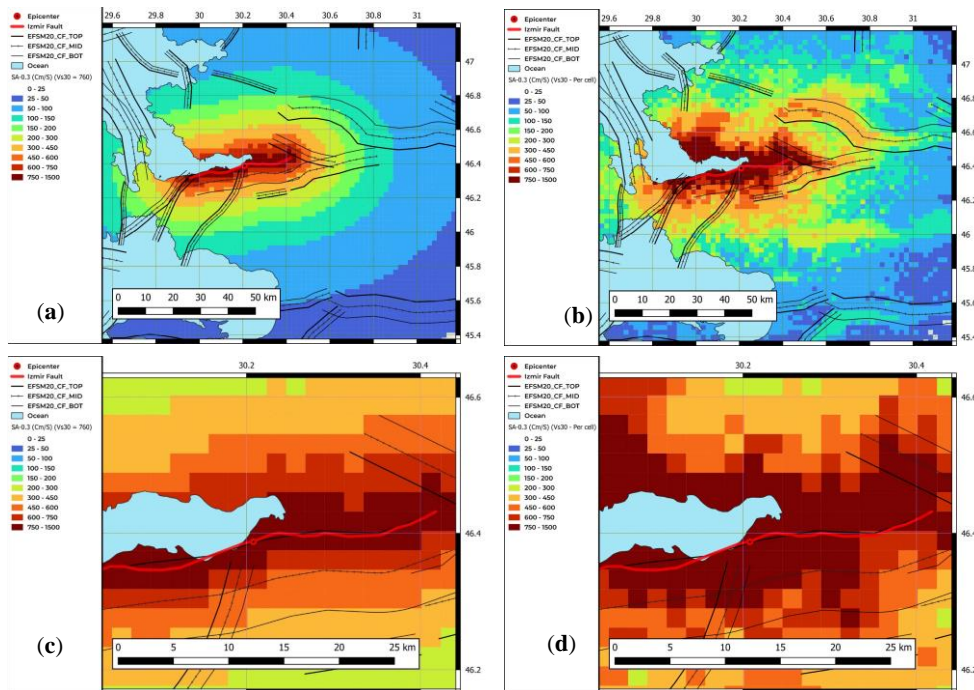**Figure 127.** (a) Distribution of SA[1 s] (in cm/s/s) at each geographic cell (0.005 x 0.005, degrees size), computed by the causative event scenario of the Izmir-Fault (in red line), for engineering bedrock (Vs30 = 760 m/s). The adjacent faults to the Izmir-Fault in the broader Greece-Türkiye CBA provided by the EFSM20, are also depicted. (b) Similar to Figure 127a, but for specific Vs30 values of each site specific "cell" (Figure 72a,b) (c) The same SA[1 s] values presented in Figure 127a, focused on the area very close to the Izmir pilot site, as it is extended within the black line. The cells included (at least their ~25%) into the examined site, are numbered. (d) Similar to Figure 127c but including the SA[1 s] values of Figure 127b.
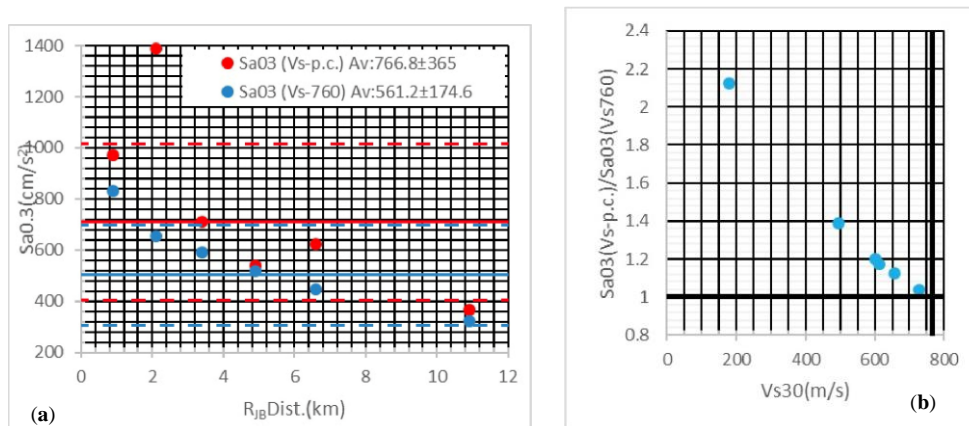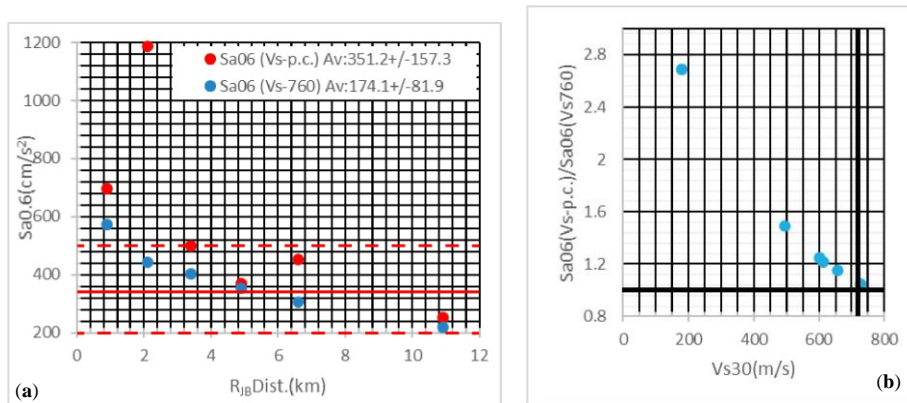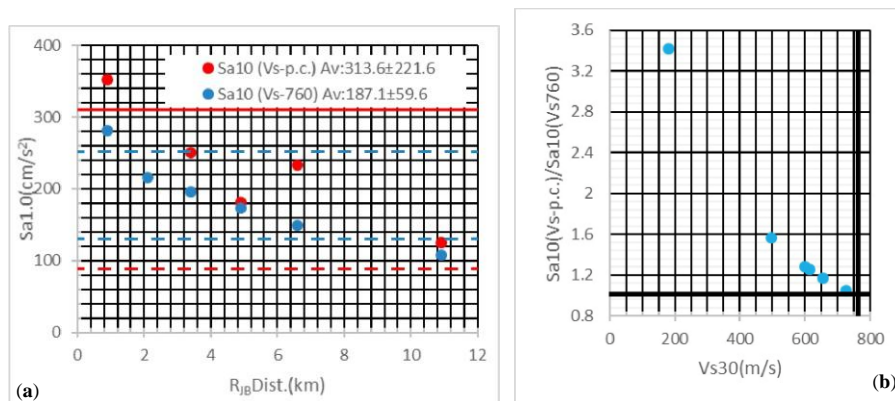

Figure 128. (a) SA[1 s] (in cm/s/s) computed by the REDAS software, for the scenario event of Izmir (Table 7, Appendix E, Figure 127a,b) for engineering bedrock Vs30=760 m/s (blue points), and for the specific Vs30 values (Figure 72a,b). These SA[1 s] values (blue and red points) correspond to the "cells" of Izmir city depicted in Figure 127c and Figure 127d, respectively (b) The ratio between the SA[1 s], of the specific Vs30 values (red points in Figure 128a) over the corresponding ones of engineering bedrockVs30=760 m/s values (blue points in Figure 128a) versus the corresponding Vs30 value of each cell.

The event.xml files of all the scenarios used in REDAS for the pilot sites Alexandroupoli, Canakkalle, Vathy, Izmir, are given in the:

- **(5) e-Supplement_5_eventxmlfiles.zip** and in the
- **Appendices A, B, C, D, E.**

In Table 4 a summary of the GMIMs of all investigated scenarios for the 4 pilot sites is presented. The estimated on 'rock' PGA values range between 0.06g to 0.46g and the PGV between 5cm/s to 39cm/s. As expected the highest values are observed in the near fault conditions of Izmir as well as of Alexandroupoli-Maronia faults.

Table 8. Ground Motion Intensity Measures (GMIMs) based on all seismic scenarios for the 4 pilot sites in the CBA.

Pilot Site →	Vathy	Alexandroupoli	Alexandroupoli	Canakkale	Izmir
Scenario fault →	N. Samos fault	Maronia-Alex/poli-fault	NAF-Ganos Fault	NAF-Ganos fault	Izmir fault
GMIMs*	Average ±1sd	Average ±1sd	Average ±1sd	Average ±1sd	Average ±1sd
PGA(cm/s/s) [s]	321.0 ±25.2	635.6 ±49.0	86.1 ±10.2	209.0 ±79.3	362.1 ±141.7
PGA(cm/s/s) [r]	294.4 ±11.9	463.3 ±06.5	55.6 ±0.8	141.8 ±58.3	294.4 ±88.1
PGV (cm/s) [s]	27.5 ±03.2	68.4 ±9.4	9.1 ±1.5	21.5 ±9.2	30.6 ±16.7
PGV (cm/s) [r]	24.0 ±01.1	39.0 ±0.7	4.7 ±0.1	11.7 ±5.2	21.4 ±7.0
SA[0.3] (cm/s/s) [s]	636.2 ±71.2	1421.5 ±148.0	166.1 ±27.5	427.4 ±181.9	766.7 ±365.6
SA[0.3] (cm/s/s) [r]	559.7 ±24.3	905.2 ±14.4	86.8 ±1.3	242.4 ±112.4	561.2 ±174.7
SA[0.6] (cm/s/s) [s]	465.5 ±62.5	1196.0 ±170.4	139.5 ±26.9	351.2 ±157.3	576.5 ±334.2
SA[0.6] (cm/s/s) [r]	397.1 ±17.7	647.0 ±11.4	64.0 ±0.9	174.1 ±81.9	382.0 ±121.5
SA[1.0] (cm/s/s) [s]	243.7 ±36.5	720.7 ±132.3	84.5 ±17.9	205.8 ±96.1	313.6 ±221.7
SA[1.0] (cm/s/s) [r]	203.4 ±09.2	330.7 ±6.1	35.5 ±0.4	91.9 ±43.2	187.1 ±59.6

* : Ground Motion Intensity Measures
[s]: Soil (Vs30<760m/s per cell)
[r]: Engin. bedrock (Vs30=760m/s per cell)

APPENDICES

Appendix A

The Samos seismic fault "Samos_fault_for_Validation.xml" used as input to the REDAS software for Validation

```
<?xml version="1.0" encoding="utf-8"?>
<earthquakes>
 <earthquake
  id="Samos_North-Simulation_Kiratzi_et_al_2022"
  lat=" 37.89190"
  lon=" 26.80660"
  mag="7.035"
  depth="8.2"
  mech="N"
  year="2020"
  month="10"
  day="30"
  hour="11"
  minute="51"
  second="25.2"
  netid="GR"
  network="NETWORK"
  timezone="LOCAL"
  locstring="Location"
  time="2020-10-30T11:51:25Z"
  created="Created By">
  <Fault
   name="Samos_North-Simulation_Kiratzi_et_al_2022"
   strike="270"
   dip="43"
   Top="0"
   Width="15.0"
   Lat="37.82401665575485   37.82453857016632   37.82532741889647   37.82587846970161
37.82653024404645       37.82574327672992       37.82442767539903       37.82380916296583
37.82215611196601 37.81742296312648"
   Lon="26.85002026906125   26.83802244226553   26.82229816794993   26.79341193536968
26.76771434251841       26.71069322732357       26.67629307233128       26.65893195617243
26.62019462433624 26.50946429601670" />
 </earthquake>
</earthquakes>
```

Appendix B
The "Samos-North.xml", including the Fault-information used as input to the REDAS software.

```
<?xml version="1.0" encoding="utf-8"?>
<earthquakes>
  <earthquake
   id="Samos-North"
   lat=" 37.8656"
   lon=" 26.8504"
   mag="7.04"
   depth="7.25"
   mech="N"
   year="0000"
   month="00"
   day="00"
   hour="00"
   minute="00"
   second="00.0"
   netid="GR"
   network="NETWORK"
   timezone="LOCAL"
   locstring="Location"
   time="0000-00-00T00:00:00Z"
   created="Created By">
   <Fault
     name="Samos-North"
     strike="274"
     dip="57"
     Top="0"
     Width="17.03"
     Lat="37.792470 37.8035  37.8121  37.8187  37.8226  37.8253  37.8265  37.8258  37.8237
37.821346"
     Lon="27.094347  27.0452  26.9903  26.9349  26.8792  26.8233  26.7673  26.7113  26.6553
26.602685" />
  </earthquake>
</earthquakes>
```

Appendix C
The "Maronia-Alexandroupolis.xml", including the Fault-information used as input to the REDAS software

```
<?xml version="1.0" encoding="utf-8"?>
<earthquakes>
  <earthquake
    id="Alexandroupolis-South"
    lat=" 40.814334"
    lon=" 25.812298"
    mag="6.96"
    depth="7.0"
    mech="N"
    year="0000"
    month="00"
    day="00"
    hour="00"
    minute="00"
    second="00.0"
    netid="GR"
    network="NETWORK"
    timezone="LOCAL"
    locstring="Location"
    time="0000-00-00T00:00:00Z"
    created="Created By">
    <Fault
      name="Alexandroupolis-South"
      strike="94"
      dip="60"
      Top="0"
      Width="16.2"
      Lat="40.84644 40.8471 40.8487 40.8513 40.851 40.8504 40.8474 40.855 40.8644
40.860625"
      Lon="26.046656 26.0137 25.9557 25.8978 25.8398 25.7818 25.7239 25.6668 25.6101
25.577492" />
  </earthquake>
</earthquakes>
```

Appendix D   The "NAF-Ganos.xml", used as input to the REDAS software

```
<?xml version="1.0" encoding="utf-8"?>
<earthquakes>
  <earthquake
    id="NAF-Ganos"
    lat=" 40.645883"
    lon=" 26.973885"
    mag="7.35"
    depth="9.5"
    mech="SS"
    year="0000"
    month="00"
    day="00"
    hour="00"
    minute="00"
    second="00.0"
    netid="GR"
    network="NETWORK"
    timezone="LOCAL"
    locstring="Location"
    time="0000-00-00T00:00:00Z"
    created="Created By">
    <Fault
      name="NAF-Ganos"
      strike="255"
      dip="82.5"
      Top="0"
      Width="19"
      Lat="40.7997557    40.80022794    40.80090625    40.80099758    40.80084108    40.80003694
40.79868961    40.79686016    40.79485723    40.7932515    40.79072418    40.78355212    40.77988461
40.77385121    40.7705556    40.76809471    40.76317867    40.75870125    40.75560538    40.75497407
40.75354651    40.75200055    40.7499877    40.74912741    40.74723131    40.74303963    40.7417369
40.74009081    40.73498095    40.73266085    40.73064635    40.7276535    40.7268758    40.7249738
40.72372583    40.72043106    40.7173483    40.71384053    40.71612857    40.71546013    40.71159703
40.70324089    40.70088305    40.69808736    40.69390717    40.69139124    40.68898323    40.68670536
40.68674738    40.68417543    40.68349956    40.68302135    40.6825047    40.68230111    40.68165555
40.67950325    40.67552393    40.67178602    40.66498863    40.66151747    40.65759982    40.65436925
40.65005063    40.645841    40.63680177    40.62699876    40.61823017    40.61731824    40.61552138
40.61526146    40.60820845    40.60643893    40.60449464    40.60318974    40.60070464    40.59846951
40.59694831    40.59497797    40.58319578    40.57937727    40.57648958    40.57420202    40.57079122
40.56804109    40.56510427    40.56171865    40.55839951    40.54943983    40.54485475    40.53859387
40.53472756 40.5258006 40.51266408 40.49841283 40.49034665 40.48450949"
      Lon="27.50530579    27.50262109    27.49647914    27.49311003    27.48784712    27.48010467
27.47342476    27.46508066    27.45942535    27.45608353    27.44887996    27.4322171    27.4238519
27.40788414    27.40291182    27.39859295    27.38996751    27.37833337    27.36986951    27.36611654
27.35623409    27.34988452    27.33951896    27.33275672    27.32593348    27.31195194    27.30501421
27.29606283    27.27871803    27.27326541    27.26472586    27.25578419    27.2498413    27.24446721
27.23813839    27.2302429    27.22162161    27.21236124    27.20722076    27.20177106    27.18196723
27.15563451    27.1487169    27.13645045    27.12221266    27.11537502    27.10993952    27.10491159
27.1020588    27.09298226    27.09142808    27.090323    27.08790274    27.08572714    27.0818696
27.07408933    27.06441549    27.05271259    27.02993865    27.02164603    27.01112579    26.99910463
26.98394853    26.97374156    26.94232838    26.91303796    26.89037282    26.88890283    26.88333133
26.88148805    26.85713452    26.85039926    26.8426088    26.83620651    26.82711141    26.81859043
26.81209924    26.80639745    26.77530902    26.76469538    26.75435802    26.74508366    26.73586258
26.72820739    26.71501072    26.70256541    26.69222134    26.66266595    26.64455812    26.62128248
26.60906431 26.58066825 26.54157868 26.50169533 26.47039888 26.4449602" />
  </earthquake>
</earthquakes>
```

Appendix E
The "Izmir.xml", used as input file to the REDAS software

```xml
<?xml version="1.0" encoding="utf-8"?>
<earthquakes>
  <earthquake
    id="Izmir"
    lat="38.41873437"
    lon="27.136118"
    mag="6.6"
    depth="13"
    mech="NN"
    year="0"
    month="0"
    day="0"
    hour="0"
    minute="0"
    second="1"
    netid="TR"
    network="NETWORK"
    timezone="LOCAL"
    locstring="Location"
    Comment=""
    time="0000-00-00T00:00:00Z"
    created="Created By">
    <Fault
      name="NAF-Ganos"
      strike="265"
      dip="67.5"
      Top="0"
      Width="13"
    Lat="38.36755898 38.38226723 38.39301604 38.39316174 38.38989113 38.38947304
38.39195451 38.39999915 38.41715612 38.41873437 38.42427539 38.42677341 38.42777117
38.4264724 38.42626671 38.42452623 38.42539722 38.4277627 38.42546482 38.42425951
38.42438649 38.42472526 38.42595879 38.43350037 38.43665747 38.44153677 38.44369355
38.44986737"
    Lon="26.91092814 26.95306374 26.98868429 27.00290567 27.01727188 27.04132929
27.06074872 27.08119527 27.12615306 27.136118 27.14910541 27.15750787 27.16337481
27.17266044 27.17956471 27.18702095 27.20328162 27.20986943 27.22652655 27.23398605
27.23914631 27.24848365 27.26919167 27.2853806 27.29752659 27.30828852 27.31316948
27.32457668" />
  </earthquake>
</earthquakes>
```

REFERENCES

Aktung, B.; Tiriakioglu I., Sozbilir, H., Özener, H., et al. (2021) "GPS derived finite source mechanism of the 30 October 2020 Samos earthquake, Mw =6.9, in the Aegean extensional region", Turkish Journal of Earth Sciences: Vol. 30: No. 8.

Algermissen, S. T., D. M. Perkins, P. C. Thenhaus, S. L. Hanson and B. L. Bender (1982). Probabilistic estimates of maximum acceleration and velocity in rock in the contiguous United-States., U.S. Geological Survey, Open file Report No 82-1033, Reston, Virginia, 99pp.

Ambraseys, N. (2009). Earthquakes in the Mediterranean and Middle East. Cambridge University Press, ISBN 9780521872928, 947pp.

Baba, A.B., Papadimitriou, E.E., Papazachos, B.C., Ch.A. Papaioannou and B.G. Karakostas, 2000. Unified local magnitude scale for earthquakes of south Balkan area. Pure Appl. Geophys., 157, 765-783

Basili, R., Danciu, L., Carafa, M. M. C., Kastelic, V., Maesano, F. E., Tiberti, M. M., Vallone, R., Gracia, E., Sesetyan, K., Atanackov, J., Sket-Motnikar, B., Zupančič, P., Vanneste, K., and Vilanova, S. (2020). Insights on the European Fault-Source Model (EFSM20) as input to the 2020 update of the European Seismic Hazard Model (ESHM20), EGU General Assembly 2020, Online, 4–8 May 2020, EGU2020-7008, https://doi.org/10.5194/egusphere-egu2020-7008.

Bernreuter, D. L., J.B. Savy, R. W. Mensing, J. C. Chen, and B. C. Davis (1985). Seismic hazard characterization of the Eastern United States, Vol. 1, Methodology and results for ten sites; UCID-20421, Vol.2 Questionnaires, Lawrence Livermore National Lab.

Bommer JJ, Scherbaum F (2008). The use and misuse of logic trees in probabilistic seismic hazard analysis. Earthquake Spectra, 24:997–1009. doi:10.1193/1.2977755.

Boore, D.; Stewart, J.P.; Skarlatoudis, A.; Seyhan, E.; Margaris, B.; Theodoulidis, N.; Scordilis, E.; Kalogeras, I.; Klimis, N.; Melis, N. (2021). A Ground-Motion Prediction Model for Shallow Crustal Earthquakes in Greece. Bull. Seism. Soc. Am., 111, 857–874, https://doi.org/10.1785/0120200270.

Caputo, R., Pavlides, S., 2013. The Greek Database of Seismogenic Sources (GreDaSS), version 2.0.0: A compilation of potential seismogenic sources (Mw > 5.5) in the Aegean Region.

Cetin K.O., G Mylonakis, A Sextos and J. P. Stewart (2020)(editors). Seismological and Engineering Effects of the M7.0 Samos Island (Aegean Sea) Earthquake, Report of HAEE:2020/02 and GEER-069, 1-374pp.

Chiou, B.S.J.; Youngs, R.R. (2014). NGA model for the average horizontal component of peak ground motion and response spectra. Earthq. Spectra, 30, 1117–1153, https://doi.org/10.1193/072813eqs219m.

Chousianitis, K., Konca, A.O., 2021. Rupture Process of the 2020 Mw7.0 Samos Earthquake and its Effect on Surrounding Active Faults. Geophys. Res. Lett. 48, 1–10.

Comninakis, P.E. and Papazachos, B.C., 1986. A catalogue of earthquakes in Greece and surrounding area for the period 1901-1985. Publ. Lab., Univ. of Thessaloniki, 1, 167 pp..

Cornell, C. A. (1968). Engineering seismic risk analysis.Bull. Seism. Soc. Am.,58,1503-1606.

Cornell, C.A. and E.H. Vanmarcke (1969). The major influences on seismic risk, Proc. Of the 3d W.C.E.E. Santiago Chile,A-1, 69-93.

Danciu, L., Nandan, S., Reyes, C., Basili, R., Weatherill, G., Beauval, C., Rovida, A., Vilanova, S., Sesetyan, K., Bard, P.-Y., et al. (2021). The 2020 update of the European Seismic Hazard Model: Model Overview, EFEHR Technical Report 001, v1.0.0; ETH Zürich: Zürich, Switzerland, 2021.

Demircioğlu, M.B., Şeşetyan, K., Duman, T.Y. et al. (2018). A probabilistic seismic hazard assessment for the Turkish territory: part II—fault source and background seismicity model. Bull Earthquake Eng 16, 3399-3438 (2018). https://doi.org/10.1007/s10518-017-0130-x.

Demirci, H.E., Karaman, M. and Bhattacharya, S., 2022. A survey of damage observed in Izmir due to 2020 Samos-Izmir earthquake. Natural Hazards, 111(1), pp.1047-1064.

Duni, L., Sh. Kuka and N. Kuka, 2010. Local relations for converting ML to MW in southern-western Balkan region. Acta Geod. Geoph. Hung., 45(3), 317–323.

Emre, Ö., Duman, T.Y., Özalp, S., Şaroğlu, F., Olgun, Ş., Elmacı, H., Çan, T., 2018. Active fault database of Turkey. Bull. Earthq. Eng. 16, 3229–3275.

Foumelis, M., Papazachos, C., Papadimitriou, E., Karakostas, V., Ampatzidis, D., Moschopoulos, G., Kostoglou, A., Ilieva, M., Minos-Minopoulos, D., Mouratidis, A., Kkallas, C., Chatzipetros, A., 2021. On rapid multidisciplinary response aspects for Samos 2020 M7.0 earthquake. Acta Geophys. 69, 1025–1048.

Engdahl, E. R., and A. Villaseñor (2002). Global seismicity: 1900–1999. In International Handbook of Earthquake and Engineering Seismology, Part A, ed. W. H. K. Lee, H. Kanamori, P. C. Jennings, and C. Kisslinger, 665–690. Boston: Academic Press.

EPET II, (1999). Seismicity of the Hellenic Arc and seismic hazard for the Heraklion site, Minist. of Industry, Energy and Techn. Gen Secr. of Research and Techn., Subprog. 1, W. 654.

Ganas, A., Oikonomou, I.A., Tsimi, C., 2013. NOAfaults: a digital database for active faults in Greece. Bull. Geol. Soc. Greece 47, 518–530.

Ganas, A., Tsironi, V., Kollia, E., Delagas, M., Tsimi, C., Oikonomou, A., 2018. Recent upgrades of the NOA database of active faults in Greece (NOAFAULTs). 19th Gen. Assem. WEGENER, Sept. 2018, Grenoble.

Ganas, A., Elias, P., Briole, P., Valkaniotis, S., Escartin, J., Tsironi, V., Karasante, I. and Kosma, C., 2021. Co-seismic and post-seismic deformation, field observations and fault model of the 30 October 2020 Mw= 7.0 Samos earthquake, Aegean Sea. Acta Geophysica, 69(3), pp.999-1024.

GEER Report, 2020. Seismological and Engineering Effects of the M7.0 Samos island (Aegean sea) Earthquake.

Gülerce, Z. and Abrahamson, N. (2020). Regionalized Ground-Motion Models for Subduction Earthquakes Based on the NGA-SUB Database, PEER Report No. 2020/25.

Gutenberg, B. and C. F. Richter (1954). Seismicity of the earth and associated phenomena, 2d edit: Princeton Univ. Press, New Jersey, 310pp.

Gutenberg, B. and Richter, C.F. (1956). Magnitude and energy of earthquakes, Ann. Geofis. 9, 1–15.

Hatzidimitriou, P.M. (1984). Seismogenic volumes and seismic sources of the Aegean and surrounding area, PhD Thesis Univ. of Thessaloniki, 162 pp.

Karnik, V. (1996). Seismicity of Europe and the Mediterranean. In: Klima, K. (ed.), Academy of Sciences of the Czech Republic, Geophysical Institute, 28 pp. plus earthquake catalogue.

Kiratzi, A., Papazachos, C., Özacar, A., Pinar, A., Kkallas, C., Sopaci, E., 2022. Characteristics of the 2020 Samos earthquake (Aegean Sea) using seismic data. Bull. Earthq. Eng. 20, 7713–7735.

Koliopoulos, P.K., B.N. Margaris, and N.S. Klimis (1998). Duration and energy characteristics of Greek strong motion records, J. of Earthquake Eng., 2, 391-417.

Koutrakis, S., B.N. Margaris, P.K. Koliopoulos and G.F. Karakaisis (1999). New trebs in seismic hazard evaluation in Greece, Proc., IUGG XXII Meeting in Birmingham, 19-30 July 1999,II , B.181 (Abst).

Kuehn, N., Bozorgnia Y., Campbell K., Gregor, N. (2020). Partially Non-Ergodic Ground-Motion Model for Subduction Regions using the NGA-Subduction Database, PEER Report No. 2020/04.

Margaris, B.N (1994). Azimuthal dependence of seismic waves and its influence in the seismic hazard assessment in the area of Greece, PhD Thesis Univ. of Thessaloniki, 324pp.

Lentas, K., Gkarlaouni, C., Kalligeris, N., Melis, N., 2021. The 30 October 2020, Mw 7.0, Samos Earthquake: Aftershock Relocation, Slip Model, Coulomb Stress Evolution and Estimation of Shaking.

Margaris B.N. and B.C. Papazachos (1994). Implication of the azimuthal variation of seismic intensities in seismic hazard assessment, Proc. of Eur. Seism. Comm. XXIV Gen. Assembly, Sept. 19-24, 1994, Athens, Greece,III, 1718-1728.

McGuire, R.K. (1976). FORTRAN computer program for seismic risk analysis, U.S. Geological Survey, Open File Rep., No 76-77, 90 pp.

Pagani, M.; Monelli, D.;Weatherill, G.; Danciu, L.; Crowley, H.; Silva, V.; Henshaw, P.; Butler, L.; Nastasi, M.; Panzeri, L.; et al. (2014). OpenQuake Engine: An Open Hazard (and Risk) Software for the Global Earthquake Model. Seismol. Res. Lett., 85, 692–702, https://doi.org/10.1785/0220130087.

Pacheco, J.F., Sykes, L.R., 1992, Seismic moment catalog of large shallow earthquakes, 1900 to 1989. Bull Seism Soc Am 82:1306-1349.

Pagani, M., V. Silva, A. Rao, M. Simionato and K Johnson (2023) OpenQuake Engine Manual, Rel.Dev.(3.19.0), pp 230.

Papaioannou, C.A.; Papazachos, B.C. (2000). Time-Independent and Time-Dependent Seismic Hazard in Greece Based on Seismogenic Sources. Bull Seismol. Soc. Am., 90, 22–33.

Papatheodorou K., Theodoulidis N., Klimis N., Zulfikar C, Vintila D., Cardanet V., Kirtas E., Toma-Danila D., Margaris B., FahjanY. et al.(2023). Rapid Earthquake Damage Assessment and Education to Improve Earthquake Response Efficiency and Community Resilience. Sustainability 2023, 15, 16603. https://doi.org/10.3390/su152416603.

Papazachos, B.C., Ch.A. Papaioannou, D.J. Papastamatiou, B.N. Margaris and N.P. Theodulidis (1990). On the reliability of different methods of seismic hazard assessment in Greece, Natural Hazards, 3, 141-151.

Papazachos, B.C., B.N. Margaris, N.P. Theodulidis, and Ch.A. Papaioannou (1992). Seismic hazard assessment in Greece based on strong motion duration, Proc. 10th W.C.E.E. Madrid, 1992,1, 425-430.

Papazachos, C.B. (1992). Anisotropic radiation modelling of macroseismic intensities for estimation of the attenuation structure of the upper crust in Greece, PAGEOPH, 138, 445-469.

Papazachos, B.C. and Ch .A. Papaioannou (1993). Long-term earthquake prediction in the Aegean area based on a time and magnitude predictable model, Pure. Appl. Geophys., 140,593-612.

Papazachos, B.C. and Ch. A. Papaioannou (1997). Seismic hazard in Greece based on new seismotectonic data.IASPEI 29th General Assembly Thessaloniki,18-30 August, 1997.

Papazachos B. and C. Papazachou, (1997). The earthquakes of Greece, Ziti publications, ISBN 960-431-416-5, 304pp.

Papazachos, B.C., Kiratzi, A.A. and Karakostas, B.G. (1997). Toward a homogeneous moment-magnitude determination for earthquakes in Greece and surrounding area, Bull. Seism. Soc. Am., 87, 474-483.

Papazachos, B.C. and Papazachou, C.B., (2003). The earthquakes of Greece, Ziti Publications, Thessaloniki, 273pp (in Greek).

Parker GA, Stewart JP, Boore DM, Atkinson GM, Hassani B. (2020). NGA-subduction global ground motion models with regional adjustment factors. PEER Report No. 2020/03.

Pavlides, S., Caputo, R., Sboras, S., Chatzipetros, A., Papathanasiou, G., Valkaniotis, S., 2010. The Greek Catalogue of Active Faults and Database of Seismogenic Sources. Bull. Geol. Soc. Greece 43, 486–494.

Plicka, V., Gallovič, F., Zahradník, J., Serpetsidaki, A., Sokos, E., Vavlas, N., Kiratzi, A., 2022. The 2020 Samos Mw7 earthquake: Source model depicting complexity and rupture directivity. Tectonophysics 843.

Poggi, V., Garcia-Peláez, J., Styron, R. et al. (2020). A probabilistic seismic hazard model for North Africa. Bulletin of Earthquake Engineering 18, 2917–2951. https://doi.org/10.1007/s10518-020-00820-4.

Rahman, A.u., Najam, F.A., Zaman, S. et al. (2021). An updated probabilistic seismic hazard assessment (PSHA) for Pakistan. Bulletin of Earthquake Engineering 19, 1625–1662. https://doi.org/10.1007/s10518-021-01054-8

Ren, C., Yue, H., Cao, B., Zhu, Y., Wang, T., An, C., Ge, Z. and Li, Z., 2022. Rupture process of the 2020 Mw= 6.9 Samos, Greece earthquake on a segmented fault system constrained from seismic, geodetic, and tsunami observations. Tectonophysics, 839, p.229497.

Sakkas, V., 2021. Ground deformation modelling of the 2020 Mw6. 9 Samos earthquake (Greece) based on INSAR and GNSS data. Remote Sensing, 13(9), p.1665.

Sboras, S., Caputo, R., Pavlides, S., Chatzipetros, A., Papathanasiou, G., Valkaniotis, S., 2009. The Greek Database of Seismogenic sources (GreDaSS): state-of-the-art. Proc. 28° Convegno Naz. di Grup. Naz. di Geofis. della Terra Solida, 16-19 November, 2009, Ext. Abstr. 126–128.

Scordilis, E. M. (2006). Empirical global relations converting Ms and mb to moment magnitude, Journal of Seismology 10, 225-236.

Scordilis, E.M., 2005. Globally valid relations converting Ms, mb and MJMA to Mw. NATO Advanced Research Workshop on Earthquake Monitoring and Seismic Hazard Mitigation in Balkan Countries, 11-17 September 2005, the Rila Mountains-Resort Borovetz, Bulgaria, Abstracts book, 158-161.

Sesetyan, K., Demircioglu, M.B., Duman, T.Y. et al. (2018). A probabilistic seismic hazard assessment for the Turkish territory—part I: the area source model. Bull Earthquake Eng 16, 3367–3397 (2018). https://doi.org/10.1007/s10518-016-0005-6.

Şeşetyan, K., Demircioğlu Tümsa, M. B., & Akinci, A. (2019). Evaluation of The Seismic Hazard in The Marmara Region (Turkey) Based on Updated Databases. Geosciences, 9(12), 489. https://doi.org/10.3390/geosciences9120489.

Skarlatoudis A.A, Papazachos C. B., Margaris B. N., Ventouzi C., Kalogeras I., the EGELADOS Group. (2013). Ground-Motion Prediction Equations of Intermediate-Depth Earthquakes in the Hellenic Arc, Southern Aegean Subduction Area. Bulletin of the Seismological Society of America; 103 (3): 1952–1968. doi: https://doi.org/10.1785/0120120265.

Sotiriadis, D., Margaris, B., Klimis, N., & Dokas, I. M. (2023). Seismic Hazard in Greece: A Comparative Study for the Region of East Macedonia and Thrace. GeoHazards, 4(3), 239-266, https://doi.org/10.3390/geohazards4030014.

Stewart J.P., Klimis N., Savvaidis A., Theodoulidis N., Zargli E., Athanasopoulos G., Pelekis P., Mylonakis G., and Margaris B. (2014). Compilation of a local Vs profile database and its application for inference of VS30 from geologic and terrain-based proxies, Bull. Seism. Soc. Am., 104 (6): 2827-2841.

Theodulidis, N.P. (1991). Contribution to the study of strong ground motion in Greece. PhD Thesis, University of Thessaloniki, 500 pp.

Theodoulidis, N., B. Margaris, D. Sotiriadis, C. Zulfikar, S.O. Akcan, C.O. Cioflan, E.F. Manea, and D. Toma-Danila. (2024). Rapid Earthquake Damage Assessment System in the Black Sea Basin: Selection/Adoption of Ground Motion Prediction Equations with Emphasis in the Cross-Border Areas. GeoHazards 5, no. 1: 255-270. https://doi.org/10.3390/geohazards5010013.

Tsampas, A.D., E.M. Scordilis, C.B. Papazachos and G.F. Karakaisis. Global magnitude scaling relations for intermediate-depth and deep-focus earthquakes, Bull. Seism. Soc. Am., doi: 10.1785/0120150201, 106, 2, 418–434, 2016.

Vamvakaris, D.A.; Papazachos, C.B.; Papaioannou Ch, A.; Scordilis, E.M.; Karakaisis, G.F (2016). A detailed seismic zonation model for shallow earthquakes in the broader Aegean area. Nat. Hazards Earth Syst. Sci., 16, 55–84.

Stewart J.P., Klimis N., Savvaidis A., Theodoulidis N., Zargli E., Athanasopoulos G., Pelekis P., Mylonakis G., and Margaris B. (2014). Compilation of a local Vs profile database and its application for inference of VS30 from geologic and terrain-based proxies, Bull. Seism. Soc. Am., 104 (6): 2827-2841.

Woessner, J.; Danciu, L.; Giardini, D.; Crowley, H.; Cotton, F.; Grünthal, G.; Valensise, G.; Arvidson, R.; Basili, R.; Demircioglu, B.; et al. (2015). The 2013 European Seismic Hazard Model: Key components and results. Bull Earthq. Eng.,13, 553–3596.

Youngs, R.R. and K.J. Coppersmith (1985). Implication of fault slip rates and earthquake recurrence models for probabilistic seismic hazard estimates, Bull. Seism. Soc. Am., 75, 939-964.